Mechanisms of Regulation of Cytoplasmic Dynein

Mechanisms of Regulation of Cytoplasmic Dynein

A dissertation presented

By

Zaw Min Htet

to

The Committee on Higher Degrees in Biophysics

in partial fulfillment of the requirements

for the degree of

Doctor of Philosophy

in the subject of

Biophysics

Harvard University

Cambridge, Massachusetts

February 2019

Dissertation Advisor: Author:

Professor Samara L. Reck-Peterson **Zaw Min Htet**

Mechanisms of Regulation of Cytoplasmic Dynein

Abstract

Cytoplasmic dynein-1 (dynein) is a microtubule-based motor protein that is essential for maintaining proper spatial and temporal organization of the cellular interior during both interphase and cell division. To do so, dynein carries out diverse functions including transport of intracellular cargos, organelle anchoring, mitotic spindle assembly and nuclear migration. To carry out these diverse functions, dynein is regulated by multiple factors including Lis1, dynactin and activating adaptors. In this thesis, I present interdisciplinary work investigating the mechanisms of regulation of dynein. In chapter 2, a combination of biochemistry, single-molecule assays and cryo-electron microscopy was used to investigate how yeast dynein is regulated by Lis1. Previous work showed that Lis1 binds directly to dynein's AAA+ motor domain and slows its motility by causing dynein to tightly bind microtubules. The work presented here revealed that in addition to this role, Lis1 can also induce dynein to weakly bind microtubules. The mode of regulation used by Lis1 is determined by the nucleotide state at dynein's third AAA domain and the stoichiometry of the Lis1-dynein interaction. Both modes of Lis1 regulation of dynein are required for dynein to position the mitotic spindle in yeast cells. In chapter 3, the mechanism of regulation of human dynein by Lis1 is investigated. Human dynein requires dynactin and an activating adaptor for directional long-distance movement on microtubules. The work presented here shows that Lis1

promotes the formation of a maximally activated dynein complex consisting of dynein, dynactin and an activating adaptor. Finally, in chapter 4, the identification of the dynein protein interactome is described. Two novel dynein activating adaptors, ninein and ninein-like, were discovered and shown to activate dynein/dynactin motility in single-molecule assays. Overall, the work presented here reveals novel insights into complex regulation of dynein.

Table of Contents

Acknowledgements

What an exhilarating adventure! This is the first thought that comes to my mind as I sit down to reflect on my graduate school journey. Writing this section is perhaps the most difficult part of writing my thesis because I get overwhelmed with many joyful memories, thanks to the following people who make my dream of getting a PhD possible and my graduate school journey fun and exciting.

First and foremost, I would like to thank my thesis advisor, Sam Reck-Peterson. Her exceptional support and mentorship made my graduate school journey smooth sailing. She gave me freedom to drive my projects yet she made sure to guide me not to lose sight of the big questions. She made sure to mentor my scientific presentation, mentoring and leadership skills so that I could become a well-rounded scientist. I admire and thank her for her dedication and effort to create a fun and collaborative lab environment with amazing and talented group of scientists. I appreciate her generosity for supporting my passion in science education by allowing me to lead a biology bootcamp and participate in a science education workshop.

I would also like to thank my unofficial advisor, Andres Leschziner. He provided me guidance from the very beginning of my graduate school journey. I would also like to thank him for fantastic collaboration with his lab for one of my projects. His keen mind for mechanistic details led our collaborative project to fantastic discovery. I would also like to thank my summer undergraduate research mentors, Aaron Hoskins and Josh Larson, and my postbaccaluarate research mentors, Ahmet Yildiz and Frank Cleary, for giving me opportunities to learn the beauty and power of single-molecule biophysics. They all ignited my passion for science, supported and made sure that I succeeded in graduate school applications.

I would also like to my qualifying exam and thesis committee members- Stirling Churchman, Joe Loparo and Wesley Wong, and my dissertation advisory committee members- Kevin Corbett, Arshad Desai and Jin Zhang for their support, keen insights and critical feedback during my graduate school journey. I would also like to thank Harvard biophysics program chair, Jim Hogle, and program administrator, Michele Eva-Pfeffer. Their support made navigating graduate school easy. I especially want to thank Jim and Michele for making sure that my move to UCSD with Sam to finish my thesis projects went as smoothly as possible.

My graduate school journey feels like an epic adventure thanks to the most amazing group of scientists at the Reck-Peterson lab, both past and present, including Morgan, John, Mike, Salo, Jenna, Aga, Bret, Tien, Ian, Anthony, David, Rachael, Alex, Andrea, Adrianna, Oscar and Kelly. Thank you all for creating a lab environment that feels like a big family. Not a single day in the lab was dull. Every day was full of stimulating scientific discussion, witty banters and contagious laughter. As Maya Angelou once said "People will forget what you said, people will forget what you did, but people will never forget how you made them feel," I won't remember the exact conversations we had or the exact things we did together. However, I will vividly remember all the great feelings of joy, admiration, inspiration, satisfaction and awe every single one of you made me feel during my graduate school journey. I thank you all for that!

I especially would like to thank Morgan and John. Thank you for being amazing collaborators and baymates. Collaborating with both of you was truly an extraordinary experience. We could talk for hours on ideas and finish each other's scientific thoughts. We truly are "scientific soulmates" as we like to call ourselves. Most importantly, thank you for being great friends. I could always talk to you about anything except maybe about the movie Crash (to Morgan) or the movie

Up (to John). Other than that, you both were amazing listeners and always there for me whenever I need to talk.

I would also like to thank Mike, Salo, Jenna and Aga for being a great colleague and even better friend. Mike, collaborating with you was an amazing experience. Your calm and composed demeanor kept my morale whenever our collaborative project seems too daunting to finish. Your keen mechanistic insights lifted our collaborative project to a greater height. Salo, thank you for our endless conversations about science and Marvel movies during our daily shuttle ride. Thank you for letting me be an unofficial uncle to two amazing children of yours. Jenna, you were the ball of sunshine in the lab. Your enthusiasm and laughter were contagious. Thank you also for being the best lab-lunch buddy one could ever ask for. Aga, our constant prank and dramatic staring contests truly were spectacular. Thank you for making me laugh every day and laughing at my silly jokes.

Last but not least, I would like to thank my family. Without their uncoditional love and support, I would not be where I am today.

My aunts, May Lee, May Lai and May Shin, and uncles, Mg Tin and Richard Lee, were the primary support system when my dad and I immigrated into the US for my higher education. You all treated me like your own son and cared for me with unconditional love and support. For that, I thank you all from the bottom of my heart. I would also like to thank my godmother, Mi Mi Khine. She ignited my curiosity for science during my middle school and continues to inspire me every single day.

Last but not least, I want to thank three most important people in my life- my mom, Mya Mya Than, dad, Khin Mg Yin, and late grandma, May. You all have made great sacrifices for me so that I can be where I am today. Thank you for always encouraging me to pursue my dreams and

supporting me unconditionally along the way. Your unwavering support and devotion got me through the ups and downs of graduate school and continue to inspire me. Thank you all for showing me the value of hard work, compassion, humility and empathy. Mom, your journey as one of the few female physicists in Myanmar and your passion as physics educators are my main source of inspirations for my passion in science and science education. Dad, I will never be able to fully grasp all the sacrifices you made so that you can be here with me in the US to support me through my education journey. Grandmom, even though you are no longer with us, your spirit is always in my heart to inspire me to be the best version of myself every day. I love you all and thank you all with all my heart.

This thesis is dedicated to my family:

my mother Mya Mya Than,

my father Khin Mg Yin,

and my grandmother May.

Chapter 1

Introduction to regulation of cytoplasmic dynein

1.1 Introduction to the microtubule cytoskeleton and microtubule-based motor proteins

The microtubule cytoskeleton and its associated motor proteins, kinesins and dyneins, carry out the spatial and temporal organization of the crowded interior of eukaryotic cells. This task is essential for proper cell function, division, survival and development. During interphase, various cellular components such as membrane-bound vesicles (Lacey and Haimo, 1992; Okada et al., 1995; Setou et al., 2000), organelles (Hirokawa, 1998; Hirokawa et al., 1990; Schnapp et al., 1985; Schroer et al., 1989), aggregated proteins (García-Mata et al., 1999; Johnston et al., 2002) and large ribonucleoprotein particles (Bullock and Ish-Horowicz, 2001; Kanai et al., 2004; Wilkie and Davis, 2001) are efficiently and accurately transported along microtubules by kinesins and dyneins to different intracellular locations according to cellular needs. During mitosis, the microtubule cytoskeleton organizes to form mitotic spindles that drive chromosome segregation and microtubule-based motor proteins assist the formation of mitotic spindles as well as other mitotic functions such as kinetochore-microtubule attachment and spindle checkpoint inactivation.

Microtubules are highly dynamic and polar structures with minus ends typically embedded in microtubule-organizing centers around the nucleus of the interphase cell and plus ends generally located near the periphery of the cell (Hyman and Karsenti, 1998; Mitchison and Kirschner, 1984). There are 45 different kinesin genes in human cells. Most of these kinesins move toward microtubule plus ends and carry out plus-end-directed transport as well as mitotic functions (Hirokawa et al., 2009). Dyneins, on the other hand, walk toward the microtubule minus ends (Paschal and Vallee, 1987; Schroer et al., 1989). Although there are 15 dynein genes in human cells, only a single dynein gene, cytoplasmic dynein-1 (dynein herein), is responsible for all minus-end-directed transport in the cytoplasm as well as mitotic functions (Reck-Peterson et al., 2018). It is remarkable how a single dynein carries out similar functions to dozens of different kinesins.

To achieve such functional versatility, dynein is heavily regulated. In this thesis, I present the work I have been involved in to investigate molecular mechanisms of dynein regulation by its ubiquitous regulators:- Lis1, dynactin and activating adaptors, using interdisciplinary approaches including proteomic, structural, biochemical and single-molecule fluorescence techniques.

1.2 Structure of dynein

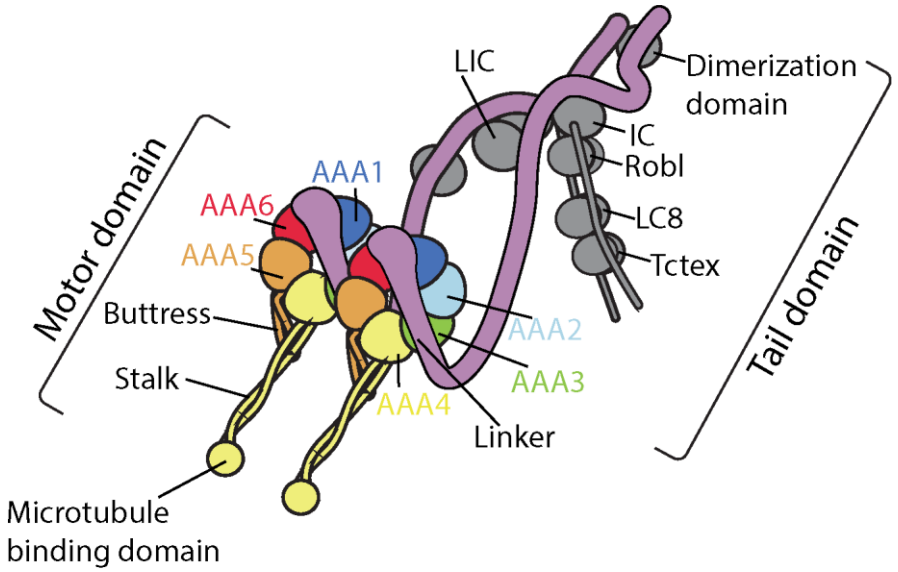

Figure 1.1. Cartoon model of cytoplasmic dynein complex. Cytoplasmic dynein is a homo-dimer consisting of two copies each of the heavy chain (shown in rainbow color), intermediate chain (IC), light intermediate chain (LIC) and three different light chains (Robl, LC8, Tctex). The intermediate chain serves as the binding platform for dynein light chains. The heavy chain can be functionally divided into the tail and motor domains. The tail domain contains the dimerization domain of the heavy chain and binds to the ICs and LICs. The motor domain consists of the AAA+ (**A**TPases **A**ssociated with various cellular **A**ctivities) ring composed of six AAA domains (AAA1-6) and three protrusions:- the linker, stalk and buttress. The linker connects the AAA+ ring to the tail domain and the coiled-coil stalk extends to the microtubule binding domain (MTBD). This figure is adapted from (Reck-Peterson et al., 2018).

Dynein is a ~1.4MDa holoenzyme complex containing dimers of six different polypeptides (Figure 1.1). The largest polypeptide is the heavy chain, which is a member of the AAA+ (**A**TPases **A**ssociated with various cellular **A**ctivities) ATPase family of proteins (Mocz and Gibbons, 2001). The dynein heavy chain can be functionally divided into two domains, an amino-terminal tail domain and a carboxy-terminal motor domain (Reck-Peterson et al., 2006). The tail domain serves as the dimerization domain of dynein and the binding platform for the other dynein polypeptide chains (two copies each of the intermediate chain [IC], the light intermediate chain [LIC] and three different light chains [Robl, LC8 and Tctex]) (Urnavicius et al., 2015; Zhang et al., 2017).

The motor domain of dynein is the minimal region necessary to generate movement and force along microtubules (Reck-Peterson et al., 2006). The motor domain consists of a ring of six concatenated AAA+ domains: AAA1-6. Out of these six AAA+ domains, AAA1 is the primary ATPase site required for dynein motility (Kon et al., 2004). AAA2 only binds ATP, however, mutations blocking ATP binding at AAA2 only have a minor effect on dynein motility (Numata et al., 2008). AAA3 and AAA4 domain both bind and hydrolyze ATP. The ATPase activity of AAA3 has been shown to play an important regulatory role in dynein motility (Cho et al., 2008; DeWitt et al., 2014; Kon et al., 2004), which will be explained in detail later in this introduction. Disrupting ATP binding or hydrolysis at AAA4 affects dynein motility to a small extent (Cho et al., 2008; Kon et al., 2004). AAA5 and AAA6 do not bind nucleotide and serve as structural domains transmitting conformational changes throughout the AAA+ ring (Gleave et al., 2014).

Three structural protrusions, the linker, stalk and buttress, emerge from the AAA+ ring. The linker is amino-terminal to AAA1 and connects the AAA+ ring to the tail domain. It undergoes large conformational change from straight to bent position during dynein's ATPase cycle (State 2 to 3 and State 5 to 6 in Figure 1.2) and this conformational change generates force to drive cargo

transport (Burgess et al., 2003; Kon et al., 2005; Roberts et al., 2009). The linker makes extensive contacts with dynein's AAA+ ring and these contacts are essential for inducing linker conformational change during dynein's ATPase cycle (Bhabha et al., 2014; Carter et al., 2011; Kon et al., 2012; Schmidt et al., 2012, 2015).

Dynein's ATPase cycle is coupled to the microtubule binding domain (MTBD) via the stalk and buttress (Carter et al., 2008; Gibbons et al., 2005; Kon et al., 2009). The stalk is a 15 nm-long, coiled-coil protrusion from AAA4, while the MTBD lies at the end of the stalk (Carter et al., 2011; Gee et al., 1997; Kon et al., 2011). The registry of the coiled-coil helices of the stalk allosterically changes the microtubule binding affinity of the MTBD (Carter et al., 2008; Gibbons et al., 2005; Kon et al., 2009; Redwine et al., 2012). A second coiled-coil protrusion from AAA5 is called the buttress, which contacts the stalk and facilitates the coiled-coil registry changes of the stalk (Carter et al., 2011; Kon et al., 2012; Schmidt et al., 2015).

Finally, the last domain of the dynein motor domain is the carboxy-terminal domain. It contacts the opposite face of the AAA+ ring as the linker (Carter et al., 2011; Kon et al., 2011; Zhang et al., 2017). The carboxy-terminal domain is only a short alpha-helix in *Saccharomyces cerevisiae*, whereas it is an extended domain in many other eukaryotes (Carter et al., 2011; Kon et al., 2012; Schmidt et al., 2015). Removal of the extended carboxy-terminal domain from *Dictyostelium discoideum* dynein decreases dynein motility in vitro (Numata et al., 2011), whereas its removal from mammalian dynein increases the force production and run length of dynein in vitro (Nicholas et al., 2015a).

1.3 Mechano-chemical cycle of dynein

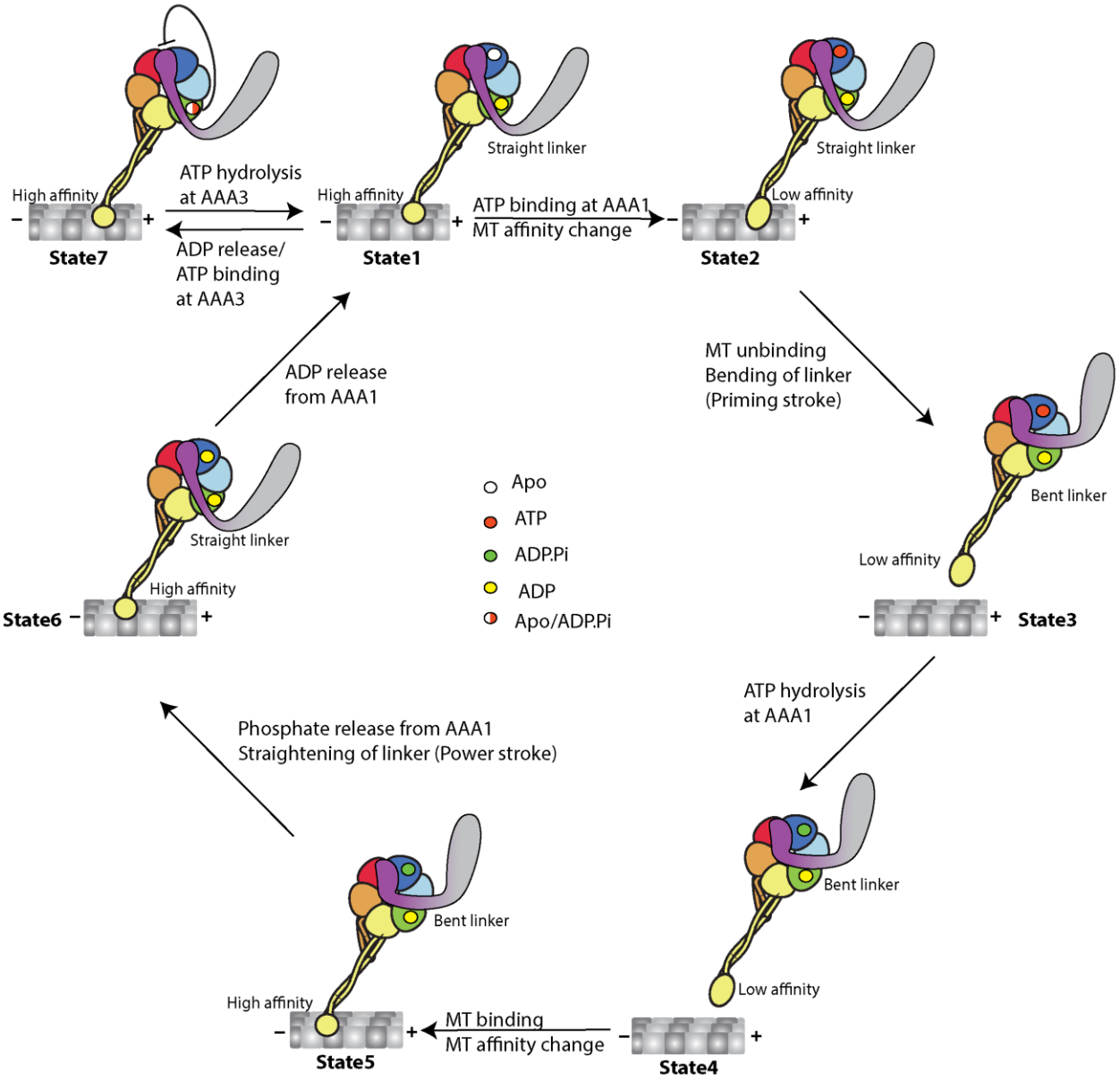

Figure 1.2. Model of dynein's mechano-chemical cycle. A monomer of the dynein heavy chain is only shown for simplicity. Refer to the main text for a detailed description of each state of the cycle. The nucleotide occupancy states of the main ATPase site, AAA1, and the master regulatory site, AAA3, are color-coded as noted. Plus and minus signs denote the polarity of microtubules. States 1-6 represent the dynein states when AAA3 is ADP-bound. State 7 occurs when AAA3 is either apo or ATP-bound and blocks the allosteric communication between the ATPase activity of

(continued) AAA1, the linker domain and the microtubule binding domain. This figure is adapted from (Cianfrocco et al., 2015).

Dynein is a complex molecular machine that undergoes major conformational changes in its AAA+ ring, linker, stalk and MTBD domains in relation to its ATPase cycle at the primary ATPase site, AAA1 (Cianfrocco et al., 2015; Roberts et al., 2013). These allosteric conformational changes within dynein's domains (termed mechano-chemical cycle) drive its ability to walk along microtubules and transport various cargos. Throughout the mechano-chemical cycle, dynein's conformational states can be simplified into two main states, high microtubule affinity and low microtubule affinity states (Figure 1.2). By simply switching between these two states, dynein walk along microtubules. Before going through the details of the dynein's mechano-chemical cycle, I will first compare and contrast these two states.

When AAA1 is either apo (no nucleotide) or ADP-bound, dynein adopts a high microtubule affinity state (State 1 and 6, Figure 1.2) (Bhabha et al., 2014; Carter et al., 2011; Kon et al., 2011, 2012; Schmidt et al., 2012). When AAA1 is either ATP-bound or ADP.Pi-bound, dynein is in a low microtubule affinity state (State 3 and 4, Figure 1.2) (Bhabha et al., 2014; Schmidt et al., 2015). The AAA+ ring is more open in the high microtubule affinity state compared to the low microtubule affinity state (Schmidt et al., 2015). The opening and closing of the AAA+ ring is allosterically transmitted to the MTBD via the changes in the coiled-coil registry of the stalk (Carter et al., 2008; Gibbons et al., 2005; Kon et al., 2009). It also leads to the conformational changes of the linker domain (Burgess et al., 2003; Kon et al., 2005; Roberts et al., 2009). The linker adopts a straight conformation, termed "post-power stroke", in the high microtubule affinity state whereas it becomes bent ("pre-power stroke" conformation) in the low microtubule affinity state (Burgess et al., 2003; Imamula et al., 2007; Kon et al., 2005; Roberts et al., 2009, 2012).

Next, I summarize the current model for how dynein transitions between these two states during its mechano-chemical cycle.

At the start of the mechano-chemical cycle, the AAA1 domain of dynein is apo and dynein is tightly bound to the microtubule with the linker in the straight post-power stroke conformation across the motor ring (state 1, Figure 1.2) (Carter et al., 2011; Schmidt et al., 2012). ATP binding to AAA1 closes the AAA+ ring and this allosterically changes the register of the coiled-coil helices of the stalk domain leading to the low microtubule affinity state of the MTBD (state 2, Figure 1.2) (Bhabha et al., 2014; Schmidt et al., 2015). This causes the unbinding of dynein from the microtubule followed by the bending of the linker (state 3, Figure 1.2) (Carter et al., 2008; Gibbons et al., 2005; Kon et al., 2009). This conformational change of the linker domain is known as the "priming stroke" and has been hypothesized to play a role in biasing dynein's motion towards the minus end of the microtubule. ATP hydrolysis takes place in AAA1 (state 4, Figure 1.2), although the precise order of ATP hydrolysis in relation to microtubule unbinding and the priming stroke is unknown (Cianfrocco et al., 2015). Nonetheless, mutagenesis studies of the AAA1 domain show that ATP binding at AAA1 is necessary and sufficient to induce microtubule unbinding and the priming stroke of dynein (Bhabha et al., 2014; DeWitt et al., 2015; Kon et al., 2005, 2011).

Unbound dynein searches and rebinds to a new binding site on the microtubule with a strong bias towards the microtubule minus end relative to its previous binding site (DeWitt et al., 2012; Qiu et al., 2012). Microtubule rebinding shifts the registry of the coiled-coil helices of the stalk domain, which in turns causes the AAA+ ring to open (state 5, Figure 1.1) (Schmidt, 2015). This leads to phosphate release from AAA1 and the straightening of the linker from the bent conformation (state 5, Figure 1.2) (Kon et al., 2012; Roberts et al., 2012). This conformational change of the linker is called the "power stroke" and it pulls the dynein tail forward (towards the

microtubule minus end) along with the other dynein protomer. Finally, ADP is released from AAA1 and the mechano-chemical cycle begins again (state 6, Figure 1.2).

The progression of dynein's mechano-chemical cycle requires that AAA3 must be in the ADP-bound state (Bhabha et al., 2014; DeWitt et al., 2015). When AAA3 is either apo or ATP-bound, it blocks the allosteric communication between the AAA+ ring, linker and MTBD (state 7, Figure 1.2). ATP binding at AAA1 no longer causes microtubule unbinding and bending of the linker unless AAA3 is ADP-bound (DeWitt et al., 2015). Therefore, AAA3 acts as a master regulatory switch for dynein's mechano-chemical cycle. Mutations in AAA4 alter dynein's run length and force production, however, the detailed mechanism is unclear (Cho et al., 2008). Structural studies suggest that AAA2 is ATP-bound throughout the mechano-chemical cycle of dynein (Schmidt et al., 2012, 2015).

The mechano-chemical cycle of dynein is explained above for one dynein motor domain for simplicity. In cells, dynein functions as a dimer and how dynein dimers coordinate is essential for understanding dynein motility. To understand this important question, yeast dynein has been used as a model system because it is processive on its own, i.e., capable of walking several micrometers on microtubules without dissociating (Reck-Peterson et al., 2006). Dynein's two motor domains step independently of each other when the two motor domains are close to each other (DeWitt et al., 2012; Qiu et al., 2012). However, when the separation between the two motor domains is further apart, tension on the linker domains promotes the release of the trailing motor domain from the microtubule but prevents the leading motor domain from unbinding from the microtubule (Cleary et al., 2014). This tension-gated microtubule release and high duty ratio (i.e., fraction of microtubule-bound time) of dynein results in the processive motion of yeast dynein

dimers. On the other hand, mammalian dynein dimers are not processive on their own due to autoinhibition (see below).

1.4 Autoinhibition and activation of dynein

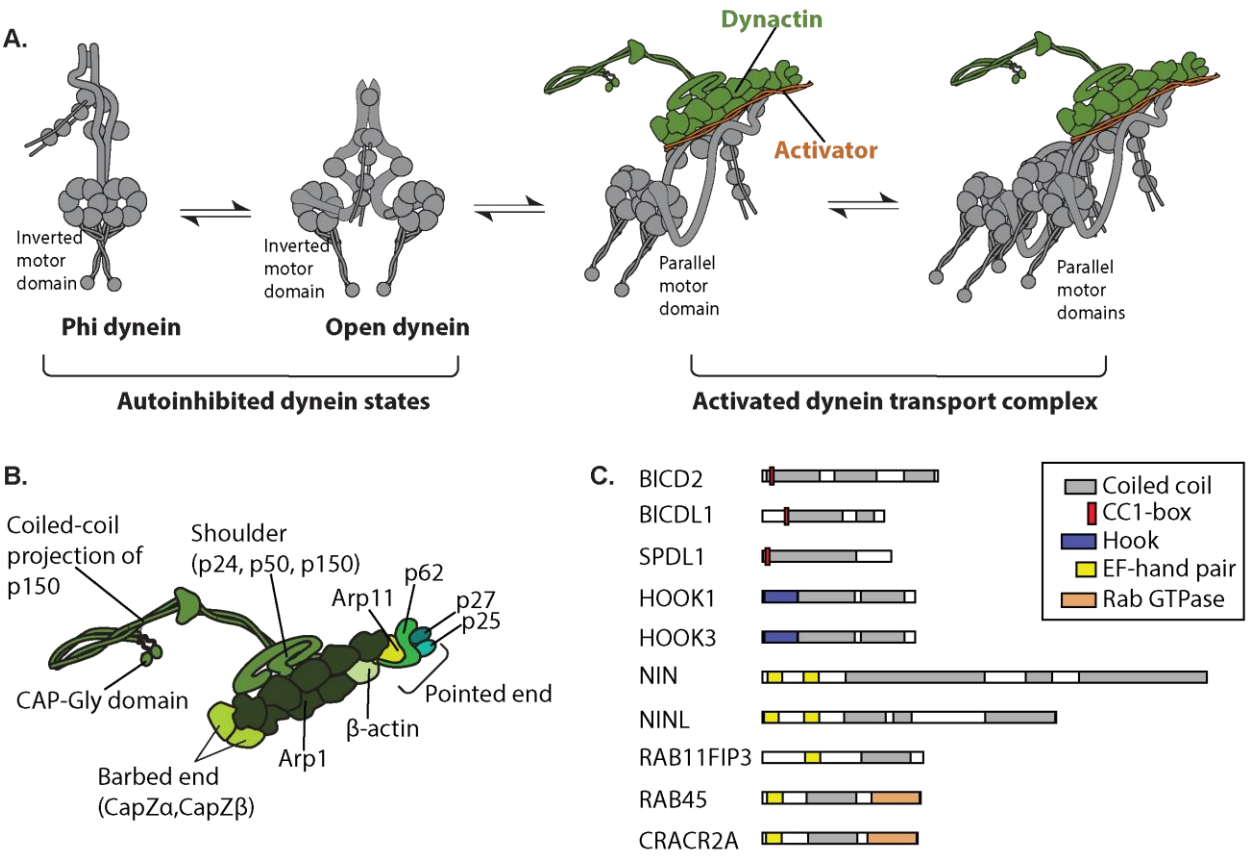

Figure 1.3. Autoinhibition and activation of mammalian dynein. (A) Model of dynein activation by dynactin (green) and activating adaptor (orange). Dynein exists in autoinhibited states (phi dynein and open dynein) where its motor domains are inverted relative to each other. Binding of dynactin and an activating adaptor to dynein reorients the two motor domains of dynein to be parallel and form an activated dynein transport complex, which can either contain one dynein dimer or two dynein dimers. (B) Cartoon model of the dynactin complex. Dynactin is composed of 23 subunits. Eight copies of actin-like protein-1 (Arp1) and one copy of β-actin form a short filament which serves as the binding interface for an activating adaptor and the dynein tails. The arp filament is capped by CapZα and Capβ at the barbed end and Arp11, p62, p25 and p27 at the

(continued) pointed end. The shoulder domain sits on the arp filament and contains the p24, p50 and p150 subunits. p150 subunits form a flexible coiled-coil extension from the shoulder domain and contain a CAP-Gly (cytoskeleton-associated glycine-rich) domain that can interact with microtubules. (C) Domain architecture of confirmed activating adaptors. Predicated regions of coiled-coil, which are the common structural features of all known activating adaptors, are shown in grey boxes. Known and proposed binding motifs for the dynein light intermediate chains (CC-1 box, Hook domain, EF-hand pair} are shown in red, blue and yellow boxes, respectively. The Rab GTPase domain is shown in orange boxes. This figure is adapted from (Carter et al., 2016) and (Reck-Peterson et al., 2018).

As mentioned previously, mammalian dynein is not processive on its own and exists in autoinhibited states known as "phi-dynein" and "open-dynein" (Figure 1.3A) (Amos, 1989; Torisawa et al., 2014; Trokter et al., 2012; Zhang et al., 2017). In a cryoelectron microscopy (cryo-EM) sample, the majority of mammalian dynein adopts the phi-conformation, where two dynein protomers self-dimerize by extensive contacts between their linkers, AAA4, AAA5 domains, the stalks of their motor domains and tail domains (Zhang et al., 2017). This self-dimerization holds both the tail and motor domains of phi-dynein in an inverted orientation relative to each other and lock dynein in low microtubule affinity state. In open-dynein, the motor domains of two dynein protomers are separate and flexible. However, they predominately adopt an inverted orientation relative to each other, likely explaining why they are still autoinhibited and unable to walk processively on microtubules. The tail domains likely dictate the inverted orientation of the motor domain in open-dynein. Artificially attaching large beads (>100nm) or a rigid rod to the dynein tail can partially relieve the autoinhibition of dynein (Belyy et al., 2016; King and Schroer, 2000; Mallik et al., 2004; Torisawa et al., 2014).

Two dynein regulators, dynactin and an activating adaptor, fully relieve dynein's autoinhibition and convert dynein into a highly processive motor (Figure 1.3A) (Chowdhury et al.,

2015; McKenney et al., 2014; Schlager et al., 2014a; Zhang et al., 2017). Dynactin and an activating adaptor bind to the tail domains of the dynein dimer, reorient the dynein tail and motor domains into a parallel orientation, relieving autoinhibition and resulting in processive motility (Chowdhury et al., 2015; Urnavicius et al., 2015; Zhang et al., 2017). Thus, the minimal dynein transport complex consists of one dynein dimer, one dynactin complex and an activating adaptor. However, it has recently been discovered that some dynactin-activating adaptor complexes can recruit two dynein dimers (Figure 1.3A) (Grotjahn et al., 2018; Urnavicius et al., 2018). The dynein transport complex with two dynein dimers exhibits faster velocity and greater force production compared to the complex with a single dynein dimer (Urnavicius et al., 2018).

1.5 Structure and function of dynactin and activating adaptors

Dynactin was initially discovered as a factor that can activate dynein-mediated vesicle movement in vitro (Gill et al., 1991; Schroer and Sheetz, 1991). Since then, it has been found to be an essential dynein regulator required for almost all of dynein functions (Cianfrocco et al., 2015; Schroer, 2004). The recent discovery that dynactin and an activating adaptor can relieve the autoinhibition of dynein and convert it into a processive motor provides a mechanistic understanding for how dynactin regulates dynein.

Dynactin is a large 1.1MDa protein complex composed of 23 subunits in vertebrates (Figure 1.3B) (Chowdhury et al., 2015; Urnavicius et al., 2015). A central feature of dynactin is a short actin-like filament, which consists of eight copies of actin-related protein-1 (Arp1) and one copy of β-actin. This filament is capped at one end (called the "barbed end") by a heterodimer of acting capping proteins, CapZα and CapZβ. The opposite end (termed the "pointed end") is capped by actin-related protein-11 (Arp11) along with three other proteins, p25, p27 and p62. The later

three subunits of dynactin have been implicated in linking dynein-dynactin to cargos (Yeh et al., 2012; Zhang et al., 2011). The arp filament of dynactin provides binding sites for activating adaptors and the dynein tail. The shoulder domain lies on top of the arp filament at the barbed end. It is primarily a large bundle of α-helices with a large (>50nm) coiled-coil projection (Urnavicius et al., 2015). The shoulder domain contains four copies of p50, two copies of p24 and two copies of p150. The large coiled-coil projection of dynactin comes from the homodimer of p150 and contains up to three stretches of coiled-coil. The amino-terminus of p150 contains a microtubule-binding domain called a CAP-Gly (cytoskeleton-associated glycine-rich) domain (Waterman-Storer et al., 1995). The microtubule binding activity of dynactin seems to be dispensable for dynein motility in vitro (McKenney et al., 2014) and for dynein-driven cargo motility in cells, but is required for spindle microtubule organization and recruitment of dynactin to microtubule plus ends (Dixit et al., 2008; Kim et al., 2007; Moughamian and Holzbaur, 2012). p150 has also been shown to bind the dynein intermediate chain (Karki and Holzbaur, 1995; King et al., 2004; Siglin et al., 2013; Vaughan and Vallee, 1995).

Although there are two dynein binding sites on dynactin, dynein and dynactin do not interact strongly in vitro (Splinter et al., 2012). Activating adaptors strengthen the interaction of dynein and dynactin, leading to the formation of a stable tripartite dynein transport complex (McKenney et al., 2014; Schlager et al., 2014a; Splinter et al., 2012). So far, 10 bona fide activating adaptors, BICD2, BICDL1, HOOK1, HOOK3, SPDL1 (spindly), NIN (ninein), NINL (ninein-like), RAB11FIP3, RAB45, CRACR2A, have been discovered and shown to form processive dynein transport complex (Figure 1.2C) (McKenney et al., 2014; Olenick et al., 2016; Reck-Peterson et al., 2018; Schlager et al., 2014a; Schroeder and Vale, 2016; Urnavicius et al., 2018; Wang et al., 2018). The discovery of the activating adaptors NIN and NINL will be discussed in

detail in chapter 4. The recent cryo-EM structural studies of the dynein-dynactin complex with three different activating adaptors, BICD2, BICDL1 and HOOK3, have shown that activating adaptors bind along the length of the arp filament of dynactin and provide additional binding sites for the dynein tails hence strengthening the interaction between the dynactin filament and dynein tails (Urnavicius et al., 2015, 2018). Amino- and carboxy-termini of the activating adaptors lie close to the barbed and pointed ends of the arp filament of dynactin respectively. BICD2 primarily recruit one dynein dimer per dynactin while BICDL1 and HOOK3 primarily recruit two dynein dimers per dynactin.

All 10 activating adaptors that have been discovered so far have no common sequence motifs. However, they all share some common structural features (Figure 1.3C). They are all dimers and contain long (>200 residues) stretches of predicted coiled-coil, which bind along the arp filament of dynactin (Reck-Peterson et al., 2018). Towards the amino-terminal part of the coiled-coil region, all activating adaptors have or are predicted to have inding sites for the DLIC. These binding sites have been shown to be indispensable for BICD2, HOOK3 and SPDL1 to promote the formation of activated dynein-dynein-activating adaptor complexes (Gama et al., 2017; Lee et al., 2018; Schlager et al., 2014b). The BICD family proteins, BICD2 and BICDL1, as well as Spindly contain a short motif called the “CC1 box” that binds to the DLIC, whereas the Hook family proteins, HOOK1 and HOOK3, use the Hook domain to bind to the DLIC. RAB11FIP3 binds to the DLIC by a region containing a pair of EF hands (Horgan et al., 2010). Although it has not been shown that NIN, NINL, RAB45 and CRACR2A bind to the DLIC, they all contain an EF hand motif, which has been proposed to mediate the interaction with the DLIC (Reck-Peterson et al., 2018; Wang et al., 2018).

The final common structural feature of activating adaptors is that their carboxy-terminal regions contain binding sites for receptor/adaptor proteins of dynein cargos or dynein cargos themselves. Therefore, activating adaptors serve a dual role of converting dynein into a processive motor and linking dynein to its cargos. In chapter 4, I will discuss in details a proteomic-based approach to determine which cargos each activating adaptor link to. Here, I will briefly highlight some of the well-characterized cargos of some activating adaptors. BICD2 is perhaps one of the best-characterized activating adaptors and it has been shown to bind to Rab6/Rab6a, which in turn binds to Golgi-derived vesicles (Huynh and Vale, 2017; Matanis et al., 2002). BICD2 has also been shown to bind to Egalitarian, which is a cargo adaptor for dynein-mediated mRNA transport (Dienstbier et al., 2009; McClintock et al., 2018; Sladewski et al., 2018). The Hook family proteins, HOOK1, HOOK2 (not yet shown to be an activating adaptor directly) and HOOK3, bind to FTS and FHIP and form a tripartite complex called the "FHF complex" (Xu et al., 2008). The FHF complex links dynein to early endosomes via the interaction between FHIP and the early endosome marker, Rab5 (Guo et al., 2016; Nielsen et al., 1999). CRACR2A and Rab45 have Rab GTPase domains in their carboxy-terminal regions (Figure 1.3C) and Rab domains generally bind directly to membrane cargos (Reck-Peterson et al., 2018; Wang et al., 2018). In the case of CRACR2A, it has been shown to localize to clarithin-independent endosomes in T cells (Wang et al., 2018).

1.6 Regulation of dynein by Lis1

Lis1 (PAFAH1B1) is another essential regulator of dynein functions. Lis1 was first discovered as the gene whose mutations lead to a neurodevelopmental disease called lissencephaly, which is characterized by smooth cerebral surface phenotype (Reiner et al., 1993). It was later linked to the

dynein pathway via genetic screens for nuclear migration and distribution in filamentous fungi (Xiang et al., 1995). Since then, Lis1 has been shown to be an ubiquitous dynein regulator in higher eukaryotes (Cianfrocco et al., 2015; Kardon and Vale, 2009). Lis1 is required for dynein localization at microtubule plus ends (Lee et al., 2003; Sheeman et al., 2003; Splinter et al., 2012), for dynein-mediated transport of various cargos (Dix et al., 2013; Egan et al., 2012; Shao et al., 2013; Splinter et al., 2012), for dynein-mediated positioning of the nucleus and centrosome (Lee et al., 2003; Sitaram et al., 2012; Tsai et al., 2007; Xiang et al., 1995), and for mitotic functions of dynein (Cockell, 2004; Moon et al., 2014).

Structurally, Lis1 is a homo-dimer consisting of an amino-terminal dimerization domain and a carboxy-terminal β-propeller domain of seven WD-40 repeats (Figure 1.4A) (Kim et al., 2004; Tarricone et al., 2004). Cryo-EM structure of dynein's motor domain with Lis1 reveals that the β-propeller domain binds directly to dynein's motor domain at the helical junction between AAA3 and AAA4 (Figure 1.4B) (Huang et al., 2012; Toropova et al., 2014). Although there are no structural and biochemical evidence, the β-propeller domain has also been shown to interact with the dynein tail domain, dynein intermediate chain and dynactin p50 subunits in co-immunoprecipitation and yeast two-hybrid assays (Tai et al., 2002).

In vitro reconstitution experiments of dynein and Lis1 have shown that Lis1 increases the microtubule binding of dynein and slows its motility (Huang et al., 2012; McKenney et al., 2010; Torisawa et al., 2011; Yamada et al., 2008a). However, Lis1 doesn't have a significant effect on dynein's basal or microtubule-stimulated ATPase rate (Huang et al., 2012; McKenney et al., 2010; Yamada et al., 2008a). Instead, Lis1 uncouples the allosteric communication between the ATPase cycle of AAA1 and dynein's microtubule binding domain (Figure 1.4C) (Huang et al., 2012; Toropova et al., 2014). As mentioned previously, during the canonical mechano-chemical cycle of

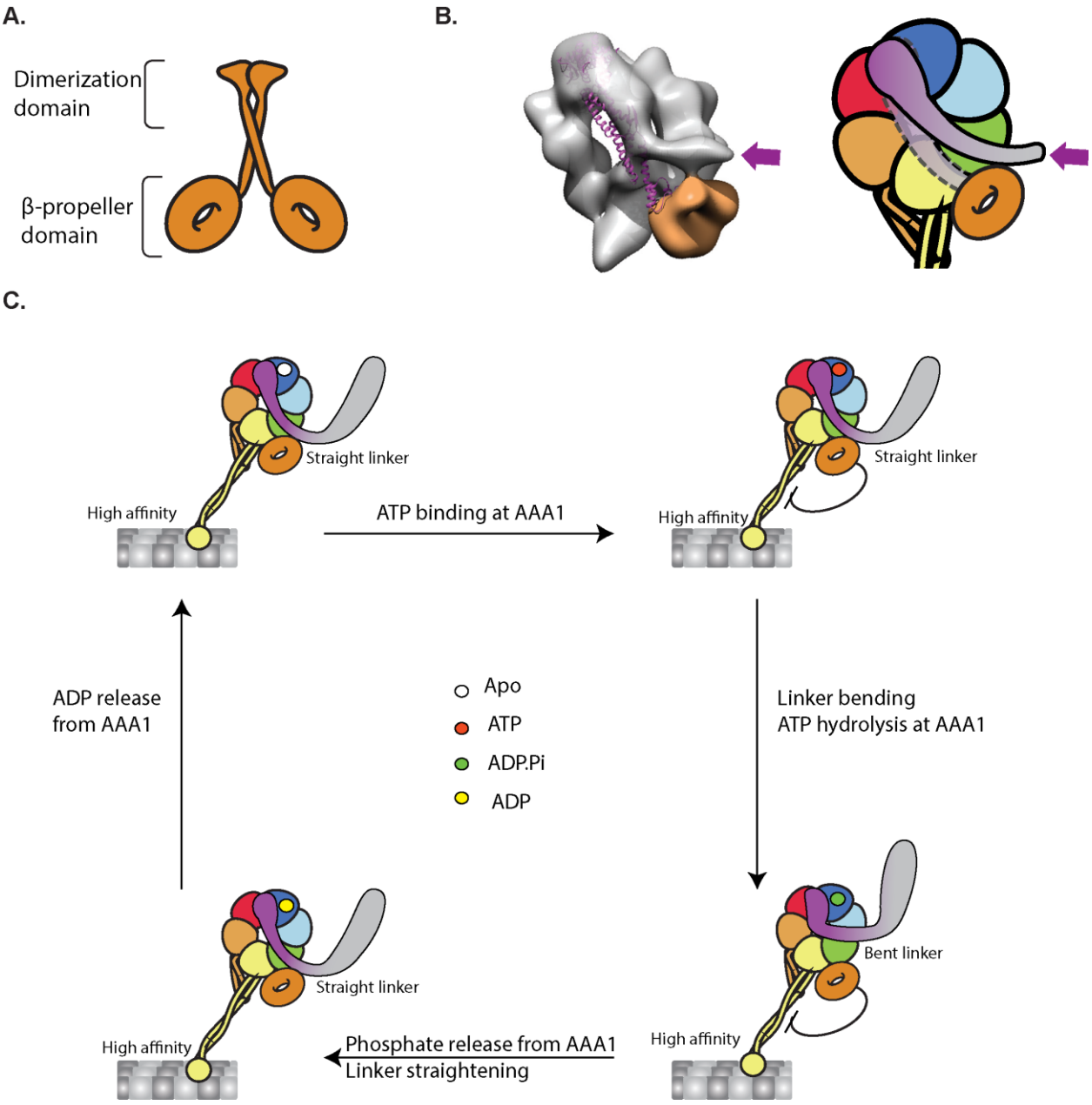

Figure 1.4. Regulation of dynein Lis1. (A) Cartoon model of Lis1. Lis1 is a homo-dimer consisting of an amino-terminal dimerization domain and a carboxy-terminal β-propeller domain. (B) Model of the dynein-Lis1 complex. Cryo-negative stain electron microscopy model of the dynein-Lis1 complex (EMDB-6008) is shown in the left panel and the corresponding cartoon model is shown in the right panel. In the cryo-negative stain electron microscopy model, the density of the dynein motor domain is shown as a gray surface and Lis1 is shown as an orange surface. The purple arrow indicates the position of the linker domain. Lis1 binding to the dynein motor domain occludes the linker domain in its straight conformation to bind at its normal position.

(continued) The canonical docking site of the straight linker is shown as a purple ribbon diagram in the left panel and a semi-transparent purple surface with dashed line in the right panel. (C) Model of Lis1 regulation of dynein's mechano-chemical cycle. The nucleotide occupancy states of AAA1 of dynein are color-coded as noted. By binding at the junction of AAA3 and 4, Lis1 prevents dynein unbinding from microtubules throughout ATP hydrolysis cycle at AAA1. Although Lis1 binding prevents the straight linker to bind at its normal position, the linker can undergo conformational change to its bent conformation upon ATP binding at AAA1.

dynein, ATP binding at AAA1 causes dynein to unbind from microtubules and bend its linker (Figure 1.2). However, in the presence of Lis1, dynein remains tightly bound to microtubules after ATP binding at AAA1 (Huang et al., 2012). Lis1 exerts this effect by binding at the junction of AAA3-4 and sterically blocks dynein's linker domain to dock at AAA5 in a straight conformation (Toropova et al., 2014). Interestingly, Lis1 only has a minor effect on the bending of the linker. The effect of Lis1 to keep dynein tightly bound to microtubules allows dynein to generate a sustained high force-producing state (McKenney et al., 2010; Reddy et al., 2016).

In addition to directly affecting on dynein's mechano-chemical cycle, it has been shown that Lis1 promotes the binding of dynein and dynactin in Xenopus egg extract (Wang et al., 2013). Recently, Lis1 has been shown to increase the velocity of activated dynein complexes consisting of dynein, dynactin and BICD2 (Baumbach et al., 2017; Gutierrez et al., 2017). However, one study found that Lis1 has no effect on the velocity of activated dynein complexes with BICD2 (Jha et al., 2017). Investigating the effect of Lis1 on activated dynein complexes is the subject of Chapter 3.

1.7 Outstanding questions and summary of thesis

Regulation of dynein by Lis1 is essential for diverse roles of dynein. However, current mechanistic understanding of Lis1 regulation on dynein from in vitro studies cannot fully explain the complex and conflicting regulatory roles of Lis1 in cells. For instance, many studies have shown that depletion or deletion of Lis1 reduces dynein-driven cargo transport (Dix et al., 2013; Egan et al., 2012; Lenz et al., 2006; Moughamian et al., 2013; Pandey and Smith, 2011). However, one study has found a conflicting result that depletion of Lis1 leads to an increase in dynein-driven cargo transport (Vagnoni et al., 2016) and one study has suggested that Lis1 regulation is required for high-load cargos but not for small vesicular cargos of dynein (Yi et al., 2011). Examinations of the motile properties of dynein-driven cargo transport following Lis1 depletion have also shown conflicting results with some studies showing increase in velocity of dynein cargos (Vagnoni et al., 2016), some showing decrease in velocity of dynein cargos (Dix et al., 2013; Pandey and Smith, 2011) and some observing no change in velocity of dynein cargos (Egan et al., 2012; Shao et al., 2013). These results suggest that Lis1 has complex regulatory roles on dynein functions and the major outstanding question is to understand how Lis1 carries out these complex regulatory functions. To answer this question, we used two approaches. The first approach, which is the subject of chapter 2, is to expand our current mechanistic understanding of regulation of Lis1 on dynein alone in the absence of other dynein regulators. Particularly, we were interested to understand how Lis1's regulatory role interplays with the intramolecular regulation of dynein by its AAA3 domain, if any, because the known Lis1 binding site on dynein is close to the ATP binding pocket of AAA3. To study this, we used the established yeast model system (Huang et al., 2012; Toropova et al., 2014). Surprisingly, we discovered that Lis1 had two opposing modes of regulation of dynein depending on the nucleotide state at AAA3. Lis1 is capable of inducing low

microtubule binding of dynein in addition to its previously known role of increasing microtubule binding of dynein. We identified a novel Lis1 binding site on dynein and showed that this novel site was required for the novel regulatory mode of Lis1 to decrease microtubule binding of dynein. We also showed that the novel Lis1 binding site on dynein was required for efficient transport of dynein to microtubule plus ends by kinesin in vitro and dynein's role in mitotic spindle positioning in yeast.

The second approach, which is the subject of chapter 3, is to understand the mechanism of regulation of Lis1 on dynein in the presence of dynactin and the activating adaptor BICD2. To study this, we used the established mammalian model system (McKenney et al., 2014; Schlager et al., 2014a). Recent studies have found that Lis1 increases the motility of the activated dynein-dynactin-BICD2 complexes (Baumbach et al., 2017; Gutierrez et al., 2017). However, the mechanism of how Lis1 is exerting such effect is unknown. We showed that Lis1 increases the velocity of the activated dynein-dynactin-BICD2 complexes by promoting the formation of the maximally activated complexes consisting of two dynein dimers. Furthermore, we demonstrated that Lis1 was not required to co-migrate with the maximally activated dynein transport complex once the complex was formed. Surprisingly, we found that none of the known Lis1 binding sites was responsible for this effect. These results of chapter 2 and 3 begin to reveal multiple modes of Lis1 regulation in vitro and provide new paradigms to understand the complexity of Lis1 regulatory roles in vivo.

Another major outstanding question is what determines or regulates the cargo specificity of dynein, which has hundreds, if not thousands of diverse cargos. To address this question, in chapter 4, we attached a promiscuous biotin ligase ('BioID') to dynein and dynactin subunits and identify their interactome using mass spectrometry. BioID technique is chosen because it can

report transient interactions as well as the spatial information of the interactors (Roux et al., 2012). Using this technique, we identified two novel dynein activating adaptors, ninein and ninein-like. Since activating adaptors link dynein to its cargos, we further set out to answer which cargos each activating adaptor links to using BioID technique. We found that each activating adaptor likely links dynein to multiple cargos. This suggests that additional factors are required to define dynein's cargo specificity in addition to activating adaptors and this study provides a wealth of proteomic data to begin dissecting the additional layer of regulation to achieve dynein's cargo specificity.

Chapter 2

Lis1 has two opposing modes of regulating cytoplasmic dynein

This chapter has been previously published as:

Morgan E. DeSantis*, Michael A. Cianfrocco*, **Zaw Min Htet***, Phuoc Tien Tran, Samara L. Reck-Peterson#, Andres E. Leschziner#. (2017). Lis1 has two opposing modes of regulating cytoplasmic dynein. ***Cell*** 170(6): 1197-1208.

* denotes equal contributions

# denotes co-senior investigators

2.1 Contributions

Morgan E. DeSantis, Michael A. Cianfrocco, Zaw Min Htet, Samara L. Reck-Peterson and Andres E. Leschziner conceptualized and designed the experiments. Zaw Min Htet designed and cloned yeast strains. Phuoc Tien Tran did yeast growth. Morgan E. DeSantis and Zaw Min Htet performed protein purification. Michael A. Cianfrocco performed electron microscopy data collection and analysis. Morgan E. DeSantis and Zaw Min Htet performed and analyzed single-molecule experiments and yeast in vivo imaging experiments. Morgan E. DeSantis, Michael A. Cianfrocco, Zaw Min Htet, Samara L. Reck-Peterson and Andres E. Leschziner interpreted the data. Samara L. Reck-Peterson and Andres E. Leschziner provided mentorship.

2.2 Abstract

Regulation is central to the functional versatility of cytoplasmic dynein, a motor involved in intracellular transport, cell division, and neurodevelopment. Previous work established that Lis1, a conserved regulator of dynein, binds to its motor domain and induces a tight microtubule-binding state in dynein. The work we present here—a combination of biochemistry, single-molecule assays, and cryo-electron microscopy—led to the surprising discovery that Lis1 has two opposing modes of regulating dynein, being capable of inducing both low and high affinity for the microtubule. We show that these opposing modes depend on the stoichiometry of Lis1 binding to dynein and that this stoichiometry is regulated by the nucleotide state of dynein's AAA3 domain. The low affinity state requires Lis1 binding to dynein at a novel conserved site, mutation of which disrupts Lis1's function in vivo. We propose a new model for the regulation of dynein by Lis1.

2.3 Introduction

Cytoplasmic dynein-1 ("dynein") is a microtubule (MT)-based motor that transports cellular cargos towards the minus-ends of MTs. In human and many other eukaryotic cells, dynein distributes and organizes organelles, proteins, RNAs, and viruses, in addition to playing essential roles in cell division. Mutations in the dynein machinery cause a range of neurological diseases (Franker and Hoogenraad, 2013).

Type-1 lissencephaly, a neurodevelopmental disease characterized by a smooth cerebral surface is caused by mutations in one of dynein's conserved regulators, Lis1 (Reiner et al., 1993). *S. cerevisiae,* where the dynein pathway has a single, non-essential function in positioning the mitotic spindle (Eshel et al., 1993; Li et al., 1993), also has a Lis1 gene, making it a powerful model system for dissecting how Lis1 regulates dynein (Huang et al., 2012; Roberts et al., 2014; Toropova et al., 2014).

There are conflicting models for the role of Lis1 in dynein regulation. Lis1 has been implicated in many dynein-dependent functions (Cianfrocco et al., 2015), such as (1) localizing and/or maintaining dynein at MT plus ends (Lee et al., 2003; Sheeman et al., 2003; Splinter et al., 2012); (2) initiating dynein transport from MT plus ends (Egan et al., 2012; Lenz et al., 2006; Moughamian et al., 2013); and (3) enabling dynein to move against high loads (McKenney et al., 2010; Reddy et al., 2016; Yi et al., 2011). Other studies have looked at the effects of altering Lis1 expression levels on dynein-based transport. Most of these showed that deletion or depletion of Lis1 reduces transport (Dix et al., 2013; Klinman and Holzbaur, 2015; Moughamian et al., 2013; Pandey and Smith, 2011; Shao et al., 2013; Smith et al., 2000; Yi et al., 2011), while one found that Lis1 depletion increases cargo transport (Vagnoni et al., 2016).

How does Lis1 regulate dynein? Because Lis1 binds directly to dynein's motor domain (Huang et al., 2012; Toropova et al., 2014), we must consider Lis1 regulation in the context of dynein's mechanochemical cycle. Dynein is a dimer of two identical "heavy chains", which can be divided into two functional units: the N-terminal "tail", required for dimerization, binding the accessory subunits, and cargo interactions; and the "motor", which is built around an AAA+ (**A**TPase **A**ssociated with diverse cellular **A**ctivities) ring containing 6 AAA domains (Figure 2.1A) (Cianfrocco et al., 2015). Dynein's motility requires cycles of ATP hydrolysis at AAA1, which are coupled to cycles of MT binding and release at dynein's MT binding domain (MTBD).

Current evidence suggests that Lis1 acts on dynein by disrupting the coupling between ATP hydrolysis and MT binding and release. Lis1 is a dimer of two β-propellers (Figure 2.1A) (Tarricone et al., 2004), with a single β-propeller binding to AAA4 on dynein's ring (Huang et al., 2012; Toropova et al., 2014). In vitro motility assays showed that Lis1 decreases dynein's velocity (Huang et al., 2012; Yamada et al., 2008b) by causing dynein to remain tightly bound to MTs in the presence of ATP, which would normally result in MT release (Huang et al., 2012; McKenney et al., 2010). This model for Lis1 regulation of dynein is at odds with some of the proposed functions of Lis1 discussed above, where depletion of Lis1 leads to a decrease in cargo transport.

The regulation of dynein motility also involves intra-motor control. The nucleotide state at AAA3 regulates dynein's motility by acting on its mechanochemical cycle (DeWitt et al., 2015; Nicholas et al., 2015b): stepping dynein contains ADP at AAA3, while ATP or no nucleotide ("apo") at this site results in a slower dynein that is tightly bound to MTs (DeWitt et al., 2015). This AAA3-mediated inhibition occurs even when ATP binds to AAA1, which normally triggers MT release.

We were struck by the similarities in the behavior of dynein in the presence of Lis1 or when its AAA3 is in an apo or ATP-bound state. The proximity of Lis1's binding site to AAA3's ATP-binding site made us wonder if Lis1 regulates dynein by acting on AAA3. Here we used mutants in yeast dynein to control the nucleotide state of AAA3 and a combination of single-molecule imaging, high-resolution cryo-electron microscopy (cryo-EM), *in vitro* reconstitutions, and *in vivo* assays to understand the relationship between Lis1 and the nucleotide state of dynein's AAA3 domain. We made the surprising discovery that Lis1 can regulate dynein in two distinct and opposing ways, depending on the nucleotide state of AAA3. Based on our data we propose a new model for the regulation of dynein by Lis1 that can explain the multiple and conflicting cellular roles of Lis1.

2.4 Results

Lis1 has two modes of regulating dynein

Previous studies led us to hypothesize that the nucleotide state at AAA3 might play a role in the regulation of dynein by Lis1 (DeWitt et al., 2015; Nicholas et al., 2015b; Toropova et al., 2014). To test this, we used a minimal *S. cerevisiae* dynein construct dimerized by GST (Dyn^{wt}) (Figure 2.1A) that is similar to full-length dynein in its motile properties (DeWitt et al., 2012; Reck-Peterson et al., 2006) and regulation by Lis1 (Huang et al., 2012). To mimic different nucleotide states at AAA3, we made well-characterized mutations that disrupt its conserved Walker A and Walker B motifs (Cho et al., 2008; DeWitt et al., 2015; Kon et al., 2004). The Walker A mutant (Dyn^{WA}) impairs ATP binding, while the Walker B mutant (Dyn^{WB}) allows ATP to bind, but prevents its hydrolysis (Figure 2.1B). Lis1 had a similar binding affinity for all three dynein variants (Figure A.1A and Supplementary table A.2).

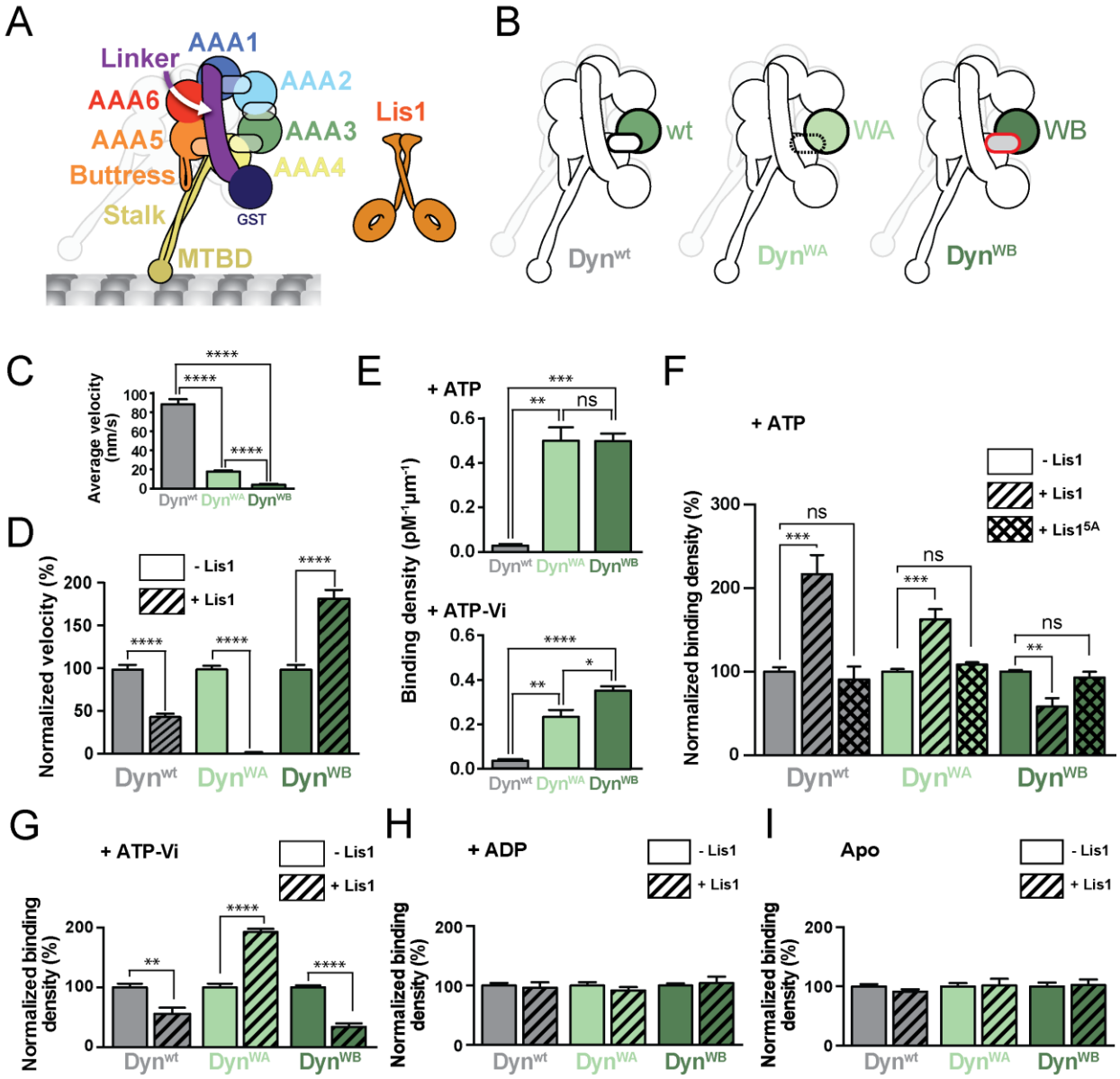

Figure 2.1. Lis1 has two modes of regulating dynein. (A) Schematic of the dynein construct used in this study. The semi-transparent ovals represent the nucleotide-binding sites in AAA1-4. The second protomer is faded out for clarity. The β-propellers in the Lis1 dimer (orange) are represented as rings. (B) AAA3 variants used in this study: Dyn^{wt} (wild type AAA3), Dyn^{WA} (Walker A mutation in AAA3), and Dyn^{WB} (Walker B mutation in AAA3). (C) Average velocities of dynein variants (n>103 events per data point). See Figure A.1B for representative kymographs. (D) Normalized average velocities of dynein variants in the absence (solid bars) and presence (hatched bars) of 300 nM Lis1 (n>103 events per data point). Velocities were normalized by setting those in the absence of Lis1 [from (C)] to 100%. (E) Binding densities of dynein variants in the

(Continued) presence of ATP (top) or ATP-Vi (bottom) (n>8 fields of view per data point). See also Supplementary table A.2. (F) Normalized binding densities of dynein variants alone (solid bars), or in the presence of 300 nM Lis1 (hatched bars), or 300 nM $Lis1^{5A}$ (cross-hatched bars) in the presence of ATP. Binding densities were normalized by setting those in the absence of Lis1 [from (E), top] to 100% (n=12 fields of view per data point). (G-I) Normalized binding densities of dynein variants alone (solid bars), or in the presence of 300 nM Lis1 (hatched bars) in the presence of 1 mM ATP-Vi (G), 1 mM ADP (H) and 2.5 units/mL apyrase ("Apo") (I) (n=8 fields of view per data point). Normalized binding densities in the absence of Lis1 shown in (G) are those in (E, bottom) without normalization. Statistical significance was calculated using an unpaired t-test with Welch's correction for both velocity (C and D) and binding density (E-I). P-values: ns, not significant; *, <0.05; **, <0.01; ***, <0.001, ****, <0.0001. Data are shown as mean and standard error of mean.

We first asked if the nucleotide state at AAA3 altered Lis1's effect on dynein's velocity using single-molecule motility assays (Figures 2.1C-D and Supplementary table A.2). In agreement with previous studies, Lis1 decreased the velocity of Dyn^{wt} (Huang et al., 2012; McKenney et al., 2010; Toropova et al., 2014; Yamada et al., 2008b) (Figure 2.1D). While both Dyn^{WA} and Dyn^{WB} had slower velocities than Dyn^{wt} on their own (Figure 2.1C and Supplementary table A.2), the effects of adding Lis1 to them were striking. Dyn^{WA} was hypersensitive to Lis1, with a velocity reduction of 99% (Figure 2.1D). Unexpectedly, the Lis1 effect was reversed with Dyn^{WB}; the velocity of this mutant almost doubled in the presence of Lis1 (Figure 2.1D). These results suggest that Lis1 can regulate dynein's velocity in opposite ways depending on the nucleotide state at AAA3.

Next, we asked if the effects of Lis1 on dynein's velocity were a result of its effect on dynein's affinity for MTs. To measure MT binding affinities, we used single-molecule total internal reflection fluorescence (TIRF) microscopy to quantify the density of dynein bound to MTs. We first characterized the binding densities of the dynein constructs by themselves in the

presence of ATP (Figure 2.1E and Supplementary table A.2). Although Dyn^{WA} and Dyn^{WB} have significantly higher affinities for MTs than Dyn^{wt} (Cho et al., 2008; DeWitt et al., 2015), their affinities are indistinguishable. Given this, we normalized most binding data with the motor alone set to 100% (non-normalized data can be found in Supplementary table A.2).

As before (Huang et al., 2012), we observed increased binding of Dyn^{wt} to MTs with Lis1 and ATP (Figure 2.1F). In agreement with our velocity data (Figure 2.1D), the two AAA3 variants were regulated by Lis1 in opposite ways: Lis1 increased the binding density of Dyn^{WA} by 62% and decreased that of Dyn^{WB} by 42% with ATP (Figure 2.1F). Importantly, a Lis1 mutant that cannot bind to dynein ($Lis1^{5A}$) (Toropova et al., 2014) had no effect on any of the variants (Figure 2.1F). Thus, Lis1 can also regulate dynein's MT binding in opposing manners depending on the nucleotide state at AAA3.

Given how unexpected Lis1's effects on Dyn^{WB} were and the intrinsic high affinity of Dyn^{WB} for MTs, we wanted to rule out mutant-specific effects. We repeated our MT binding experiments with Dyn^{wt} trapped with AAA3 in a nucleotide state as similar to that of Dyn^{WB} (ATP) as possible. For this we used ATP plus Vanadate (ATP-Vi), which generates ADP-Vi upon ATP hydrolysis (Burgess et al., 2003). Dyn^{wt} bound MTs with the same affinity with ATP-Vi or ATP (Figure 2.1E and Supplementary table A.2). More importantly, under ATP-Vi conditions, Dyn^{wt} and Dyn^{WB} both showed decreased MT binding with Lis1 (Figure 2.1G), in striking contrast to the increased MT binding we saw for Dyn^{wt} with ATP (Figure 2.1F), where AAA3 is expected to be mainly in an ADP state (DeWitt et al., 2015). The affinity of Dyn^{WA}, which cannot bind nucleotide at AAA3, still increased with ATP-Vi and Lis1 (Figure 2.1G). Performing these experiments with ADP or no nucleotide abolished all relative differences among the three variants (Figure 2.1H, I),

suggesting that dynein's AAA1 must be in an ATP or ADP-Pi state for Lis1 regulation to be apparent.

We next sought to understand the mechanistic basis for the dual role of Lis1 by determining the structures of dynein:Lis1 complexes using different AAA3 variants.

Structural basis for the tight microtubule binding state of dynein induced by Lis1

Figure 2.2A summarizes aspects of dynein's structure relevant to the results presented below. More detailed reviews of dynein's structure can be found elsewhere (Cianfrocco et al., 2015; Gleave et al., 2014).

We first used single particle cryo-EM to determine the structure of Dynein:Lis1 in the presence of ATP, a state with high affinity for MTs. We used a monomeric dynein construct lacking GST ($Dyn^{wt\text{-}M}$), which is otherwise identical to the dimeric dynein constructs used above. We solved a 7.7Å resolution structure of $Dyn^{wt\text{-}M}$ bound to Lis1 in the presence of ATP and built an atomic model into the density using Rosetta (Figures 3.2B, C, A.2, and Supplementary table A.1) (Wang et al., 2016).

This map, at higher resolution than our previous structure of the same complex (Toropova et al., 2014), provided a detailed view of the interface between dynein and Lis1 and revealed the conformation of dynein's ring. As before, a single Lis1 β-propeller was bound to $Dyn^{wt\text{-}M}$, even though Lis1 was present as a dimer in our sample. The second β-propeller, as well as the rest of Lis1, are likely disordered and thus averaged out during the reconstruction process. The EM density suggested that Lis1 interacts not only with an alpha helix in AAA4 (Toropova et al., 2014), but also with a loop from AAA5, and possibly another from AAA3 (Figure 2.2C, D), although the resolution of the map does not establish this last interaction unambiguously.

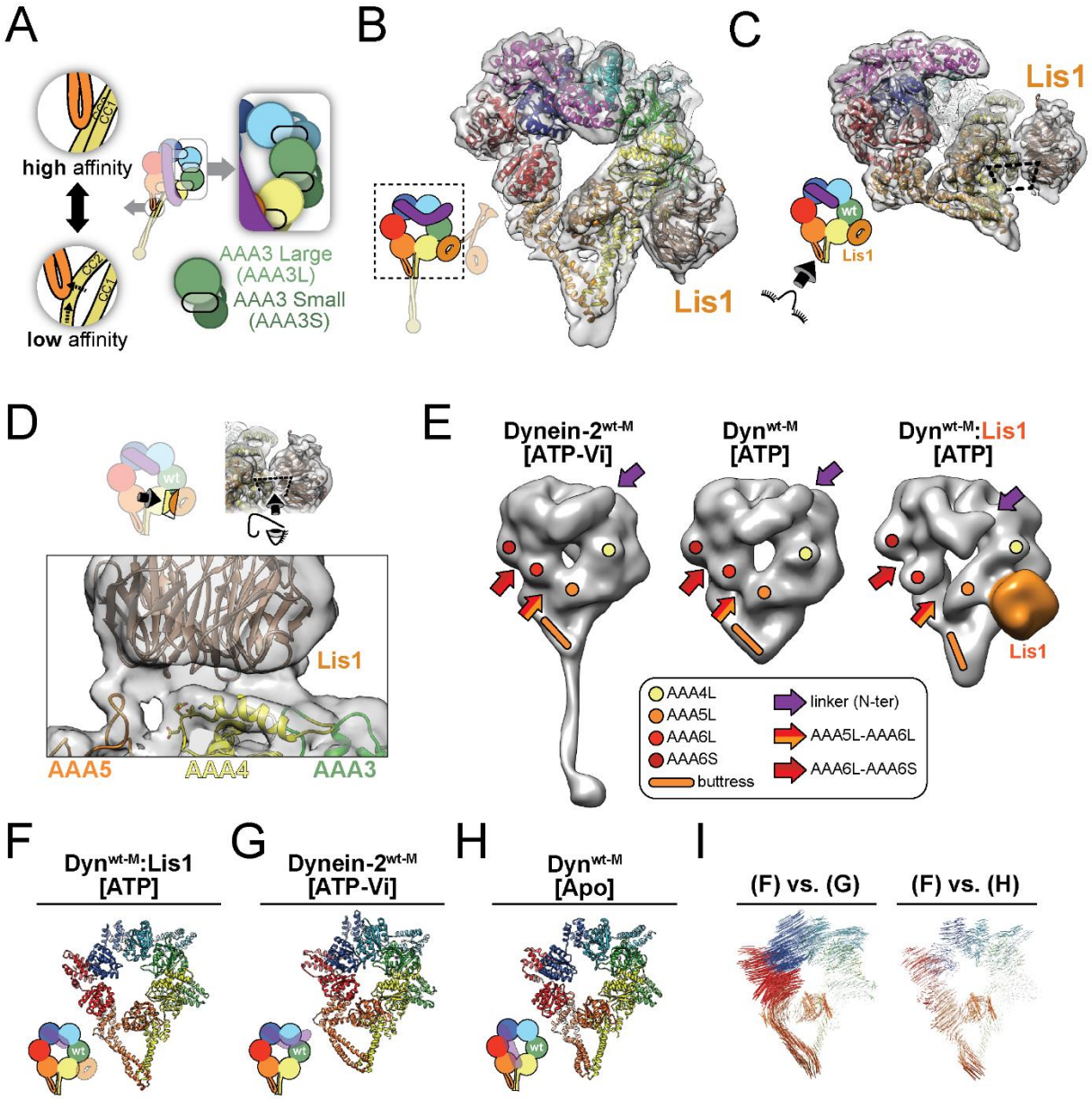

Figure 2.2. Structural basis for the tight microtubule binding state of dynein induced by Lis1. (A) Additional structural features of the schematic shown in Figure 2.1A. The inset on the right shows the architecture of the AAA ring, with each AAA domain composed of both large (AAAL) and small (AAAS) subdomains (exemplified for AAA3). Large and small subdomains are arranged in two separate planes. Semi-transparent ovals represent nucleotide-binding sites. The linker domain forms a third layer, above the AAA ring. Insets on the left illustrate how the buttress couples the conformation of dynein's ring to dynein's affinity for MTs by changing the register between the two helices (CC1 and CC2) in the stalk's coiled coil. (B) Cryo-EM structure of the

(continued) Dyn^{wt-M}:Lis1 complex, solved in the presence of ATP. The cryo-EM map was filtered using local resolution and is shown as a semi-transparent surface, with the atomic model shown as a ribbon diagram. The cartoon (bottom left) indicates the portion of dynein observed in our cryo-EM map. (C) The structure viewed from the stalk, with the Dyn^{wt-M}-Lis1 interface indicated by the dashed rectangle. (D) Close-up view of the Dyn^{wt-M}-Lis1 interface, seen in a direction perpendicular to the dashed rectangle. Side chains shown on AAA4 are residues that prevent Lis1 binding when mutated (KDEE) (Huang et al., 2012). AAA domains that contribute motifs to the interface are labeled. (E) Ring architecture of human Dynein-2^{wt-M} (ATP-Vi) (Schmidt et al., 2015) (PDB: 4RH7), yeast Dyn^{wt-M} (ATP) (Bhabha et al., 2014) (EMDB 6054), and our map of Dyn^{wt-M}:Lis1 (ATP). Colored dots and rod highlight equivalent positions in AAA4 (yellow), AAA5 (orange) and AAA6 (red). Colored arrows indicate the N-terminus of the linker (purple), the boundary between AAA5 and AAA6L (orange/red), and the boundary between AAA6L and AAA6S (red/dark red). The structure of human dynein-2 was converted into an EM-like density and both it and our Dyn^{wt-M}:Lis1 map were filtered to 20Å. The structure of Dyn^{wt-M} (ATP) (EMDB: 6054) has a resolution of 17Å. (F-I) Ring conformations of the Dyn^{wt-M}:Lis1 structure (F); the low-affinity, wild-type human Dynein-2^{wt-M} solved in the presence of ATP-Vi (PDB: 4RH7) (G); and the high-affinity, wild-type *S. cerevisiae* dynein solved in the absence of nucleotide (PDB: 4AKI) (H). We removed the linker and, when present, Lis1 for clarity. (I) Maps of pairwise alpha carbon interatomic distances between the Dyn^{wt-M}:Lis1 structure and the low-affinity, wild-type human Dynein-2^{wt-M} (left), and high-affinity, wild-type *S. cerevisiae* Dyn^{wt-M} (right). Structures were aligned using their AAA4L domains. The length and thickness of the vectors are proportional to the calculated interatomic distances.

Next we examined how Lis1 affected the conformation of dynein's ring by comparing our structure to existing structures of dynein. Our map of Dyn^{wt-M}:Lis1 appears to show the linker in its pre-power stroke position; although the N-terminal half of the linker is not visible in the 7.7Å map, an extension pointing towards AAA2 becomes apparent at lower resolution (Figures 3.2E and A.2J). Given the pre-power stroke position of the linker and the fact that we obtained the structure in ATP, AAA1 must contain either ATP or ADP-Pi, as phosphate release results in the

power stroke (Mogami et al., 2007). Since this conformation of the linker was observed in the structures of human dynein-2 with ATP-Vi (Schmidt et al., 2015) and yeast $Dyn^{wt\text{-}M}$ with ATP (Bhabha et al., 2014) we chose them for our comparison (Figure 2.2E).

Human dynein-2 (ATP-Vi) and yeast $Dyn^{wt\text{-}M}$ (ATP) both show a closed conformation of the AAA ring, associated with a low-affinity state (Figure 2.2E). $Dyn^{wt\text{-}M}$:Lis1 (ATP), however, shows an open-ring conformation, associated with a high-affinity state (Figure 2.2E). Given that the only difference between our structure and that of $Dyn^{wt\text{-}M}$ (ATP) is the presence of Lis1, the open conformation of the ring must be a consequence of Lis1 binding to dynein.

The ring opening and the similarities between the $Dyn^{wt\text{-}M}$:Lis1 and nucleotide-free dynein structures are further highlighted by an analysis of interatomic distances between alpha carbons in $Dyn^{wt\text{-}M}$:Lis1, human dynein-2 (ATP-Vi) (Schmidt et al., 2015) and nucleotide-free yeast dynein (Schmidt et al., 2012) (Figure 2.2F-I, Supplementary file A.2).

Two Lis1 β-propellers are bound to dynein in the weak microtubule binding state

We then moved on to the most puzzling aspect of our data: why does introducing a Walker B mutation in AAA3 lead to such a dramatic difference in how Lis1 regulates dynein? For this, we solved a 10.5Å-resolution cryo-EM structure of the $Dyn^{WB\text{-}M}$:Lis1 complex in the presence of ATP-Vi and used Rosetta to build an atomic model (Figures 3.3A, B, A.3, and Supplementary table A.1). As in the $Dyn^{wt\text{-}M}$:Lis1 structure, $Dyn^{WB\text{-}M}$ is a monomeric construct lacking GST and Lis1 is a dimer.

Surprisingly, the cryo-EM map of $Dyn^{WB\text{-}M}$:Lis1 showed not one, but two Lis1 β-propellers bound to dynein (Figure 2.3A, B). One β-propeller binds to the previously identified site on the ring (AAA4) ("$Site_{Ring}$"), while the other binds to dynein's stalk, specifically coiled-coil 1 (CC1)

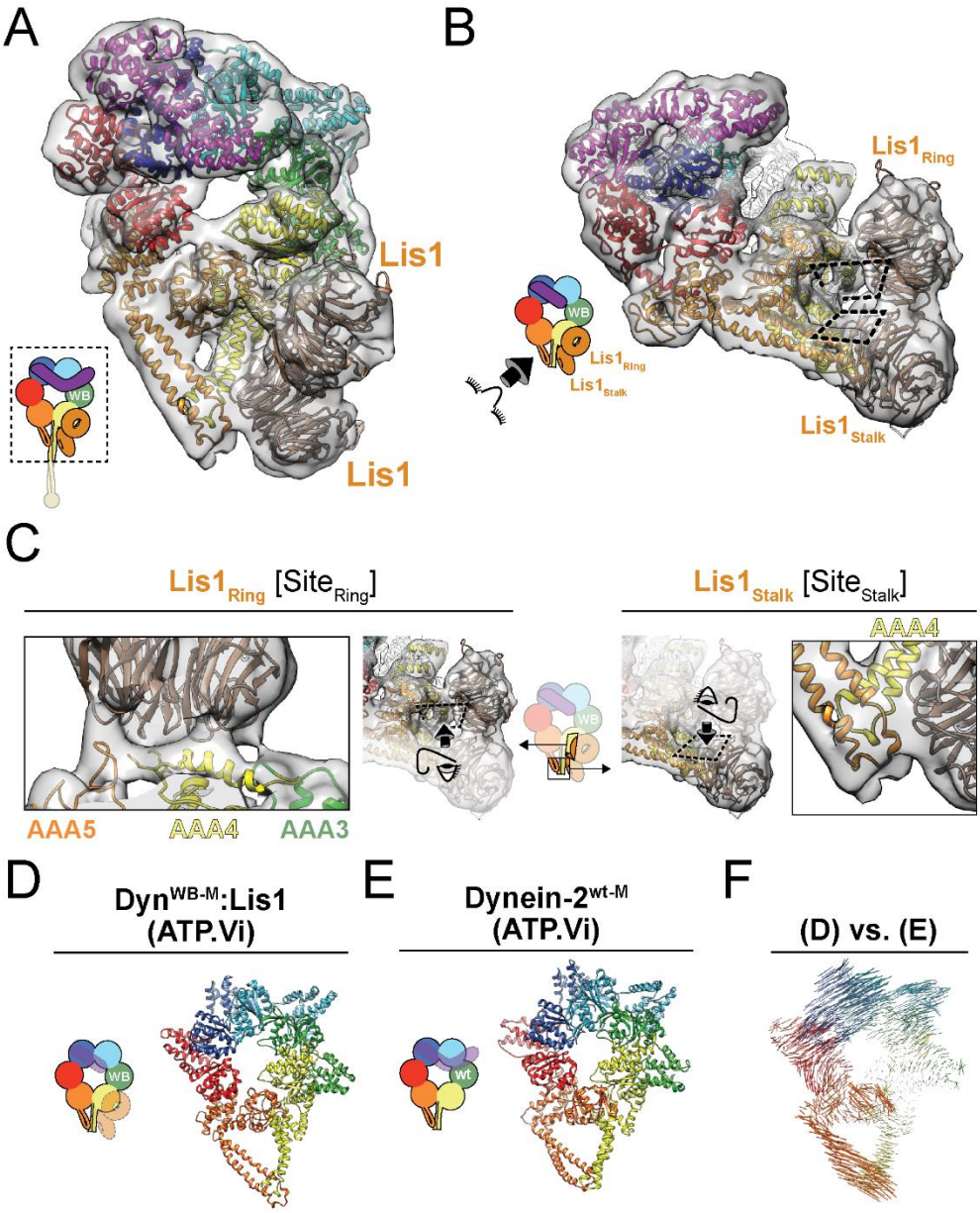

Figure 2.3. Two Lis1 β-propellers are bound to dynein in the weak microtubule binding state. (A) Cryo-EM structure of the Dyn^{WB-M}:Lis1 complex, solved in the presence of ATP-Vi. The cryo-EM map is shown as a semi-transparent surface, with the atomic model generated with Rosetta shown as a ribbon diagram. The cartoon (bottom left) indicates the portion of dynein observed in our cryo-EM map. (B) Structure viewed from the stalk, with the two Dyn^{WB-M}-Lis1 interfaces indicated by the dashed rectangles. (C) Close-up views of the two Dyn^{WB-M}-Lis1 interfaces, located on dynein's ring (Site$_{Ring}$) and stalk (Site$_{Stalk}$), viewed perpendicular to the dashed rectangles. AAA

(continued) domains that contribute motifs to the interfaces are labeled. (D-E) Ring conformations of the Dyn^{WB-M}:Lis1 structure (D) and the low-affinity, wild-type human dynein-2 solved in the presence of ATP-Vi (PDB: 4RH7) (E). We removed the linker and, when present, Lis1 for clarity. (F) Map of pairwise alpha carbon interatomic distances between the Dyn^{WB-M}:Lis1 structure and the low-affinity, wild-type human dynein-2. Structures were aligned using their AAA3L domains. The length and thickness of the vectors are proportional to the calculated interatomic distances.

("$Site_{Stalk}$") (Figure 2.3A-C). Each Lis1 β-propeller uses a different surface to interact with dynein (Figure 2.3C). The density encompassing the two Lis1 β-propellers is contiguous, suggesting they interact with each other (Figure 2.3B), although our current resolution does not allow us to determine their rotational orientations and thus the nature of this interface. Analysis of the stoichiometry of our Dyn^{wt-M}:Lis1 complex using size-exclusion chromatography suggests that both β-propellers in the structure belong to the same Lis1 dimer (Figure A.4).

The closed conformation of dynein's ring in the Dyn^{WB-M}:Lis1 structure, similar to that seen in the crystal structure of the low MT affinity state of human dynein-2 (Figure 2.3D, E) (Schmidt et al., 2015), is consistent with the weak MT binding of the complex. This similarity is further supported by an analysis of interatomic distances between alpha carbons in our Dyn^{WB-M}:Lis1 structure and those in the structure of human dynein-2 (ATP-Vi) (Figure 2.3F, Supplementary file A.2).

Lis1's opposite modes of dynein regulation are associated with rigid body motion conformational changes in dynein's ring

To understand how structural changes in dynein's ring relate to the two modes of Lis1 regulation and how Lis1 binding at $Site_{Stalk}$ in Dyn^{WB-M}:Lis1 stabilizes a low affinity state in dynein we calculated the inter-atomic distances between Dyn^{wt-M}:Lis1 and Dyn^{WB-M}:Lis1 (Figure 2.4A,

Figure 2.4. Lis1's opposite modes of dynein regulation are associated with rigid body motion conformational changes in dynein's ring. (A) Map of pairwise alpha carbon interatomic distances between the $Dyn^{wt\text{-}M}$:Lis1 and $Dyn^{WB\text{-}M}$:Lis1 structures. We removed the linker and Lis1 for clarity. Structures were aligned using their AAA3L domains. The length and thickness of the vectors are proportional to the calculated interatomic distances. (B) 1D plot of the interatomic distances shown in panel (A). Large and small AAA subdomains are indicated below the plot, along with amino acid numbers at their boundaries. The positions of the arginine fingers of domains AAA2-5, which act on domains AAA1-4, are labeled ("R"). (C) Superposition of the $Dyn^{wt\text{-}M}$:Lis1 and $Dyn^{WB\text{-}M}$:Lis1 structures, aligned using their AAA4S domains. The $Dyn^{wt\text{-}M}$:Lis1 structure is shown in lighter colors and the Lis1 bound to $Site_{Stalk}$ in $Dyn^{WB\text{-}M}$:Lis1 was faded for clarity. The square highlights $Site_{Ring}$, and is the area represented in panels (D) and (E). (D) Close-up of the $Site_{Ring}$ in dynein, with Lis1 faded for clarity. The bi-tone yellow arrow indicates good alignment for the base of the stalks. The tri-color multi-headed arrows point to the AAA3, AAA4 and AAA5 elements in $Site_{Ring}$ in both $Dyn^{wt\text{-}M}$:Lis1 and $Dyn^{WB\text{-}M}$:Lis1. (E) Positions of the $Site_{Ring}$-bound Lis1 in the $Dyn^{wt\text{-}M}$:Lis1 and $Dyn^{WB\text{-}M}$:Lis1 structures. Same view as in (D) but with dynein faded for clarity. Light and dark orange arrows point to the equivalent positions in Lis1 in the $Dyn^{wt\text{-}M}$:Lis1 and $Dyn^{WB\text{-}M}$:Lis1 structures, respectively. (F) Modeling of a second Lis1 into the $Dyn^{wt\text{-}M}$:Lis1 structure interacting either with $Site_{Stalk}$ (left) or with the Lis1 bound at $Site_{Ring}$ (right). Grey arrows point to gaps present in the models. (G) For comparison, we show the same view of the experimentally observed $Dyn^{WB\text{-}M}$:Lis1 structure.

Figure 2.4 (Continued).

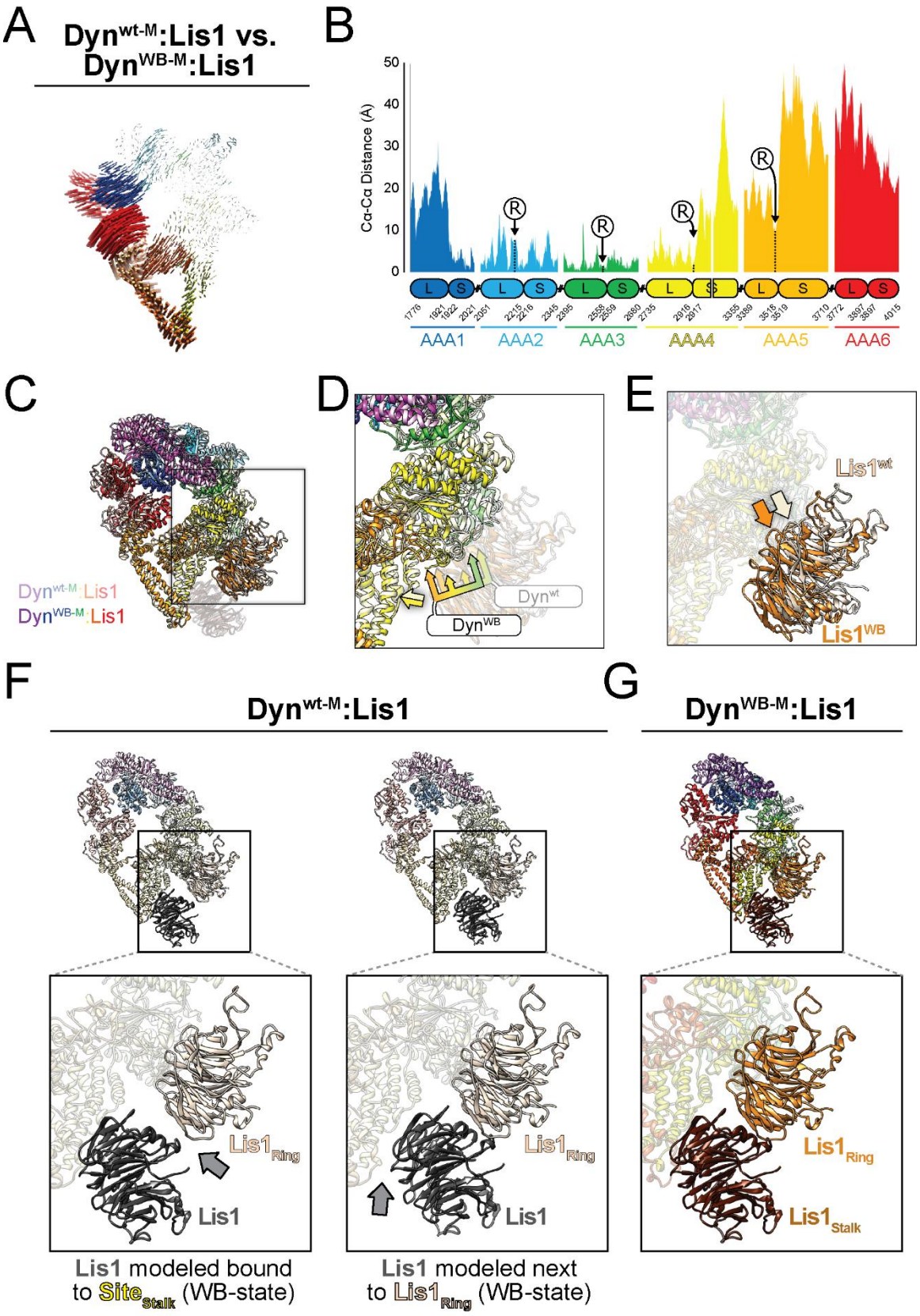

Supplementary file A.2). We found that the differences were captured by a rigid motion of elements on one half of dynein's ring—comprising the stalk, AAA5, AAA6 and part of AAA1—relative to the rest (Figure 2.4A, B).

The conformational change illustrated in Figure 2.4A results in the two Lis1 binding sites ($Site_{Ring}$ and $Site_{Stalk}$) being closer together in Dyn^{WB-M}:Lis1 relative to Dyn^{wt-M}:Lis1 (Figure 2.4C-E). This shorter distance means that the interaction between the two Lis1's cannot be satisfied in the Dyn^{wt-M}:Lis1 structure, where we only observed a single Lis1 β-propeller bound (Figure 2.4).

The putative second Lis1 binding site is conserved

The resolution of our cryo-EM map of the Dyn^{WB-M}:Lis1 complex is not sufficient to unambiguously dock Lis1 and determine which residues interact with $Site_{Stalk}$ in dynein. However, the segment of CC1 containing $Site_{Stalk}$ is short, limiting the number of candidate binding residues (Figure 2.3C). We aligned dynein sequences corresponding to this region of the stalk and identified three residues—E3012, Q3014 and N3018 in the yeast sequence (Figure 2.5A, B)—that are conserved from yeast to humans (Figure 2.5A). These residues are not conserved in a subset of fission yeasts. Supporting the idea that these residues are central features of $Site_{Stalk}$, we could not identify a Lis1 orthologue in these fission yeast genomes, while organisms with a conserved EQN triad have clear Lis1 orthologues (Figure 2.5A).

The second Lis1 binding site is required for Lis1-mediated weak microtubule binding

Our data show that Lis1 induces or stabilizes a weak MT binding state in dynein when AAA3 carries a Walker B mutation, and that in this complex (Dyn^{WB-M}:Lis1) a second Lis1 β-propeller interacts with dynein's stalk ($Site_{Stalk}$). To determine if $Site_{Stalk}$ is required for Lis1 to induce the

weak binding state in dynein we mutated the conserved E3012, Q3014, and N3018 residues to alanine (Dyn^{EQN}). Our prediction was that the Lis1-induced weak binding state would no longer be available in Dyn^{EQN}.

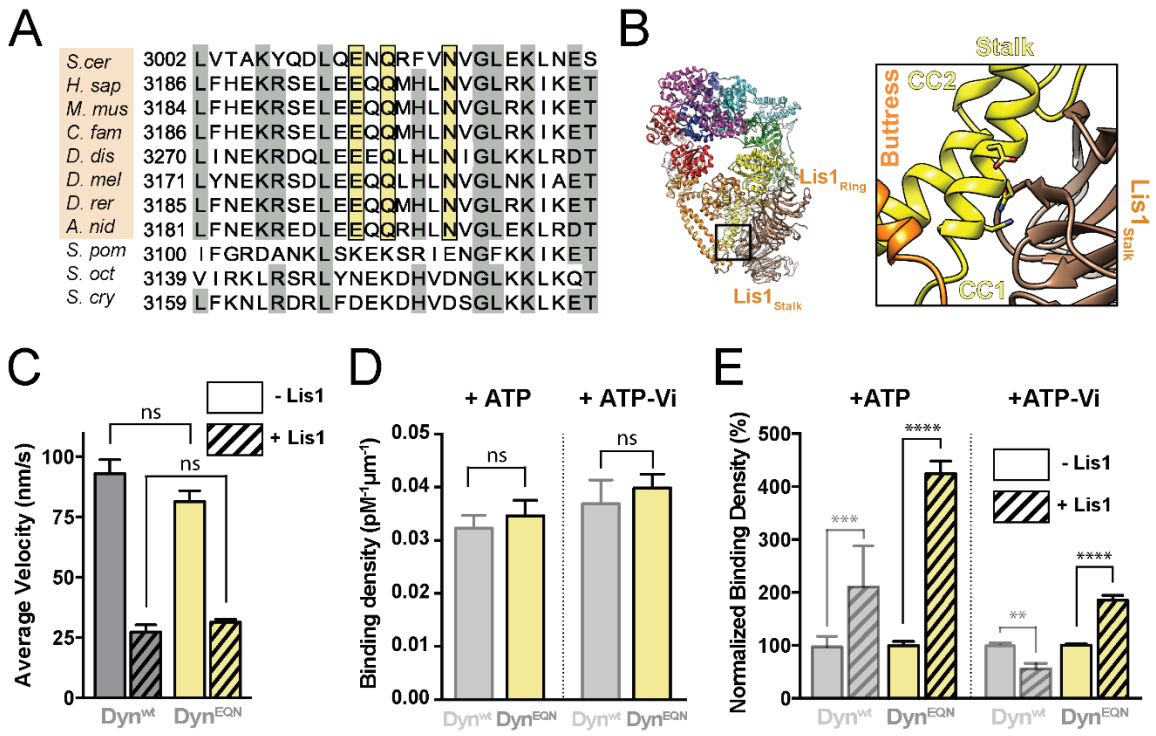

Figure 2.5. The second Lis1 binding site is required for the Lis1-induced weak microtubule binding state of dynein. (A) Sequence conservation around the putative $Site_{Stalk}$. Sequence in the region of dynein's stalk identified as the putative second binding site for Lis1, extracted from a full sequence alignment of dynein heavy chain genes. Residues with 70% conservation or higher are shaded grey. The three residues we mutated—E, Q, N, shaded in yellow—are conserved in model organisms that have Lis1 orthologs in their genomes (*Saccharomyces cerevisiae; Homo sapiens; Mus musculus; Canis familiaris; Dictyostelium discoideum; Drosophila melanogaster; Danio rerio; Aspergillus nidulans*, shaded in orange), but not in a group of fission yeasts (*Schizosaccharomyces pombe; Schizosaccharomyces octosporus; Schizosaccharomyces cryophilus*) that do not appear to have a Lis1 ortholog in their genome. (B) Atomic model of the Dyn^{WB-M}:Lis1 complex and close-up view of $Site_{Stalk}$. The conserved EQN triad is shown in stick representation and nearby dynein motifs are labeled. Dyn^{EQN} is a construct that carries an EQN to AAA mutation but has a wild-type AAA3. (C) Average velocities of Dyn^{wt} (grey) and Dyn^{EQN}

(continued) (yellow) in the absence (solid bars) or presence (hatched bars) of 300 nM Lis1 (n>154 events per data point). See Figure S5B for representative kymographs. (D) Binding densities of Dyn^{wt} (semi-transparent grey; data reproduced from Figure 2.1 for comparison) and Dyn^{EQN} (yellow) in the presence of ATP (left) or ATP-Vi (right). See also Table S1. (E) Normalized binding densities of Dyn^{wt} (semi-transparent grey) and Dyn^{EQN} (yellow) in the absence (solid bars) or presence (hatched bars) of 300 nM Lis1 (n=12 fields of view per data point), in the presence of ATP (left) or ATP-Vi (right). Binding densities were normalized by setting those in the absence of Lis1 to 100%. Data for Dyn^{wt} are reproduced from Figure 2.1 for comparison). Statistical significance was calculated using unpaired t-test with Welch's correction for both velocity (C) and binding density (D-E). P-values: ns, not significant; **, <0.01; ***, <0.001, ****, <0.0001. Data are shown as mean and standard error of mean.

By itself, Dyn^{EQN} moved with the same velocity as Dyn^{wt}, suggesting that the $Site_{Stalk}$ mutations do not grossly impair dynein's structure or function (Figures 3.5C and A.5A). Dyn^{EQN} binds to Lis1 with reduced affinity compared to Dyn^{wt} in ATP-Vi (Figure A.5B), which is compatible with the loss of one of the two Lis1 binding sites. In addition, the velocities of Dyn^{EQN} and Dyn^{wt} were lowered by similar amounts in the presence of 300 nM Lis1 (Figure 2.5C), suggesting that mutation of $Site_{Stalk}$ does not impair Lis1's interaction with dynein at $Site_{Ring}$.

To test our hypothesis that $Site_{Stalk}$ is required for the Lis1-induced weak MT binding state, we measured Dyn^{EQN}'s affinity for MTs under conditions that would normally lead to this state (ATP-Vi). Our prediction was that Dyn^{EQN} would show higher affinity for MTs than Dyn^{wt} under those conditions. In the absence of Lis1, Dyn^{EQN} and Dyn^{wt} had a similar affinity for MTs, suggesting that mutating $Site_{Stalk}$ does not alter the ability of Dyn^{EQN} to interact with MTs (Figure 2.5D). In the presence of Lis1, as we predicted, Dyn^{EQN} showed an 85% increase in MT affinity relative to Dyn^{wt} (Figure 2.5E).

With ATP, where AAA3 can sample different nucleotide states, both weak and tight binding states should be available to Dyn^{wt} in the presence of Lis1, while the weak binding state would be unavailable to Dyn^{EQN}. Dyn^{wt}'s affinity for MTs in the presence of Lis1 should reflect a mixture of weak and tight binding states, while that of Dyn^{EQN} should come from tight binding states only. As predicted, in the presence of ATP, Lis1 increased Dyn^{EQN}'s binding density on MTs two-fold more than it did for Dyn^{wt} (Figure 2.5E).

We also mutated the conserved EQN triad to alanine in dynein with a AAA3 Walker B mutation ($Dyn^{WB/EQN}$). While Lis1 increased the velocity of Dyn^{WB}, it decreased the velocity of $Dyn^{WB/EQN}$ (Figures 3.1D, A.5C and D). Similarly, while Lis1 decreased the MT affinity of Dyn^{WB}, this decrease was no longer observed in $Dyn^{WB/EQN}$ with ATP or ATP-Vi (Figure A.5E). These results suggest that the conserved second Lis1 binding site ($Site_{Stalk}$) is required to decrease dynein's MT affinity when AAA3 contains ATP or ADP-Pi.

The second binding site for Lis1 is required for dynein localization

Yeast dynein positions the mitotic spindle (Eshel et al., 1993; Li et al., 1993) by "pulling" on spindle pole body (SPB)-anchored MTs from the cell cortex (Figure 2.6A) (Adames and Cooper, 2000). Dynein reaches the cortex by localizing to MT plus ends, either via kinesin-dependent transport or recruitment from the cytosol (Carvalho et al., 2004; Caudron et al., 2008; Markus et al., 2009). Dynein's plus-end-localization, kinesin-dependent transport, and later "off-loading" to the cell cortex all require Lis1 (Lee et al., 2003; Li et al., 2005; Markus and Lee, 2011; Markus et al., 2009, 2011; Sheeman et al., 2003). The requirement of Lis1 for plus-end-localization and off-loading to the cortex is compatible with a model where Lis1 promotes a tight MT-binding state in dynein. However, this model is at odds with Lis1's requirement in the kinesin-dependent transport

Figure 2.6. The second binding site for Lis1 is required for dynein's microtubule plus end localization in vivo and in vitro. (A) Schematic of dynein and Lis1 function in spindle positioning in *S. cerevisiae*. Dynein is localized to the SPB (1), transported to the MT plus end by a kinesin in a process that also requires Lis1 (2), maintained at the MT plus end by Lis1 (3), and "off-loaded" to the cell cortex (4), where it pulls on SPB-attached MTs to position the mitotic spindle. (B) Dynein localization in dividing *S. cerevisiae*. First column: Representative brightfield images. Second column: maximum projections of 3xGFP-labeled dynein ($Dynein^{wt}$ or $Dynein^{EQN}$). Third column: maximum projections of tdTomato-labeled SPC110, a SPB marker. Fourth column: merged 3xGFP-dynein and tdTomato-SPB images. White arrowheads: co-localized dynein and SPB signals. Strains imaged: $Dynein^{wt}$ (top row); $Dynein^{wt}$ in a ΔLis1 background (middle row); $Dynein^{EQN}$ (bottom row). Both dynein-3xGFP and SPC110-tdTomato are expressed under their endogenous promoters. (C, D) Quantification of the data presented in (B). (C) Average number of dynein foci per cell colocalized with SPBs; and (D) Average number of dynein foci per cell not colocalized with SPBs for $Dynein^{wt}$ (grey), $Dynein^{wt}$/ΔLis1 (hatched grey) and $Dynein^{EQN}$ (yellow) strains (n>50 cells per data point). (E) Schematic representation of our in vitro reconstitution of kinesin-mediated dynein transport to the MT plus end. Brightly-labeled, GMPCPP-stabilized MT seeds are attached to the coverslip via biotin-streptavidin interactions. A dimly-labeled MT extension grows faster at the plus end of the seed, allowing MT polarity to be determined. Addition of dynein (labeled with TMR), Lis1, Bik1, Kip2 and Bim1 results in plus-end-directed transport of dynein by kinesin. Known interactions are shown with double-headed arrows color-coded according to the proteins involved. MT plus and minus ends are labeled. (F, G) Representative kymographs from the assay outlined in (E), with MT (488) and dynein (TMR) channels shown in black and white, and the merged image in pseudocolor, for Dyn^{wt} (F) and Dyn^{EQN} (G). Plus (+) and minus (-) indicate MT polarity. White arrowheads point to the start of plus-end-directed runs. (H) Quantification of the percentage of plus- and minus-end-directed runs for Dyn^{wt} (Grey) and Dyn^{EQN} (Yellow). (I) Quantification of the percentage of non-motile runs. (n = 4 technical replicates). Statistical significance was calculated using Mann-Whitney test for both average number of foci per cell (C, D) and percentage of runs (H, I). P-values: ns, not significant; *, < 0.05; **, <0.01; ****, <0.0001. Data are shown as mean and standard error of mean.

Figure 2.6 (continued).

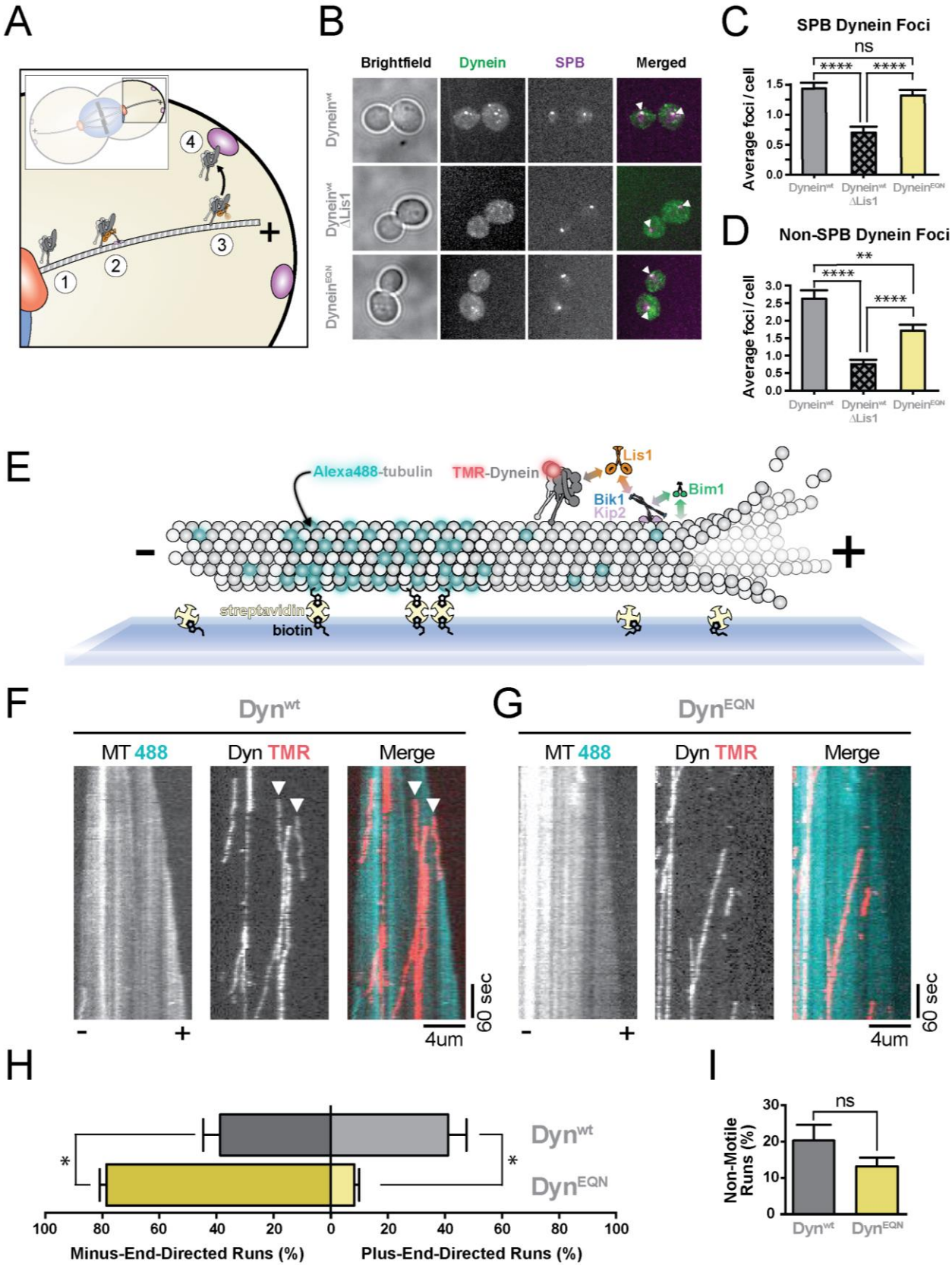

of dynein to MT plus ends, as efficient transport by kinesin would be favored when dynein weakly interacts with MTs (Roberts et al., 2014).

To determine the cellular role of $Site_{Stalk}$, we monitored dynein's localization in vivo by fusing 3X-GFP to full-length dynein or a version carrying the EQN $Site_{Stalk}$ mutation ($dynein^{EQN}$) at the endogenous locus. We also determined dynein localization in cells lacking Lis1 (ΔLis1). Dynein localizes to both the SPB and MT plus ends/ the cortex (Figure 2.6B) (Lee et al., 2003). We could not distinguish between MT plus ends and the cortex in our experiments, but localization to both sites requires Lis1. Deletion of Lis1 caused mislocalization of dynein (Lee et al., 2003; Sheeman et al., 2003) (Figure 2.6B), with ~2- and ~3-fold reductions in dynein "foci" (diffraction-limited spots) at the SPB (Figure 2.6C) and MT plus ends/cortex (Figure 2.6D), respectively. Interestingly, while yeast carrying the $dynein^{EQN}$ mutant contained the same number of dynein foci at the SPB as wild type yeast, they showed significantly reduced dynein at the MT plus end/cortex (Figure 2.6B, C). These data suggest that $Site_{Stalk}$ is required for dynein's localization in vivo.

The second binding site for Lis1 is required for dynein to be transported by kinesin

Kinesin is required for the plus-end-localization of dynein in yeast (Carvalho et al., 2004; Caudron et al., 2008; Markus et al., 2009), filamentous fungi (Zhang et al., 2010a), and mammalian neurons (Twelvetrees et al., 2016). Previously, we reconstituted yeast dynein plus-end-localization in vitro, showing that dynein is transported by a kinesin, Kip2, to MT plus ends in a process that requires Lis1 and two MT plus tip proteins Bik1 (CLIP170) and Bim1 (EB1) (Roberts et al., 2014). During transport, dynein and kinesin engage in a tug-of-war that results in dynein being slowly pulled towards the plus end of MTs by kinesin, with Bik1 and Bim1 enhancing kinesin's processivity.

We hypothesized that binding of Lis1 to $Site_{Stalk}$ might be required for kinesin to localize dynein to MT plus ends, explaining the in vivo localization defect of Dyn^{EQN} (Figure 2.6B, C). To test this, we reconstituted Dyn^{wt} and Dyn^{EQN} trafficking to the plus ends of dynamic MTs (Figure 2.6E). We monitored the directionality of dynein movement in the presence of Kip2, Lis1, Bik1, and Bim1. Dyn^{wt} was transported to the plus end in 41% of events (Figure 2.6F, H). In contrast, only 8.2% of events were plus-end-directed with Dyn^{EQN} (Figure 2.6G, H). The number of non-motile runs and the average velocity of plus-end runs observed with Dyn^{wt} and Dyn^{EQN} were not statistically different, although the average velocity of minus-end runs for Dyn^{EQN} was slightly faster than those for Dyn^{wt} (Figure 2.6I and A.6A). Dynein movement in the plus end direction indicates that the transport complex can form (Roberts et al., 2014). To test if the EQN mutation affected complex formation we monitored the ability of dynein to be recruited to MTs by kinesin (in the presence of Lis1, Bik1 and Bim1). This experiment must be done in a dynein background engineered to have a weak affinity for MTs (Dyn^{weak}) (Redwine et al., 2012; Roberts et al., 2014). As expected, Lis1 was required for the recruitment of both $Dyn^{weak/wt}$ and $Dyn^{weak/EQN}$ to MTs. $Dyn^{weak/wt}$ was recruited to MTs ~5 times more efficiently than $Dyn^{weak/EQN}$ (Figure A.6B), showing that the ability of Lis1 to bind at $Site_{stalk}$ leads to more efficient kinesin transport complex formation. Thus, $Site_{stalk}$ is required for dynein to reach MT plus ends and promotes its interaction with the kinesin transport complex.

2.5 Discussion

Here we report the surprising discovery that Lis1 has two opposing modes of regulating dynein, being capable of enhancing or inhibiting its affinity for MTs (Figure 2.7). This is a major revision

of the model for how Lis1 regulates dynein with important implications for the biological roles of this ubiquitous and highly conserved dynein regulator.

Structural basis for the opposing modes of dynein regulation by Lis1

How does Lis1 stabilize dynein's ring in a high affinity conformation when AAA3 is nucleotide-free? The higher resolution of the $Dyn^{wt\text{-}M}$:Lis1 structure presented here revealed that in addition to the interaction with AAA3 and AAA4 (Huang et al., 2012; Toropova et al., 2014), Lis1 also interacts with AAA5 (Figure 2.2D). The transition from the high affinity, open conformation of the ring to its low affinity, closed conformation involves the rotation of AAA5 relative to a rigid module comprised of AAA2-4 (Schmidt et al., 2015). This motion leads to the buttress-mediated change in the register of the stalk, and ultimately in changes in the conformation and affinity of the MTBD (Figure 2.2A) (Cianfrocco et al., 2015). We propose that Lis1 keeps dynein in a high MT affinity state by clamping AAA3/4 and AAA5 together, thus blocking the ring rearrangements necessary for dynein to adopt a low MT affinity state. We were unable to test this hypothesis here because the region of AAA5 where Lis1 interacts with dynein had the lowest local resolution in our structure (Figure A.2H, I).

How do the two Lis1 β-propellers prevent dynein from switching to a high-affinity state upon binding to MTs when AAA3 contains ATP or ADP-Pi? Normally, dynein binding to MTs triggers a conformational change in its MTBD that alters the register of its coiled coil stalk and ultimately results in the open, high-affinity conformation of dynein's ring (Cianfrocco et al., 2015). The sliding of the two helices in the stalk (CC1 and CC2) changes their position with respect to the ring (Schmidt et al., 2015) (Figure 2.2A) as well as the distance between $Site_{Stalk}$ and $Site_{Ring}$. Our $Dyn^{WB\text{-}M}$:Lis1 structure showed that $Site_{Ring}$ is closer to $Site_{Stalk}$ than in $Dyn^{wt\text{-}M}$:Lis1 (Figure 2.4C-E), likely allowing for the interaction between the two Lis1 β-propellers, as suggested by the

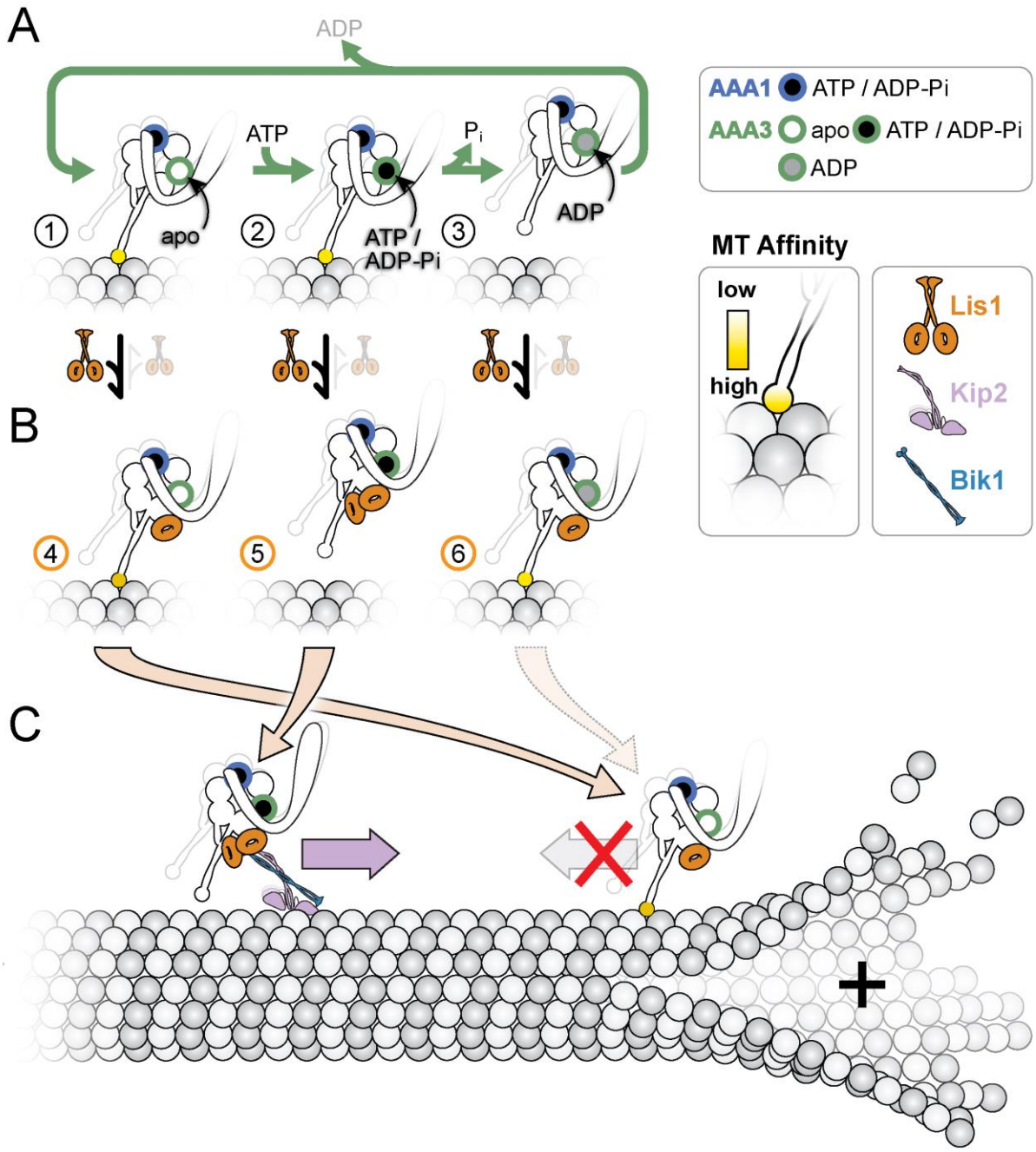

Figure 2.7. Model for the opposing modes of regulation of dynein by Lis1) (A, B) The nucleotide state of AAA3 determines which regulatory mode is used by Lis1. The figure illustrates how the ATP hydrolysis cycle at AAA3 affects the affinity of dynein for MTs (A) and how Lis1 acts on these different states (B). We show dynein with ATP/ADP-Pi bound at its AAA1 site to reflect that our data suggest this is the state where Lis1 regulation is apparent. Dynein alone has high affinity for MTs when its AAA3 is either empty ("apo") (A, state 1), or bound to ATP/ADP-Pi (A, state 2). Phosphate release from AAA3 leads to the AAA3:ADP-bound, low-affinity state

(continued) of the motor (A, state 3), which is expected to be the predominant state when dynein walks along MTs. Lis1 acts in opposite ways on states 1/3 versus 2: one β-propeller binds when AAA3 is either empty or contains ADP, leading to tight MT binding (B, states 4 and 6); while 2 β-propellers bind when AAA3 has ATP/ADP-Pi, leading to weak MT binding (B, state 5). (C) Proposed biological roles of the Lis1-mediated weak and tight MT-binding states of dynein. In *S. cerevisiae*, dynein is transported towards the plus-end of MTs by Kip2, a process that requires Lis1. Binding of two Lis1 β-propellers (B, state 5) keeps the motor in a weak affinity state and promotes the formation of the kinesin transport complex. Once at the plus-end of the MT, dynein cycles to a AAA3:ADP or AAA3:apo state (by a process not currently understood); binding of one Lis1 β-propeller (B, states 4 and 6) keeps the motor in a tightly bound to the MT in preparation for cargo loading.

continuous density we observed (Figure 2.3A, B). We hypothesize that bridging of CC1 and the ring by the two Lis1 β-propellers bound to dynein when AAA3 contains ATP or ADP-Pi prevents CC1 from sliding towards its high-affinity register. Future experiments could test this idea by disrupting the interaction between the two β-propellers, but this will require a higher resolution map where the rotational orientation of the β-propellers is unambiguous.

We had previously shown that the displacement of the linker from its docking site at AAA5 by Lis1 bound at $Site_{Ring}$ played a role in the formation of the high-affinity state; shortening the linker to a point where it would no longer be obstructed by Lis1 made dynein Lis1-insensitive (Toropova et al., 2014). While it is likely that the position of the linker affects allosteric changes in dynein's ring, establishing how the short linker circumvents the effect of Lis1 at $Site_{Ring}$ will require a high-resolution structure of $Dyn^{wt\text{-}M}$:Lis1 carrying a short linker docked at AAA5.

Both modes of Lis1 regulation are required for dynein function

In *S. cerevisiae* and other organisms, some of Lis1's known functions have been difficult to reconcile with its reported molecular function to induce a tight MT binding state in dynein. Our new model for Lis1 regulation of dynein can resolve these apparent contradictions.

As described above, dynein's function in spindle positioning in yeast is composed of multiple steps (Figure 2.6A). Our data showed that less dynein was found at MT plus ends/ the cortex in dynein with a mutant $Site_{Stalk}$ (Figure 2.6B, D). We found that less dynein moved in the plus end direction (Figure 2.6F-H), but also that a mutant $Site_{Stalk}$ reduced the formation of the kinesin transport complex (Figure A.6B). Thus, the defect in plus-end-localization of the dynein $Site_{Stalk}$ mutant could be due to a reduction in the formation of the transport complex and/or dynein's inability to access the weak MT binding state. Our current experiments do not allow us to differentiate between these two possibilities or the relative contributions of each. However, our results show that dynein's $Site_{Stalk}$ is required for dynein's localization to MT plus ends both in vivo and in vitro. Other dynein functions in yeast require high affinity MT binding, such as being retained at MT plus ends. In this context we propose that Lis1 engages dynein only at $Site_{Ring}$.

The dual functionality of Lis1 we have uncovered (Figure 2.7) provides a possible explanation for the cellular function of Lis1 in other organisms, some of which have been difficult to reconcile with a model where Lis1 exclusively promotes high-affinity MT binding by dynein. For example, Lis1 overexpression increases the velocity of acidic organelles in mouse neurons (Pandey and Smith, 2011) while its removal decreases the velocity of mRNAs in *Drosophila* embryos (Dix et al., 2013), pointing to a role for Lis1 in reducing dynein's affinity for MTs (and thus increasing dynein velocity). We propose that in these cases both Lis1 β-propellers bind to dynein. In fact, binding of Lis1 to an activated human dynein/dynactin complex has recently been

shown to increase its velocity in vitro (Baumbach et al., 2017; Gutierrez et al., 2017). Other functions for dynein are more aligned with Lis1 increasing dynein's affinity for MTs. These include stabilizing dynein at MT plus ends (Li et al., 2005; Splinter et al., 2012), facilitating cargo loading on dynein (Egan et al., 2012; Lenz et al., 2006; Moughamian et al., 2013), aiding in dynein trafficking of high-load cargo (McKenney et al., 2010; Reddy et al., 2016; Yi et al., 2011), and slowing motility of some dynein cargo (Vagnoni et al., 2016). We propose that in these cases Lis1 is bound to dynein by a single β-propeller at $Site_{Ring}$.

How are the two modes of Lis1 activity regulated?

The underlying basis for the switch between the two modes of Lis1 activity must involve regulating the nucleotide state at AAA3. There are several mechanisms we envision that could achieve this. Local fluctuations in the concentration of ATP or ADP could alter the rate of hydrolysis at AAA3, potentially making Lis1 regulation tunable to different cellular locations or events. Other dynein-binding partners, including Lis1 itself, could play a role in controlling ATP turnover at AAA3. For example, NudE/NudEL binds both dynein and Lis1 and has been implicated in many Lis1-dependent functions (Cianfrocco et al., 2015). Finally, an intriguing possibility is that a backward force exerted on dynein (such as that from a pulled cargo) could influence the nucleotide state of AAA3 (Nicholas et al., 2015b). If a backward force on dynein promoted an apo state in AAA3, this would favor a single Lis1 β-propeller binding (at $Site_{Ring}$) and maintain dynein in a high MT affinity state, which would be advantageous when dynein is transporting a high load cargo. Future work will be required to understand this complex process.

2.6 Methods

Yeast strains

S. cerevisiae strains used in this study are listed in Supplemental Table A.3. The endogenous genomic copies of *DYN1, PAC1, NDL1, KIP2, TUB1* and *SPC110* were modified or deleted using PCR-based methods and transformed using the lithium acetate method. Cultures of *S. cerevisiae* for protein purification were grown, harvested and frozen as described (Reck-Peterson et al., 2006).

Protein Purification

Protein purification steps were done at 4°C unless otherwise indicated. Dynein constructs were purified from *S. cerevisiae* as described previously (Reck-Peterson et al., 2006). Briefly, liquid nitrogen-frozen yeast cell pellets were lysed by grinding with a chilled coffee grinder and resuspending in dynein lysis buffer (DLB: final concentration 30 mM HEPES [pH 7.4], 50 mM potassium acetate, 2 mM magnesium acetate, 1 mM EGTA, 10% glycerol, 1 mM DTT) supplemented with 0.1 mM Mg-ATP, 0.5 mM Pefabloc, 0.05% Triton and cOmplete EDTA-free protease inhibitor cocktail tablet (Roche). The lysate was clarified by centrifuging at 264,900 x g for 1 hr or at 125,100 x g for 2 hr. The clarified supernatant was incubated with IgG sepharose beads (GE Healthcare Life Sciences) for 1.5 hr. The beads were transferred to a gravity flow column, washed with DLB buffer supplemented with 250 mM potassium chloride, 0.1 mM Mg-ATP, 0.5 mM Pefabloc and 0.1% Triton, and with TEV buffer (10 mM Tris–HCl [pH 8.0], 150 mM potassium chloride, 10% glycerol, 1 mM DTT, 0.1 mM Mg-ATP and 0.5 mM Pefabloc). GST-dimerized dynein constructs were labeled with 5 μM Halo-TMR (Promega) in the column for 10 min at room temperature and unbound dyes were washed with TEV buffer at 4°C. Dynein

was cleaved from IgG beads via incubation with 0.15 mg/mL TEV protease for 1 hr at 16°C. For dynein monomer constructs, the TEV cleavage step was done overnight at 4°C and the cleaved proteins were concentrated using 100K MWCO concentrator (EMD Millipore) to 1.5-5 mg/mL. Cleaved proteins were filtered by centrifuging with Ultrafree-MC VV filter (EMD Millipore) in a tabletop centrifuge and flash frozen in liquid nitrogen.

Lis1 and Kip2 were purified from *S. cerevisiae* as described previously (Huang et al., 2012; Roberts et al., 2014). Lysis and clarification steps were similar to dynein purification except buffer A (final concentration: 50 mM potassium phosphate [pH 8.0], 150 mM potassium acetate, 150 mM sodium chloride, 2mM magnesium acetate, 5mM β-mercaptoethanol, 10% glycerol, 0.2% Triton, 0.5 mM Pefabloc) supplemented with 10 mM imidazole (pH 8.0) and cOmplete EDTA-free protease inhibitor cocktail tablet was used as lysis buffer. The clarified supernatant was incubated with Ni-NTA agarose (Qiagen) for 1 hr. The Ni beads were transferred to the column, washed with buffer A + 20 mM imidazole (pH 8.0) and eluted with buffer A + 250 mM imidazole (pH 8.0). The eluted protein was incubated with IgG sepharose beads for 1 hr. IgG beads were transferred to a gravity flow column, washed with buffer A + 20 mM imidazole (pH 8.0) and with modified TEV buffer (50 mM Tris–HCl [pH 8.0], 150 mM potassium acetate, 2 mM magnesium acetate, 1 mM EGTA, 10% glycerol, 1 mM DTT, and 0.5 mM Pefabloc). TEV cleavage was done as described for dynein purification.

Bik1 was purified from Baculovirus as described previously (Roberts et al., 2014). Cell pellets were resuspended in buffer B (final concentration: 50 mM Tris-HCl [pH 8.5], 300 mM potassium chloride, 5 mM β-mercaptoethanol, 5% glycerol, 10 mM imidazole) supplemented with 1% NP-40 and cOmplete EDTA-free protease inhibitor cocktail tablet and lysed using a Dounce homogenizer (15 strokes with loose plunger and 10 strokes with tight plunger). The lysate was

clarified by centrifuging at 183,960 x g for 30 min. The clarified supernatant was incubated with Ni-NTA agarose for 1 hr. The Ni beads were transferred to a gravity flow column, washed with buffer C (20 mM Tris-HCl [pH 8.5], 500 mM potassium chloride, 5 mM β-mercaptoethanol, 20 mM imidazole), buffer D (20 mM Tris-HCl [pH 8.5], 1 M potassium chloride, 5 mM β-mercaptoethanol, 20 mM imidazole), buffer C and buffer E (20 mM Tris-HCl [pH 7.5], 200 mM potassium chloride, 5 mM β-mercaptoethanol, 10% glycerol). Bik1 was eluted with buffer E + 300 mM imidazole and flash frozen in liquid nitrogen.

Bim1 was purified from *E. Coli* as described previously (Roberts et al., 2014). Protein expression was induced in BL-21[DE3] cells (NEB) at OD 0.6 with 0.1 mM IPTG for 16 hr at 18°C. Cell pellets were resuspended in buffer B with 1 mg/mL lysozyme, incubated for 30 min on ice and lysed by sonication. The lysate was clarified by centrifuging at 154,980 x g for 30 min. The clarified supernatant was passed over Strep-Tactin agarose resin (IBA Life Sciences) three times in a gravity flow column. The resin was washed with buffer D and with modified TEV buffer. TEV cleavage was done as described for the dynein purification.

TIRF microscopy

Imaging was performed with an inverted microscope (Nikon, Ti-E Eclipse) equipped with a 100x 1.49 N.A. oil immersion objective (Nikon, Plano Apo). The xy position of the stage was controlled by ProScan linear motor stage controller (Prior). The microscope was equipped with a MLC400B laser launch (Agilent), with 405 nm, 488 nm, 561 nm and 640 nm laser lines. The excitation and emission paths were filtered using appropriate single bandpass filter cubes (Chroma). The emitted signals were detected with an electron multiplying CCD camera (Andor Technology, iXon Ultra

897). Illumination and image acquisition is controlled by NIS Elements Advanced Research software (Nikon).

Single-molecule motility and microtubule binding assay on taxol-stabilized microtubules

Single-molecule motility and MT binding assays were performed in flow chambers made with double stick tape using the TIRF microscopy set up described above. No. 1-1/2 coverslips (Corning) were used for the flow chamber assembly and sonicated in 100% ethanol for 10 min to reduce non-specific binding. Taxol-stabilized MTs with ~10% biotin-tubulin and ~10% Alexa488-tubulin were attached to the flow chamber via biotin-BSA and streptavidin as described previously (Huang et al., 2012). Dynein was labeled with Halo-TMR for visualization. For each frame, Alexa488-tubulin and TMR-dynein were exposed for 100 ms with the 488 nm laser and 561 nm laser, respectively.

For motility assays, 1-25 pM dynein was incubated with 300 nM Lis1 or modified TEV buffer (to buffer match for experiments without Lis1) for 10 min on ice, and flowed into the flow chamber pre-assembled with taxol-stabilized MTs. The final imaging buffer contained DLB supplemented with 50 mM potassium acetate (hence a total of 100 mM potassium acetate), 20 μM taxol, 1 mM Mg-ATP, 1 mg/mL casein, 71.5 mM β-mercaptoethanol and an oxygen scavenger system (0.4% glucose, 45 μg/ml glucose catalase, and 1.15 mg/ml glucose oxidase). MTs were imaged first by taking a single-frame snapshot. Dyneins were imaged every 1 sec (for wild-type dynein) or 2 sec (for mutant dyneins) for 10 min. At the end, MTs were imaged again by taking a snapshot to check for stage drift. Movies showing significant drift were not analyzed. Each sample was imaged no longer than 30 min.

For the single-molecule MT binding assays, 0.5-10 pM dynein was incubated with 300 nM Lis1 or modified TEV buffer (to buffer match for experiments without Lis1) for 10 min on ice. Dynein concentrations were varied to ensure that single dynein molecules could be resolved on each MT. Based on the dissociation constants measured (Figure A.1 and Supplementary table A.2) and using a one-site model of association, we have calculated that in the presence of 300nM Lis1, between 85%-88% of each dynein variant is in complex with Lis1, regardless of the dynein concentration. Given that the Lis1-dynein dissociation constants were determined with monomeric dynein constructs and at a higher salt than is present in the MT binding experiments, it is likely that the complex percentages we report here are underestimations. The final imaging buffer contained DLB supplemented with 20 μM taxol, 1 mg/mL casein, 71.5 mM β-mercaptoethanol, an oxygen scavenger system, and 1 mM nucleotides (Mg-ATP, Mg-ATP/$NaVO_4$, Mg-ADP) or 2.5 units/mL apyrase for the no nucleotide condition. Nucleotides or apyrase were added to the incubated dynein samples immediately before adding to the flow chamber. Dynein was incubated for an additional 10 min in the flow chamber at room temperature to reach steady-state before imaging. For MT binding assays with ATP, dynein was imaged by taking a single-frame snapshot. For MT binding assays with other nucleotide conditions, dynein was imaged every 1 sec for a total of 5 sec. Each sample was imaged at 4 different fields of view and there were between 5 and 10 MTs in each field of view. In single-molecule assays, it is not possible to precisely control the amount of MTs that attach to the coverslip surface on different days due to variations in the surface quality of the coverslips and small variations in the concentration of each taxol-stabilized MT preparation. Therefore, in order to compare and combine replicates taken on different days without bias, the samples with and without Lis1 for each nucleotide condition were imaged in two separate flow chambers made on the same coverslip on the same day with the same stock of polymerized

tubulin. The sample without Lis1 served as an internal control for normalization of the binding density (see below).

Size exclusion chromatography to determine the binding stoichiometry

2 μM Dyn^{WB-M} and 4 μM Lis1 were mixed and incubated for 10 min in DLB supplemented with 200 μM Mg-ATP/$NaVO_4$. Samples were fractionated on a Superdex 200 Increase 3.2/300 using an ÄKTAmicro system (GE Healthcare) that had been equilibrated in DLB buffer supplemented with 200 μM Mg-ATP/$NaVO_4$. Fractions were analyzed by SDS-PAGE on 4-12% Bis-Tris gels (Invitrogen) and visualized with SYPRO Red (Invitrogen). Peak fractions were then diluted so that both Dyn^{WB-M} and Lis1 were within the 50-500 ng range. Diluted samples were then re-analyzed via SDS-PAGE with an actin standard curve on the same gel to determine the absolute amount (ng) of each protein. Moles of each protein were calculated using 331,000 Da for Dyn^{WB-M} and 113,800 Da for dimeric Lis1. Molar ratios were then determined. We ensured that each protein binds SYPRO Red in a linear fashion by running titrations of Dyn^{WB-M} and Lis1 on SDS-PAGE gels and staining with SYPRO Red.

Cryo-EM sample preparation

Protein samples were thawed quickly and kept on ice prior to grid preparation. For Dyn^{wt-M}:Lis1, the sample was prepared using the following steps: dynein and Lis1 were incubated on ice for 10 min, after which ATP was added to a final concentration of 5 mM and the sample was incubated on ice for another 10 min. This resulted in both dynein and Lis1 at a final concentration of 0.75 μM in buffer (50 mM Tris–HCl [pH 8.0], 150 mM potassium acetate, 2 mM magnesium acetate, 1 mM EGTA, 1 mM DTT, and 5 mM Mg-ATP).

For Dyn^{WB-M}:Lis1, the sample was prepared using the following method: dynein and Lis1 were incubated on ice for 10 min, after which Mg-ATP/$NaVO_4$ was added to a final concentration of 1.2 mM and the sample was incubated on ice for another 10 min. This resulted in both dynein and Lis1 at a final concentration of 0.75 μM in buffer (50 mM Tris–HCl [pH 8.0], 150 mM potassium acetate, 1 mM EGTA, 1 mM DTT, 1.2 mM Mg- ATP/$NaVO_4$).

After incubation, both samples were treated identically: 4 μl of sample was applied directly to an untreated (no glow discharge or plasma cleaning) UltrAuFoil 1.2/1.3 grid (Quantifoil) in a Vitrobot (FEI Company) kept at 100% humidity and 4°C. After applying the sample, the excess liquid was immediately blotted in the Vitrobot using a blot force of 20 and a blot time of 4 sec prior to plunge-freezing into liquid ethane.

Cryo-EM data collection and image analysis

Both datasets (Dyn^{wt-M}:Lis1 and Dyn^{WB-M}:Lis1) were collected on a Talos Arctica transmission electron microscope (FEI Company) operating at 200 keV with a K2 Summit direct electron detector (Gatan Inc.) (See also Supplementary table A.1). Images were collected automatically using Leginon (Suloway et al., 2005) in super-resolution mode with a calibrated pixel size of 0.60 Å/pixel. The movies were then processed in the Appion pipeline (Lander et al., 2009) for all subsequent steps. Initial movie alignment and gain reference correction were performed with MotionCor (Li et al., 2013).

For the Dyn^{wt-M}:Lis1 dataset (see also Figure A.2 and Supplementary table A.1), 485,102 particles were picked from 5,614 micrographs using FindEM (Roseman, 2004) with templates generated from forward projections at 25 degree angular increments of EMDB: 6013 (Toropova et al., 2014) (dynein motor domain without nucleotide). Using these particle coordinates, particles

were extracted from micrographs that were aligned using MotionCor2 (Zheng et al., 2017) in Relion-1.4 (Scheres, 2012) using defocus values calculated by CTFFIND4 (Rohou and Grigorieff, 2015) on MotionCor2 micrographs. Micrographs were discarded if CTF confidence fits from CTFFIND4 did not go beyond 10 Å. For initial 2D classification in Relion-1.4, particles were extracted at a box size of 80 x 80 pixels and a pixel size of 4.8 Å/pixel. These particles were classified into 200 classes over 11 iterations with a mask diameter of 210 Å From the resulting averages, 347,462 particles were selected from classes that did not have contaminating ice or gold particulates. These particles were subjected to another round of 2D classification using Relion-1.4, classifying them into 200 classes over 25 iterations with a mask diameter of 190 Å From the resulting class averages (of which a subset is shown in Figure A.2B), 151,470 particles (80 x 80 pixels; 4.8 Å/pixel) were selected for 3D refinement to determine a structure at 9.96 Å using gold-standard FSC=0.143, using EMDB6016 filtered to 60 Å as an initial model. A summary of the 3D refinement and classification strategy is shown in Figure A.2C. This refinement and all subsequent 3D classification and refinement routines were performed using Relion-2.0beta (Kimanius et al., 2016) on Amazon Web Services using EM-packages-in-the-cloud-v4.0-GPU (Cianfrocco and Leschziner, 2015). Next, particles were re-extracted at a pixel size of 1.2 Å/pixel (324 x 324 pixels) and subjected to 3D classification without alignment, using orientations determined in the previous 3D refinement step. After classifying into 3 groups over 15 iterations, 10 more iterations of classification were performed using a local angular search range of 10 degrees. From this classification, one class was selected for further refinement (45,219 particles) to obtain a 9.48 Å structure using gold-standard FSC=0.143 because the two other classes did not have high resolution features present. With this refined 3D structure, we classified the particles into 2 groups over 15 iterations, followed by 10 iterations of local angular search ranges of 10 degrees. This

resulted in one class containing high resolution features that was used for a final round of 3D refinement (25,520 particles). After this last 3D refinement step, the overall resolution was calculated to be 7.7 Å applying a *B*-factor of -50 Å^2 after combining the half-maps and masking during post-processing (Figure A.2D). However, due to the presence of flexible regions of the structure, we calculated local resolution and filtered the map using Blocres in Bsoft (Heymann and Belnap, 2007), which displayed a range of resolutions from 6 – 10 Å (Figure A.2E).

For the Dyn^{WB-M}:Lis1 dataset (see also Figure A.3 and Supplementary table A.1), 414,277 particles were picked from 4,826 micrographs using FindEM (Roseman, 2004) with templates generated from forward projections at 25 degree angular increments of EMDB: 6013 (Toropova et al., 2014) (dynein motor domain without nucleotide). Using these particle coordinates, particles were extracted from micrographs that were aligned using MotionCor2 (Zheng et al., 2017) in Relion-1.4 (Scheres, 2012) using defocus values calculated by CTFFIND4 (Rohou and Grigorieff, 2015) on MotionCor2 aligned micrographs. Micrographs were discarded if CTF confidence fits from CTFFIND4 did not go beyond 10 Å Particles were extracted using a box size of 64 x 64 pixels and a pixel size of 4.8 Å/pixel. Prior to 2D classification, all particles that had gold particulates (as defined by size and pixel values) were removed from the extracted particle stack. This produced a dataset that had 223,981 particles that were subsequently classified into 250 classes using Relion-1.4 (Figure A.3B). After this classification, particles that belong to homogenous classes were selected for further 3D analysis (107,273 particles). Prior to 3D analysis, particles were re-extracted at a box size of 128 x 128 pixels and a pixel size of 2.4 Å/pixel. After performing 3D classification into 3 classes (Figure A.3C) using EMDB6016 as a starting model, filtered to 60 Å, we obtained a single class that could be determined to an overall resolution 10.2 Å with a *B*-factor of -800 Å^2 using Relion-1.4 (Figure A.3D). Local resolution assessment using

Blocres in Bsoft (Heymann and Belnap, 2007) displayed a range of resolutions from 9 – 13 Å (Figure A.3E), however the map was filtered to a single value of 10.2 Å with a *B*-factor of -800 $Å^2$ using Relion-1.4.

All figures were generated using UCSF Chimera.

Model building using Rosetta

The initial model for dynein was generated based on homology detection to the *S. cerevisiae dyn1* sequence using Hidden Markov Model as implemented in HHpred (https://toolkit.tuebingen.mpg.de/hhpred), using the top 3 scoring homologous models (PDB: 4RH7 (Schmidt et al., 2015), 3VKG (Kon et al., 2012), and 4AKG (Schmidt et al., 2012)). This model was split into three parts: 1) Linker -> AAA4(Stalk CC1), 2) AAA4(Stalk CC2) -> AAA5 Large, 3) AAA5S -> C-terminus, and each was refined using Rosetta with cryo-EM maps Dyn^{wt-M}:Lis1 and Dyn^{WB-M}:Lis1 (Wang et al., 2016). In each case 200 models were generated, and the RMSD values for the top five models are shown in Figures A.2H and A.3H, with most RMSD values being <1 Å for Cα backbone atoms. Finally, the top-scoring model from each part was combined for a final refinement to ensure inter-domain contacts were satisfied.

Cα distance calculations

For Cα distance measurements and comparisons, atomic coordinates were used for only large and small AAA domains in the dynein ring. PDB coordinates from the previously published structure of human dynein-2 with ADP.Vi (PDB 4RH7) (Schmidt et al., 2015) were used to create a homology model using the sequence from *S. cerevisiae* with SWISS-MODEL (Biasini et al., 2014). Using these coordinates, distances between Cα atoms were calculated and displayed using

UCSF Chimera (Pettersen et al., 2004). For each distance measurement the lines shown represent the distance between the Cα atoms, and the thickness of the linearly scaled with the distance between atoms. Program is available upon request to the authors.

Single-molecule motility assay on dynamic microtubules

Single-molecule motility assays on dynamic MTs were performed using the TIRF microscopy set up described above. Flow-chambers were prepared as described above using biotin-PEG-functionalized coverslips (Microsurfaces). Brightly-labeled, biotinylated and GMPCPP-stabilized MT seeds were prepared as described (Roberts et al., 2014). Flow chambers were incubated sequentially with the following solutions, interspersed with two washes with assay buffer (BRB80 [80 mM PIPES-KOH pH 6.8, 1 mM magnesium chloride, 1 mM EGTA], 0.5 mg/mL casein and 1 mM DTT): (1) 0.8% pluronic F-127 and 5 mg/mL casein in water (6 min incubation); (2) 0.5 mg/mL streptavidin in BRB80 (3 min incubation); (3) a fresh dilution of MT seeds in assay buffer (3 min incubation); and (4) the final imaging solution containing 2.5-5 pM dynein-TMR, 1 nM Kip2, 5 nM Bim1, 50 nM Bik1, 25 nM Lis1, 15 μM tubulin (~7.5% Alexa488 labeled and ~92.5% unlabeled), 1 mM Mg-ATP, 1 mM Mg-GTP, 0.1% methylcellulose, 71.5 mM β-mercaptoethanol and an oxygen scavenger system in assay buffer. Two-color sequential TIRF movies of MTs and dynein were imaged every 3 sec for a total of 10 min. For each frame, Alexa488-tubulin and TMR-dynein were exposed for 100 ms with the 488 nm laser and for 200 ms with the 561 nm laser, respectively.

Microtubule recruitment assay of weak microtubule binding dynein variants

MT recruitment assay was performed using the TIRF microscopy set up described above. Flow chambers were incubated with the following solutions, with two washes of assay buffer (BRB80, 20μM taxol, 0.5 mg/mL casein and 1 mM DTT) in between: (1) 0.5 mg/mL streptavidin in BRB80 (3 min incubation); (2) a fresh dilution of taxol-stabilized Alexa488-labeled MTs in assay buffer (3 min incubation); and (3) the final imaging solution containing 100pM $Dyn^{weak\text{-}variant}$-TMR, 2 nM Kip2, 5 nM Bim1, 50 nM Bik1, 25 nM Lis1, 71.5 mM β-mercaptoethanol and an oxygen scavenger system in assay buffer. The weak MT binding dynein variants contains the following additional mutations: K3166A, K3117A, E3122A, R3124A (Redwine et al., 2012). The final solution containing dynein was incubated for an additional 5 min in the flow chamber at room temperature to reach steady-state before imaging. Dynein was imaged every 1 sec for a total of 5 sec. Each sample was imaged at 4 different fields of view.

Lis1 affinity capture to determine Lis1-dynein binding affinities

Sixteen μL of magnetic SNAP-Capture beads (NEB) were incubated with increasing concentrations of SNAP-Lis1 (0-600 nM) in modified TEV buffer for 1 hour at room temperature with agitation. The supernatant was removed, the beads were washed with 1 ml of modified TEV buffer followed by 1 ml of TEV buffer supplemented with 1 mM DTT, 0.1% NP40, 2 mM $MgCl_2$, 1 mM ATP, and 1 mM $NaVO_4$. 20 nM $Dyn^{(variant)\text{-}M}$ was incubated with the beads conjugated to Lis1 for 30 min at room temperature with agitation. The supernatant was removed, ran on a 4-12% Bis Tris gel, and stained with Sypro Red (Thermo Fisher) to visualize the fraction of dynein depleted.

Sequence alignment

Protein sequences of dynein were obtained from UniProt. Sequence alignments were performed with Clustal Omega web services (http://www.ebi.ac.uk/Tools/msa/clustalo/) and annotated using Jalview (http://www.jalview.org/).

Yeast *in vivo* dynein localization assay

To quantify dynein localization during mitosis, yeast strains containing 3xGFP-labeled dynein and tdTomato-labeled SPB marker, SPC110, were used. Overnight cultures grown from a single colony were diluted to OD_{600} of 0.1 in 10 mL YPD. Diluted cultures were then grown for 2-3 hours with rotation at 30°C to reach mid-log phase (OD_{600} 0.6-0.8). 100-200 µL of mid-log phase culture were spun down using a table-top centrifuge, the media was discarded and the cells were resuspended in 6 µL of phosphate-saline buffer with calcium and magnesium. The resupended cells were then added to freshly-made synthetic complete media agarose pad on glass slide. No. 1-1/2 coverslips (Corning) were placed on top of the sample and sealed with nail polish. Imaging was performed with a spinning-disk confocal (Yokogawa, CSU10) inverted microscope (Nikon, Eclipse TE2000-E) equipped with a 100X 1.40 N.A. oil-immersion objective (Nikon, Plano Apo), and an electron multiplying CCD (Andor Technology, iXon DV887). The excitation and emission paths were filtered using appropriate single bandpass filter cubes (Chroma). Images were collected for 15 x 500 nm Z-sections (7.5 µm total Z stack). For each Z section, a bright field image, a 3xGFP-labeled dynein image via 488 nm laser excitation, and a tdTomato-labeled SPB image via 568 nm laser excitation were collected. Illumination and image acquisition is controlled by iQ2.6 imaging software (Andor Technology).

Quantification and Statistical Analysis

Single-molecule motility assay on taxol-stabilized or dynamic microtubules

Dynein velocity was calculated from kymographs generated using an ImageJ macro as described (Roberts et al., 2014). In the assay with dynamic MTs, MT plus ends were assigned as the ends with faster growth rate. The directionality of individual dynein runs was subsequently assigned as a plus-end run if it moved toward MT plus end or a minus-end run if it moved in the opposite directions. Each pixel corresponds to 157 nm in our single-molecule assays. Only runs that lasted at least 4 frames were included in the analysis. Bright aggregates, which were less than 5% of the population, were excluded from the analysis. Statistical analyses for velocities were done using unpaired t-test with Welch's correction in Prism7 (GraphPad). Statistical comparisons of the percentage of plus-end moving events, minus-end moving events or non-motile events were performed using Mann-Whitney test in Prism7. Exact value of n and evaluation of statistical significance are described in the corresponding figure legends.

Single-molecule microtubule binding assay

Dynein binding density on MTs and recruitment to MTs by Kip2 was calculated using ImageJ. A minimum projection of 5 movie frames of dynein was generated to minimize counting non-specific binding events. In the MT decoration assay with ATP, a single-frame snapshot of dynein was used due to dynein motility in the presence of ATP. Intensity profiles of dynein spots were generated over a 5-pixel wide line drawn perpendicular to the long axis of the MT. Intensity peaks at least 2-fold higher than the background intensity were counted as dynein spots bound to MTs. Bright aggregates that were 5-fold brighter than neighboring intensity peaks were not counted as dynein spots. The total number of dynein spots was divided by the total MT length in each field of view

to calculate the binding density. Normalized binding density was calculated by dividing by the average binding density of dynein without Lis1 collected on the same coverslip (see above) in each nucleotide condition. Statistical significance was determined using an unpaired t-test with Welch's correction in Prism7. The exact value of n and evaluation of statistical significance are described in the corresponding figure legends.

Yeast in vivo dynein localization assay

Only yeast cells with large buds and two SPB foci were included in the analysis. Maximum intensity projections of the GFP-Dynein and tdTomato-SPC110 channels were generated. Dynein and SPB foci were identified using the ImageJ plugin, *Find Maxima*, and a maxima cutoff of at least 1.5-fold higher than the neighboring background pixel intensity value. Dynein foci were separated into two categories: localized at SPB and not localized at SPB. The latter category includes cortical and MT plus-end-localized dynein. We cannot differentiate between these two populations because MTs were not imaged (or labeled in our strains). Statistical comparisons of the average number of dynein foci per cell were done using a Mann-Whitney test in Prism7. The exact value of n and evaluation of statistical significance are described in the corresponding figure legends.

Data Availability

Cryo-EM maps and Rosetta models for the structures of Dyn^{wt}:Lis1 (PDB ID: 5VH9, EMDB: EMD-8673) and Dyn^{WB}:Lis1 (PDB ID: 5VLJ, EMDB: EMD-8706) have been deposited.

2.7 Acknowledgements

We thank Elizabeth Kellogg (UC Berkeley) for the distance comparison script, the UCSD Cryo-EM facility, Arshad Desai for access to a spinning disk microscope, the UCSD Physics IT group, and Wei-Lih Lee (U Mass Amherst) for yeast strains. We used the Extreme Science and Engineering Discovery Environment (XSEDE) for computing allocations (MCB160079 to Zaw Min Htet and MCB140257 to Andres E. Leschziner), supported by NSF grant ACI-1548562. Morgan E. DeSantis is supported by the Jane Coffin Childs Memorial Fund, Michael A. Cianfrocco by the Damon Runyon Cancer Research Foundation, Zaw Min Htet by a NSF graduate research fellowship, Samara L. Reck-Peterson and Andres E. Leschziner by NIH grant R01GM107214, and Samara L. Reck-Peterson by HHMI and the Simons Foundation.

Chapter 3

Lis1 promotes the formation of maximally activated dynein complexes

3.1 Contributions

Zaw Min Htet, John P. Gillies, Morgan E. DeSantis and Samara L. Reck-Peterson conceptualized and designed the experiments. Zaw Min Htet and John P. Gillies designed and cloned constructs. Zaw Min Htet, John P. Gillies and Morgan E. DeSantis performed protein purification. Zaw Min Htet and John P. Gillies performed single-molecule experiments. Zaw Min Htet, John P. Gillies and Morgan E. DeSantis analyzed single-molecule experiments. John P. Gillies and Morgan E. DeSantis performed in vitro immunoprecipitation experiments. Zaw Min Htet, John P. Gillies, Morgan E. DeSantis and Samara L. Reck-Peterson interpreted the data. Samara L. Reck-Peterson provided mentorship.

3.2 Abstract

Cytoplasmic dynein-1 (dynein) is a microtubule-based motor that facilitates the long-distance transport of many different cargos toward the minus end of microtubules. Human dynein does not move processively on its own. Instead, it must form a complex with dynactin and a coiled-coil-containing activating adaptor, such as BICD2, to achieve motility. Complexes containing two dynein dimers move faster. Another highly conserved dynein regulator, Lis1, is also required for nearly all of dynein's functions. In vitro Lis1 increases the velocity of activated human dynein complexes, but the mechanistic basis for this remains unclear. Using in vitro reconstitution of pure proteins and single-molecule imaging, we have found that this increase in velocity is due to Lis1 recruiting an additional dynein dimer to the complex. We hypothesize that Lis1 has a general role in the formation of optimally activated dynein complexes.

3.3 Introduction

The microtubule cytoskeleton and its associated motors are responsible for the long-distance transport of cellular cargos in humans and many other eukaryotic organisms. MTs are polarized structures that have plus ends generally oriented toward the plasma membrane and minus ends originating from microtubule organizing centers usually found near the center of the cell. Cytoplasmic dynein-1 (dynein) is a microtubule-based motor that moves towards the minus end. It is responsible for the transport of hundreds of different cargos, including organelles, vesicles, RNAs and viruses, as well as having roles in cell division (Reck-Peterson et al., 2018). Mutations in the dynein machinery cause a variety of neurological diseases (Lipka et al., 2013).

Dynein is tightly regulated by ubiquitous regulators such as dynactin, activating adaptors and Lis1 and this regulation is crucial for fine-tuning dynein motor to its diverse set of functions. Dynactin and activating adaptors are essential for activating mammalian dynein, which exists in autoinhibited states and rarely exhibits processive movement on its own (McKenney et al., 2014; Schlager et al., 2014a; Torisawa et al., 2014; Zhang et al., 2017). Binding of dynactin and activating adaptors to dynein relieves autoinhibition and converts dynein into a highly processive motor (McKenney et al., 2014; Schlager et al., 2014a; Zhang et al., 2017). Dynactin has been implicated in almost every dynein-dependent role in cells (Schroer, 2004). Activating adaptors serve not only to activate dynein but also to bind it to cargo (Reck-Peterson et al., 2018). Recently it was shown that a second dynein dimer can be recruited to these activated dynein complexes, which allows them to move faster (Grotjahn et al., 2018; Urnavicius et al., 2018).

Lis1 is another conserved regulator of dynein and mutations in Lis1 gene result in Type-1 lissencephaly, a neurodevelopmental disease characterized by a smooth cerebral phenotype (Reiner et al., 1993). Lis1 has been linked to many dynein functions, including

localizing/maintaining dynein at MT plus ends (Lee et al., 2003; Sheeman et al., 2003; Splinter et al., 2012), initiating dynein transport from plus ends (Egan et al., 2012; Lenz et al., 2006; Moughamian et al., 2013), and enabling dynein to move against high load (McKenney et al., 2010; Reddy et al., 2016; Yi et al., 2011). Deletion or depletion of Lis1 has generally been shown to reduce dynein based transport (Dix et al., 2013; Klinman and Holzbaur, 2015; Moughamian et al., 2013; Pandey and Smith, 2011; Shao et al., 2013; Smith et al., 2000; Yi et al., 2011), although in one case Lis1 depletion was found to cause increased transport (Vagnoni et al., 2016). Lis1 is a dimer of two β-propellers with which it binds directly to the dynein motor domain at two distinct sites (DeSantis et al., 2017; Huang et al., 2012; Toropova et al., 2014). In vitro experiments in yeast have revealed two opposing modes of regulation by Lis1, as it can both increase and decrease dynein's velocity (DeSantis et al., 2017).

Even though regulation of dynein alone by Lis1 has been explored in mechanistic details in vitro, it remains relatively obscure how Lis1 regulates dynein in the presence of its other essential regulators, dynactin and activating adaptor. Recently, it has been shown that Lis1 increases the velocity of activated dynein complexes formed with dynein, dynactin and activating adaptor BicD2 (Baumbach et al., 2017; Gutierrez et al., 2017). However, how Lis1 exerts this effect is unknown. Here we use in vitro reconstitution, single molecule imaging and cryo-electron microscopy to understand the mechanism of Lis1's regulation of dynein-dynactin-activating adaptor complexes. Based on our data, we conclude that Lis1 aids in the formation of maximally activated dynein complexes containing two dynein dimers.

3.4 Results

Lis1 increases the microtubule binding and velocity of dynein-dynactin-BicD2S complex

To study the regulation of Lis1 on mammalian dynein-dynactin-activating adaptor complexes, we mixed full-length human dynein and Lis1 purified from insect cells, dynactin complex from HEK-293T cells and an activating adaptor BicD2 from bacteria and assayed their microtubule binding and motility behavior in single-molecule experiments (Figure 3.1A). Since full-length BicD2 is known to be auto-inhibited, we used a well-characterized BicD2 truncation from 25-398 amino acid residues (BicD2S herein), which has been shown to be sufficient to activate dynein in the presence of dynactin in vitro as well as in cells (Figure 3.1B) (Hoogenraad et al., 2003; McKenney et al., 2014; Schlager et al., 2014a; Splinter et al., 2012).

We first tested the effect of Lis1 on the microtubule binding of dynein alone in a single-molecule assay as described previously (DeSantis et al., 2017). Lis1 increased the microtubule binding density of dynein alone by ~1.3-fold (Figure 3.1C). This is consistent with the regulatory effect of Lis1 on the microtubule binding affinity of yeast dynein (DeSantis et al., 2017; Huang et al., 2012) as well as the motor domain of rat dynein (McKenney et al., 2010).

Next, we characterized the effect of Lis1 on activated dynein-dynactin-BicD2S complexes (DDBS-WT). We assembled DDBS-WT complexes by mixing dynein, dynactin and BicD2S at 1:2:10 molar ratio. We first measured the effect of Lis1 on the microtubule binding of DDBS-WT complexes. We counted the binding density of BicD2S foci on microtubules as DDBS-WT complexes because BicD2S bound to microtubules minimally without the presence of both dynein and dynactin (Figure B.1). Lis1 increased the microtubule binding density of BicD2S foci of DDBS-WT complexes by ~5.1-fold (Figure 3.1D). We next tested the effect of Lis1 on DDBS-WT motility in a single-molecule assay. In agreement with previous studies, Lis1 significantly

increased the velocity of processive DDBS-WT complexes (Figure 3.1E) (Baumbach et al., 2017; Gutierrez et al., 2017). Taken together, these results show that Lis1 increases the microtubule binding as well as the velocity of dynein-dynactin-BicD2S complexes.

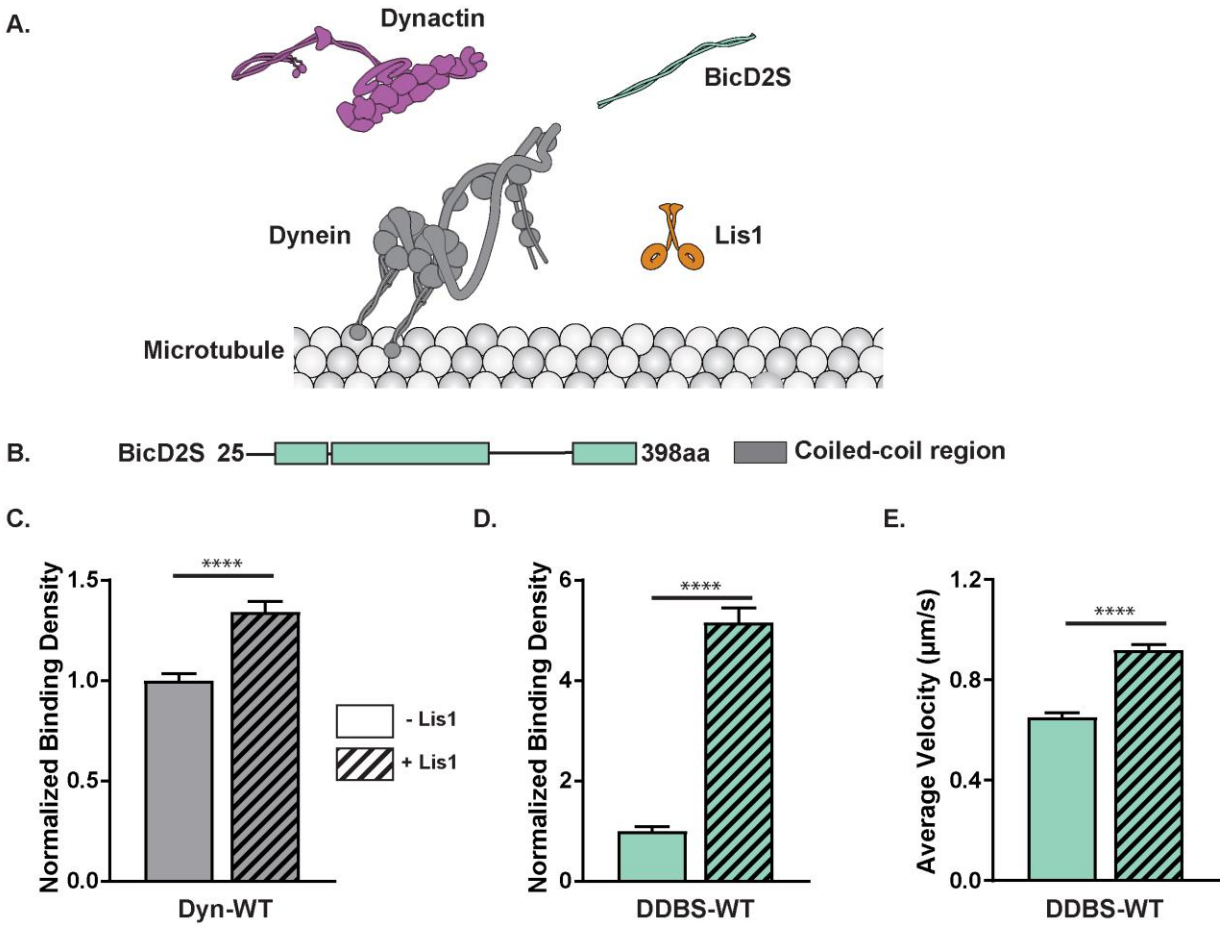

Figure 3.1. Lis1 increases the microtubule binding and velocity of activated dynein complexes. (A) Cartoons of the constructs used in this study. (B) Schematic of the BicD2S construct used in this study. (C) Normalized dynein binding density on microtubules in the absence (solid bars) and presence (hatched bars) of 300 nM Lis1. Data was normalized so that the binding density was 1 in the absence of Lis1. (D) Normalized DDBS binding density on microtubules in the absence (solid bars) and presence (hatched bars) of 300 nM Lis1, measured by BicD2S foci. Data was normalized so that the binding density was 1 in the absence of Lis1. (E) Average velocity of DDBS complexes in the absence (solid bars) and presence (hatched bars) of 300 nM Lis1. p

(continued) values: ns, not significant; *, <0.05; **, <0.01; ***, <0.001, ****, <0.0001. Data are shown as mean and standard error of mean.

Functional dissection of known Lis1 binding sites on dynein and dynein binding sites on Lis1

We next set out to dissect which of the known Lis1 binding sites mediate the effect of Lis1 on the microtubule binding and velocity of DDBS complexes. Previous structural studies of yeast dynein monomer and Lis1 have revealed that there are two highly conserved Lis1 binding sites on dynein motor domain (Figure 3.2A) (DeSantis et al., 2017; Huang et al., 2012; Toropova et al., 2014). The first binding site, which will be referred to as Site1, has been shown to induce tight microtubule binding state of yeast dynein. We mutated the corresponding mutations of Site1, K2898A, E2902G, E2903S and E2904G, in human dynein and tested the effect of Lis1 on dynein alone with Site1 mutations (Dyn-Site1) as well as DDBS complexes with Site1 mutations (DDBS-Site1). Similar to previous findings in yeast system, Lis1 no longer increased the microtubule binding of Dyn-Site1 (Figure 3.2B). Surprisingly, Lis1 still increased the microtubule binding density of BicD2S foci of DDBS-Site1 complexes as well as the velocity of processive DDBS-Site1 complexes (Figure 3.2 C, D). These results suggest that the residues identified in yeast for Site 1 are required to increase the microtubule binding of dynein alone but not responsible for the Lis1-mediated increase in the microtubule binding and velocity of activated dynein complexes.

We next tested the role of the second Lis1 binding site (Site2 herein), which is required for Lis1-mediated weak microtubule binding state of yeast dynein (DeSantis et al., 2017). We mutated the corresponding Site2 mutations, E3196A, Q3198A, N3202A, in human dynein. Similar to the yeast system, Lis1 increased the microtubule binding of dynein alone with Site2 mutations (Dyn-Site2) by ~1.5-fold (Figure 3.2B). In addition, mutating Site2 did not disrupt the Lis1-mediated increase in the microtubule binding and velocity of activated dynein-dynactin-BicD2S complexes

Figure 3.2. Functional dissection of known Lis1 binding sites on dynein's motor domain and dynein binding sites of Lis1. (A) Schematic of the two known Lis1 binding sites from yeast, indicating location of mutations in dynein variants. (B) Average dynein binding density on microtubules with dynein variants in the absence of Lis1 (solid bars), the presence of 300 nM Lis1 (hatched bars), and the presence of 300nM Lis1-5A (cross-hatched bars). Data was normalized so that the density was 1 in the absence of Lis1. Data in semi-transparent grey reproduced from Figure 3.1 for reference. (C) Average DDB binding density on microtubules with dynein variants in the absence of Lis1 (solid bars), the presence of 300 nM Lis1 (hatched bars), and the presence of 300nM Lis1-5A (cross-hatched bars). Measured by BicD2S foci. Data was normalized so that the density was 1 in the absence of Lis1. Data in semi-transparent grey reproduced from Figure 3.1 for reference. (D) Average velocity of DDBS complexes with dynein variants in the absence of Lis1 (solid bars), the presence of 300 nM Lis1 (hatched bars), and the presence of 300nM Lis1-5A (cross-hatched bars). p values: ns, not significant; *, <0.05; **, <0.01; ***, <0.001, ****, <0.0001. Data are shown as mean and standard error of mean.

Figure 3.2 (continued).

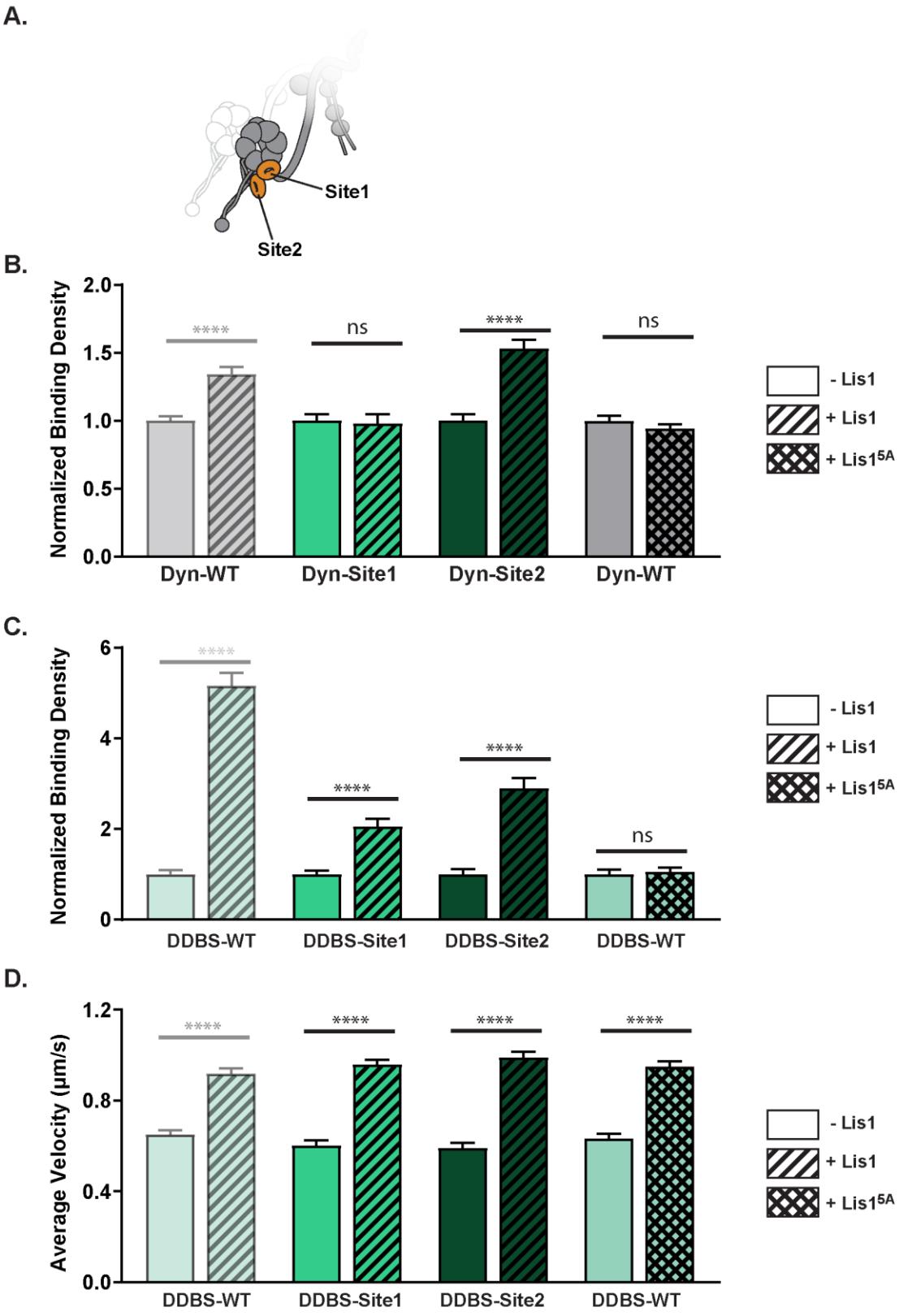

with Site2 mutations (DDBS-Site2) (Figure 3.2C, D). These results suggest that the Lis1 binding Site2 residues identified in yeast system do not account for Lis1's ability to increase the microtubule binding of dynein alone and activated dynactin complexes nor the velocity of activated dynein complexes.

Since none of the Lis1 binding sites on dynein seemed to be required for the Lis1-mediated increase in the velocity of DDBS complexes, we mutated the known dynein binding sites on Lis1, R275A, R301A, R378A, W419A and K437A ($Lis1^{5A}$) (Toropova et al., 2014). Consistent with previous findings in yeast system, $Lis1^{5A}$ no longer increased the microtubule binding of dynein alone (Figure 3.2B). We also found that $Lis1^{5A}$ had no effect on the microtubule binding of BicD2S foci of DDBS-WT complexes (Figure 3.2C). However, $Lis1^{5A}$ still increased the velocity of DDBS-WT to a similar extent as wild-type Lis1 (Figure 3.2D). Taken together, the known dynein binding site on Lis1 is required for the Lis1-mediated increase in the microtubule binding of dynein alone as well as activated dynein complexes but not for the Lis1-mediated increase in the velocity of dynein-dynactin-BicD2S complexes.

Lis1 promotes the recruitment of a second dynein dimer to dynein-dynactin-BicD2S complex

We then sought to understand how Lis1 increases the velocity of DDBS complexes. Previous studies have shown that Lis1 promotes dynein-dynactin association in cells as well as in cell extracts (Dix et al., 2013; Wang et al., 2013). Therefore, we hypothesized that Lis1 promotes the formation of dynein-dynactin-BicD2S complexes. To test our hypothesis, we measured the DDBS complex formation using an in vitro immunoprecipitation assay. We mixed an equal molar amount of dynein and dynactin with 7.5-fold molar excess of BicD2S conjugated to magnetic beads via Halo tags. In the absence of Lis1, we only saw ~1% of dynein was depleted (Figure 3.3A). The

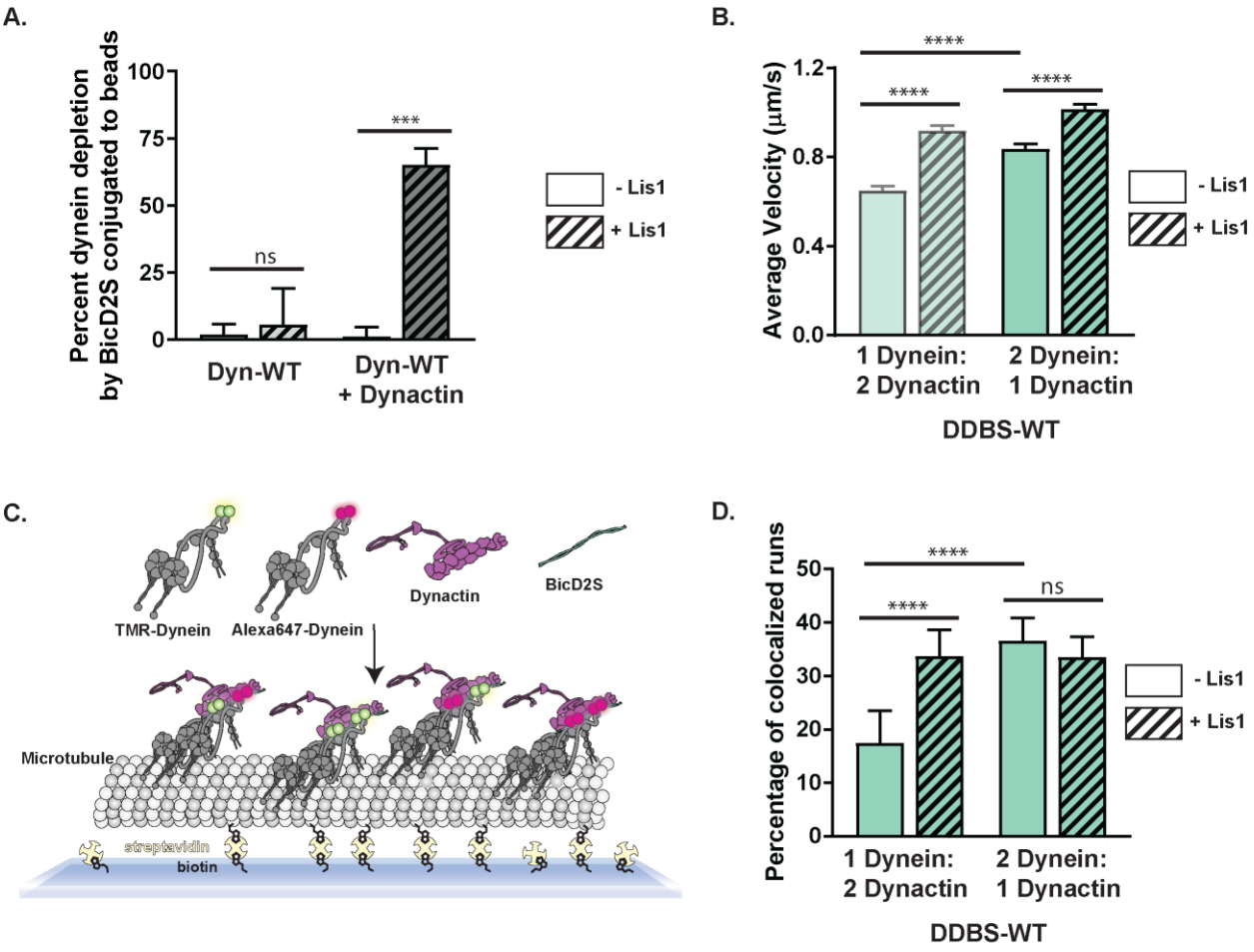

Figure 3.3. Lis1 promotes the recruitment of second dynein dimers to activated dynein complexes. (A) Percent depletion of dynein by BicD2S conjugated to beads in the absence (light grey) and presence (dark grey) of dynactin and in the absence (solid bars) and presence (hatched bars) of 150 nM Lis1. (B) Average velocity of activated dynein complexes with different ratios of dynein:dynactin in the absence (solid bars) and presence (hatched bars) of 300 nM Lis1. Data in semi-transparent grey reproduced from Figure 3.1 for reference. (C) Schematic of possible two color DDBS complexes. (D) Percentage of two-color colocalized runs with activated dynein complexes with different ratios of dynein:dynactin in the absence (solid bars) and presence (hatched bars) of 300 nM Lis1. p values: ns, not significant; *, <0.05; **, <0.01; ***, <0.001, ****, <0.0001. Data are shown as mean and standard error of mean.

addition of Lis1 increased the percentage of dynein depletion to ~65% (Figure 3.3A). To ensure that Lis1 is promoting the formation of tripartite complex, we measured the percent depletion of

dynein without dynactin and observed very little depletion either in the presence or absence of Lis1 (Figure 3.3A). Taken together, this suggests that Lis1 promotes the formation of dynein-dynactin-BicD2S complexes.

Recent structural studies have shown that activated dynein-dynactin-BicD2S complexes can contain either one dynein dimer or two dynein dimers per complex (Grotjahn et al., 2018; Urnavicius et al., 2018). The majority of complexes contains only one dynein dimer. It has been shown that dynein-dynactin-activating adaptor complexes containing two dynein dimers move with faster velocity (Urnavicius et al., 2018). We therefore hypothesized that Lis1 promotes the recruitment of a second dynein dimer to form a maximally activated DDBS complex. Single-molecule motility measurements of DDBS mentioned above as well as previous single molecule studies of DDBS were done by assembling DDBS complex with 2-fold molar excess of dynactin over dynein (Schlager et al., 2014a; Zhang et al., 2017). We wondered if the assembly of DDBS complexes with limiting dynein concentration hindered the formation of DDBS complex with two dynein dimers. Therefore, we assembled DDBS complex at 2 dynein to 1 dynactin molar ratio and measured its velocity in single-molecule motility assay. We observed a significant increase in the velocity of these DDBS-WT complexes compared to those assembled with 1 dynein to 2 dynactin molar ratio (Figure 3.3B). Lis1 further increased the velocity of DDBS-WT complexes assembled with 2 dynein to 1 dynactin molar ratio (Figure 3.3B).

We then proceeded to test the recruitment of two dynein complexes directly in single-molecule motility assay by mixing an equal molar amount of two dynein preparations labelled with two different fluorophores, TMR and Alexa647. If all moving dynein complexes contained two dynein dimers, we would expect 50% of processive events to be two-color colocalized runs (Figure 3.3C). However, in our experiments, the labeling efficiency of TMR was ~94% and

Alexa647 was ~99%. Therefore, the maximum amount of two-color colocalized runs would be ~47%. Similar to previous findings, DDBS-WT complexes formed by assembling with 1 dynein to 2 dynactin molar ratio only had ~17% processive events that had both TMR and Alexa647 signals. The addition of Lis1 significantly increased the number of colocalized runs to ~34% (Figure 3.3D, B.2). For DDBS-WT complexes assembled with 2dynein to 1 dynactin molar ratio, we also observed the increase in the number of colocalized DDBS-WT runs to ~37%. Lis1 did not significantly change the number of colocalized runs of these complexes. Taken altogether, we conclude that Lis1 promotes the recruitment of a second dynein dimer to form a maximally activated dynein-dynactin-BicD2S complex.

Lis1 does not frequently colocalize with maximally activated dynein-dynactin-BicD2S complexes

We next asked if Lis1 needs to remain bound to DDBS complexes with two dynein dimers to stabilize the complex during processive runs. To test this, we labeled Lis1 with TMR and investigated the colocalization of TMR-Lis1 with DDBS-WT complex labeled with Alexa647 on dynein. For our previous single-molecule motility assays with unlabeled Lis1, we used 300nM Lis1. However, 300nM TMR-Lis1 introduced too high background signal to be able to clearly observe its signals in our single-molecule motility assay. Therefore, we used 50nM TMR-Lis1, which significantly increased the velocity of DDBS-WT complexes with minimal background signal. (Figure 3.4A). At this concentration, we observed only ~14% of DDBS-WT processive runs were colocalized with TMR-Lis1 (Figure 3.4C). Surprisingly, DDBS-WT runs colocalized with TMR-Lis1 were slower than those with no detectable TMR-Lis1 signals (Figure 3.4B). In addition, we observed that the disappearance of TMR-Lis1 signals from DDBS-WT runs coincided

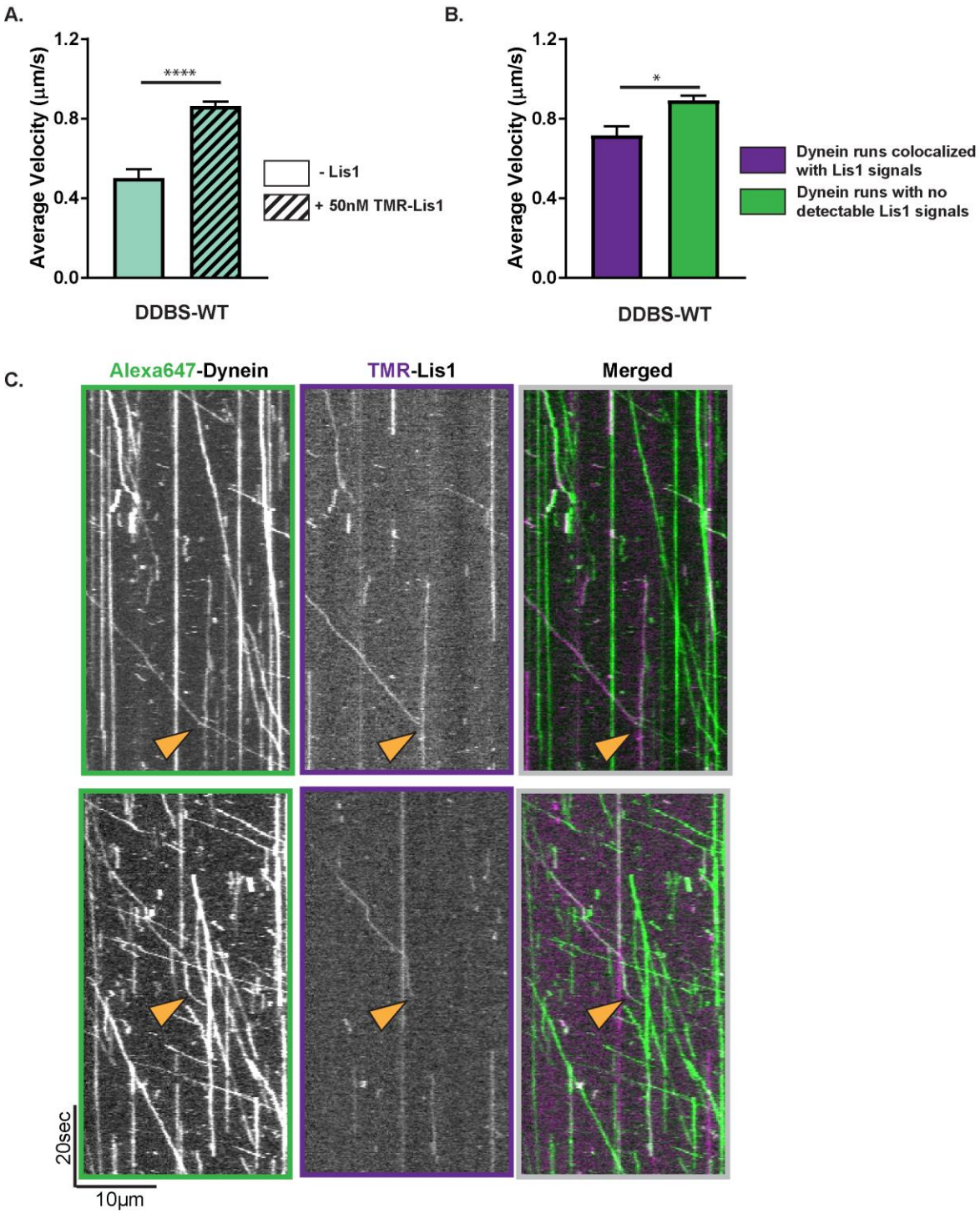

Figure 3.4. Lis1 does not frequently colocalize with processive dynein complexes. (A) Average velocity of DDBS complexes in the absence (solid bars) and presence (hatched bars) of 50 nM TMR-Lis1. (B) Average velocity of DDBS complexes colocalized with TMR-Lis1 signals (magenta) and without detectable TMR-Lis1 signals (green). (C) Representative kymographs with the dynein and Lis1 channels shown in black and white and the merged image shown in

(continued) pseudocolor. p values: ns, not significant; *, <0.05; **, <0.01; ***, <0.001, ****, <0.0001. Data are shown as mean and standard error of mean.

with velocity increase (Figure 3.4C). However, we were not able to test the significance of this observation because such events were rare. These results suggest that Lis1 does not seem to be stably bound to DDBS complexes and Lis1 binding to moving complexes seems to hinder their motility.

Lis1 is able to promote the complex formation and increase the velocity of dynein-dynactin-BicD2S complexes formed with dynein mutants that are relieved from an autoinhibited phi-particle conformation

Recent cryo-EM studies have revealed a model for the activation of dynein by dynactin and an activating adaptor (Figure 3.5A) (Urnavicius et al., 2018; Zhang et al., 2017). In the absence of dynactin and an activating adaptor, dynein exists in two autoinhibited states termed phi and open conformations. The binding of dynactin and an activating adaptor such as BicD2S relieves the autoinhibition of dynein and activates it into a processive motor capable of long-distance and directional movement along microtubules. It has also been shown that relieving the predominant phi-conformation in dynein promotes the complex formation of dynein-dynactin-BicD2S complexes (Zhang et al., 2017). We wondered if Lis1 can still affect the DDBS complex formation with dynein mutants that are relieved from the autoinhibited phi-particle state. To test this, we mutated the previously shown mutations in dynein, K1610E and R1567E, to disrupt the formation of phi-dynein. These mutants are referred to as Dyn-Open. We first compared the binding affinity of Lis1 to Dyn-WT versus Dyn-Open and found that Lis1 bound Dyn-Open with higher affinity compared to Dyn-WT (Figure 3.5B). To understand this further, we docked Lis1 density on the

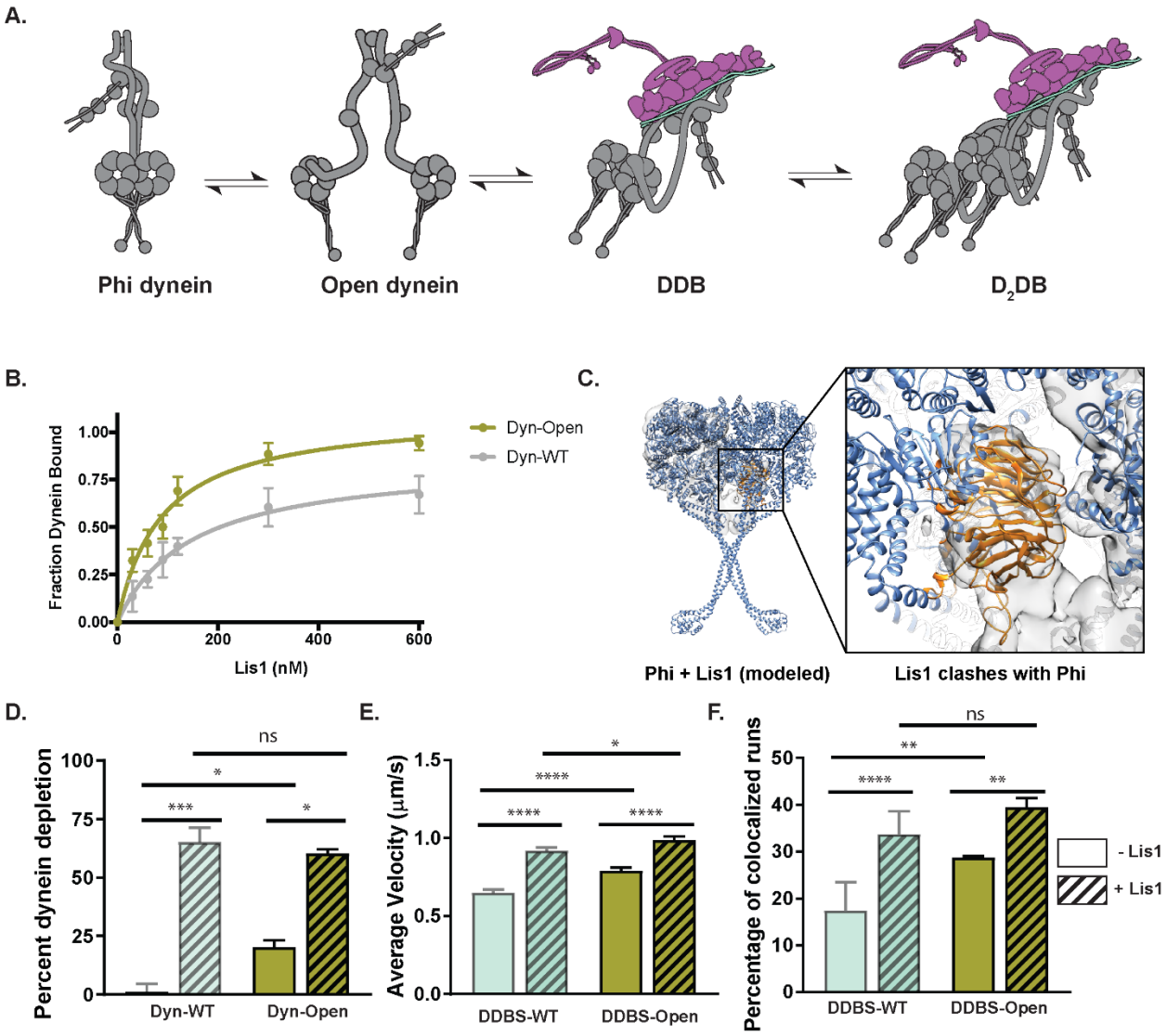

Figure 3.5. Effect of Lis1 on a dynein mutant incapable of forming an autoinhibited phi conformation. (A) Schematic of model of dynein activation by dynactin and activating adaptor. (B) Determination of the binding affinity of Lis1 for Dyn-WT (grey) and Dyn-Open (yellow). (C) Lis1 cryo-EM density docked onto the phi dynein cryo-EM structure (EMDB: EMD-3698). (D) Percent depletion of Dyn-WT (grey) and Dyn-Open (yellow) by BicD2S conjugated to beads in the absence (solid bars) and presence (hatched bars) of 150 nM Lis1. Data in semi-transparent grey reproduced from Figure 3.3 for reference. (E) Average velocity of DDBS complexes with Dyn-WT (grey) and Dyn-Open (yellow) in the absence (solid bars) and presence (hatched bars) of 300 nM Lis1. Data in semi-transparent grey reproduced from Figure 3.1 for reference. (F) Percentage of two-color colocalized runs with activated dynein complexes with Dyn-WT (grey) and

(continued) Dyn-Open (yellow) in the absence (solid bars) and presence (hatched bars) of 300 nM Lis1. Data in semi-transparent grey reproduced from Figure 3.3 for reference. p values: ns, not significant; *, <0.05; **, <0.01; ***, <0.001, ****, <0.0001. Data are shown as mean and standard error of mean.

cryo-EM structure of dynein in the phi-particle conformation at the primary Lis1 binding site on dynein's motor ring (Figure 3.5C). We observed that Lis1 density sterically clashed with dynein in the phi-particle information. This suggests that the phi-particle conformation of dynein reduces the binding affinity of Lis1.

Next, we tested the effect of Lis1 on dynein-dynactin-BicD2S complex formation with Dyn-Open using in vitro immunoprecipitation assay mentioned above. In the presence of dynactin, BicD2S conjugated to magnetic beads pulled down Dyn-Open more efficiently than Dyn-WT (Figure 3.5D). Thus, Dyn-Open forms dynein-dynein-BicD2S complexes more efficiently than Dyn-WT, consistent with a previous study (Zhang et al., 2017). However, the amount of dynein depletion for Dyn-Open in the absence of Lis1 was much lower than that for Dyn-WT in the presence of Lis1. This suggests that the complex formation of Dyn-Open is not optimal. We measured the depletion of Dyn-Open by BicD2S and dynactin in the presence of Lis1 and we found that Lis1 significantly increased the amount of depletion of Dyn-Open from ~20% to ~60% (Figure 3.5D).

From these results, we predicted that dynein-dynactin-BicD2S complexes formed with Dyn-Open (DDBS-Open) would have faster velocity and higher number of two dynein dimer complexes compared to Dyn-WT and Lis1 would further increase these parameters of DDBS-Open. To test our predictions, we first measured the velocity of DDBS-Open with and without Lis1. As predicted, in the absence of Lis1, DDBS-Open moved with faster velocity than DDBS-

WT and Lis1 further increased the velocity of DDBS-Open (Figure 3.5E). We next tested the amount of DDBS-Open complex with two dynein dimers using an equimolar ratio of two dynein preparations labelled with two different fluorophores, TMR and Alexa647 as mentioned above. We observed that the amount of two-color colocalized runs in DDBS-Open complex was significantly higher than DDBS-WT complex and Lis1 further increased the amount of colocalized runs (Figure 3.5F). These results were consistent with our predictions. Taken altogether, our results show that Lis1 increases the velocity of dynein-dynactin-BicD2S complexes formed with dynein mutants relieved from the autoinhibited phi-particle conformation by promoting the recruitment of two dynein dimers to the complex.

3.5 Discussion

Previous studies have shown that Lis1 increases the velocity of DDBS complexes (Baumbach et al., 2017; Gutierrez et al., 2017). However, the mechanism by which Lis1 exerts this effect is unclear. Here, our results show that Lis1 increases the velocity of DDBS complexes by promoting the formation of maximally activated complexes containing two dynein dimers (Figure 3.3D). The emerging model of dynein motility shows that dynein requires dynactin and an activating adaptor to be able to move processively along microtubules (McKenney et al., 2014; Schlager et al., 2014a; Zhang et al., 2017). Therefore, the ability of Lis1 to promote the association of dynein, dynactin and an activating adaptor highlights the role of Lis1 as an essential dynein regulator. Indeed, it has been shown that depletion or reduction of Lis1 reduces dynein-mediated transport of various cargos in cells (Dix et al., 2013; Egan et al., 2012; Lenz et al., 2006; Moughamian et al., 2013; Pandey and Smith, 2011).

We also observed that Lis1 does not seem to frequently co-migrate with DDBS complexes (Figure 3.4C). This is consistent with previous study in Aspergillus where Lis1 is required for the initiation of endosome movement but absent from moving endosomes (Egan et al., 2012). We found that occasional DDBS runs that comigrated with Lis1 were slower (Figure 3.4B). In rare examples, we observed an increase in the velocity of DDBS runs when Lis1 colocalization disappears (Figure 3.4C). It is possible that Lis1 binding to DDBS complexes hinders their motility. Intriguingly, it has been shown that depletion of Lis1 in adult *Drosophila* wing neurons increases the frequency and velocity of mitochondria (Vagnoni et al., 2016). This suggests that Lis1 can hinder dynein-mediated transport of mitochondria in this system. Future work will aim to understand this rare phenomenon in vitro and the factor needed to enrich this phenomenon. One such possible factor is Nude/Nudel, which has been proposed to act as a tether for Lis1 to bind to dynein in budding yeast (Huang et al., 2012).

How might Lis1 promote the formation of maximally activated dynein complexes? Recent structural study has shown that dynein exists in two distinct autoinhibited states, phi-dynein and open-dynein, in the absence of dynactin and an activating adaptor (Zhang et al., 2017) (Figure 3.5A). In these states, dynein motor domains are inverted and hence unable to walk processively on microtubules. We demonstrated that dynein mutant incapable of forming the phi-dynein autoinhibited state forms more maximally activated DDBS complexes with two dynein dimers than the wildtype dynein (Figure 3.5F). Lis1 furthers increases the formation of maximally activated DDBS complexes formed with this mutant (Figure 3.5F). It has previously shown that this mutant is still autoinhibited in the open-dynein state (Zhang et al., 2017). We propose that Lis1 assists in the reorientation of inverted dynein motor domains to parallel conformations to promote the formation of maximally activated DDBS complexes. We also found that Lis1 binds

to a dynein mutant incapable of forming phi-conformation with higher affinity than the wildtype dynein (Figure 3.5B). When we modeled the Lis1 density to the EM structure of phi-dynein, we observed that Lis1 density is sterically incompatible at its primary binding site on the dynein motor domain. Therefore, it is conceivable that Lis1 binding to dynein could assist in the opening of phi-particle. Future EM structures of dynein with Lis1 will be required to test these hypotheses.

Structural studies of Lis1 regulation on yeast dynein has revealed Lis1 binds to dynein in two distinct binding sites on the dynein motor domain (DeSantis et al., 2017; Huang et al., 2012; Toropova et al., 2014). Surprisingly, mutating the corresponding Lis1 binding sites of human dynein does not abolish the ability of Lis1 to increase the velocity of DDBS complexes (Figure 3.2C). The simplest explanation would be that these Lis1 binding sites are not responsible for the Lis1-mediated increase in the velocity of DDBS complexes. However, these binding sites were determined using sequence conservation between yeast dynein and human dynein. It is possible that there are additional residues in these sites of human dynein. Another possibility is that Lis1 exerts this effect via other potential Lis1 binding sites on the tail region or dynein intermediate chain previously identified using yeast two-hybrid and pulldown experiments (Tai et al., 2002). Future structural studies of human dynein with Lis1 will address these possibilities.

We have also shown that Lis1 increases the microtubule binding of full-length dynein as well as DDBS complexes (Figure 3.1C-D). This is similar to the tight microtubule binding effect previously observed with yeast dynein and human dynein motor domain (DeSantis et al., 2017; Huang et al., 2012; McKenney et al., 2010; Toropova et al., 2014). Lis1-mediated increase in the microtubule binding of full-length dynein is mediated by the previously identified Lis1 binding site at the junction of the AAA3-4 domain of dynein motor ring (Figure 3.2B). However, mutating the same Lis1 binding site doesn't abolish the Lis1-mediated increase in the microtubule binding

of DDBS complexes. It is possible that Lis1 increases the microtubule binding of DDBS complexes by promoting the complex formation. The aforementioned structural studies of human dynein with Lis1 will be required to dissect this multifaceted regulation of dynein by Lis1.

3.6 Methods

Cloning and plasmid construction

The pDyn1 plasmid (the pACEBac1 expression vector containing insect cell codon optimized DHC fused to a His-ZZ-LTLT tag on the N-terminus and a C-terminal SNAPf tag) and the pDyn2 plasmid (the pIDC expression vector with codon optimized IC2C, LIC2, TcTex1, LC8, and Robl) were recombined in vitro with a Cre recombinase (New England Biolabs) to generate the pDyn3 plasmid. The presence of all six dynein chains were verified by PCR. pDyn1, pDyn2 and the pFastBac plasmid with codon-optimized human full-length Lis1 fused to an N-terminal His-ZZ-LTLT tag were gifts from Andrew Carter. The BICD2S construct (25-398aa) was amplified from a human cDNA library generated from RPE1 cells, fused to a ZZ-LTLT-Halo tag on the N-terminus and inserted into a pET28a expression vector. All additional tags were added via Gibson assembly and all mutations and truncations were made via site-directed mutagenesis (Agilent).

Protein expression and purification

Human full-length dynein and Lis1 constructs were expressed in Sf9 cells as described previously (Baumbach et al., 2017; Schlager et al., 2014a). Briefly, the pDyn3 plasmid containing full-length human dynein genes or the pFastBac plasmid containing full-length Lis1 construct was transformed into DH10EmBacY chemically competent cells with 42°C heat shock for 15 seconds followed by incubation at 37°C for 5 hours in SOC media. The cells were then plated on LB-agar

plates containing kanamycin (50 μg/ml), gentamicin (7 μg/ml), tetracyclin (10 μg/ml), BluoGal (100 μg/ml) and IPTG (40 μg/ml) and successful clones were identified in a blue/white color screening after 48 hours. For full-length human dynein constructs, white colonies were additionally tested for the presence of all six dynein genes using PCR. The correct white colonies were inoculated overnight in LB media containing kanamycin (50 μg/ml), gentamicin (7 μg/ml) and tetracyclin (10 μg/ml) at 37°C. Bacmid DNA was extracted from overnight cultures using an isopropanol precipitation method as described previously (Zhang et al., 2017). 2mL of Sf9 cells at $0.5x10^6$ cells/mL were transfected with 2μg of fresh bacmid DNA and FuGene HD transfection reagent (Promega) at a 3:1 transfection reagent to DNA ratio according to manufacturer's instructions. After three days, the supernatant containing the V0 virus was harvested by centrifugation at 1000 x g for 5 minutes at 4°C. To generate V1, 1mL of the V0 virus was used to transfect 50mL of Sf9 cells at $1x10^6$ cells/mL. After three days, the supernatant containing the V1 virus was harvested by centrifugation at 1000 x g for 5 minutes at 4°C and stored in the dark at 4°C until use. For protein expression, 4mL of the V1 virus was used to transfect 400mL of Sf9 cells at $1x10^6$ cells/mL. After three days, cells were harvested by centrifugation at 3500 x g for 10 minutes at 4°C. The pellet was resuspended in 10mL of ice-cold PBS and pelleted again. The pellet was flash frozen in liquid nitrogen and stored at -80°C until protein purification.

Protein purification steps were done at 4°C unless otherwise indicated. Full-length dynein was purified from frozen Sf9 pellets transfected with the V1 virus as described previously (Schlager et al., 2014a). Frozen cell pellets from 400mL culture were resuspended in 40mL of Dyn-lysis buffer (50 mM HEPES [pH 7.4], 100 mM sodium chloride, 1 mM DTT, 0.1 mM Mg-ATP, 0.5 mM Pefabloc, 10% (v/v) glycerol) supplemented with 1 cOmplete EDTA-free protease inhibitor cocktail tablet (Roche) per 50 mL and lysed using a Dounce homogenizer (10 strokes

with loose plunger and 15 strokes with tight plunger). The lysate was clarified by centrifuging at 183,960 x g for 88 min in Type 70 Ti rotor (Beckman). The clarified supernatant was incubated with 4 mL of IgG Sepharose 6 Fast Flow beads (GE Healthcare Life Sciences) for 3-4 hr on a roller. The beads were transferred to a gravity flow column, washed with 200 mL of Dyn-lysis buffer and 300 mL of TEV buffer (50 mM Tris–HCl [pH 8.0], 250 mM potassium acetate, 2 mM magnesium acetate, 1 mM EGTA, 1 mM DTT, 0.1 mM Mg-ATP, 10% (v/v) glycerol). For fluorescent labeling of C-terminal SNAPf tag, dynein-coated beads were labeled with 5 μM SNAP-Cell-TMR (New England Biolabs) in the column for 10 min at room temperature and unbound dyes were washed with 300 mL of TEV buffer at 4°C. The beads were then resuspended and incubated in 15 mL of TEV buffer supplemented with 0.5 mM Pefabloc and 0.2 mg/mL TEV protease overnight on a roller. The supernatant containing cleaved proteins were concentrated using a 100K MWCO concentrator (EMD Millipore) to 500 μL and purified via size exclusion chromatography on a TSKgel G4000SWXL column (TOSOH Bioscience) with GF150 buffer (25 mM HEPES [pH7.4], 150 mM KCl, 1mM MgCl2, 5 mM DTT, 0.1 mM Mg-ATP) at 1 mL/min. The peak fractions were collected, buffer exchanged into a GF150 buffer supplemented with 10% glycerol, concentrated to 0.1-0.5 mg/mL using a 100K MWCO concentrator (EMD Millipore) and flash frozen in liquid nitrogen.

Lis1 constructs are purified from frozen cell pellets from 400 mL culture. Lysis and clarification steps were similar to full-length dynein purification except Lis1-lysis buffer (30 mM HEPES [pH 7.4], 50 mM potassium acetate, 2 mM magnesium acetate, 1 mM EGTA, 300 mM potassium chloride, 1 mM DTT, 0.5 mM Pefabloc, 10% (v/v) glycerol) supplemented with 1 cOmplete EDTA-free protease inhibitor cocktail tablet (Roche) per 50 mL was used. The clarified supernatant was incubated with 0.5 mL of IgG Sepharose 6 Fast Flow beads (GE Healthcare Life

Sciences) for 2-3 hr on a roller. The beads were transferred to a gravity flow column, washed with 20 mL of Lis1-lysis buffer, 100 mL of modified TEV buffer (10 mM Tris–HCl [pH 8.0], 2 mM magnesium acetate, 150mM potassium acetate, 1 mM EGTA, 1 mM DTT, 10% (v/v) glycerol) supplemented with 100 mM potassium acetate, and 50 mL of modified TEV buffer. For fluorescent labeling of Lis1 constructs with N-terminal Halo tags, Lis1-coated beads were labeled with 200 μM SNAP-Cell-TMR (New England Biolabs) for 2.5 hr at 4°C on a roller and unbound dyes were washed with 200 mL of modified TEV buffer supplemented with 250 mM potassium acetate. Lis1 was cleaved from IgG beads via incubation with 0.2 mg/mL TEV protease overnight on a roller. Cleaved proteins were filtered by centrifuging with Ultrafree-MC VV filter (EMD Millipore) in a tabletop centrifuge and flash frozen in liquid nitrogen.

Dynactin was purified from stable HEK293 cell lines expressing p62-Halo-3xFlag as described previously (Redwine et al., 2017). Briefly, frozen pellets collected from 160 15cm plates were resuspended in 80mL of Dynactin-lysis buffer (30 mM HEPES [pH 7.4], 50 mM potassium acetate, 2 mM magnesium acetate, 1 mM EGTA, 1 mM DTT, 10% (v/v) glycerol) supplemented with 0.5 mM Mg-ATP, 0.2% Triton X-100 and 1 cOmplete EDTA-free protease inhibitor cocktail tablet (Roche) per 50 mL and rotated slowly for 15 min. The lysate was clarified by centrifuging at 66,000 x g for 30 min in Type 70 Ti rotor (Beckman). The clarified supernatant was incubated with 1.5 mL of anti-Flag M2 affinity gel (Sigma-Aldrich) for overnight on a roller. The beads were transferred to a gravity flow column, washed with 50 mL of wash buffer (Dynactin-lysis buffer supplemented with 0.1 mM Mg-ATP, 0.5 mM Pefabloc and 0.02% Triton X-100), 100 mL of wash buffer supplemented with 250 mM potassium acetate, and again with 100 mL of wash buffer. For fluorescent labeling of Halo tag, dynactin-coated beads were labeled with 5 μM Halo-JF646 (Janelia) in the column for 10 min at room temperature and unbound dyes were washed with 100

mL of wash buffer at 4°C. Dynactin was eluted from beads with 1 mL of elution buffer (wash buffer with 2 mg/mL of 3xFlag peptide). Elution was collected, filtered by centrifuging with Ultrafree-MC VV filter (EMD Millipore) in a tabletop centrifuge and diluted to 2 mL in Buffer A (50 mM Tris-HCl [pH 8.0], 2 mM MgOAc, 1 mM EGTA, and 1 mM DTT) and injected onto a MonoQ 5/50 GL column (GE Healthcare and Life Sciences) at 1 mL/min. The column was pre-washed with 10 CV of Buffer A, 10 CV of Buffer B (50 mM Tris-HCl [pH 8.0], 2 mM MgOAc, 1 mM EGTA, 1 mM DTT, 1 M KOAc) and again with 10 CV of Buffer A at 1 mL/min. To elute, a linear gradient was run over 26 CV from 35-100% Buffer B. Pure dynactin complex eluted from ~75-80% Buffer B. Peak fractions containing pure dynactin complex were pooled, buffer exchanged into a GF150 buffer supplemented with 10% glycerol, concentrated to 0.02-0.1 mg/mL using a 100K MWCO concentrator (EMD Millipore) and flash frozen in liquid nitrogen.

Halo-BicD2S construct was expressed in BL-21[DE3] cells (NEB) at OD 0.6 with 0.1 mM IPTG for 16 hr at 18°C. Frozen cell pellets from 2 L culture was resuspended in 60mL of BicD2-lysis buffer (30 mM HEPES [pH 7.4], 50 mM potassium acetate, 2 mM magnesium acetate, 1 mM EGTA, 1 mM DTT, 0.5 mM Pefabloc, 10% (v/v) glycerol) supplemented with 1 cOmplete EDTA-free protease inhibitor cocktail tablet (Roche) per 50 mL and 1 mg/mL lysozyme. The resuspension was incubated on ice for 30 min and lysed by sonication. The lysate was clarified by centrifuging at 66,000 x g for 30 min in Type 70 Ti rotor (Beckman). The clarified supernatant was incubated with 2 mL of IgG Sepharose 6 Fast Flow beads (GE Healthcare Life Sciences) for 2 hr on a roller. The beads were transferred to a gravity flow column, washed with 100 mL of BicD2-lysis buffer supplemented with 150 mM potassium acetate and 50mL of cleavage buffer (50 mM Tris–HCl [pH 8.0], 150 mM potassium acetate, 2 mM magnesium acetate, 1 mM EGTA, 1 mM DTT, 0.5 mM Pefabloc, 10% (v/v) glycerol). The beads were then resuspended and incubated in 15 mL of

cleavage buffer supplemented with 0.2 mg/mL TEV protease overnight on a roller. The supernatant containing cleaved proteins were concentrated using a 50K MWCO concentrator (EMD Millipore) to 1 mL, filtered by centrifuging with Ultrafree-MC VV filter (EMD Millipore) in a tabletop centrifuge, diluted to 2 mL in Buffer A (30 mM HEPES [pH 7.4], 50 mM potassium acetate, 2 mM magnesium acetate, 1 mM EGTA, 10% (v/v) glycerol and 1 mM DTT) and injected onto a MonoQ 5/50 GL column (GE Healthcare and Life Sciences) at 1 mL/min. The column was pre-washed with 10 CV of Buffer A, 10 CV of Buffer B (30 mM HEPES [pH 7.4], 1 M potassium acetate, 2 mM magnesium acetate, 1 mM EGTA, 10% (v/v) glycerol and 1 mM DTT) and again with 10 CV of Buffer A at 1 mL/min. To elute, a linear gradient was run over 26 CV from 0-100% Buffer B. The peak fractions containing Halo-BicD2S were collected and concentrated to using a 50K MWCO concentrator (EMD Millipore) to 0.2 mL. For fluorescent labeling Halo tags, the concentrated peak fractions of Halo-BicD2S were incubated with 5uM of Halo-Alexa488 dyes (Promega) for 10 min at room temperature. Unbound dyes were removed by PD-10 desalting column (GE Healthcare and Life Sciences) according to the manufacturer's instructions. The labeled Halo-BicD2S sample was concentrated to using a 50K MWCO concentrator (EMD Millipore) to 0.2 mL, diluted to 0.5 mL in GF150 buffer and further purified via size exclusion chromatography on a Superose 6 Increase 10/300 GL column (GE Healthcare and Life Sciences) with GF150 buffer at 0.5 mL/min. The peak fractions were collected, buffer exchanged into a GF150 buffer supplemented with 10% glycerol, concentrated to 0.2-1 mg/mL using a 50K MWCO concentrator (EMD Millipore) and flash frozen in liquid nitrogen.

Single molecule TIRF microscopy

Single-molecule imaging was performed with an inverted microscope (Nikon, Ti-E Eclipse) equipped with a 100x 1.49 N.A. oil immersion objective (Nikon, Plano Apo) and a ProScan linear motor stage controller (Prior). The microscope was equipped with a LU-NV laser launch (Nikon), with 405 nm, 488 nm, 532 nm, 561 nm and 640 nm laser lines. The excitation and emission paths were filtered using appropriate single bandpass filter cubes (Chroma). For two-color colocalization imaging, the emission signals were further filtered and split using W-view Gemini image splitting optics (Hamamatsu). The emitted signals were detected with an electron multiplying CCD camera (Andor Technology, iXon Ultra 897). Illumination and image acquisition is controlled by NIS Elements Advanced Research software (Nikon).

Single-molecule motility and microtubule binding assays were performed in flow chambers assembled as described previously (Case et al., 1997) using the TIRF microscopy set up described above. Either biotin-PEG-functionalized coverslips (Microsurfaces) or No. 1-1/2 coverslips (Corning) sonicated in 100% ethanol for 10 min were used for the flow-chamber assembly. Taxol-stabilized microtubules with ~10% biotin-tubulin and ~10% fluorescent-tubulin (Alexa405, 488 or 647 labeled) were prepared as described previously (Huang et al., 2012). Flow chambers were assembled with taxol-stabilized microtubules by incubating sequentially with the following solutions, interspersed with two washes with assay buffer (30 mM HEPES [pH 7.4], 2 mM magnesium acetate, 1 mM EGTA, 10% glycerol, 1 mM DTT) supplemented with 20 μM Taxol in between: (1) 1 mg/mL biotin-BSA in assay buffer (3 min incubation); (2) 0.5 mg/mL streptavidin in assay buffer (3 min incubation) and (3) a fresh dilution of taxol-stabilized microtubules in assay buffer (3 min incubation). After flowing in microtubules, the flow chamber was washed twice with assay buffer supplemented with 1 mg/mL casein and 20 μM Taxol.

To assemble dynein-dynactin-BicD2S complexes, purified dynein (10-20 nM concentration), dynactin and BicD2S were mixed at 1:2:10 molar ratio or 2:1:20 molar ratio as mentioned in the main text and incubated on ice for 10 min. These dynein-dynactin-BicD2S complexes or dynein alone were then incubated with Lis1 or modified TEV buffer (to buffer match for experiments without Lis1) for 10 min on ice. The mixtures of dynein, dynactin, BicD2S and Lis1 were then flowed into the flow chamber assembled with taxol-stabilized microtubules. The final imaging buffer contained the assay buffer supplemented with 20 μM taxol, 1 mg/mL casein, 71.5 mM β-mercaptoethanol, an oxygen scavenger system, and 1 mM Mg-ATP. The final concentration of dynein in the flow chamber was 0.5-1 pM for experiments with dynein-dynactin-BicD2S complexes and 0.3-0.5 pM for dynein alone experiments. The final concentration of Lis1 was 300 nM for experiments with unlabeled Lis1 and 50 nM for experiments with TMR-labeled Lis1. For single-molecule motility assay, microtubules were imaged first by taking a single-frame snapshot. Dynein and/or BicD2S labeled with fluorophores (TMR, Alexa647 or Alexa488) was imaged every 300 msec for 3 min. At the end, microtubules were imaged again by taking a snapshot to check for stage drift. Movies showing significant drift were not analyzed. Each sample was imaged no longer than 15 min. For single-molecule microtubule binding assays, the final imaging mixture containing dynein was incubated for an additional 5 min in the flow chamber at room temperature to reach steady-state before imaging. After 5 min incubation, microtubules were imaged first by taking a single-frame snapshot. Dynein and/or BicD2S labeled with fluorophores (TMR, Alexa647 or Alexa488) was imaged by taking a single-frame snapshot. Each sample was imaged at 4 different fields of view and there were between 5 and 10 microtubules in each field of view. In order to compare the effect of Lis1 on microtubule binding, the samples with and without

Lis1 were imaged in two separate flow chambers made on the same coverslip on the same day with the same stock of polymerized tubulin as mentioned previously (DeSantis et al., 2017).

Single-molecule motility assay analysis

Kymographs were generated from motility movies and dynein velocity was calculated from kymographs using ImageJ macros as described (Roberts et al., 2014). Only runs that were longer than 4 frames (1.2 s) were included in the analysis. Bright aggregates, which were less than 5% of the population, were excluded from the analysis. For two-color colocalization analysis, the kymographs from each channel were generated and merged in ImageJ and the number of colocalized runs was determined manually. Data plotting and statistical analyses was performed in Prism7 (GraphPad).

Single-molecule microtubule binding assay analysis

Intensity profiles of dynein or BicD2S spots from a single-frame snapshot were generated over a 5-pixel wide line drawn perpendicular to the long axis of microtubules in ImageJ. Intensity peaks at least 2-fold higher than the neighboring background intensity were counted as dynein or BicD2S spots bound to microtubules. Bright aggregates that were 5-fold brighter than neighboring intensity peaks were not counted. The average binding density was calculated as the total number of dynein or BicD2S spots divided by the total microtubule length in each snapshot. Normalized binding density was calculated by dividing by the average binding density of dynein or BicD2S without Lis1 collected on the same coverslip (see above). Data plotting and statistical analyses was performed in Prism7 (GraphPad).

Immunoprecipitation assays

Complex formation pulldowns with BicD2S were performed using 15 µL of Magne HaloTag Beads (Promega) in 2mL Protein Lo-Bind Tubes (Eppendorf). Beads were washed twice with 1mL of GF150 without ATP supplemented with 10% glycerol and 0.1%NP40. BicD2S was diluted in this buffer to 75 nM. 25uL of diluted to BicD2S was added to the beads and gently shaken for one hour. Once the hour was up 20 µL of supernatant was taken for a gel to confirm complete depletion of BicD2S. The beads were then washed once with 1mL GF150 with 10% glycerol and 0.1% NP40 and once with 1mL of binding buffer (30 mM HEPES [pH 7.4], 2 mM magnesium acetate, 1 mM EGTA, 10% glycerol, 1 mM DTT, 1mg/mL casein, 0.1% NP40, 1mM ADP) supplemented with 15.7 mM KCl and 8.3 mM KOAc. 10 nM dynein, 10nM dynactin and 150nM Lis1 were diluted in binding buffer which resulted in 15.7 mM KCl and 8.3 mM KOAc. For dropout experiments of dynactin or Lis1 the protein dilutions were supplemented with equivalent amounts of their purification buffers. 25 µL of the dynein, dynactin and Lis1 mixture was added to the beads pre-bound with BicD2S and gently shaken for 45 minutes. After incubation, 20 µL of the supernatant was taken, and 6.67 µL of NuPAGE® LDS Sample Buffer (4X) and 1.33 µL of Beta-mercaptoethanol was added to each. The samples were boiled for 5 minutes before being ran on a 4-12% NuPAGE Bis-Tris gel at 4C. Depletion was determined using densitometry in ImageJ.

Lis1 binding curves were determined as above with minor variations. 25 µL of beads were used, and washed twice with 1mL modified TEV buffer. 0, 30, 60, 90, 120, 300 and 600nM Lis1 was bound to beads which were then washed with 1 mL of modified TEV buffer and 1 mL of binding buffer supplemented with 30mM KCl and 6mM KOAc. 10nM of dynein was diluted in binding buffer supplemented with salt to 30mM KCl and 6mM KOAc. Binding and determination of depletion was carried out as above.

3.7 Acknowledgments

Zaw Min Htet is supported by the NSF graduate research fellowship, John P. Gillies by the UCSD molecular biophysics training grant, Morgan E. DeSantis the NIH K99/R00 grant and Samara L. Reck-Peterson by NIH grant R01GM107214 and the HHMI investigator program.

Chapter 4

The human cytoplasmic dynein interactome reveals novel activating adaptors of motility

This chapter has been previously published as:

W. B. Redwine*, M. E. DeSantis*, I. Hollyer, **Z. M. Htet**, P. T. Tran, S. K. Swanson, L. Florens, M. P. Washburn, S. L. Reck-Peterson. (2017) The human cytoplasmic dynein interactome reveals novel activators of motility. ***eLife*** 6, e28257.

* denotes equal contributions

4.1 Contributions

William B. Redwine, Morgan E. DeSantis and Samara L. Reck-Peterson conceptualized and designed the experiments. William B. Redwine, Morgan E. DeSantis, Ian Hollyer and Phuoc Tien Tran performed BioID and immunoprecipitation experiments. William B. Redwine, Morgan E. DeSantis, Selene K. Swanson and Luarence Florens curated, analyzed and interpreted the mass spectrometry data. Morgan E. DeSantis, Ian Hollyer and Zaw Min Htet performed, analyzed and interpreted single-molecule motility experiments. Michael P. Washburn and Samara L. Reck-Peterson supervised the project.

4.2 Abstract

In human cells, cytoplasmic dynein-1 is essential for long-distance transport of many cargos, including organelles, RNAs, proteins, and viruses, towards microtubule minus ends. To understand how a single motor achieves cargo specificity, we identified the human dynein interactome or "transportome" by attaching a promiscuous biotin ligase ("BioID") to seven components of the dynein machinery, including a subunit of the essential cofactor dynactin. This method reported spatial information about the large cytosolic dynein/dynactin complex in living cells. To achieve maximal motile activity and to bind its cargos, human dynein/dynactin requires "activating adaptors", of which only five have been described. We developed methods to identify new activating adaptors in our BioID data, and discovered that ninein and ninein-like are a new family of dynein activating adaptors. Analysis of the protein interactomes for six activating adaptors, including ninein and ninein-like, suggests that each dynein activating adaptor has multiple cargos.

4.3 Introduction

Microtubules and their motors are the primary means of long-distance intracellular transport in humans and many other eukaryotic organisms. Mutations in the transport machinery cause both neurodevelopmental and neurodegenerative diseases (Lipka et al., 2013). Microtubules are polar structures, with dynamic "plus" ends typically found near the cell periphery and "minus" ends anchored in internal microtubule organizing centers. Dynein motors move towards the microtubule minus end, whereas most kinesins move in the opposite direction. The human genome contains 15 dynein genes (Vale, 2003), but only cytoplasmic dynein-1 (DYNC1H1; "dynein" hereafter) is involved in long-distance, minus-end-directed transport in the cytoplasm. Dynein transports dozens of distinct cargos including organelles, ribonucleoprotein complexes, proteins and viruses (Kardon and Vale, 2009). A major outstanding question in the field is to understand how dynein achieves temporal and spatial specificity for cargo interactions.

Most cytoskeletal motors that transport cargos over long distances in cells are processive motors, capable of taking multiple steps along their track. While dimers of the *S. cerevisiae* dynein heavy chain move processively in the absence of cofactors (Reck-Peterson et al., 2006), mammalian dynein requires the 1.1 MDa dynactin complex and a coiled coil-containing activating adaptor ("activating adaptor" hereafter) for robust processive motility (McKenney et al., 2014; Schlager et al., 2014a; Trokter et al., 2012). Activating adaptors have a second function; they also link dynein/dynactin to cargo (Figure 4.1A) (Cianfrocco et al., 2015).

Currently, there are five proteins that likely function as dynein activating adaptors. The activating adaptors BICD2 and HOOK3 have been definitively shown, using purified components, to activate dynein/dynactin motility *in vitro* (McKenney et al., 2014; Schlager et al., 2014a; Schroeder and Vale, 2016). HOOK1, Spindly (SPDL1), and RAB11FIP3 are also likely activating

adaptors based on their ability to co-purify and co-migrate with dynein/dynactin in *in vitro* motility assays (McKenney et al., 2014; Olenick et al., 2016). Other proteins may be activating adaptors based on their homology to BICD and HOOK family activating adaptors, including BICD1, BICDL1, BICDL2, HOOK2, and the HOOK domain-containing proteins CCDC88A/girdin, CCDC88B/gipie and CCDC88C/daple (Hoogenraad and Akhmanova, 2016; Simpson et al., 2005). These activating adaptors all contain long stretches of predicted coiled coil and share very little sequence homology (Gama et al., 2017); currently it is not possible to identify activating adaptors based on sequence alone. Central to understanding how dynein performs so many tasks is to determine if it has additional activating adaptors.

Here we used new proteomics tools to address major unanswered questions about dynein-based transport. What is the dynein protein interactome? How many activating adaptors does dynein have in a given cell type? Which cargos do activating adaptors link to? Does each cargo have its own activating adaptor? To answer these questions, we used proximity-dependent labeling in living human cells. Traditionally, protein-protein interaction discovery using immunoprecipitation followed by mass spectrometry has been confined to relatively stable interactions. However, recently developed methods such as BioID (Roux et al., 2012) and APEX (Rhee et al., 2013) allow the discovery of weak and short-lived interactions in living cells, in addition to more stable interactions. The BioID method relies on expressing a protein of interest fused to a promiscuous biotin ligase that releases activated biotin-AMP in the absence of substrate (Roux et al., 2012). Biotin-AMP covalently modifies the primary amines of proximal proteins within a nanometer-scale labeling radius (Kim et al., 2014). Biotinlyated proximal proteins are identified by isolation with streptavidin followed by tandem mass spectrometry (MS/MS). For

example, this approach has been used to map protein interactions at human centrosomes and cilia (Gupta et al., 2015), focal adhesions (Dong et al., 2016) and the nuclear pore (Kim et al., 2014).

Using these methods we describe the human dynein/dynactin interactome. We developed methods to identify dynein activating adaptors within these datasets and identified two new activating adaptors that constitute a novel activating adaptor family. Finally, to determine the candidate cargos of six distinct activating adaptors we elucidated their individual interactomes. Our results suggest that each dynein activating adaptor has multiple cargos. We propose that activating adaptors provide the first layer of defining cargo specificity for cytoplasmic dynein, but that refinement of cargo selection will require additional factors.

4.4 Results

Identification of the dynein/dynactin interactome

To identify the human dynein/dynactin interactome, we began by biochemically characterizing dynein and dynactin subunits fused to BioID that were stably expressed in HEK-293 cells. The 1.4 MDa dynein holoenzyme is composed of dimers of heavy chains (HC; DYNC1H1), intermediate chains (IC1 or IC2; DYNC1I1 and 2), light intermediate chains (LIC1 or LIC2; DYNC1LI1 and 2), and three types of light chains: Roadblock (RB; DYNLRB1 and 2), LC8 (DYNLL1 and 2), and TCTEX (DYNLT1 and 2) (Figure 4.1A and Figure C.1). We first generated a cell line stably expressing IC2 with C-terminal BioID G2 ("BioID" here) (Kim et al., 2016a) and 3×FLAG tags. Immunoprecipitations confirmed that IC2-BioID was incorporated into the dynein/dynactin complex (Figure 4.1B—E). Gel filtration analysis of IC2 immunoprecipitates revealed that 51% of the BioID-tagged IC2 was incorporated into the dynein complex (Figure 4.1E). We obtained similar results when BioID was fused to the C-terminus of the p62 dynactin

Figure 4.1. Validation of BioID-tagged dynein and dynactin subunits. (A) A cartoon of the dynein/dynactin/activating adaptor complex based on cryo-EM structural studies (Chowdhury et al., 2015; Urnavicius et al., 2015) with proteins drawn to scale. (B) BioID-3×FLAG or IC2-BioID-3×FLAG were immunoprecipitated from stable HEK-293 cell lines using α-FLAG antibodies. A Sypro Red stained SDS-PAGE gel of the immunoprecipitates is shown. (C) MS/MS analysis of the immunoprecipitates from (B). Core dynein subunit dNSAF (distributed normalized spectral abundance factor) (Zhang et al., 2015) values are displayed as a gray scale heat map. (D) Immunoprecipitations were performed as in (B) with mild (M) or harsh (H) detergent conditions (see Materials and Methods). Harsh detergent conditions disrupt IC2 incorporation into the dynein/dynactin complex as shown by Western blots with α-HC and α-p150 (dynactin subunit) antibodies. (E) IC2-BioID was immunoprecipitated from a stable HEK-293 cell line using α-FLAG antibodies and fractionated by gel filtration FPLC chromatography. Fractions were analyzed by Western blotting with α-FLAG and α-HC antibodies. The signal intensity for IC2-BioID-3×FLAG (magenta) and HC (gray) in each fraction is plotted as a fraction of the summed intensity of all fractions. The elution volumes of molecular weight standards are indicated (dashed lines). (F) BioID-3×FLAG or p62-BioID-3×FLAG were immunoprecipitated from stable HEK-293 cell lines using α-FLAG antibodies. Immunoprecipitations were performed with mild (M) or harsh (H) detergent concentrations. Harsh detergent conditions disrupt p62 incorporation into the dynein/dynactin complex. (G) p62-BioID-3×FLAG was immunoprecipitated from a stable HEK-293 cell line using α-FLAG antibodies and analyzed as described in (E) with α-FLAG and α-p150 antibodies. The signal intensities for p62 (magenta) and p150 (gray) are plotted as a fraction of the summed intensity of all fractions. The elution volumes of molecular weight standards are indicated (dashed lines).

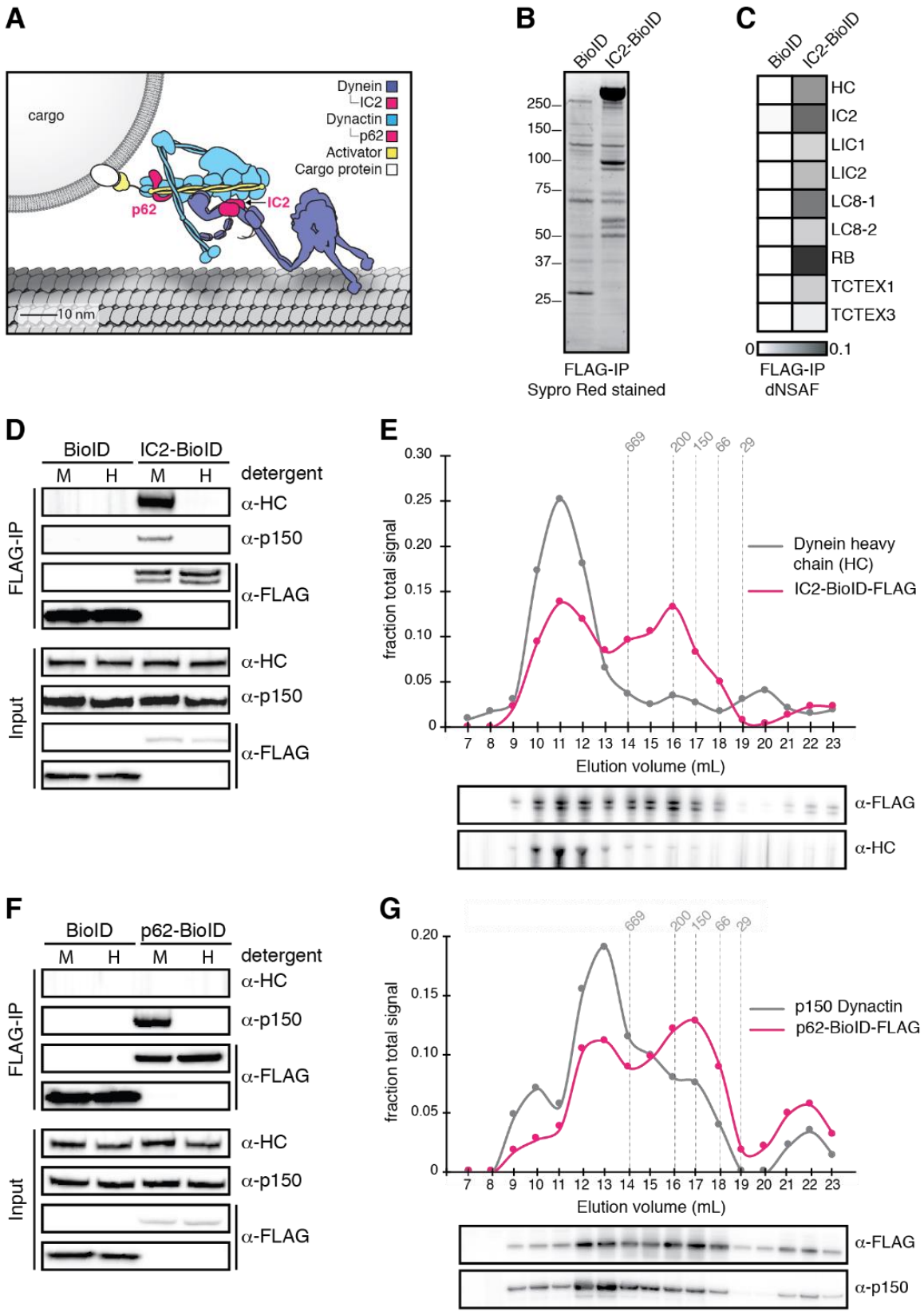
A
cargo
Dynein
IC2
Dynactin
p62
Activator
Cargo protein
p62
IC2
10 nm
B
BioID
IC2-BioID
250
150
100
75
50
37
25
FLAG-IP
Sypro Red stained
C
BioID
IC2-BioID
HC
IC2
LIC1
LIC2
LC8-1
LC8-2
RB
TCTEX1
TCTEX3
0
0.1
FLAG-IP
dNSAF
D
BioID
IC2-BioID
M
H
M
H
detergent
FLAG-IP
α-HC
α-p150
α-FLAG
Input
α-HC
α-p150
α-FLAG
E
669
200
150
66
29
fraction total signal
0.30
0.25
0.20
0.15
0.10
0.05
0
7 8 9 10 11 12 13 14 15 16 17 18 19 20 21 22 23
Elution volume (mL)
Dynein heavy chain (HC)
IC2-BioID-FLAG
α-FLAG
α-HC
F
BioID
p62-BioID
M
H
M
H
detergent
FLAG-IP
α-HC
α-p150
α-FLAG
Input
α-HC
α-p150
α-FLAG
G
669
200
150
66
29
fraction total signal
0.20
0.15
0.10
0.05
0
7 8 9 10 11 12 13 14 15 16 17 18 19 20 21 22 23
Elution volume (mL)
p150 Dynactin
p62-BioID-FLAG
α-FLAG
α-p150

subunit. The stably expressed p62-BioID-3×FLAG subunit incorporated into the dynactin complex as shown by immunoprecipitations (Figure 4.1F), and gel filtration analysis of these immunoprecipitations revealed that 47% was incorporated into the high molecular weight dynactin complex (Figure 4.1G).

To perform BioID experiments, we lysed cells in the presence of additional detergents (see Materials and Methods), which disrupt both the dynein and dynactin complexes (Figure 4.1D and F). Disruption of the complexes makes it likely that our BioID experiments identified only proximal proteins that were modified with biotin prior to cell lysis. All BioID experiments with tagged dynein or dynactin subunits were performed in quadruplicate using a label-free quantitative proteomics approach to calculate the enrichment of each identified protein relative to a soluble BioID alone control (Figure 4.2A) (Zhang et al., 2015). "Hits" were proteins with greater than 3-fold enrichment and p-values greater than 0.05 relative to the control. We first characterized the IC2 subunit of dynein, which is known to be centrally located within the tripartite dynein/dynactin/activating adaptor complex based on cryo-electron microscopy (cryo-EM) structural studies (Figure 4.1A) (Chowdary et al., 2018; Urnavicius et al., 2015). Our IC2 BioID dataset identified all dynein subunits, as well as a number of dynactin subunits (Figure 4.2B-D and Supplementary files C.1 and C.2). In addition, the dataset contained the known activating adaptors BICD2, HOOK1, and HOOK3, as well as BICD1, a homolog of BICD2 that is a likely activating adaptor (Figure 4.2D and Supplementary files C.1 and C.2). The only known dynein activating adaptors that we did not identify were Spindly and RAB11FIP4. Spindly regulates mitotic-specific dynein functions in human cells (Gassmann et al., 2010; Ying et al., 2009), likely the reason we did not identify it in an unsynchronized cell population. RAB11FIP3 is poorly expressed in HEK-293T cells (Huttlin et al., 2015) (Table 4.1). These experiments show that the dynein IC is well

positioned within the dynein/dynactin/activating adaptor complex for the BioID-based identification of activating adaptors.

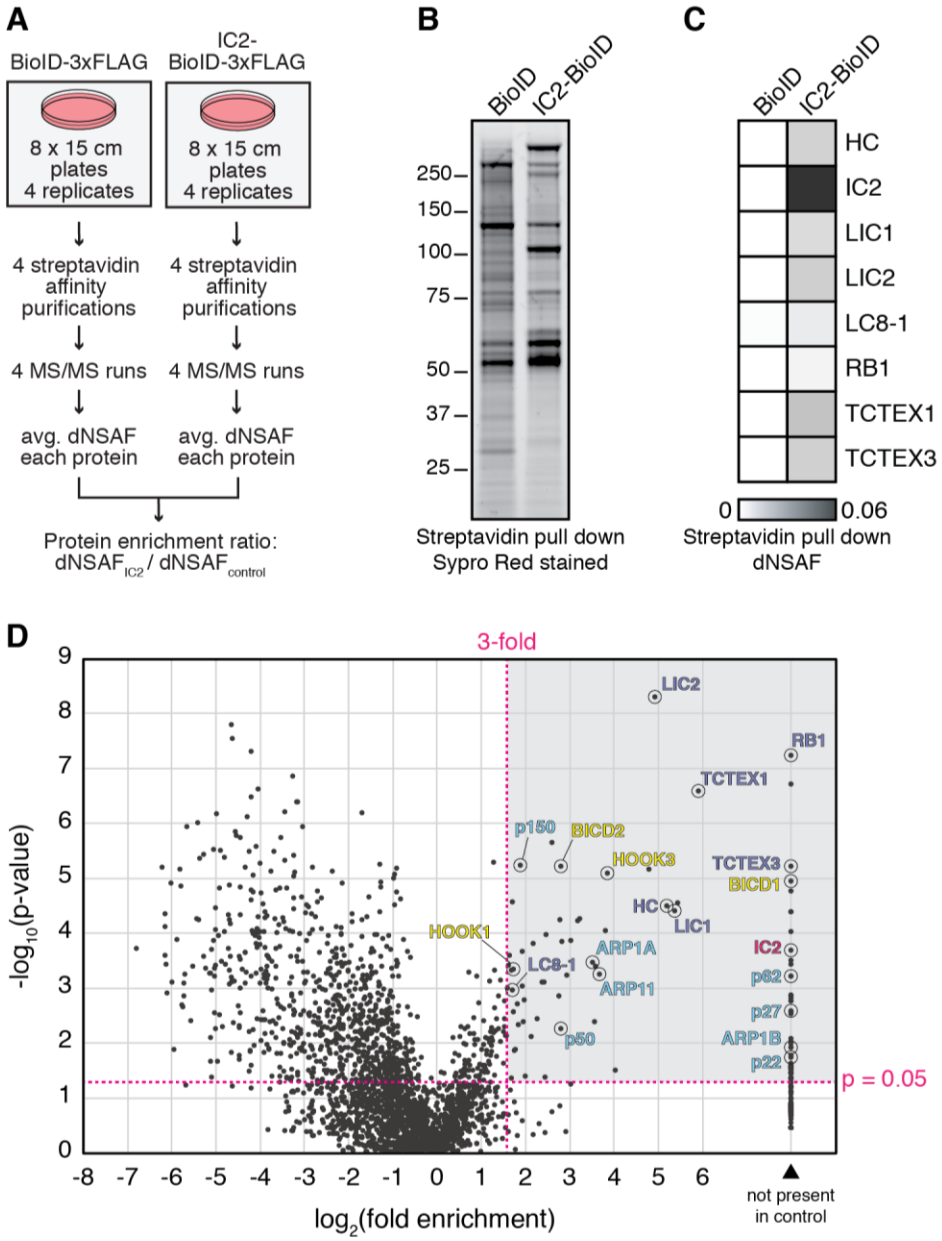

Figure 4.2. BioID with the dynein IC reports on activated dynein/dynactin/activating adaptor complexes in living human cells. (A) BioID experimental design. For each stably expressed BioID-tagged subunit reported in this study, quadruplicate samples were prepared, analyzed, and compared to a quadruplicate BioID only control. Fold enrichment was calculated as the ratio of dNSAF between the BioID-tagged subunit and the BioID control. (B) Biotinylated

(continued) proteins were isolated from cells stably expressing either IC2-BioID or BioID by streptavidin affinity purification. A Sypro Red stained SDS-PAGE gel is shown. (C) MS/MS analysis of the immunoprecipitates from (B). Core dynein subunit dNSAF (Zhang et al., 2015) values are displayed as a heat map. (D) A volcano plot showing enrichment versus significance of proteins identified in IC2-BioID experiments relative to control (BioID alone) experiments. A quadrant (dashed magenta line) bounded by a p-value of 0.05 and 3-fold enrichment contained dynein (dark blue) and dynactin (light blue) subunits, as well as the known activating adaptors BICD2, HOOK1, and HOOK3, and the candidate activating adaptor BICD1 (yellow).

Table 4.1. Total protein expression levels of activating adaptors or candidate activating adaptors or adaptors in HEK-293T cells. The number of peptides or phosphopeptides from HEK-293T cells (Huttlin et al., 2015) is shown. Activating adaptors or candidate activating adaptors identified in our secondary screen are highlighted in bold.

Activating adaptor or candidate activating adaptor	Peptides	Phospho-peptides
BICD1	**35**	**0**
BICD2	**151**	**6**
BICDL1	not present	
BICDL2	not present	
HOOK1	**183**	**13**
HOOK2	57	2
HOOK3	**130**	**0**
CCDC88A (girdin)	**247**	**51**
CCDC88B (gipie)	not present	
CCDC88C (daple)	**55**	**17**
SPDL1 (CCDC99)	107	0
RAB11FIP3	4	2
NIN	**114**	**20**
NINL	**8**	**5**
TRAK1	17	8
TRAK2	3	1
HAP1	not present	
RILP	not present	

To further explore the ability of BioID to report on the spatial organization of the dynein/dynactin/activating adaptor complex, we tagged additional dynein and dynactin subunits with BioID. Specifically, we generated five additional HEK-293 cell lines stably expressing BioID fused to the IC1, LIC1, LIC2, RB1, and TCTEX1 dynein subunits and analyzed these along with the tagged dynein IC2 and dynactin p62 subunits. Each BioID fusion protein incorporated into their respective complexes based on their ability to co-immunoprecipitate with dynein and dynactin (Figure 4.3A and B). Validating our approach, a protein-protein interaction network consisting of the hits shared between BioID-tagged subunits revealed that 13 of 20 hits present in three or more datasets were dynein/dynactin subunits and activating adaptors (Figure C.2 and Supplementary file C.3).

Analyses of the dynein/dynactin hits enriched in each subunit dataset were also consistent with recent structural studies (Figure 4.3C) (Chowdhury et al., 2015; Urnavicius et al., 2015). IC1 and IC2 BioID samples detected more dynactin subunits than either LIC1 or 2, consistent with the dynein LIC being further away from dynactin compared to the IC (Figure 4.3C). With respect to activating adaptors, we found that the IC1, LIC1 and LIC2 dynein subunits and the p62 dynactin subunit identified dynein activating adaptors (Figure 4.3C and Supplementary files C.1 and C.3). This finding is consistent with the current structural model of the dynein/dynactin/activating adaptor complex (Chowdhury et al., 2015; Urnavicius et al., 2015). Thus, BioID provides spatial information about the large dynein complex, which is capable of moving in the cytoplasm. Importantly, these results also show that BioID experiments with the dynein IC and LIC subunits and dynactin p62 subunit can be used to identify activating adaptors, providing a method to discover dynein activating adaptors in other cell types or tissues.

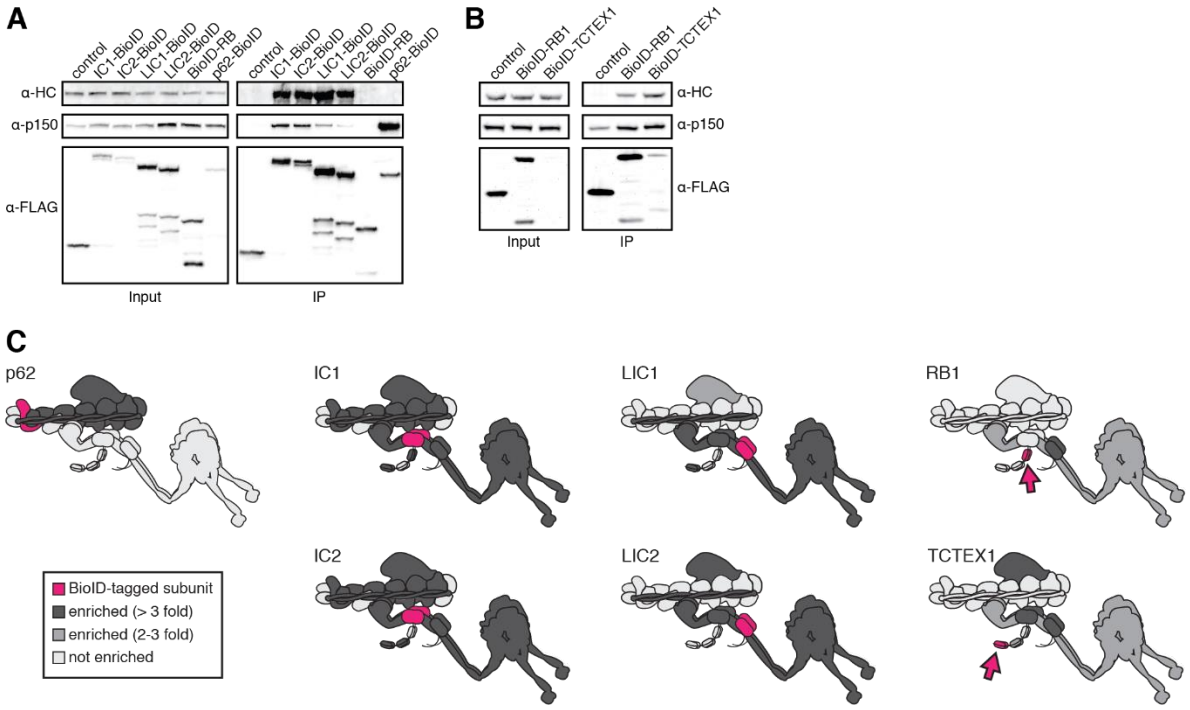

Figure 4.3. BioID reports on the spatial organization of the dynein/dynactin/activating adaptor complex. (A and B) Dynein (IC1, IC2, LIC1, LIC2, RB1, TCTEX1) and dynactin (p62) subunits tagged with BioID-3×FLAG were immunoprecipitated (for 16 hours in A or 2 hours in B) from stable HEK-293 cell lines using α-FLAG antibodies. All subunits incorporated into the dynein/dynactin complex based on Western blots with α-HC and α-p150 antibodies. (C) BioID experiments were performed with cells expressing the indicated dynein and dynactin subunits (magenta and magenta arrows). Other dynein and dynactin subunits enriched in the BioID experiments are shaded light gray (2-3 fold) or dark gray (≥3-fold), $p<0.05$, Student's two-tailed t-test.

Ninein and ninein-like constitute a new family of dynein activating adaptors

To identify novel dynein activating adaptors in the dynein/dynactin interactome, we performed a secondary screen (Figure 4.4A). Because all known activating adaptors contain long stretches of coiled coil (Figure 4.4B), we pooled datasets with known activating adaptors present (IC1, IC2, LIC1, LIC2, and p62) and selected a set of proteins with predicted coiled coils of at least 100 amino acids. We then expressed each predicted coiled coil domain tagged with GFP and

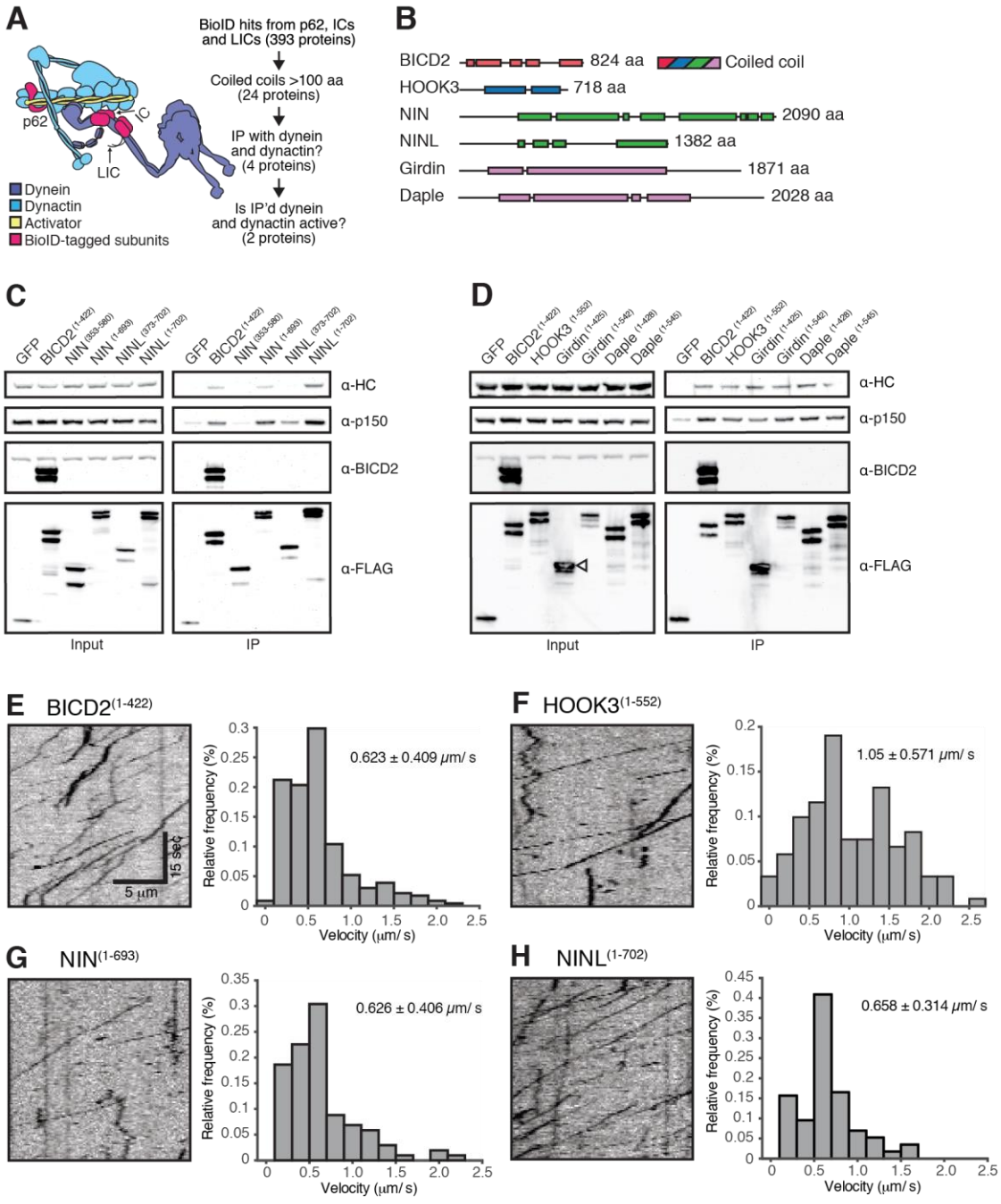

Figure 4.4. A secondary screen identifies candidate activating adaptors of dynein/dynactin motility. (A) A schematic of our secondary screen. (B) Location of predicted coiled coils (rectangles) in known and candidate dynein/dynactin activating adaptors. (C, D) Candidate and known (BICD2 and HOOK3) activating adaptors tagged with 3×FLAG were immunoprecipitated with α-FLAG antibodies from HEK-293 cells. Western blots with α-HC and α-p150 antibodies

(continued) were used to determine which proteins co-immunoprecipitated dynein and dynactin. (E—H) The candidate NIN (1-693) and NINL (1-702) activating adaptors, as well as the known BICD2 (1-422) and HOOK3 (1-552) activating adaptors were tagged with GFP and 3×FLAG and were immunoprecipitated with α-FLAG antibodies from HEK-293 cells. The motility of immunoprecipitated dynein/dynactin/activating adaptor complexes was monitored by GFP fluorescence using TIRF microscopy. Kymographs (left) and velocity histograms (right) with mean velocity (± S.D.) shown, *n* is greater than 102.

3×FLAG in HEK-293 cells (Figure C.3). A hallmark of known activating adaptors is their ability to co-immunoprecipitate dynein and dynactin (McKenney et al., 2014; Olenick et al., 2016). Four proteins analyzed in our secondary screen, ninein (NIN), ninein-like (NINL), daple (CCDC88C) and girdin (CCDC88A), co-immunoprecipitated dynein and dynactin, as did our positive controls BICD2 and HOOK3 (Figure 4.4C-D and C.3). Some construct optimization was necessary to determine the dynein/dynactin interacting region of each candidate activating adaptor and we used the literature to guide this process (Casenghi, 2005; Schroeder and Vale, 2016) (Figure 4.4 C-D and C.4A).

To determine whether these candidate activating adaptors were part of activated dynein/dynactin complexes, we next performed in vitro single-molecule motility assays. We immunoprecipitated GFP-tagged BICD2 (aa 1-422), HOOK3 (aa 1-552), NIN (aa 1-693), NINL (aa 1-702), daple (aa 1-545) and girdin (aa 1-542) from HEK-293 cells and observed the motility of any co-purifying dynein and dynactin on microtubules using total internal reflection fluorescence (TIRF) microscopy. Our positive controls, BICD2 and HOOK3, exhibited robust processive motility, as did NIN and NINL (Figure 4.4 E-H). In contrast, daple and girdin showed only a very modest ability to isolate activated dynein/dynactin complexes (Figure C.4B-C). Because reconstituted purified dynein and dynactin occasionally show processive runs in the

absence of an activating adaptor (McKenney et al., 2014; Schlager et al., 2014a), we cannot yet conclude if daple and girdin are bona fide dynein activating adaptors.

The gold standard assay for dynein activating adaptors is to reconstitute dynein/dynactin/activating adaptor motility from purified components (McKenney et al., 2014; Schlager et al., 2014a). To this end, we purified dynein and dynactin individually from HEK-293 cell lines stably expressing either IC2 or p62 tagged with SNAP or Halo tags (for fluorophore labeling) and 3×FLAG (for purification) (Figure 4.5A and C.5A). The coiled coil domains of BICD2, NIN, and NINL were tagged with GFP and purified from *E. coli* (Figure C.5A). After reconstituting the complexes, we used near-simultaneous three-color TIRF microscopy to visualize the motility of single dynein/dynactin/activating adaptor complexes on microtubules. As expected, BICD2 activated and co-migrated with processively moving dynein and dynactin (Figure 4.5B). Both NIN and NINL also activated and co-migrated with moving dynein/dynactin complexes (Figure 4.5C and D). In the absence of an activating adaptor dynein/dynactin is largely stationary, with some diffusive and rare processive runs observed (Figure 4.5E and C.5B). Together, our results show that the BioID method can identify dynein activating adaptors, including the members of a new family of activating adaptors we discovered here: NIN and NINL.

Identification of the interactomes of six dynein activating adaptors

A major goal in the transport field is to determine the molecular rules that govern cargo recognition and specificity. This is especially critical for dynein, which moves all microtubule minus-end-directed cargos in the cytoplasm. How many cargos does each activating adaptor recognize? Does each activating adaptor allow dynein/dynactin to recognize a specific subset of cargo, or is there overlap in the number of activating adaptors that can recognize any given cargo? To address

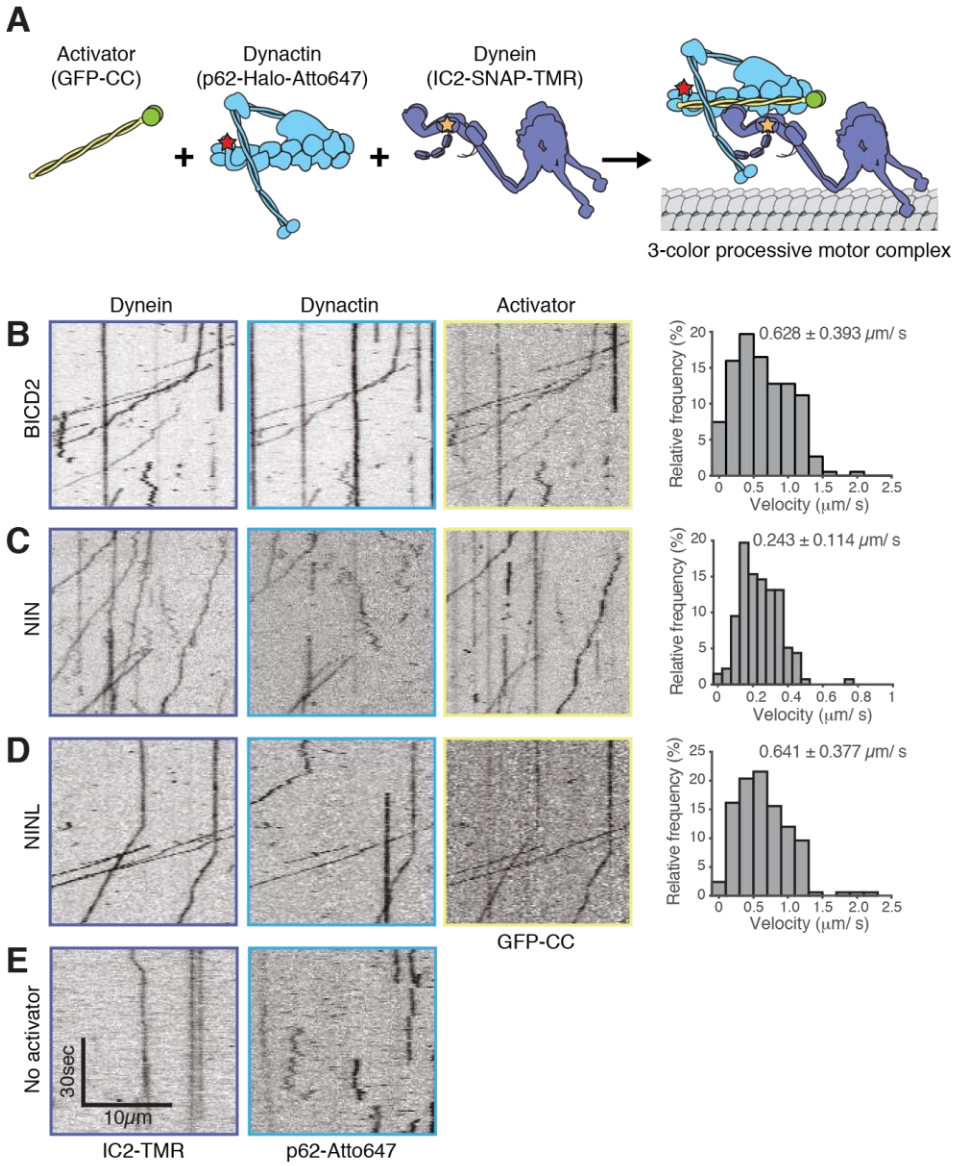

Figure 4.5. NIN and NINL are novel activating adaptors of dynein/dynactin motility. (A) A schematic of the components added to the single-molecule motility assay. (B—E). Dynein (IC2-TMR), dynactin (p62-Atto647) and GFP-tagged activating adaptors (BICD2) or candidate activating adaptors (NIN and NINL) were purified separately, mixed, and the motility of the complex along microtubules was monitored by nearly simultaneous three-color TIRF microscopy. Kymographs of each imaging channel (left) and velocity histograms (right) with mean velocity (± S.D.) are shown, *n* is greater than 146. NIN had a slower velocity in this assay compared to Figure 4G. We attribute this to difficulties in purifying the truncated NIN protein.

these questions, and to provide a starting point for future exploration of activating adaptor-cargo interactions, we used BioID to identify the interactomes of six dynein activating adaptors. We made both N- and C-terminal BioID fusions with each activating adaptor because, for the known activating adaptors BICD2 and HOOK3, their N-termini interact with dynein/dynactin and their C-termini bind to cargos or cargo adaptor proteins (Cianfrocco et al., 2015). We generated HEK-293 cell lines stably expressing full-length BICD1, BICD2, HOOK1, HOOK3, NIN, and NINL with BioID tags at either their N- or C-termini, and used MS/MS to detect activating adaptor proximal proteins from these twelve cell lines (Figure 4.6A and Supplementary files C.1 and C.4). As with our earlier experiments, we used detergent conditions (see Materials and Methods) that made it likely we only identified proteins that were directly biotinylated and considered hits to be proteins with greater than 3-fold enrichment and p-values greater than 0.05 relative to a soluble BioID control.

BICD1 and 2, the best structurally characterized dynein activating adaptors, are known to be elongated structures (Liu et al., 2013; Terawaki et al., 2015; Urnavicius et al., 2015). Given this, and the likely elongated nature of other activating adaptors, we reasoned that BioID would be ideally suited to report on the spatially separated functional differences between the N- and C-termini of activating adaptors. We analyzed the N- and C-terminal BioID datasets from all six activating adaptors. We contrasted the N- and C-terminal datasets separately, in both cases seeking to reveal activating adaptor-specific interactions and those shared between multiple activating adaptors. The shared interactions were used to construct interaction networks revealing the connections between activating adaptors (Figure 4.6B). Overall, in comparison to N-terminal datasets, the C-terminal datasets had more unique hits (except for NIN), more hits shared between activating adaptors, and more total hits (Figure 4.6C).

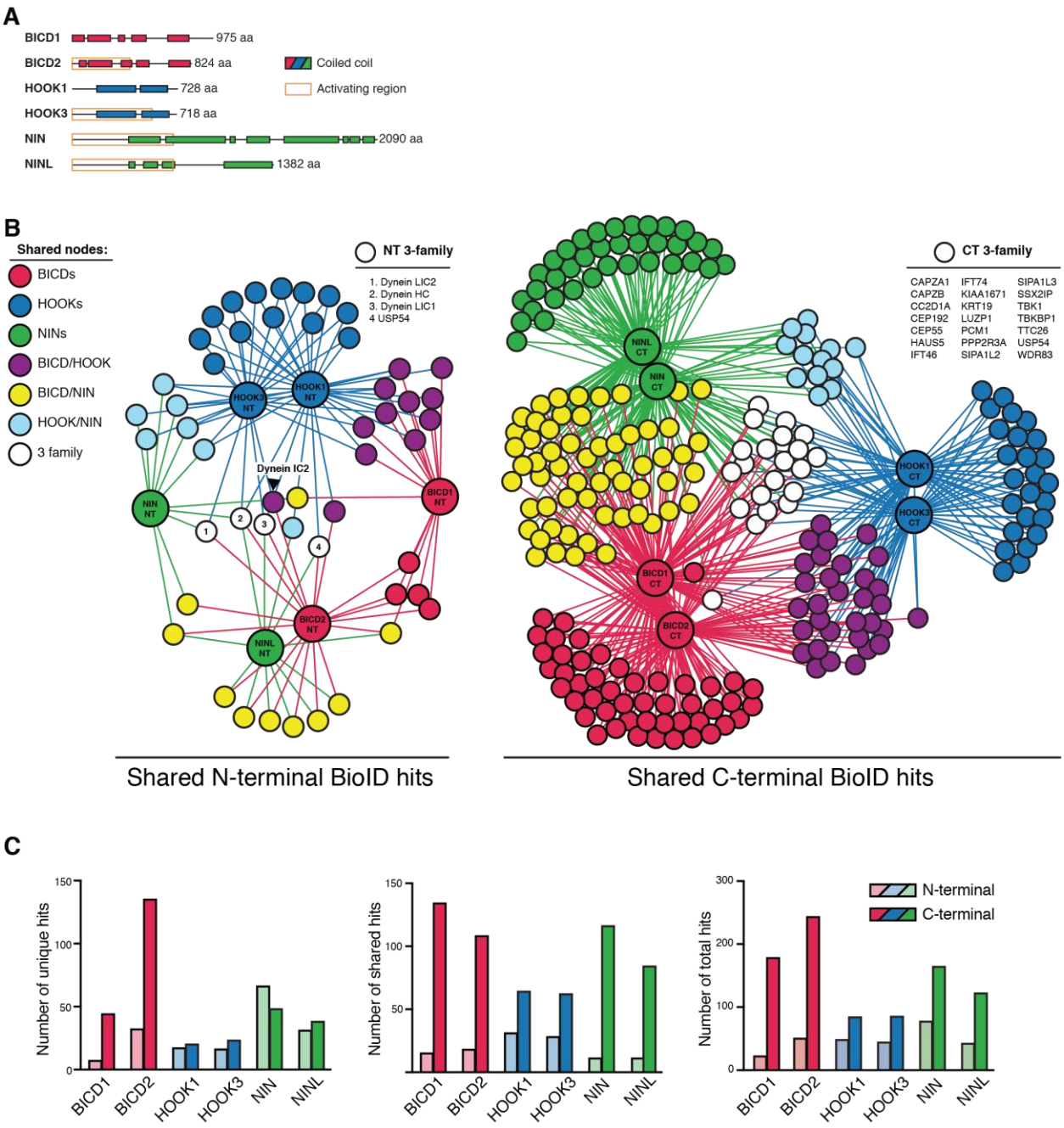

Figure 4.6. Dynein activating adaptors have distinct proteomes. (A) Location of predicted coiled coils in dynein activating adaptors, with minimal activating regions shown (orange rectangles). (B) Enriched and significant hits from N- and C-terminal datasets of six activating adaptors were used to construct two separate protein-protein interaction networks. Hits specific to an activating adaptor family (color-coded according to their respective activating adaptors), and hits shared between activating adaptor families (HOOK/BICD, purple; BICD/NIN, yellow; NIN/HOOK, cyan) are shown. White spheres ("3-family") represent hits enriched in at least one

(continued) activating adaptor from each family. For this figure enrichment is ≥ 3 fold, significance is $p < 0.05$, Student's two-tailed t-test; and average spectral counts are ≥2. The location of dynein and dynactin subunits and select hits discussed in the text are indicated. (C) The number of total, unique (occurring in a single activating adaptor N- or C-terminal dataset), and shared (occurring in multiple activating adaptor N- or C-terminal datasets) hits for individual activating adaptor N- and C-termini are shown.

We next identified proteins that were found in all activating adaptor families (BICD1/2, HOOK1/3, and NIN/NINL). When we performed this analysis for the N-terminal datasets only four out of 225 unique proteins were present in at least one dataset from each activating adaptor family (Figure 4.6B, white circles). Strikingly, this included three dynein subunits (HC, LIC1, and LIC2), highlighting that the shared function associated with the N-termini of activating adaptors is their interaction with dynein. When we performed this analysis with the C-terminal datasets we found 21 out of 547 unique proteins were present in each activating adaptor family (Figure 4.6B). Gene ontology (GO) enrichment analysis (Blake et al., 2015) of these 21 proteins revealed an association with cellular locations that correlate with microtubule minus ends ("ciliary basal body", "microtubule organizing center", and "centrosome") (Supplementary file C.5). Other GO terms that were enriched included "F-actin capping complex", "intraciliary transport particle B", and "ciliary tip". In contrast to the N-terminal dataset we did not detect any dynein subunits in the C-terminal dataset. Overall, this data highlights the power of the BioID technique to report on the distinct protein interactions of different regions of the dynein activating adaptors.

We next contrasted all 12 activating adaptor datasets (Figure C.6 and Supplementary files C.1 and C.4). This analysis allowed for the removal of hits shared between the N- and C-termini of activating adaptors and focus on C-terminal-specific activating adaptor interactions, as this is the region of cargo interaction for characterized activating adaptors (Cianfrocco et al., 2015). Each

activating adaptor had dozens of C-terminal specific hits (Figure C.6 and Supplementary files C.1 and C.4). These proteins are candidates for activating adaptor-specific cargos, cargo adaptors, or proteins that regulate how dynein connects to its cargo. GO term enrichment analysis of these activating adaptor-specific hits revealed several trends. The BICD2 C-terminal interactome was enriched for GO terms relating to cortical actin cytoskeleton structures, including adherens junctions and focal adhesions (Supplementary file C.5), consistent with previous studies that have linked dynein to these cortical actin-based structures (Ligon et al., 2001; Rosse et al., 2012). The HOOK3 C-terminal interactome was enriched for GO terms relating to clathrin coated vesicles and both the NIN and NINL C-terminal interactomes were enriched for GO terms generally related to structures found at microtubule minus ends (Supplementary file C.5).

We also analyzed the shared interactions of activating adaptors within the same family (e.g. BICD1/2, HOOK1/3 and NIN/NINL). Activating adaptors within families share significant sequence similarity (global identity, global similarity: BICD1/BICD2 = 54.6%, 65.2%; HOOK1/HOOK3 = 57.0%, 74.2%; NIN/NINL = 21.1%, 34.9%). Reflecting this protein conservation, activating adaptors from the same protein family had more C-terminal-specific overlap than activating adaptors from different families (Table 4.2). The BICD activating adaptor family was enriched for GO terms associated with the actin cytoskeleton. The HOOK family with GO terms related to kinesin motors and the NIN family with GO terms related to microtubule minus ends (Supplementary File C.5).

Validating our approach, our analysis of activating adaptor- and activating adaptor family-specific hits identified several known activating adaptor-cargo interactions. HOOK1 and HOOK3 are members of the FHF complex, which is involved in endosomal sorting (Xu et al., 2008). We identified proteins in this complex (AKTIP/FTS and FAM160A2/FHIP), as well as two proteins

Table 4.2. Specific pairwise overlap between activating adaptor C-terminal BioID datasets. Twelve activating adaptor BioID datasets were contrasted (6 N-terminal and 6 C-terminal) to determine for each activating adaptor which of its C-terminal hits were specifically shared with other datasets. Those shared with N-terminal datasets were removed. The specific pairwise overlap of the remaining hits with each activating adaptor is reported (*n* and %). Input *n* = BICD1 (92), BICD2 (87), HOOK1 (39), HOOK3 (37), NIN (74), NINL (53). Only pairwise overlap is represented in this analysis; overlap with multiple activating adaptors (e.g. BICD1 overlap with both BICD2 and HOOK1) is not shown.

	BICD1		**BICD2**		**HOOK1**		**HOOK3**		**NIN**		**NINL**	
	n	%	*n*	%	*n*	%	*n*	%	*n*	%	*n*	%
BICD1			44	50.6	4	10.3	0	0	5	6.8	5	9.4
BICD2	44	47.8			4	10.3	7	18.9	6	8.1	0	0
HOOK1	4	4.3	4	4.6			14	37.8	3	4.1	1	1.9
HOOK3	0	0	7	8.0	14	35.9			2	2.7	1	1.9
NIN	5	5.4	6	6.9	3	7.7	2	5.4			27	50.9
NINL	5	5.4	0	0	1	2.6	1	2.7	27	36.5		

that are homologous to FAM160A2 (FAM160A1, FAM160B1) as specifically enriched in the HOOK1 and HOOK3 datasets. FAM160A1 and FAM160A2 share sequence identity (global identity 36.4%, global similarity 50.5%), and FAM160A2 was reported to interact with HOOK3 and AKTIP/FTS in a recent high-throughput proteomics study (Huttlin et al., 2015). In addition, we identified C-terminal-specific interactions of HOOK1 and HOOK3 with the kinesins KIF1C and KIF5B, as well as the KIF5B associated light chains, KLC2 and KLC4. Although Hook proteins are not known to interact with kinesins in humans, studies in filamentous fungi have linked dynein, Hook, and kinesin (Bielska et al., 2014; Zhang et al., 2014). We also identified RIMBP3, a known HOOK1 interacting protein involved in spermatogenesis, as a HOOK1 C-terminal-specific hit (Zhou et al., 2009). In the BICD2 interactome, we identified RANBP2, a well-characterized BICD2-interacting protein that is responsible for targeting dynein/dynactin/BICD2 to nuclear pore complexes (Splinter et al., 2010). The NINL C-terminal interactome was

specifically enriched for MICAL3, a protein that interacts with Rab8 and is localized to the base of primary cilia in a NINL-dependent manner (Bachmann-Gagescu et al., 2015).

We were intrigued by the presence of kinesin, including the kinesin-3 KIF1C, in the HOOK datasets (Supplementary file C.4). Although Hook proteins are not known to interact with kinesins in humans, studies in filamentous fungi have linked dynein, Hook, and kinesin (Bielska et al., 2014). We used co-immunoprecipitation experiments to verify the interaction of HOOK3 with the dynein heavy chain, FAM160A2/FHIP, and KIF1C (Figure C.7). Our BioID data had identified the interaction of HOOK3 with KIF1C and FAM160A2/FHIP as C-terminal-specific and the interaction with dynein/dynactin as N-terminal-specific. In agreement with our BioID data, immunoprecipitation experiments showed that the interaction of KIF1C and FAM160A2/FHIP with HOOK3 was specific to the C-terminus of HOOK3 (553–718) (Figure C.7), while dynein's interaction was specific to the N-terminus of HOOK3 (aa 1–552) (McKenney et al., 2014). This data further validates the BioID approach and highlights how BioID can identify spatially restricted interactions. In addition, this data suggests that HOOK3 may represent a new class of dynein activating adaptor, one that not only activates dynein/dynactin, but can also recruit the opposite polarity motor KIF1C.

4.5 Discussion

We applied proximity-dependent biotinylation to identify the dynein/dynactin/activating adaptor transportome. Our data show that BioID reports on the spatial organization of both the tripartite dynein/dynactin/activating adaptor complex, as well as the domain organization of dynein activating adaptors. Using a secondary screen of our dynein/dynactin BioID data, we developed an approach to identify novel dynein activating adaptors. We identified ninein and ninein-like as

a new family of dynein activating adaptors and two Hook-related proteins, girdin and daple, as candidate dynein/dynactin activating adaptors. Our analysis of the activating adaptor interactomes suggests that there are dozens of unique interactions for each activating adaptor, as well as shared interactions particularly among activating adaptors of the same class. We propose that these proteins represent novel dynein cargos, cargo adaptors or regulators of motor-cargo interactions and that each activating adaptor will link dynein to multiple cargos.

BioID provides spatial information about the large cytosolic dynein transport machinery

We tagged seven distinct dynein or dynactin subunits with the BioID tag. Our analysis of their interactomes suggests that BioID can provide spatial information about the large dynein machinery, capable of moving in the live cells we used for our experiments. The recent cryo-EM structures of the dynein/dynactin/activating adaptor complex (Chowdhury et al., 2015; Urnavicius et al., 2015) allowed us to roughly map the interactions we identified. The interactomes of each dynein or dynactin subunit identified other dynein and dynactin subunits that were located in close proximity based on these structural studies. Important for future discovery efforts, we found that proteins that were in the vicinity of the activating adaptor (the dynein ICs and LICs and the p62 subunit of dynactin) had interactomes containing activating adaptors. Thus, tagging these proteins with proximity-dependent biotinylation tags will allow future efforts to identify dynein activating adaptors in other cell types and tissues. We also found that each activating adaptor, all of which contain long stretches of predicted coiled coil and likely have elongated structures, had largely non-overlapping protein interactions depending on whether their N- or C-terminus was tagged with BioID. Our data agrees with published data showing that the N-termini of activating adaptors

interact with dynein/dynactin and that the C-termini with cargos or cargo adaptors (Cianfrocco et al., 2015).

BioID identifies ninein and ninein-like as members of a new class of dynein/dynactin activating adaptors.

Our secondary screen of predicted coiled coil-containing proteins identified in the dynein/dynactin interactome identified four proteins that could co-immunoprecipitate with dynein and dynactin: NIN, NINL, girdin and daple. Further analysis of these proteins demonstrated that NIN and NINL activated dynein/dynactin motility in single-molecule motility assays, while girdin and daple did not. Here, we focused on predicted coiled coil-containing proteins for their ability to activate dynein/dynactin motility. Future analysis of the hits found in the dynein/dynactin interactome could identify additional positive or negative regulators of dynein motor activity. It is also possible that there will be dynein activating adaptors lacking large stretches of coiled coil, which were not assessed in our secondary screen.

Both NIN and NINL localize to the centrosome, are involved in microtubule nucleation, and have been shown previously to immunoprecipitate with dynein/dynactin (Casenghi, 2005; Casenghi et al., 2003; Delgehyr et al., 2005; Wang et al., 2015). The ability of NIN and NINL to activate dynein suggests that they control their own, as well as any associated proteins, recruitment to the centrosome or other sites of microtubule nucleation. NINL has also been implicated in dynein-based vesicle trafficking (Dona et al., 2015), in support of the idea that each activating adaptor has multiple cargos (see below).

Girdin and daple are Hook-related proteins (Simpson et al., 2005), which also act as guanine nucleotide exchange factors for small G proteins (Aznar et al., 2015, 2016). While both

robustly co-immunoprecipitated dynein and dynactin, they did not conclusively activate dynein/dynactin motility. We used girdin and daple constructs that were identical in length to a HOOK3 construct that could activate motility. However, it is possible that longer girdin or daple constructs will be required for activation or that post-translational modifications regulate their ability to activate dynein/dynactin motility. For example, both daple and girdin are phosphoproteins (Table 4.1) (Huttlin et al., 2015). It is also possible that girdin and daple regulate dynein by blocking the ability of motility-inducing activating adaptors to bind to dynein. CCDC88B/gipie is related to girdin and daple and interacts with dynein and dynactin (Ham et al., 2015). We did not identify gipie in our screen, likely because it is not expressed in HEK-293T cells (Table 4.1) (Huttlin et al., 2015). Future studies of these Hook-related proteins will be aimed at exploring if and how they regulate dynein/dynactin activity.

Activating adaptors have many new candidate cargos

Our findings suggest that the number of dynein activating adaptors is much smaller than the number of dynein cargos, strongly implying that each activating adaptor links dynein to multiple cargos. There are hints of this concept in the literature as BICD2 interacts with both Rab6 and RanBP2 (Hoogenraad and Akhmanova, 2016), and in *Drosophila* the RNA binding protein egalitarian (Dienstbier et al., 2009). Consistent with this, our GO analysis of the interactomes of six distinct dynein activating adaptors suggests that each of these activating adaptors is involved in multiple dynein-based functions. Overall, our data imply a tiered mode of dynein regulation in which activating adaptors, such as members of the BICD, HOOK and NIN families constitute the first step in cargo recognition, but additional layers must be required to achieve cargo specificity.

Our data raise a number of interesting questions for future exploration. How are activating adaptors released from dynein/dynactin? Which factors mediate this? Given that the dynein/dynactin machinery may be relatively invariant compared to activating adaptors, are activating adaptors exchanged? And, if so which factors mediate this? Are there proteins that bind to the same region of dynein/dynactin as activating adaptors, but don't activate motility? Finally, are activating adaptors promiscuous and if so what is the balance of stochastic versus regulated motor-cargo interactions? Our dynein transport machinery transportome provides a rich dataset to address these fundamental questions.

4.6 Materials and Methods

Molecular cloning and generation of stable cell lines

All plasmids used in this study were constructed by PCR and Gibson isothermal assembly. BioID G2 (Kim et al., 2016b) was the kind gift of Kyle Roux (Sanford School of Medicine, University of South Dakota). ORFs (isoforms indicated where applicable) were obtained from several sources. IC1 (isoform 2, 628 aa), IC2 (isoform 2C, 612 aa), LIC1, Roadblock (isoform 1, 96 aa), TCTEX1, and p62 (isoform 1, 460 aa) were amplified from a RPE1 cell cDNA library (generated in the Reck-Peterson lab). LIC2 (isoform 1, 492 aa) and HOOK1 (isoform 1, 728 aa) were obtained from the Harvard Medical School PlasmID Repository, BICD2 (isoform 1, 824 aa) from Thermo Fisher Scientific, BICD1 (isoform 1, 975 aa) from Genescript, HOOK3 from GE Dharmacon, and NIN was the kind gift of Dr. Yi-Ren Hong (Department of Biochemistry, Kaohsiung Medical University, Taiwan). NINL (isoform 1, 1382 aa) was synthesized in segments (IDT) and assembled by Gibson isothermal assembly. For constitutive expression, ORFs were inserted into pcDNA5/FRT (Invitrogen). IC1, IC2, LIC1, LIC2, and p62 were constructed as C-terminal fusions

with BioID (e.g. pcDNA5-FRT-IC1-5×GA-BioID-3×FLAG); Roadblock1 and TCTEX1 were constructed as N-terminal fusions (e.g. pcDNA5-FRT-BioID-5×GA-Roadblock1-3×FLAG); and activating adaptors (BICD1, BICD2, HOOK1, HOOK3) were constructed as both N- and C-terminal fusions. To obtain inducible expression, NIN-BioID, BioID-NIN, NINL-BioID, BioID-NINL, and a BioID control were inserted into pcDNA5/FRT/TO (Invitrogen). All constructs had 5×glycine-alanine linkers added between BioID and the ORFs to provide flexibility between the modules. All constructs were sequence verified and expression was verified by Western blotting with an anti-FLAG M2-HRP antibody (Sigma).

For all experiments, HEK-293 stable cell lines were maintained at 37°C with 5% CO2 in Dulbecco's Modified Eagle Medium (DMEM, Corning) supplemented with 10% fetal bovine serum (FBS, Gibco) and 1% Penicillin/Streptomycin (PenStrep, Corning). T-Rex HEK293 cells (Thermo Fisher), which constitutively express the Tet repressor, were used for all stable cell lines. Stable cell lines were generated by transfection with Lipofectamine 2000 (Thermo Fisher) and a combination of the appropriate pcDNA5 construct and pOG44, which expresses Flipase. After recovery from transfection, cells were grown in DMEM containing 10% FBS, 1% PenStrep, and 50 μg/mL Hygromycin B. Colonies were isolated, expanded, and screened for expression of the fusion proteins by Western Blotting with an anti-FLAG M2-HRP antibody (A8592, Sigma; see "Western analysis and antibodies" below for details).

Protein sequence analysis

Protein sequences were downloaded from UniProt (Apweiler et al., 2017). Multiple sequence alignments were calculated with Clustal Omega, and pairwise alignments used to calculate percent identity and similarity between proteins were calculated with EMBOSS Needle (Li et al., 2015).

BioID: cell growth and sample preparation

To initiate a BioID experiment, low passage cells were plated at 20% confluence in 15 cm dishes as 4 replicates, with each replicate consisting of 8 x 15 cm plates. After 24 hours, biotin was added to the media to a final concentration of 50 μM, and the cells were incubated for an additional 16 hours. Tetracycline was added to tetracycline-inducible stable cell lines (1 μg/mL final concentration) at the same time as biotin. After decanting the media, cells were dislodged from each plate by pipetting with ice-cold PBS. Cells were centrifuged at 1000 x g for 2 minutes and the PBS was decanted. Cells were washed once more with ice cold PBS before proceeding to cell lysis. Cells were resuspended and lysed in 10 mL modified RIPA buffer (25 mM Tris-HCl, pH 8.0; 150 mM NaCl, 1% (v/v) NP-40, 0.5% (w/v) sodium deoxycholate, 0.1% (w/v) SDS, 1 mM DTT, and protease inhibitors (Roche cOmplete Protease Inhibitor Cocktail) by gentle rocking for 5-10 minutes at 4°C. The cell lysate was clarified via centrifugation at 66,000 x g for 30 min in a Type 70 Ti rotor (Beckman) at 4°C. The clarified lysate was retrieved and dialyzed twice against dialysis buffer (50 mM Tris-HCl, pH 8.0; 150 mM NaCl, 1 mM DTT, 0.01% Triton X-100) for 2 hours per exchange. The dialysate was retrieved, supplemented with fresh protease inhibitors, and combined with 1 mL streptavidin-conjugated beads (Dynabeads MyOne Streptavidin T1, Thermo Fisher Scientific) and incubated overnight at 4°C with gentle rocking. Bead/lysate mixtures were collected on a magnetic stand into a single 2 mL round-bottom microcentrifuge tube. The beads were then washed 4 times with 2 mL RIPA buffer, with immobilization and solution removal performed on the magnetic stand. To elute bound immobilized proteins, the beads were boiled for 10 minutes at 100°C in 100 μL elution buffer (50 mM Tris, pH 6.8, 2% SDS (w/v), 20 mM DTT, 12.5 mM EDTA, 2 mM biotin). Typically, 10 μL was analyzed by SDS-PAGE and Sypro Red staining and the remaining eluate (90 μL) was diluted to a final volume of 400 μL with 100 mM

Tris-HCl, pH 8.5. 100% trichloroacetic acid was added to a final concentration of 20% and the solution was incubated overnight at 4°C. The precipitate was collected by centrifugation at maximum speed in a microcentrifuge for 30 minutes at 4°C. The supernatant was removed, the pellet was washed with 500 µL ice cold 100% acetone, and was centrifuged at maximum speed in a microcentrifuge for 10 minutes at 4°C. The acetone was removed, and the wash was repeated. After removing the final acetone wash, the pellet was dried in a laminar flow cabinet for 30-60 minutes.

Mass spectrometry

Preparation of peptide mixtures

TCA-precipitated protein samples from streptavidin affinity purifications or FLAG immunoprecipitations were solubilized in 30 µl of freshly made 0.1 M Tris-HCl, pH 8.5, 8 M urea, 5 mM TCEP (Tris [2-Carboxylethyl]-Phosphine Hydrochloride, Pierce). After 30 minutes at room temperature, freshly made 0.5 M 2-Chloroacetamide (Sigma) was added to a final concentration of 10 mM, and the samples were left at room temperature for another 30 minutes in the dark. Endoproteinase Lys-C (Roche) was first added at an estimated 1:100 (wt/wt) enzyme to protein ratio, for at least 6 hours at 37°C. Urea was then diluted to 2 M with 0.1 M Tris-HCl, pH 8.5, $CaCl_2$ was added to 0.5 mM, and modified trypsin (Promega), 1:100 (wt/wt), was added for over 12 hours at 37°C. All enzymatic digestions were quenched by the addition of formic acid to 5% final concentration.

Data Acquisition

Each trypsin-digested sample was analyzed independently by Multidimensional Protein Identification Technology (MudPIT) as described previously (Washburn et al., 2001; Wolters et al., 2001). Peptide mixtures were pressure-loaded onto a 250 μm fused-silica column packed first with 2 cm of 5 μm C18 reverse phase particles (Aqua, Phenomenex), followed by 3 cm of 5 μm strong cation exchange material (Partisphere SCX, Whatman). The loaded microcapillary columns were then connected to a 100 μm fused-silica column pulled to a 5 μm tip using a P 2000 CO2 laser puller (Sutter Instruments) packed with 8 cm of 5 μm C18 reverse phase particles. Loaded and assembled microcapillaries were placed in line with either a LTQ ion trap mass spectrometer (Thermo Fisher Scientific; for all datasets except Figure 4.2D) or a Velos Orbitrap Elite mass spectrometer (Thermo Fisher Scientific; for Figure 4.2D), both of which were interfaced with quaternary Agilent 1100 quaternary pumps (Agilent Technologies). Overflow tubing was used to decrease the flow rate from 0.1 mL/min to about 200–300 nL/min. During the course of fully automated chromatography, ten 120-minute cycles of increasing salt concentrations followed by organic gradients slowly released peptides directly into the mass spectrometer (Florens and Washburn, 2006). Three different elution buffers were used: 5% acetonitrile, 0.1% formic acid (Buffer A); 80% acetonitrile, 0.1% formic acid (Buffer B); and 0.5 M ammonium acetate, 5% acetonitrile, 0.1% formic acid (Buffer C). The last two chromatography steps consisted in a high salt wash with 100% Buffer C followed by the acetonitrile gradient. The application of a 2.5 kV distal voltage electrosprayed the eluting peptides directly into LTQ linear ion trap mass spectrometers equipped with a nano-LC electrospray ionization source (ThermoFinnigan). For LTQ MS runs, each full MS scan (from 400 to 1600 m/z) was followed by five MS/MS events using data-dependent acquisition where the 1st most intense ion was isolated and fragmented by

collision-induced dissociation (at 35% collision energy), followed by the 2nd to 5th most intense ions. For Orbitrap Elite MS runs, full MS spectra were recorded on the peptides over a 400 to 1,600 m/z range, followed by 10 tandem mass (MS/MS) events sequentially generated in a data-dependent manner on the first to tenth most intense ions selected from the full MS spectrum (at 35% collision energy). Dynamic exclusion was enabled for 90 sec.

Data Analysis

RAW files were extracted into ms2 file format (McDonald et al., 2004) using RAW_Xtract (J.R. Yates, Scripps Research Institute). MS/MS spectra were queried for peptide sequence information on a 157-node dual processor Beowulf Linux cluster dedicated to SEQUEST analyses (Eng, 1994). MS/MS spectra were searched without specifying differential modifications against a protein database consisting of 55508 human proteins (downloaded from NCBI on 2014-02-04), and 177 usual contaminants (such as human keratins, IgGs, and proteolytic enzymes). In addition, to estimate false discovery rates, each non-redundant protein entry was randomized. The resulting "shuffled" sequences were added to the database and searched at the same time as the "forward" sequences. To account for carboxamidomethylation by CAM, +57 Da were added statically to cysteine residues for all the searches.

Results from different runs were compared and merged using CONTRAST (Tabb et al., 2002). Spectrum/peptide matches were only retained if peptides were at least 7 amino acids long and fully tryptic. The DeltCn had to be at least 0.08, with minimum XCorrs of 1.8 for singly-, 2.5 for doubly-, and 4.5 for triply-charged spectra, and a maximum Sp rank of 10. Finally, combining all runs, proteins had to be detected by at least 2 such peptides, or 1 peptide with 2 independent spectrB. Proteins that were a subset of others were removed.

NSAF7 (Tim Wen) was used to create the final report on all detected proteins across the different runs, calculate their respective distributed Normalized Spectral Abundance Factor (dNSAF) values, and estimate false discovery rates (FDR).

Spectral FDR is calculated as:

$$\text{FDR} = \frac{2 \times \text{Shuffled Spectral Counts}}{\text{Total Spectral Counts}} \times 100$$

Protein level FDR is calculated as:

$$\text{Protein FDR} = \frac{\text{Shuffled Proteins}}{\text{Total Proteins}} \times 100$$

Under these criteria the overall FDRs at the spectra and peptide levels were less than 1%. To estimate relative protein levels, dNSAFs were calculated for each non-redundant protein, as described (Florens et al., 2006; Mosley et al., 2009; Paoletti et al., 2006; Zhang et al., 2010b; Zybailov et al., 2006). Average dNSAFs were calculated for each protein using replicates with non-zero dNSAF values. Selected average dNSAF values for proteins detected in FLAG immunoprecipitations and streptavidin affinity purifications (Figures 2.1C and 2.2C) were visualized using Multi Experiment Viewer. Enrichment of proteins in streptavidin affinity purifications from BioID-tagged stable cell lines relative to a control BioID stable cell line were calculated as the ratio of average dNSAF (ratio = avg. $\text{dNSAF}_{\text{ORF-BioID}}$: avg. $\text{dNSAF}_{\text{BioID}}$). The volcano plot in Figure 2D was generated by plotting the $\log_2$(fold enrichment) against the $-\log_{10}$(p-value), where the p-value (2-tailed Student's t-test) was generated by comparing the replicate dNSAF values of IC2-BioID to the BioID control. Mapping of dynein/dynactin subunits detected in dynein core subunit BioID datasets was performed by first calculating fold enrichment and p-values. Hits within the dynein/dynactin complex were mapped if they had either 2-3 fold or >3-fold enrichment and had p-values < 0.05 (Figure 4.3C).

To compare and contrast BioID datasets (core [Figure C.2], activating adaptor NT [Figure 4.6B], activating adaptor CT [Figure 4.6B], and combined activating adaptor NT-CT [Figure C.6]) we first sorted proteins based on enrichment and significance. Protein hits with >3-fold enrichment, p-values < 0.05 (Students two-tailed t-test), and average spectral counts > 2 from activating adaptor datasets were used for all analysis. One replicate each for NIN-BioID and HOOK3-BioID were discarded due to extremely low overall spectral counts, and one replicate for BioID-BICD1 was lost due to a faulty LC column. Hits were contrasted to generate categorized lists of hits (http://bioinformatics.psb.ugent.be/webtools/Venn/). For network analysis, we constructed protein-protein interaction networks using Cytoscape (Figure C.2, 2.6B, C.6; cytoscape.org).

For the core dynein/dynactin subunit network we contrasted 7 datasets (IC1-BioID, IC2-BioID, LIC1-BioID, LIC2-BioID, BioID-TCTEX1, BioID-RB1, and p62-BioID) to determine the proteins unique to each dataset and those shared between multiple datasets. Those shared between datasets were used to construct the network (Figure C.2).

Similarly, we constructed networks comprising the 6 N-terminal activating adaptor datasets (NT: BioID-BICD1, BioID-BICD2, BioID-HOOK1, BioID-HOOK3, BioID-NIN, BioID NINL), 6 C-terminal activating adaptor datasets (CT: BICD1-BioID, BICD2-BioID, HOOK1-BioID, HOOK3-BioID, NIN-BioID, NINL-BioID) (Figure 4.6B and Supplementary file C.4 [“NT hits” tab and “CT hits” tab]), and a combination of all 12 NT and CT datasets (Figure C.6 and Supplementary file C.4 [“NT-CT combined hits” tab]). Activating adaptor NT-specific hits (Supplementary file C.4 [“NT hits” tab, “NT Specific” columns]) were tabulated. The remaining shared hits (Supplementary file C.4 [“NT hits” tab, “NT Shared” columns]) were assigned their respective activating adaptor interactions and then used to create a network. The same process was

repeated to construct a CT-network. Activating adaptor CT-specific hits (Supplementary file C.4 [“CT hits” tab, “CT Specific” columns]) were tabulated. The remaining shared hits (Supplementary file C.4 [“CT hits” tab, “CT Shared” columns]) were assigned their respective activating adaptor interactions and then used to create a network. To construct the complete NT-CT network all 12 activating adaptor datasts were contrasted to determine the unique and shared hits for each activating adaptor NT and CT (Supplementary file C.4 [“NT-CT hits” tab, “NT Specific”, “CT Specific”, “NT Shared” and “CT Shared” columns]). Shared hits were used to construct the 12-way network. Hits used for network analysis refer to proteins with designated NCBI gene names. Predicted proteins lacking NCBI gene names were omitted from this analysis. All networks were organized using the Cytoscape “yFiles Layouts-Organic” option. Regions of the interaction map were color coded and then selected for gene ontology analysis using the “cellular component” option (GO, geneontology.org). The GO terms with p-values < 0.05 were tabulated (Supplementary file C.5).

Immunoprecipitations

For small-scale immunoprecipitations (Figures 2.1D, 2.1F, 2.3A and 2.3B) from stable cell lines, cells were split into 10 cm dishes at 40% confluence the day before harvesting. For immunoprecipitations from transiently transfected cells (Figures 2.4C and D and Figure C.3), cells were plated on 10 cm dishes at 10-15% confluence the day before transfection. Transfections were performed with Lipofectamine 2000 (Invitrogen) and 2 µg of transfection-grade DNA (Invitrogen Purelink midi prep kit) per dish in OPTI-MEM mediB. After 6 hours the media was exchanged for DMEM containing 10% FBS and 1% PenStrep. Cells were then grown for 24-48 hours before lysate preparation. For both approaches (transient or stable cell lines), cell collection, lysis, and

immunoprecipitation conditions were the same. Cells were collected by decanting the media and washing the cells off the dish with ice-cold PBS. Cells were collected by centrifugation at 1000 x g for 2 minutes, washed again with PBS, and then transferred with PBS to Eppendorf tubes for lysis. After spinning 2000 x rpm in a microcentrifuge for 1 min and removing the PBS, cells were lysed in 500 µL of either "mild" detergent buffer (all immunoprecipitations except "harsh" detergent samples in Figure 4.1D, F) ("mild" detergent buffer = 25 mM Tris-HCl, pH 8.0; 50 mM potassium acetate, 1 mM magnesium acetate, 1 mM EGTA, pH 8.0; 0.2% Triton X-100, 10% glycerol, 0.5 mM ATP, 1 mM DTT, 1X protease inhibitor cocktail (cOmplete, Roche) or a modified RIPA buffer containing high concentrations of detergent ("harsh" detergent samples, Figure 4.1D and F, "harsh" detergent buffer = 50 mM Tris-HCl, pH 8.0, 150 mM NaCl, 0.1% SDS (wt/v), 0.5% sodium deoxycholate (wt/v), 1% NP40 (v/v), 0.5 mM ATP, 1 mM DTT, 1X protease inhibitor cocktail) with gentle mixing at 4°C for 20 minutes. All lysates were centrifuged at maximum speed in a 4°C microcentrifuge for 15 minutes. The clarified lysate was retrieved and added to 50 µL packed volume of anti-FLAG M2 agarose (Sigma) and incubated for either 2 (Figures 2.3B, 2.4C and D and Figure C.3) or 16 hours (Figures 2.1D and F) at 4°C. Cells were washed four times in the appropriate lysis buffer, and elutions were performed with 50 µL of lysis buffer supplemented with 0.4 mg/mL 3×FLAG peptide.

One large scale FLAG-immunoprecipitation experiment was carried out (Figure 4.1B and C) in order to analyze the composition of dynein complexes isolated from cells expressing IC2-BioID-3×FLAG (Figure 4.1B and C). This experiment followed "mild" detergent lysis conditions described above. Four replicates of 8 x 15 cm plates were prepared from BioID-3×FLAG and IC2-BioID-3×FLAG stable cell lines. Each replicate was lysed in 10 mL "mild" detergent buffer by mixing gently at 4°C for 20 minutes. The mixture was centrifuged at 66,000 x g for 30 min in a

Type 70 Ti rotor (Beckman) at 4°C. The lysate was recovered and incubated with 250 µL packed volume anti-FLAG agarose for 16 hours at 4°C with gentle mixing. Beads were collected by centrifugation at 1000 rpm in a microcentrifuge for 2 minutes and washed 4 times with lysis buffer. Proteins were eluted with 250 µL lysis buffer containing 0.4 mg/mL 3×FLAG peptide at 4°C for 30 minutes. Eluates were precipitated with TCA as described above. MS/MS analysis was performed as described above.

We used FLAG-immunoprecipitation combined with FPLC to determine the percent incorporation of BioID-tagged subunits into their respective complexes. Cells expressing either IC2-BioID-3×FLAG or p62-BioID-3×FLAG were collected from 8 x15 cm plates as described above. Cells were lysed in 10 mL "mild" detergent lysis buffer and centrifuged as described. The lysate was added to 200 µL packed Anti-FLAG M2 Affinity Gel (Sigma-Aldrich) for 16 hours at 4°C with gentle mixing. After washing in batch twice with 50 mL "mild" detergent lysis buffer, elutions were performed with 250 µL of lysis buffer with 0.5 mg/mL 3×FLAG peptide at 4°C for 30 minutes. A Superose 6 Increase 10/300 GL was equilibrated in "mild" detergent lysis buffer containing 5 % glycerol. Molecular weight standards analyzed first, and consisted of a mixture of thyroglobulin (669 kDa), beta-amylase (200 kDa), alcohol dehydrogenase (150 kDa), albumin (66 kDa), and carbonic anhydrase (29 kDa). 200 µL of each BioID fusion protein eluate were then run separately, and 1 mL fractions were collected for each. Selected fractions were mixed with 10 µL packed Anti-FLAG M2 Affinity Gel (Sigma-Aldrich) and incubated with mixing at 4°C for 2 hours. This mixture was then centrifuged briefly, the supernatant was removed, and the resin was boiled in 2X SDS sample buffer. Released proteins were analyzed by Western blotting with anti-FLAG, anti-dynein heavy chain, and anti-p150 dynactin antibodies (see "Western analysis and antibodies, below, for details). Image intensities of bands were quantified using FIJI. Peak anti-

FLAG Western band signal intensities of the low molecular weight (= free) and high molecular weight (= incorporated) IC2- and p62-containing species were used to calculate the percent incorporation of IC2 and p62 into the dynein and dynactin complexes, respectively (Figure 4.1E and G). The percent incorporation was calculated as $intensity_{incorporated}/(intensity_{free}+ intensity_{incorporated})$. To construct the graphs in Figure 4.1E and G the intensity of each fraction was divided by the sum of the intensities for all fractions and plotted against the elution volume.

Western analysis and antibodies

Lysates and eluates were run on 4-12% polyacrylamide gels (NuPage, Invitrogen) and transferred to PVDF (Immobilon-P, Millipore) for 1.5 hours at 300 mA constant current. Blots were blocked for 10 minutes with TBST + 5% dry milk (w/v), and immunoblotted with appropriate antibodies. All antibodies were diluted in TBST + 5% milk (w/v). Primary antibodies were incubated overnight at 4°C, while secondary antibodies were incubated for 1 hour at room temperature. Antibodies used were anti-FLAG conjugated HRP (A8592, Sigma, 1:5000 dilution), rabbit anti-dynein heavy chain (R325, Santa Cruz Biotechnology, 1:500-1:1000 dilution), mouse anti-p150 dynactin (610474, BD Biosciences, 1:500-1:1000 dilution), rabbit anti-BICD2 (ab117818, Abcam, 1:5000 dilution), goat anti-rabbit HRP (sc-2030, Santa Cruz Biotechnology, 1:5000 dilution) and goat anti-mouse HRP (sc-2031, Santa Cruz Biotechnology, 1:5000 dilution). Westerns were visualized with Supersignal West Pico Chemiluminescent reagent (Thermo Fisher) and a VersaDoc imaging system (BioRad). Image intensity histograms were adjusted and images were converted to 8-bit with FIJI before being imported into Adobe Illustrator to make figures.

Secondary screen

For the secondary screen described in Figure 4.4, we pooled BioID datasets from the core dynein/dynactin subunits where at least one known activating adaptor (BICD1, BICD2, HOOK1, or HOOK3) was enriched. Proteins were selected for coiled coil analysis if they had a $dNSAF_{ORF\text{-}BioID}$:$dNSAF_{BioID}$ ratio greater than 3, were present in 3 of 4 replicates, and contained a predicted coiled coil of at least 100 aB. Predicted coiled coil sequences were extracted from UniProt; those from nuclear proteins, dynein/dynactin subunits, and a single protein that was entirely coiled coil (GOLGA4), were discarded. Each coiled coil was then codon optimized for synthesis and expression in mammalian cells, synthesized (IDT), and cloned by isothermal assembly into pcDNA5/FRT/TO as fusions with super folder (sf) GFP (e.g. pcDNA5/FRT/TO-sfGFP-CC_x-3×FLAG). A negative control was used consisting of sfGFP-3×FLAG alone, and two known activating adaptor coiled coil constructs were used as positive controls (sfGFP-BICD2 [1-422]-3×FLAG, sfGFP-HOOK3 [1-552]-3×FLAG). Transient transfections, "mild" detergent immunoprecipitations and Western blot analysis were performed as described above.

The length of expression constructs for the positive hits (NINL, daple and girdin), and NIN, a protein closely related to NINL were further optimized (Figure 4.4C and D). Although our initial girdin construct (sfGFP-girdin [1-425]-3×FLAG) immunoprecipitated dynein/dynactin, it was expressed as a truncated protein (open triangle, Figure 4.4D). Informed by a recent study of Hook proteins (both daple and girdin contain a Hook domain) (Schroeder and Vale, 2016), we made longer girdin and daple constructs (1-542 and 1-545, respectively). Since girdin was truncated, yet still produced a FLAG positive Western signal, we reasoned that GFP was proteolytically cleaved from the construct in cells. To circumvent this, we moved the sfGFP module to the C-terminus of girdin (girdin [1-542]-sfGFP-3×FLAG). This construct was not proteolyzed, as was the case with

a longer version of daple (sfGFP-daple [1-545]-3×FLAG); both constructs immunoprecipitated dynein/dynactin (Figure 4D). In our secondary screen NINL (373-702) immunoprecipitated dynein/dynactin (Figure 4—figure supplement 1A), while a construct from the closely related protein, NIN (353-580), did not. Based upon a previous report (Casenghi, 2005), we generated longer versions of NIN (1-693) and NINL (1-702); both immunoprecipitated dynein/dynactin (Figure 4.4C).

Protein purification

Dynein and dynactin were purified from stable HEK293 cell lines expressing IC2-SNAPf-3xFLAG or p62-HALO-3xFLAG, respectively. Cell lines were constructed using the FLP/FRT system (Thermo Fisher) as outlined above. Between 60-100 80% confluent, 15 cm plates were harvested per purification. Cells were collected by pipetting with ice-cold PBS and centrifuged at 1000 x g for 2 minutes to pellet. Cells were washed once more with ice-cold PBS. Cell pellets were either snap-frozen in liquid nitrogen in 50mL conical tubes or immediately lysed for protein purification. To lyse, cell pellets were resuspended in lysis buffer (25 mM HEPES pH 7.4, 50 mM KOAc, 2 mM MgOAc, 1 mM EGTA, 10% glycerol (v/v), and 1 mM DTT) supplemented with 0.2% Triton X-100, 0.5 mM Mg-ATP, and 1X protease inhibitors (Roche cOmplete Protease Inhibitor Cocktail). To ensure complete lysis, resuspended cells were slowly rotated lengthwise at 4°C for 15 min. The lysate was clarified via centrifugation at 66,000 x g for 30 min in a Type 70 Ti rotor (Beckman) at 4°C. The clarified supernatant was mixed with 0.75-1 mL of Anti-FLAG M2 Affinity Gel (Sigma-Aldrich) overnight at 4°C. During incubation, the slurry was rotated about its long axis in a full 50 mL falcon tube. Beads were collected by gravity flow and washed with 50 mL wash buffer (lysis buffer with 0.02% Triton X-100 and 0.5 mM Mg-ATP) supplemented

with protease inhibitors (Roche cOmplete Protease Inhibitor Cocktail). Beads were then washed with 50 mL high salt wash buffer (25 mM HEPES, pH 7.4, 300 mM KOAc, 2 mM MgOAc, 10% glycerol, 1mM DTT, 0.02% Triton X-100, 0.5 mM Mg-ATP, and 1X protease inhibitor (Roche cOmplete Protease Inhibitor Cocktail) and then with 100 mL wash buffer.

To label with a fluorophore the beads were resuspended in 1 mL wash buffer and incubated with either 5 μM SNAP-Cell TMR Star (New England BioLabs) (to label IC2) or 5 μM Halo-Atto647N (Promega) (to label p62) for 10 min at room temperature. Unreacted dye was removed from beads with 50-80 mL of wash buffer. Protein complexes were eluted with 0.5-1 mL of elution buffer (wash buffer with 2 mg/mL 3xFLAG peptide). Elution was collected, diluted to 2 mL in Buffer A (50 mM Tris pH 8, 2 mM MgOAc, 1 mM EGTA, and 1 mM DTT) and injected onto a MonoQ 5/50 GL column (GE Healthcare and Life Sciences) at 0.5 mL/min. The column was washed with 20 CV of Buffer A at 1 mL/min. To elute, a linear gradient was run over 40 CV into Buffer B (50 mM Tris pH 8, 2 mM MgOAc, 1 mM EGTA, 1 mM DTT, 1 M KOAc). Pure dynein complex elutes from ~60-70% Buffer B, while pure dynactin complex elutes around ~70-80% Buffer B. Peak fractions were pooled and concentrated, Mg-ATP was added to 0.1 mM and glycerol was added to 10%. Samples were then snap frozen in 2μl aliquots. .

Activating adaptors and potential activating adaptors were cloned into pet28a vectors with an N-terminal StrepII-sfGFP tag. Mouse BICD2 (mBICD2) (aa 25-400) was a gift from Rick McKenney (University of California, Davis), while NIN (aa 1-693) and NINL (aa 1-702) were sub-cloned from ORFs outlined above. All constructs were transformed into BL21-CodonPlus (DE3)-RIPL cells (Agilent). 2L of cells were grown at 37°C in LB media to a 600 nm optical density of 0.4-0.8 before the temperature was reduced to 18°C and expression was induced with 0.5 mM IPTG. After 16-18 hours, cells were harvested via centrifugation for 6 min at 4°C at 6,000

rpm in a Beckman-Coulter JLA 8.1000 fixed angle rotor. Pellets were resuspended in 30-40 mL of lysis buffer with 0.5 mM PefaBloc SC (Sigma-Aldrich) and 1mg/mL lysozyme and incubated at 4°C for 30 min. Cells were lysed via sonication (Branson Digital Sonifier) and clarified via centrifugation at 66,000 x g for 30 min in a Type 70 Ti rotor (Beckman) at 4°C. Supernatant was loaded onto a 5 mL StrepTrap column (GE Healthcare) and washed with 50-100 mL of lysis buffer. Activating adaptors were then eluted with 25-50 mL of elution buffer (lysis buffer with 3 mM d-Desthiobiotin). Finally, all activating adaptors were purified via size exclusion chromatography on either a Superdex 200 Increase 10/300 GL or a Superose 6 Increase 10/300 GL column (GE Healthcare and Life Sciences) that had been equilibrated with degassed lysis buffer. Peak fractions were collected and used for single molecule motility experiments immediately or snap-frozen in 2-20 µL aliquots. Care was taken not to concentrate the activating adaptors as we observed that this led to aggregation and inactivity.

Single-molecule motility assays and data analysis

Two types of single-molecule motility assays were performed. Owing to the presence of sfGFP on each construct from the secondary screen described above, we were able to use a TIRF-based motility assay to determine if dynein/ dynactin present in coiled coil immunoprecipitations was activated. Here, the "mild" detergent elution was imaged in a single-molecule motility assay (see "Immunoprecipitation" section above for sample preparation details). In this experiment, microtubules were labeled with HiLyte 647 tubulin (Cytoskeleton, Inc.) for visualization.

In the second type of single-molecule assay, purified ~6 nM dynein (labeled with TMR), ~60 nM dynactin (labeled with Atto-647N) and ~24-260 nM bacterially expressed and purified activating adaptor (labeled with sfGFP) were mixed together for ten minutes at 4°C before

imaging. Immediately before imaging, the dynein/ dynactin/ activating adaptor complexes were diluted 1:20-1:80 in imaging buffer (see below for composition). In this experiment, microtubules were labeled with Alexa Fluor 405 tubulin (Thermo Fisher).

Each type of single-molecule motility assay was performed in flow chambers. Biotinylated and PEGylated coverslips (Microsurfaces) were used to reduce non-specific binding. Microtubules contained ~10% biotin-tubulin for attachment to streptavidin-coated cover slip and ~10% HiLyte 647 tubulin (Cytoskeleton, Inc.) or ~10% Alexa Fluor 405 (Thermo Fisher) tubulin for visualization. The imaging buffer used consisted of lysis buffer supplemented with 0.75-1 mg/mL casein, 1 mM Mg-ATP, 71.5 mM βME (beta-mercaptoethanol) and an oxygen scavenger system (0.4% glucose, 45 μg/ml glucose catalase (Sigma-Aldrich), and 1.15 mg/ml glucose oxidase (Sigma-Aldrich)). Images were recorded every 0.5 sec for 10 min. Each individual sample was imaged no longer than 35 min.

Motility assays were performed with an inverted Nikon Ti-E Eclipse microscope equipped with 100x 1.4 N.B. oil immersion Plano Apo Nikon objective. The xy position of the stage was controlled by ProScan linear motor stage controller (Prior). The microscope was equipped with an MLC400B laser launch (Agilent) equipped with 405 nm (30 mW), 488 nm (90 mW), 561 nm (90 mW), and 640 nm (170 mW) laser lines. The excitation and emission paths were filtered using appropriate filter cubes (Chroma). The emitted signals were detected with an iXon Ultra electron multiplier CCD camera (Andor Technology). Illumination and image acquisition is controlled by NIS Elements Advanced Research software (Nikon).

The velocity of moving particles was calculated form kymographs generated in ImageJ as described (Roberts et al., 2014). For the “mild” detergent immunoprecipitation experiments, particles moving in the 488 channel (activating adaptor) were used for velocity calculations. For

the motility experiments with purified components, the 561 channel (dynein) was used for quantification of velocity. Velocities were only calculated from molecules that moved processively for greater than 5 frames. Non-motile or diffusive events were not considered in velocity calculation.

Processive events were defined as events that move uni-directionally and do not exhibit directional changes greater than 600 nm. Diffusive events were defined as events that exhibit at least one bi-directional movement greater than 600 nm in each direction. Single-molecule movements that change apparent behavior (e.g. shift from non-motile to processive) were counted as multiple events.

4.7 Acknowledgements

We thank Chris Patil, Agnieszka Kendrick, John Salogiannis, and Andres Leschziner for critical comments on the manuscript, Kyle Roux for sharing the G2 BioID plasmid ahead of publication, and Wade Harper and members of the Harper lab for scientific advice. Michael P Washburn, Laurence Florens and Selene K Swanson are supported by the Stowers Institute for Medical Research. Samara L Reck-Peterson is supported by the NIH (R01GM121772 and R01GM107214) and is a Howard Hughes Medical Institute-Simons Faculty Scholar. Morgan E DeSantis is a Jane Coffin Childs Fellow and Zaw Min Htet is supported by a NSF graduate fellowship.

Chapter 5

Concluding discussion and future directions

Dynein is a microtubule-based motor protein that transports various intracellular cargos such as organelles, membrane-bound vesicles, protein aggregates and ribonucleoprotein complexes toward microtubule minus-ends. It also carries out several important mitotic functions such as kinetochore-microtubule attachment, spindle pole focusing and spindle checkpoint silencing. Although previous structural, biochemical and biophysical studies have revealed the detailed mechanisms of how dynein uses elegant allosteric communication between its ATPase cycle and microtubule affinity to walk along microtubules, it remains unclear how dynein carries out its diverse sets of functions. The key to understanding this question is to dissect the mechanisms of how dynein's activity is altered by its essential regulators: - Lis1, dynactin and activating adaptors. In this chapter, I will summarize our findings on how dynein is regulated by Lis1, dynactin and activating adaptors and discuss future directions our insights have led to.

5.1 Multi-modal regulation of dynein by Lis1

Lis1 is an essential and ubiquitous dynein regulator and involved in almost all dynein activities. However, there is a large gap in our understanding of how Lis1 functions in cells and our mechanistic understanding of Lis1 regulation of dynein in vitro. In chapter 2 and 3, we set out to narrow this gap and uncovered multiple modes of Lis1 regulation on yeast dynein as well as human dynein. We showed that Lis1 can induce both high and low microtubule binding states of yeast dynein. In the case of human dynein, we showed that Lis1 can increase its microtubule binding and promote the formation of maximally activated dynein-dynactin-activating adaptor complexes containing two dynein dimers. The Lis1-mediated increase in the microtubule binding of both human and yeast dynein are mediated via the same conserved Lis1 binding site on dynein's AAA+ ring. However, it is still unclear whether yeast Lis1's ability to decrease dynein's microtubule

binding is conserved in the human system or if human Lis1's ability to promote the complex formation of dynein, dynactin and activating adaptors is conserved in the yeast system. There are a number of experiments that can be done to address these outstanding questions. In vitro reconstitution experiments of yeast dynein, dynactin, a candidate coiled-coil containing adaptor Num1 (Lammers and Markus, 2015) and Lis1 can be used to reveal if Lis1 can promote the complex formation of dynein, dynactin and Num1 in the yeast system. In the human system, in vitro studies of Lis1's effect on dynein's microtubule binding using mutagenesis and nucleotide analogs (as described in chapter 2) can be used to dissect if Lis1 can induce two opposing microtubule binding states of dynein.

The key question to answer next is what determines the regulatory modes of Lis1 on dynein. In order to answer this question, it is necessary to understand the mechanistic details of the multiple modes of Lis1 regulation. In chapter 2, we showed that Lis1's two opposing modes of regulation on dynein's microtubule binding was determined by two distinct Lis1 binding sites on dynein's motor domain. The stoichiometry of Lis1's β-propellers bound to these sites dictates whether Lis1 increases or decreases dynein's microtubule binding. This stoichiometry is further determined by the nucleotide state of AAA3. An important future experiment will be to dissect what controls the nucleotide state of AAA3. One possible mechanism is that cellular environments with altered local concentration of ATP or ADP can bias the nucleotide occupancy of AAA3. Photo-caged ATP or ADP could be used to directly test this hypothesis in vitro as well as in cells (Ellis-Davies, 2007). Another possible mechanism is that backward force exerted on dynein from cargos could influence the nucleotide state of AAA3. Optical trap experiments could be used to carefully characterize the nucleotide state of AAA3 against opposing pulling force on dynein.

In comparison, the mechanism of how human Lis1 promotes the formation of maximally activated dynein-dynactin-activating adaptor complexes is less clear. However, our results from chapter 3 hint at potential mechanisms. We have shown that Lis1 binds to open-dynein mutants incapable of forming the phi-conformation with higher affinity. This suggests that Lis1 binding can either release the phi-autoinhibited state or stabilize dynein in the open conformation (Figure 5.1). Although these open-dynein mutants can form more maximally activated complexes with dynactin and activating adaptors than the wild-type dynein, we have shown that Lis1 further promotes the formation of maximally activated complexes with these mutants. A previous structural study has shown that the motor domains of open-dynein mutants primarily exist in inverted orientations and that the binding of dynactin-activating adaptors reorients them into a parallel orientation (Zhang et al., 2017). Our results suggest that Lis1 may assist in the reorientation of inverted dynein motor domains of open-dynein mutants (Figure 5.1). Cryo-EM structural studies as well as single-molecule FRET-based studies of full-length dynein with Lis1 could be used to directly probe this proposed model of the Lis1-mediated release of dynein from its autoinhibited states.

One open question is where Lis1 binds human dynein to mediate its regulation. We made mutations based on our yeast dynein-Lis1 structures in chapter 3 and did not observe changes in the ability of human Lis1's ability to promote the formation of maximally activated dynein complexes. It seems likely that give the high evolutionary conservation of dynein, dynactin and Lis1 from yeast to human that these sites will be functionally conserved. Structures of the human dynein-Lis1 complex will be required to determine precisely which amino acids to mutate if the general Lis1 binding sites are indeed conserved. However, it is possible that additional Lis1 binding sites on the dynein-dynactin complex exist. For example, previous co-

immunoprecipitation and yeast two-hybrid experiments have suggested that Lis1 can interact with the tail domains and intermediate chains of dynein, and the p50 subunits of dynactin (Tai et al., 2002). Our cryo-EM structures of yeast dynein and Lis1 were solved with a truncated form of dynein lacking the tail domain or accessory chains. Therefore, the aforementioned cryo-EM structures of full-length dynein with Lis1 as well as the dynein-dynactin-activating adaptor complex with Lis1 might identify additional Lis1 binding sites. If there are additional Lis1 binding sites, these structural studies will inform mutagenesis strategies to disrupt any new Lis1 binding sites and mechanistically dissect the role of these sites in single-molecule and biochemical assays.

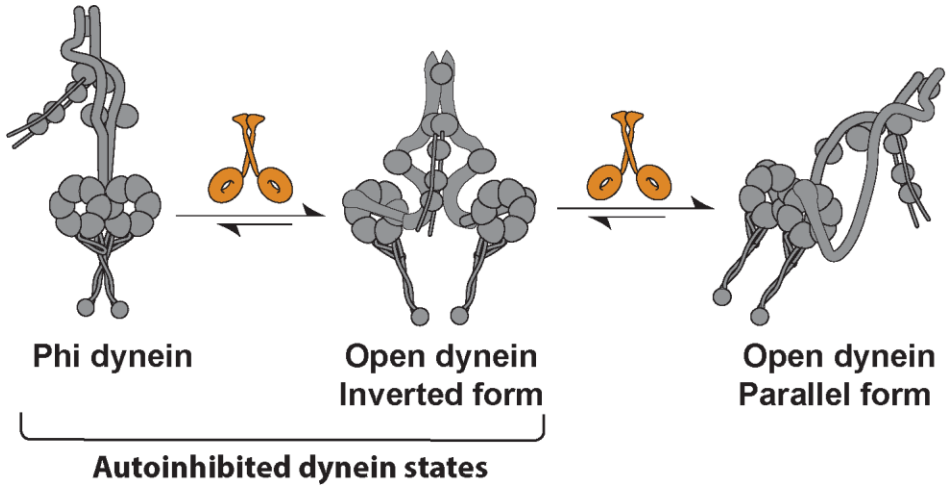

Figure 5.1. Proposed model for the Lis1-mediated release of dynein autoinhibition. Dynein exists in two autoinhibited states: phi-dynein and open-dynein. In order to be fully relieved from autoinhibition, open-dynein must reorient from an inverted form to a parallel form (Zhang et al., 2017). We propose that Lis1 binding to dynein relieves dynein from its autoinhibited states and promotes the formation of open-dynein in parallel form.

In addition to understanding the mechanistic basis of multiple modes of Lis1 regulation, it is important to determine if there are other factors that can fine-tune the regulatory modes of Lis1 regulation. Two such candidate factors are two homologs, NudE and Nudel (Bradshaw and

Hayashi, 2016; Cianfrocco et al., 2015; Kardon and Vale, 2009). They are dimeric coiled-coil containing proteins that can interact with both dynein and Lis1 (McKenney et al., 2011; Wang and Zheng, 2011; Zyłkiewicz et al., 2011). Several genetic and cell biological studies have implicated that NudE and Nudel are involved in many Lis1 regulatory roles of dynein functions (Cianfrocco et al., 2015; Kardon and Vale, 2009). They have been shown to act as a tether for Lis1 binding to dynein in vitro (Huang et al., 2011; Wang et al., 2013). In vitro reconstitution studies of dynein, dynactin, activating adaptors, Lis1 and NudE/Nudel will be required to dissect whether NudE/Nudel can dictate the regulatory modes of Lis1 on dynein. In addition, the BioID technique can be used to identify novel dynein regulators that can influence Lis1's regulatory modes. Posttranslational modifications of dynein, Lis1, NudE and Nudel could also affect the switch between Lis1 regulatory modes as well as the interplay between different dynein regulators. There have been several studies that show the effect of phosphorylation of dynein and its regulators on dynein localization and binding to its regulators (Addinall et al., 2001; Gao et al., 2015; Sapir et al., 1999; Whyte et al., 2008). Therefore, systematic studies of the role of posttranslational modifications of dynein, Lis1, NudE and Nudel will be necessary to understand the interplay between different dynein regulators.

Most importantly, our results on the multiple modes of Lis1 regulation provide new paradigms to understand the complex role of Lis1 regulation in cells. For example, in the yeast model system, Lis1 is required for transporting dynein to microtubule plus-ends by kinesin, as well as for maintaining dynein at microtubule plus-ends once it is transported (Lee et al., 2003; Li et al., 2005; Markus et al., 2009, 2011; Sheeman et al., 2003). Although the previously known function of Lis1 to increase dynein's microtubule binding can explain why it is required to keep dynein at microtubule plus ends, this function cannot be reconciled with Lis1's role in promoting

the microtubule plus-end transport of dynein by kinesin. One would expect that keeping dynein tightly bound to microtubules would be unproductive towards the goal of promoting dynein transport to microtubule plus ends by kinesin. However, the role of Lis1 in this process can be explained by our discovery of Lis1's ability to induce a weak microtubule binding state in dynein. Using CRISPR technology, dynein with mutations at different Lis1 binding sites could be introduced in cells to further probe the physiological consequences of these mutations on various dynein functions. Along with the aforementioned structural and mechanistic studies of multiple modes of Lis1 regulation, these in vivo studies will undoubtedly reveal the complex regulatory roles of Lis1 on dynein functions in cells.

5.2 Factors determining dynein's cargo specificity

In chapter 4, we set out to answer the fundamental question of what determines the cargo specificity of dynein. To do so, we determined the protein interactome of dynein in HEK293-T cells by fusing a promiscuous biotin ligase (BioID) to the components of the dynein transport machinery and determining their interacting partners using mass spectrometry. We identified new dynein activating adaptors using this approach. Dynein activating adaptors have emerged to play important dual roles in dynein-mediated transport:- (i) to activate dynein's motility by forming dynein-dynactin-activating adaptor complexes and (ii) to link these complexes to their cargos (Reck-Peterson et al., 2018). In our dynein interactome dataset, we identified previously known activating adaptors: - BICD1, BICD2, HOOK1 and HOOK3, as well as novel activating adaptors: NIN and NINL. We also identified three candidate activating adaptors: CCDC88A, CCDC88B and CCDC88C. However, we did not detect other known activating adaptors (BICDL1, BICDL2, SPDL1 and RAB11FIP3) in our dataset. Looking closely into the proteome of HEK293-T cells

used for our experiments, we found that BICDL1 and BICDL2 are not expressed and RAB11FIP3 is poorly expressed compared to the other activating adaptors. SPDL1 is expressed well in HEK293-T cells, however, it has been previously shown that SPDL1 regulates dynein during mitosis (Gassmann et al., 2010; Ying et al., 2009). These results suggest that the expression levels of dynein activating adaptors and/or the interaction between dynein and activating adaptors is tightly controlled in different cell types as well as during different cell cycle stages. Therefore, future experiments comparing the interactome of the dynein transport machinery during cellular differentiation, mitosis or in different cell types could be powerful ways to determine how dynein achieves cargo specificity and how its function is fine-tuned according to cellular needs. This should be achievable using new variants of the biotin ligase: TurboID and miniTurbo, both of which have faster kinetics requiring only a 10-minute incubation with biotin (as opposed to ~12 hours) (Branon et al., 2018).

We also identified the protein interactome of six dynein activating adaptors in HEK293-T cells and discovered that each dynein activating adaptor has many candidate cargos. This suggests that activating adaptors are the first layer for determining dynein's cargo specificity. This raises an essential question to address in order to decode the molecular rules that determine dynein's cargo recognition and specificity. What are the additional factors/adaptors that regulate dynein-cargo interactions? Our interactome of dynein activating adaptors provides a rich dataset and starting point to identify such factors. The most promising and exciting candidate hits are the AKIP and FAM160 family proteins (FAM160A1, FAM160A2, FAM160B1, FAM160B2) identified in both the HOOK1 and HOOK3 protein interactomes. The interaction between HOOK family proteins, AKTIP (FTS) and FAM160A2 (FHIP) has been previously identified and shown to link dynein to early endosomes (Guo et al., 2016; Nielsen et al., 1999; Xu et al., 2008). It is possible

that different homologs of the FAM160 family further dictate the cargo specificity of dynein activated by HOOK family activating adaptors. Proteomic, cell biological and structural studies could be used to further test this idea.

It is important to determine whether the interactions between dynein and activating adaptors are promiscuous or regulated. In the case of BICD2, the formation of dynein-dynactin-BICD2 complexes is regulated. BICD2 is autoinhibited and this autoinhibition is relieved upon the binding of the cargo adaptors, Rab6 (Hoogenraad et al., 2001, 2003; Huynh and Vale, 2017). BICDL1, on the other hand, doesn't seem to be autoinhibited and is able to bind dynein-dynactin complexes and activate dynein motility in the absence of other cargo adaptors (Urnavicius et al., 2018). This suggests that the activities of different dynein activating adaptors are different and perhaps optimized for diverse sets of dynein functions. In the future, it will be essential to dissect if other dynein activating adaptors are autoinhibited using biochemical and single-molecule assays. In chapter 3, we have also shown that Lis1 promotes the complex formation of dynein, dynactin and a truncated form of BICD2. Is this regulatory effect of Lis1 on the interaction between dynein, dynactin and an activating adaptor universal regardless of the identity of activating adaptors or the presence of additional cargo adaptors such as Rab6? Do other dynein regulators such as NudE and Nudel have effects on the complex formation of dynein, dynactin and activating adaptors? In vitro reconstitution experiments will be able to answer these questions. Finally, posttranslational modifications could affect the interactions between dynein and activating adaptors and more sensitive mass spectrometry analysis will be require to determine the posttranslational modification states of the dynein transport machinery.

5.3 Interplay between opposite-polarity motors

My thesis has primarily focused on the regulation of dynein to carry out its diverse functions. However, in cells, many cargos are associated with both dynein and kinesin, and exhibit bidirectional motility along microtubules (Egan et al., 2012; Hendricks et al., 2010; Schlager et al., 2010). In agreement with these findings, we identified several kinesins as the potential interacting partners of all six dynein activating adaptors in chapter 4. This result was particularly striking in the HOOK1 and HOOK3 datasets, where we observed an enrichment of GO terms related to kinesin motors. We showed that HOOK3 could interact with the kinesin-3 family member, KIF1C, via its carboxy-terminus in addition to its interaction with dynein-dynactin on its amino-terminus. In addition, it has been shown that BICD2 interacts with kinesin-1 (Grigoriev et al., 2007) and BICDL1 with KIF1C (Schlager et al., 2010). Taken together, these results suggest that some activating adaptors can interact with both dynein and kinesin and raise several interesting questions. Can activating adaptors facilitate the simultaneous binding of dynein and dynactin? If so, which factors dictate the directionality of the movement of dynein-kinesin complexes? If not, which factors regulate the binding of dynein or kinesin to activating adaptors? To answer these questions, in vitro reconstitutions with purified dyneins, kinesins and activating adaptors will be necessary. In addition, we have shown that Lis1 promotes the association of dynein, dynactin and BICD2 in chapter 3. Given that BICD2 can also interact with kinesin-1, does Lis1 bias the binding of dynein to BICD2 over kinesin? Does Lis1 affect the binding of dynein to other activating adaptors over kinesin? In vitro reconstitution experiments of dynein, dynactin, activating adaptors and kinesins could directly answer these questions.

The two opposing modes of Lis1 regulation on dynein's microtubule binding shown in chapter 2 could differentially regulate the directionality of the dynein-kinesin complexes according

to cellular needs. We have demonstrated such effects in the context of recycling dynein to microtubule plus ends by kinesin in the yeast system. Our lab showed that in the presence of Lis1 and two microtubule plus-end proteins (CLIP170 and EB1), dynein is transiently transported to the microtubule plus ends by kinesin (Roberts et al., 2014). During this transport, Lis1 and CLIP170 couple the opposite-polarity motors, dynein and kinesin. CLIP170 and EB1 together increase the processivity of kinesin to overcome dynein's minus-end-directed motility. In chapter 2, we showed that the novel Lis1 binding site, which mediates the weak microtubule binding state of dynein, is required for this kinesin-mediated plus-end transport of dynein in yeast system. It has been shown that kinesin transports dynein to microtubule plus ends in filamentous fungi (Zhang et al., 2010a) and mammalian neurons (Twelvetrees et al., 2016). Future cellular imaging experiments could be used to determine if this novel regulatory mode of Lis1 we discovered in the yeast system is used in filamentous fungi and mammalian neurons for kinesin-driven transport of dynein to microtubule plus ends.

5.4 Concluding remarks

In summary, the results I presented in this thesis highlight that dynein regulation is incredibly sophisticated and provide novel insights towards a molecular understanding of how dynein is tightly regulated to perform its diverse set of functions. Our findings of the multi-modal regulation of dynein by Lis1 provide novel paradigms to further explore how Lis1 can fine-tune dynein activity in response to cellular needs. The rich protein interactome of the dynein transport machinery we identified provides a major resource to bridge the disconnect between our mechanistic understanding of how dynein walks along microtubules and our knowledge of dynein's diverse functions in cells.

References

Adames, N.R., and Cooper, J.A. (2000). Microtubule interactions with the cell cortex causing nuclear movements in Saccharomyces cerevisiae. J. Cell Biol. *149*, 863–874.

Addinall, S.G., Mayr, P.S., Doyle, S., Sheehan, J.K., Woodman, P.G., and Allan, V.J. (2001). Phosphorylation by cdc2-CyclinB1 Kinase Releases Cytoplasmic Dynein from Membranes. J. Biol. Chem. *276*, 15939–15944.

Amos, L.A. (1989). Brain dynein crossbridges microtubules into bundles. J. Cell Sci. *93*, 19–28.

Apweiler, R., Bairoch, A., Wu, C.H., Barker, W.C., Boeckmann, B., Ferro, S., Gasteiger, E., Huang, H., Lopez, R., Magrane, M., et al. (2017). UniProt: The universal protein knowledgebase. Nucleic Acids Res. *45*, D158–D169.

Aznar, N., Midde, K.K., Dunkel, Y., Lopez-Sanchez, I., Pavlova, Y., Marivin, A., Barbazán, J., Murray, F., Nitsche, U., Janssen, K.P., et al. (2015). Daple is a novel non-receptor GEF required for trimeric G protein activation in Wnt signaling. Elife *4*.

Aznar, N., Kalogriopoulos, N., Midde, K.K., and Ghosh, P. (2016). Heterotrimeric G protein signaling via GIV/Girdin: Breaking the rules of engagement, space, and time. BioEssays *38*, 379–393.

Bachmann-Gagescu, R., Dona, M., Hetterschijt, L., Tonnaer, E., Peters, T., de Vrieze, E., Mans, D.A., van Beersum, S.E.C., Phelps, I.G., Arts, H.H., et al. (2015). The Ciliopathy Protein CC2D2A Associates with NINL and Functions in RAB8-MICAL3-Regulated Vesicle Trafficking. PLoS Genet. *11*.

Baumbach, J., Murthy, A., McClintock, M.A., Dix, C.I., Zalyte, R., Hoang, H.T., and Bullock, S.L. (2017). Lissencephaly-1 is a context-dependent regulator of the human dynein complex. Elife *6*, 1–31.

Belyy, V., Schlager, M.A., Foster, H., Reimer, A.E., Carter, A.P., and Yildiz, A. (2016). The mammalian dynein–dynactin complex is a strong opponent to kinesin in a tug-of-war competition. Nat. Cell Biol.

Bhabha, G., Cheng, H.-C., Zhang, N., Moeller, A., Liao, M., Speir, J. a., Cheng, Y., and Vale, R.D. (2014). Allosteric Communication in the Dynein Motor Domain. Cell *159*, 857–868.

Biasini, M., Bienert, S., Waterhouse, A., Arnold, K., Studer, G., Schmidt, T., Kiefer, F., Cassarino, T.G., Bertoni, M., Bordoli, L., et al. (2014). SWISS-MODEL: Modelling protein tertiary and quaternary structure using evolutionary information. Nucleic Acids Res. *42*.

Bielska, E., Schuster, M., Roger, Y., Berepiki, A., Soanes, D.M., Talbot, N.J., and Steinberg, G. (2014). Hook is an adapter that coordinates kinesin-3 and dynein cargo attachment on early endosomes. J. Cell Biol. *204*, 989–1007.

Blake, J.A., Christie, K.R., Dolan, M.E., Drabkin, H.J., Hill, D.P., Ni, L., Sitnikov, D., Burgess, S., Buza, T., Gresham, C., et al. (2015). Gene ontology consortium: Going forward. Nucleic Acids Res. *43*, D1049–D1056.

Bradshaw, N.J., and Hayashi, M.A.F. (2016). NDE1 and NDEL1 from genes to (mal)functions: parallel but distinct roles impacting on neurodevelopmental disorders and psychiatric illness. Cell. Mol. Life Sci. 1–20.

Branon, T.C., Bosch, J.A., Sanchez, A.D., Udeshi, N.D., Svinkina, T., Carr, S.A., Feldman, J.L., Perrimon, N., and Ting, A.Y. (2018). Efficient proximity labeling in living cells and organisms with TurboID. Nat. Biotechnol. *36*, 880–898.

Bullock, S.L., and Ish-Horowicz, D. (2001). Conserved signals and machinery for RNA transport in Drosophila oogenesis and embryogenesis. Nature *414*, 611–616.

Burgess, S.A., Walker, M.L., Sakakibara, H., Knight, P.J., and Oiwa, K. (2003). Dynein structure and power stroke. Nature *421*, 715–718.

Carter, a. P., Garbarino, J.E., Wilson-Kubalek, E.M., Shipley, W.E., Cho, C., Milligan, R. a., Vale, R.D., and Gibbons, I.R. (2008). Structure and Functional Role of Dynein's Microtubule-Binding Domain. Science *322*, 1691–1695.

Carter, A.P., Cho, C., Jin, L., and Vale, R.D. (2011). Crystal structure of the dynein motor domain. Science *331*, 1159–1165.

Carter, A.P., Diamant, A.G., and Urnavicius, L. (2016). How dynein and dynactin transport cargos: a structural perspective. Curr. Opin. Struct. Biol. *37*, 62–70.

Carvalho, P., Gupta, M.L., Hoyt, M.A., and Pellman, D. (2004). Cell cycle control of kinesin-mediated transport of Bik1 (CLIP-170) regulates microtubule stability and dynein activation. Dev. Cell *6*, 815–829.

Case, R.B., Pierce, D.W., Hom-Booher, N., Hart, C.L., and Vale, R.D. (1997). The directional preference of kinesin motors is specified by an element outside of the motor catalytic domain. Cell *90*, 959–966.

Casenghi, M. (2005). Phosphorylation of Nlp by Plk1 negatively regulates its dynein-dynactin-dependent targeting to the centrosome. J. Cell Sci. *118*, 5101–5108.

Casenghi, M., Meraldi, P., Weinhart, U., Duncan, P.I., Körner, R., and Nigg, E.A. (2003). Polo-like kinase 1 regulates Nlp, a centrosome protein involved in microtubule nucleation. Dev. Cell *5*, 113–125.

Caudron, F., Andrieux, A., Job, D., and Boscheron, C. (2008). A new role for kinesin-directed transport of Bik1p (CLIP-170) in Saccharomyces cerevisiae. J. Cell Sci. *121*, 1506–1513.

Cho, C., Reck-Peterson, S.L., and Vale, R.D. (2008). Regulatory ATPase sites of cytoplasmic dynein affect processivity and force generation. J. Biol. Chem. *283*, 25839–25845.

Chowdary, P.D., Kaplan, L., Che, D.L., and Cui, B. (2018). Dynamic Clustering of Dyneins on Axonal Endosomes: Evidence from High-Speed Darkfield Imaging. Biophys. J. 1–12.

Chowdhury, S., Ketcham, S.A., Schroer, T.A., and Lander, G.C. (2015). Structural organization of the dynein–dynactin complex bound to microtubules. Nat. Struct. Mol. Biol. *22*, 345–347.

Cianfrocco, M.A., and Leschziner, A.E. (2015). Low cost, high performance processing of single particle cryo-electron microscopy data in the cloud. Elife *4*, 1–10.

Cianfrocco, M. a., DeSantis, M.E., Leschziner, A.E., and Reck-Peterson, S.L. (2015). Mechanism and Regulation of Cytoplasmic Dynein. Annu. Rev. Cell Dev. Biol. *31*, annurev-cellbio-100814-125438.

Cleary, F.B., Dewitt, M. a, Bilyard, T., Htet, Z.M., Belyy, V., Chan, D.D., Chang, A.Y., and Yildiz, A. (2014). Tension on the linker gates the ATP-dependent release of dynein from microtubules. Nat. Commun. *5*, 4587.

Cockell, M.M. (2004). lis-1 is required for dynein-dependent cell division processes in C. elegans embryos. J. Cell Sci. *117*, 4571–4582.

Delgehyr, N., Sillibourne, J., and Bornens, M. (2005). Microtubule nucleation and anchoring at the centrosome are independent processes linked by ninein function. J. Cell Sci. *118*, 1565–1575.

DeSantis, M.E., Cianfrocco, M.A., Htet, Z.M., Tran, P.T., Reck-Peterson, S.L., and Leschziner, A.E. (2017). Lis1 Has Two Opposing Modes of Regulating Cytoplasmic Dynein. Cell *170*, 1197–1208.e12.

DeWitt, M.A., Chang, A.Y., Combs, P.A., and Yildiz, A. (2012). Cytoplasmic Dynein Moves Through Uncoordinated Stepping of the AAA+ Ring Domains. Science *335*, 221–225.

DeWitt, M.A., Cypranowska, C.A., Cleary, F.B., Belyy, V., and Yildiz, A. (2014). The AAA3 domain of cytoplasmic dynein acts as a switch to facilitate microtubule release. Nat. Struct. Mol. Biol. *22*, 73–80.

DeWitt, M.A., Cypranowska, C.A., Cleary, F.B., Belyy, V., and Yildiz, A. (2015). The AAA3 domain of cytoplasmic dynein acts as a switch to facilitate microtubule release. Nat. Struct. Mol. Biol. *22*, 73–80.

Dienstbier, M., Boehl, F., Li, X., and Bullock, S.L. (2009). Egalitarian is a selective RNA-binding protein linking mRNA localization signals to the dynein motor. Genes Dev. *23*, 1546–1558.

Dix, C.I., Soundararajan, H.C., Dzhindzhev, N.S., Begum, F., Suter, B., Ohkura, H., Stephens, E., and Bullock, S.L. (2013). Lissencephaly-1 promotes the recruitment of dynein and dynactin to transported mRNAs. J. Cell Biol. *202*, 479–494.

Dixit, R., Levy, J.R., Tokito, M., Ligon, L.A., and Holzbaur, E.L.F. (2008). Regulation of dynactin through the differential expression of p150 Glued isoforms. J. Biol. Chem. *283*, 33611–33619.

Dona, M., Bachmann-Gagescu, R., Texier, Y., Toedt, G., Hetterschijt, L., Tonnaer, E.L., Peters, T.A., van Beersum, S.E.C., Bergboer, J.G.M., Horn, N., et al. (2015). NINL and DZANK1 Co-function in Vesicle Transport and Are Essential for Photoreceptor Development in Zebrafish. PLoS Genet. *11*.

Dong, J.M., Tay, F.P.L., Swa, H.L.F., Gunaratne, J., Leung, T., Burke, B., and Manser, E. (2016). Proximity biotinylation provides insight into the molecular composition of focal adhesions at the nanometer scale. Sci. Signal. *9*.

Egan, M.J., Tan, K., and Reck-Peterson, S.L. (2012). Lis1 is an initiation factor for dynein-driven organelle transport. J. Cell Biol. *197*, 971–982.

Ellis-Davies, G.C.R. (2007). Caged compounds: Photorelease technology for control of cellular chemistry and physiology. Nat. Methods *4*, 619–628.

Eng, J. (1994). An approach to correlate tandem mass spectral data of peptides with amino acid sequences in a protein database. J. Am. Soc. Mass Spectrom. *5*, 976–989.

Eshel, D., Urrestarazu, L.A., Vissers, S., Jauniaux, J.C., van Vliet-Reedijk, J.C., Planta, R.J., and Gibbons, I.R. (1993). Cytoplasmic dynein is required for normal nuclear segregation in yeast. Proc. Natl. Acad. Sci. *90*, 11172–11176.

Florens, L., and Washburn, M.P. (2006). Proteomic analysis by multidimensional protein identification technology. Methods Mol. Biol. *328*, 159–175.

Florens, L., Carozza, M.J., Swanson, S.K., Fournier, M., Coleman, M.K., Workman, J.L., and Washburn, M.P. (2006). Analyzing chromatin remodeling complexes using shotgun proteomics and normalized spectral abundance factors. Methods *40*, 303–311.

Franker, M.A.M., and Hoogenraad, C.C. (2013). Microtubule-based transport - basic mechanisms, traffic rules and role in neurological pathogenesis. J. Cell Sci. *126*, 2319–2329.

Gama, J.B., Pereira, C., Simões, P.A., Celestino, R., Reis, R.M., Barbosa, D.J., Pires, H.R., Carvalho, C., Amorim, J., Carvalho, A.X., et al. (2017). Molecular mechanism of dynein recruitment to kinetochores by the Rod – Zw10 – Zwilch complex and Spindly.

Gao, F.J., Hebbar, S., Gao, X. a., Alexander, M., Pandey, J.P., Walla, M.D., Cotham, W.E., King, S.J., and Smith, D.S. (2015). GSK-3β phosphorylation of cytoplasmic dynein reduces Ndel1 binding to intermediate chains and alters dynein motility. Traffic n/a-n/a.

García-Mata, R., Bebök, Z., Sorscher, E.J., and Sztul, E.S. (1999). Characterization and dynamics of aggresome formation by a cytosolic GFP- chimera. J. Cell Biol. *146*, 1239–1254.

Gassmann, R., Holland, A.J., Varma, D., Wan, X., Çivril, F., Cleveland, D.W., Oegema, K., Salmon, E.D., and Desai, A. (2010). Removal of Spindly from microtubule-attached kinetochores controls spindle checkpoint silencing in human cells. Genes Dev. *24*, 957–971.

Gee, M.A., Heuser, J.E., and Vallee, R.B. (1997). An extended microtubule-binding structure within the dynein motor domain. Nature *390*, 636–639.

Gibbons, I.R., Garbarino, J.E., Tan, C.E., Reck-Peterson, S.L., Vale, R.D., and Carter, A.P. (2005). The affinity of the dynein microtubule-binding domain is modulated by the conformation of its coiled-coil stalk. J. Biol. Chem. *280*, 23960–23965.

Gill, S.R., Schroer, T. a., Szilak, I., Steuer, E.R., Sheetz, M.P., and Cleveland, D.W. (1991). Dynactin, a conserved, ubiquitously expressed component of an activator of vesicle motility mediated by cytoplasmic dynein. J. Cell Biol. *115*, 1639–1650.

Gleave, E.S., Schmidt, H., and Carter, A.P. (2014). A structural analysis of the AAA+ domains in Saccharomyces cerevisiae cytoplasmic dynein. J. Struct. Biol. *186*, 367–375.

Grigoriev, I., Splinter, D., Keijzer, N., Wulf, P.S., Demmers, J., Ohtsuka, T., Modesti, M., Maly, I. V., Grosveld, F., Hoogenraad, C.C., et al. (2007). Rab6 Regulates Transport and Targeting of Exocytotic Carriers. Dev. Cell *13*, 305–314.

Grotjahn, D.A., Chowdhury, S., Xu, Y., McKenney, R.J., Schroer, T.A., and Lander, G.C. (2018). Cryo-electron tomography reveals that dynactin recruits a team of dyneins for processive

motility. Nat. Struct. Mol. Biol. *25*, 203–207.

Guo, X., Farías, G.G., Mattera, R., and Bonifacino, J.S. (2016). Rab5 and its effector FHF contribute to neuronal polarity through dynein-dependent retrieval of somatodendritic proteins from the axon. Proc. Natl. Acad. Sci. *113*, E5318–E5327.

Gupta, G.D., Coyaud, É., Gonçalves, J., Mojarad, B.A., Liu, Y., Wu, Q., Gheiratmand, L., Comartin, D., Tkach, J.M., Cheung, S.W.T., et al. (2015). A Dynamic Protein Interaction Landscape of the Human Centrosome-Cilium Interface. Cell *163*, 1483–1499.

Gutierrez, P.A., Ackermann, B.E., Vershinin, M., and McKenney, R.J. (2017). Differential effects of the dynein-regulatory factor Lissencephaly-1 on processive dynein-dynactin motility. J. Biol. Chem. *292*, 12245–12255.

Ham, H., Huynh, W., Schoon, R.A., Vale, R.D., and Billadeau, D.D. (2015). HkRP3 Is a Microtubule-Binding Protein Regulating Lytic Granule Clustering and NK Cell Killing. J. Immunol. *194*, 3984–3996.

Hendricks, A.G., Perlson, E., Ross, J.L., Schroeder, H.W., Tokito, M., and Holzbaur, E.L.F. (2010). Motor Coordination via a Tug-of-War Mechanism Drives Bidirectional Vesicle Transport. Curr. Biol. *20*, 697–702.

Heymann, J.B., and Belnap, D.M. (2007). Bsoft: Image processing and molecular modeling for electron microscopy. J. Struct. Biol. *157*, 3–18.

Hirokawa, N. (1998). Kinesin and dynein superfamily proteins and the mechanism of organelle transport. Science *279*, 519–526.

Hirokawa, N., Sato-Yoshitake, R., Yoshida, T., and Kawashima, T. (1990). Brain dynein (MAP1C) localizes on both anterogradely and retrogradely transported membranous organelles in vivo. J. Cell Biol. *111*, 1027–1037.

Hirokawa, N., Noda, Y., Tanaka, Y., and Niwa, S. (2009). Kinesin superfamily motor proteins and intracellular transport. Nat. Rev. Mol. Cell Biol. *10*, 682–696.

Hoogenraad, C.C., and Akhmanova, A. (2016). Bicaudal D Family of Motor Adaptors: Linking Dynein Motility to Cargo Binding. Trends Cell Biol. *xx*, 1–14.

Hoogenraad, C.C., Akhmanova, A., Howell, S. a., Dortland, B.R., De Zeeuw, C.I., Willemsen, R., Visser, P., Grosveld, F., and Galjart, N. (2001). Mammalian golgi-associated Bicaudal-D2 functions in the dynein-dynactin pathway by interacting with these complexes. EMBO J. *20*, 4041–4054.

Hoogenraad, C.C., Wulf, P., Schiefermeier, N., Stepanova, T., Galjart, N., Small, J.V., Grosveld, F., De Zeeuw, C.I., and Akhmanova, A. (2003). Bicaudal D induces selective dynein-mediated microtubule minus end-directed transport. EMBO J. *22*, 6004–6015.

Horgan, C.P., Hanscom, S.R., Jolly, R.S., Futter, C.E., and McCaffrey, M.W. (2010). Rab11-FIP3 links the Rab11 GTPase and cytoplasmic dynein to mediate transport to the endosomal-recycling compartment. J. Cell Sci. *123*, 181–191.

Huang, F., Sirinakis, G., Allgeyer, E.S., Schroeder, L.K., Duim, W.C., Kromann, E.B., Phan, T.,

Rivera-Molina, F.E., Myers, J.R., Irnov, I., et al. (2011). Ultra-High Resolution 3D Imaging of Whole Cells. Cell *0*, 353–359.

Huang, J., Roberts, A.J., Leschziner, A.E., and Reck-Peterson, S.L. (2012). Lis1 acts as a "clutch" between the ATPase and microtubule-binding domains of the dynein motor. Cell *150*, 975–986.

Huttlin, E.L., Ting, L., Bruckner, R.J., Gebreab, F., Gygi, M.P., Szpyt, J., Tam, S., Zarraga, G., Colby, G., Baltier, K., et al. (2015). The BioPlex Network: A Systematic Exploration of the Human Interactome. Cell *162*, 425–440.

Huynh, W., and Vale, R.D. (2017). Disease-associated mutations in human BICD2 hyperactivate motility of dynein-dynactin. J. Cell Biol. *216*, 3051–3060.

Hyman, A., and Karsenti, E. (1998). The role of nucleation in patterning microtubule networks. J Cell Sci *111 (Pt 1*, 2077–2083.

Imamula, K., Kon, T., Ohkura, R., and Sutoh, K. (2007). The coordination of cyclic microtubule association/dissociation and tail swing of cytoplasmic dynein. Proc. Natl. Acad. Sci. U. S. A. *104*, 16134–16139.

Jha, R., Roostalu, J., Cade, N.I., Trokter, M., and Surrey, T. (2017). Combinatorial regulation of the balance between dynein microtubule end accumulation and initiation of directed motility. EMBO J. *36*, 3387–3404.

Johnston, J.A., Illing, M.E., and Kopito, R.R. (2002). Cytoplasmic dynein/dynactin mediates the assembly of aggresomes. Cell Motil. Cytoskeleton *53*, 26–38.

Kanai, Y., Dohmae, N., and Hirokawa, N. (2004). Kinesin transports RNA: Isolation and characterization of an RNA-transporting granule. Neuron *43*, 513–525.

Kardon, J.R., and Vale, R.D. (2009). Regulators of the cytoplasmic dynein motor. Nat. Rev. Mol. Cell Biol. *10*, 854–865.

Karki, S., and Holzbaur, E.L.F. (1995). Affinity chromatography demonstrates a direct binding between cytoplasmic dynein and the dynactin complex. J. Biol. Chem. *270*, 28806–28811.

Kim, D.I., KC, B., Zhu, W., Motamedchaboki, K., Doye, V., and Roux, K.J. (2014). Probing nuclear pore complex architecture with proximity-dependent biotinylation. Proc. Natl. Acad. Sci. *111*, E2453–E2461.

Kim, D.I., Jensen, S.C., and Roux, K.J. (2016a). Identifying protein-protein associations at the nuclear envelope with bioid. In Methods in Molecular Biology, pp. 133–146.

Kim, D.I., Jensen, S.C., Noble, K.A., KC, B., Roux, K.H., Motamedchaboki, K., and Roux, K.J. (2016b). An improved smaller biotin ligase for BioID proximity labeling. Mol. Biol. Cell *27*, 1188–1196.

Kim, H., Ling, S.C., Rogers, G.C., Kural, C., Selvin, P.R., Rogers, S.L., and Gelfand, V.I. (2007). Microtubule binding by dynactin is required for microtubule organization but not cargo transport. J. Cell Biol. *176*, 641–651.

Kim, M.H., Cooper, D.R., Oleksy, A., Devedjiev, Y., Derewenda, U., Reiner, O., Otlewski, J.,

and Derewenda, Z.S. (2004). The structure of the N-terminal domain of the product of the lissencephaly gene Lis1 and its functional implications. Structure *12*, 987–998.

Kimanius, D., Forsberg, B.O., Scheres, S.H.W., and Lindahl, E. (2016). Accelerated cryo-EM structure determination with parallelisation using GPUs in RELION-2. Elife *5*.

King, S.J., and Schroer, T.A. (2000). Dynactin increases the processivity of the cytoplasmic dynein motor. Nat. Cell Biol. *2*, 20–24.

King, S.J., Brown, C.L., Maier, K.C., Quintyne, N.J., and Schroer, T.A. (2004). Analysis of the Dynein–Dynactin Interaction In Vitro and In Vivo. Mol. Biol. Cell *15*, 3751–3737.

Klinman, E., and Holzbaur, E.L.F. (2015). Stress-Induced CDK5 Activation Disrupts Axonal Transport via Lis1/Ndel1/Dynein. Cell Rep. *12*, 1–12.

Kon, T., Nishiura, M., Ohkura, R., Toyoshima, Y.Y., and Sutoh, K. (2004). Distinct functions of nucleotide-binding/hydrolysis sites in the four AAA modules of cytoplasmic dynein. Biochem. *43*, 11266–11274.

Kon, T., Mogami, T., Ohkura, R., Nishiura, M., and Sutoh, K. (2005). ATP hydrolysis cycle-dependent tail motions in cytoplasmic dynein. Nat. Struct. Mol. Biol. *12*, 513–519.

Kon, T., Imamula, K., Roberts, A.J., Ohkura, R., Knight, P.J., Gibbons, I.R., Burgess, S. a, and Sutoh, K. (2009). Helix sliding in the stalk coiled coil of dynein couples ATPase and microtubule binding. Nat. Struct. Mol. Biol. *16*, 325–333.

Kon, T., Sutoh, K., and Kurisu, G. (2011). X-ray structure of a functional full-length dynein motor domain. Nat. Struct. Mol. Biol. *18*, 638–642.

Kon, T., Oyama, T., Shimo-Kon, R., Imamula, K., Shima, T., Sutoh, K., and Kurisu, G. (2012). The 2.8 Å crystal structure of the dynein motor domain. Nature *484*, 345–350.

Lacey, M.L., and Haimo, L.T. (1992). Cytoplasmic dynein is a vesicle protein. J. Biol. Chem. *267*, 4793–4798.

Lammers, L.G., and Markus, S.M. (2015). The dynein cortical anchor Num1 activates dynein motility by relieving Pac1/LIS1-mediated inhibition. J. Cell Biol. 1–22.

Lander, G.C., Stagg, S.M., Voss, N.R., Cheng, A., Fellmann, D., Pulokas, J., Yoshioka, C., Irving, C., Mulder, A., Lau, P.W., et al. (2009). Appion: An integrated, database-driven pipeline to facilitate EM image processing. J. Struct. Biol. *166*, 95–102.

Lee, I.G., Olenick, M.A., Boczkowska, M., Franzini-Armstrong, C., Holzbaur, E.L.F., and Dominguez, R. (2018). A conserved interaction of the dynein light intermediate chain with dynein-dynactin effectors necessary for processivity. Nat. Commun. *9*.

Lee, W.L., Oberle, J.R., and Cooper, J.A. (2003). The role of the lissencephaly protein Pac1 during nuclear migration in budding yeast. J. Cell Biol. *160*, 355–364.

Lenz, J.H., Schuchardt, I., Straube, A., and Steinberg, G. (2006). A dynein loading zone for retrograde endosome motility at microtubule plus-ends. EMBO J. *25*, 2275–2286.

Li, J., Lee, W.-L., and Cooper, J. a (2005). NudEL targets dynein to microtubule ends through

LIS1. Nat. Cell Biol. *7*, 686–690.

Li, W., Cowley, A., Uludag, M., Gur, T., McWilliam, H., Squizzato, S., Park, Y.M., Buso, N., and Lopez, R. (2015). The EMBL-EBI bioinformatics web and programmatic tools framework. Nucleic Acids Res. *43*, W580–W584.

Li, X., Mooney, P., Zheng, S., Booth, C.R., Braunfeld, M.B., Gubbens, S., Agard, D.A., and Cheng, Y. (2013). Electron counting and beam-induced motion correction enable near-atomic-resolution single-particle cryo-EM. Nat. Methods *10*, 584–590.

Li, Y.Y., Yeh, E., Hays, T., and Bloom, K. (1993). Disruption of mitotic spindle orientation in a yeast dynein mutant. Proc. Natl. Acad. Sci. *90*, 10096–10100.

Ligon, L.A., Karki, S., Tokito, M., and Holzbaur, E.L.F. (2001). Dynein binds to β-catenin and may tether microtubules at adherens junctions. Nat. Cell Biol. *3*, 913–917.

Lipka, J., Kuijpers, M., Jaworski, J., and Hoogenraad, C.C. (2013). Mutations in cytoplasmic dynein and its regulators cause malformations of cortical development and neurodegenerative diseases. Biochem. Soc. Trans. *41*, 1605–1612.

Liu, Y., Salter, H.K., Holding, A.N., Johnson, C.M., Stephens, E., Lukavsky, P.J., Walshaw, J., and Bullock, S.L. (2013). Bicaudal-D uses a parallel, homodimericcoiled coil with heterotypic registry tocoordinate recruitment of cargos to dynein. Genes Dev. *27*, 1233–1246.

Mallik, R., Carter, B.C., Lex, S.A., King, S.J., and Gross, S.P. (2004). Cytoplasmic dynein functions as a gear in response to load. Nature *427*, 649–652.

Markus, S.M., and Lee, W.L. (2011). Regulated offloading of cytoplasmic dynein from microtubule plus ends to the cortex. Dev. Cell *20*, 639–651.

Markus, S.M., Punch, J.J., and Lee, W.L. (2009). Motor- and Tail-Dependent Targeting of Dynein to Microtubule Plus Ends and the Cell Cortex. Curr. Biol. *19*, 196–205.

Markus, S.M., Plevock, K.M., St. Germain, B.J., Punch, J.J., Meaden, C.W., and Lee, W.L. (2011). Quantitative analysis of Pac1/LIS1-mediated dynein targeting: Implications for regulation of dynein activity in budding yeast. Cytoskeleton *68*, 157–174.

Matanis, T., Akhmanova, A., Wulf, P., Del Nery, E., Weide, T., Stepanova, T., Galjart, N., Grosveld, F., Goud, B., De Zeeuw, C.I., et al. (2002). Bicaudal-D regulates COPI-independent Golgi-ER transport by recruiting the dynein-dynactin motor complex. Nat. Cell Biol. *4*, 986–992.

McClintock, M.A., Dix, C.I., Johnson, C.M., McLaughlin, S.H., Maizels, R.J., Hoang, H.T., and Bullock, S.L. (2018). RNA-directed activation of cytoplasmic dynein-1 in reconstituted transport RNPs. BioRxiv 273912.

McDonald, W.H., Tabb, D.L., Sadygov, R.G., MacCoss, M.J., Venable, J., Graumann, J., Johnson, J.R., Cociorva, D., and Yates, J.R. (2004). MS1, MS2, and SQT - Three unified, compact, and easily parsed file formats for the storage of shotgun proteomic spectra and identifications. Rapid Commun. Mass Spectrom. *18*, 2162–2168.

McKenney, R.J., Vershinin, M., Kunwar, A., Vallee, R.B., and Gross, S.P. (2010). LIS1 and NudE induce a persistent dynein force-producing state. Cell *141*, 304–314.

McKenney, R.J., Weil, S.J., Scherer, J., and Vallee, R.B. (2011). Mutually exclusive cytoplasmic dynein regulation by NudE-Lis1 and dynactin. J. Biol. Chem. *286*, 39615–39622.

McKenney, R.J., Huynh, W., Tanenbaum, M.E., Bhabha, G., and Vale, R.D. (2014). Activation of cytoplasmic dynein motility by dynactin-cargo adapter complexes. Science *345*, 337–341.

Mitchison, T., and Kirschner, M. (1984). Microtubule assembly nucleated by isolated centrosomes. Nature *312*, 232–237.

Mocz, G., and Gibbons, I.R. (2001). Model for the motor component of dynein heavy chain based on homology to the AAA family of oligomeric ATPases. Structure *9*, 93–103.

Mogami, T., Kon, T., Ito, K., and Sutoh, K. (2007). Kinetic characterization of tail swing steps in the ATPase cycle of Dictyostelium cytoplasmic dynein. J. Biol. Chem. *282*, 21639–21644.

Moon, H.M., Youn, Y.H., Pemble, H., Yingling, J., Wittmann, T., and Wynshaw-Boris, A. (2014). LIS1 controls mitosis and mitotic spindle organization via the LIS1-NDEL1-dynein complex. Hum. Mol. Genet. *23*, 449–466.

Mosley, A.L., Florens, L., Wen, Z., and Washburn, M.P. (2009). A label free quantitative proteomic analysis of the Saccharomyces cerevisiae nucleus. J. Proteomics *72*, 110–120.

Moughamian, A.J., and Holzbaur, E.L.F. (2012). Dynactin Is Required for Transport Initiation from the Distal Axon. Neuron *74*, 331–343.

Moughamian, A.J., Osborn, G.E., Lazarus, J.E., Maday, S., and Holzbaur, E.L.F. (2013). Ordered Recruitment of Dynactin to the Microtubule Plus-End is Required for Efficient Initiation of Retrograde Axonal Transport. J. Neurosci. *33*, 13190–13203.

Nicholas, M.P., Höök, P., Brenner, S., Wynne, C.L., Vallee, R.B., and Gennerich, A. (2015a). Control of cytoplasmic dynein force production and processivity by its C-terminal domain. Nat. Commun. *6*.

Nicholas, M.P., Berger, F., Rao, L., Brenner, S., Cho, C., and Gennerich, A. (2015b). Cytoplasmic dynein regulates its attachment to microtubules via nucleotide state-switched mechanosensing at multiple AAA domains. Proc. Natl. Acad. Sci. *112*, 201417422.

Nielsen, E., Severin, F., Backer, J.M., Hyman, a a, and Zerial, M. (1999). Rab5 regulates motility of early endosomes on microtubules. Nat. Cell Biol. *1*, 376–382.

Numata, N., Kon, T., Shima, T., Imamula, K., Mogami, T., Ohkura, R., Sutoh, K., and Sutoh, K. (2008). Molecular mechanism of force generation by dynein, a molecular motor belonging to the AAA+ family. Biochem. Soc. Trans. *36*, 131–135.

Numata, N., Shima, T., Ohkura, R., Kon, T., and Sutoh, K. (2011). C-sequence of the Dictyostelium cytoplasmic dynein participates in processivity modulation. FEBS Lett. *585*, 1185–1190.

Okada, Y., Yamazaki, H., Sekine-Aizawa, Y., and Hirokawa, N. (1995). The neuron-specific kinesin superfamily protein KIF1A is a uniqye monomeric motor for anterograde axonal transport of synaptic vesicle precursors. Cell *81*, 769–780.

Olenick, M.A., Tokito, M., Boczkowska, M., Dominguez, R., and Holzbaur, E.L.F. (2016). Hook

adaptors induce unidirectional processive motility by enhancing the Dynein-Dynactin interaction. J. Biol. Chem. *291*, 18239–18251.

Pandey, J.P., and Smith, D.S. (2011). A Cdk5-Dependent Switch Regulates Lis1/Ndel1/Dynein-Driven Organelle Transport in Adult Axons. J. Neurosci. *31*, 17207–17219.

Paoletti, A.C., Parmely, T.J., Tomomori-Sato, C., Sato, S., Zhu, D., Conaway, R.C., Conaway, J.W., Florens, L., and Washburn, M.P. (2006). Quantitative proteomic analysis of distinct mammalian Mediator complexes using normalized spectral abundance factors. Proc. Natl. Acad. Sci. *103*, 18928–18933.

Paschal, B.M., and Vallee, R.B. (1987). Retrograde transport by the microtubule-associated protein MAP 1C. Nature *330*, 181–183.

Pettersen, E.F., Goddard, T.D., Huang, C.C., Couch, G.S., Greenblatt, D.M., Meng, E.C., and Ferrin, T.E. (2004). UCSF Chimera - A visualization system for exploratory research and analysis. J. Comput. Chem. *25*, 1605–1612.

Qiu, W., Derr, N.D., Goodman, B.S., Villa, E., Wu, D., Shih, W., and Reck-Peterson, S.L. (2012). Dynein achieves processive motion using both stochastic and coordinated stepping. Nat. Struct. Mol. Biol. *19*, 193–200.

Reck-Peterson, S.L., Yildiz, A., Carter, A.P., Gennerich, A., Zhang, N., and Vale, R.D. (2006). Single-Molecule Analysis of Dynein Processivity and Stepping Behavior. Cell *126*, 335–348.

Reck-Peterson, S.L., Redwine, W.B., Vale, R.D., and Carter, A.P. (2018). The cytoplasmic dynein transport machinery and its many cargoes. Nat. Rev. Mol. Cell Biol. 1–29.

Reddy, B.J.N., Mattson, M., Wynne, C.L., Vadpey, O., Durra, A., Chapman, D., Vallee, R.B., and Gross, S.P. (2016). Load-induced enhancement of Dynein force production by LIS1–NudE in vivo and in vitro. Nat. Commun. *7*, 12259.

Redwine, W.B., Hernández-López, R., Zou, S., Huang, J., Reck-Peterson, S.L., and Leschziner, A.E. (2012). Structural basis for microtubule binding and release by dynein. Science *337*, 1532–1536.

Redwine, W.B., DeSantis, M.E., Hollyer, I., Htet, Z.M., Tran, P.T., Swanson, S.K., Florens, L., Washburn, M.P., and Reck-Peterson, S.L. (2017). The human cytoplasmic dynein interactome reveals novel activators of motility. Elife *6*, 1–27.

Reiner, O., Carrozzo, R., Shen, Y., Wehnert, M., Faustinella, F., Dobyns, W.B., Caskey, C.T., and Ledbetter, D.H. (1993). Isolation of a Miller-Dicker lissencephaly gene containing G protein β-subunit-like repeats. Nature *364*, 717–721.

Rhee, H.W., Zou, P., Udeshi, N.D., Martell, J.D., Mootha, V.K., Carr, S.A., and Ting, A.Y. (2013). Proteomic mapping of mitochondria in living cells via spatially restricted enzymatic tagging. Science *339*, 1328–1331.

Roberts, A.J., Numata, N., Walker, M.L., Kato, Y.S., Malkova, B., Kon, T., Ohkura, R., Arisaka, F., Knight, P.J., Sutoh, K., et al. (2009). AAA+ Ring and Linker Swing Mechanism in the Dynein Motor. Cell *136*, 485–495.

Roberts, A.J., Malkova, B., Walker, M.L., Sakakibara, H., Numata, N., Kon, T., Ohkura, R., Edwards, T.A., Knight, P.J., Sutoh, K., et al. (2012). ATP-driven remodeling of the linker domain in the dynein motor. Structure *20*, 1670–1680.

Roberts, A.J., Kon, T., Knight, P.J., Sutoh, K., and Burgess, S. a (2013). Functions and mechanics of dynein motor proteins. Nat. Rev. Mol. Cell Biol. *14*, 713–726.

Roberts, A.J., Goodman, B.S., and Reck-Peterson, S.L. (2014). Reconstitution of dynein transport to the microtubule plus end by kinesin. Elife *2014*, 1–16.

Rohou, A., and Grigorieff, N. (2015). CTFFIND4: Fast and accurate defocus estimation from electron micrographs. J. Struct. Biol. *192*, 216–221.

Roseman, A.M. (2004). FindEM - A fast, efficient program for automatic selection of particles from electron micrographs. In Journal of Structural Biology, pp. 91–99.

Rosse, C., Boeckeler, K., Linch, M., Radtke, S., Frith, D., Barnouin, K., Morsi, A.S., Hafezparast, M., Howell, M., and Parker, P.J. (2012). Binding of dynein intermediate chain 2 to paxillin controls focal adhesion dynamics and migration. J. Cell Sci. *125*, 3733–3738.

Roux, K.J., Kim, D.I., Raida, M., and Burke, B. (2012). A promiscuous biotin ligase fusion protein identifies proximal and interacting proteins in mammalian cells. J. Cell Biol. *196*, 801–810.

Sapir, T., Cahana, A., Seger, R., Nekhai, S., and Reiner, O. (1999). LIS1 is a microtubule-associated phosphoprotein. Eur. J. Biochem. *265*, 181–188.

Scheres, S.H.W. (2012). RELION: Implementation of a Bayesian approach to cryo-EM structure determination. J. Struct. Biol. *180*, 519–530.

Schlager, M. a, Hoang, H.T., Urnavicius, L., Bullock, S.L., and Carter, A.P. (2014a). In vitro reconstitution of a highly processive recombinant human dynein complex. EMBO J. *33*, 1–14.

Schlager, M.A., Kapitein, L.C., Grigoriev, I., Burzynski, G.M., Wulf, P.S., Keijzer, N., De Graaff, E., Fukuda, M., Shepherd, I.T., Akhmanova, A., et al. (2010). Pericentrosomal targeting of Rab6 secretory vesicles by Bicaudal-D-related protein 1 (BICDR-1) regulates neuritogenesis. EMBO J. *29*, 1637–1651.

Schlager, M.A., Serra-Marques, A., Grigoriev, I., Gumy, L.F., Esteves da Silva, M., Wulf, P.S., Akhmanova, A., and Hoogenraad, C.C. (2014b). Bicaudal D Family Adaptor Proteins Control the Velocity of Dynein-Based Movements. Cell Rep. *8*, 1248–1256.

Schmidt, H. (2015). Dynein motors: How AAA+ ring opening and closing coordinates microtubule binding and linker movement. Bioessays *37*, 532–543.

Schmidt, H., Gleave, E.S., and Carter, A.P. (2012). Insights into dynein motor domain function from a 3.3-Å crystal structure. Nat. Struct. Mol. Biol. *19*, 492–497.

Schmidt, H., Zalyte, R., Urnavicius, L., and Carter, A.P. (2015). Structure of human cytoplasmic dynein-2 primed for its power stroke. Nature *518*, 435–438.

Schnapp, B.J., Vale, R.D., Sheetz, M.P., and Reese, T.S. (1985). Single microtubules from squid axoplasm support bidirectional movement of organelles. Cell *40*, 455–462.

Schroeder, C.M., and Vale, R.D. (2016). Assembly and activation of dynein–dynactin by the cargo adaptor protein Hook3. J. Cell Biol. *214*, 309–318.

Schroer, T. a (2004). Dynactin. Annu. Rev. Cell Dev. Biol. *20*, 759–779.

Schroer, T. a., and Sheetz, M.P. (1991). Two activators of microtubule-based vesicle transport. J. Cell Biol. *115*, 1309–1318.

Schroer, T.A., Steuer, E.R., and Sheetz, M.P. (1989). Cytoplasmic dynein is a minus end-directed motor for membranous organelles. Cell *56*, 937–946.

Setou, M., Nakagawa, T., Seog, D.H., and Hirokawa, N. (2000). Kinesin superfamily motor protein KIF17 and mLin-10 in NMDA receptor- containing vesicle transport. Science *288*, 1796–1802.

Shao, C.Y., Zhu, J., Xie, Y.J., Wang, Z., Wang, Y.N., Wang, Y., Su, L. Da, Zhou, L., Zhou, T.H., and Shen, Y. (2013). Distinct Functions of Nuclear Distribution Proteins LIS1, Ndel1 and NudCL in Regulating Axonal Mitochondrial Transport. Traffic *14*, 785–797.

Sheeman, B., Carvalho, P., Sagot, I., Geiser, J., Kho, D., Hoyt, M.A., and Pellman, D. (2003). Determinants of S. cerevisiae dynein localization and activation: Implications for the mechanism of spindle positioning. Curr. Biol. *13*, 364–372.

Siglin, A.E., Sun, S., Moore, J.K., Tan, S., Poenie, M., Lear, J.D., Polenova, T., Cooper, J.A., and Williams, J.C. (2013). Dynein and Dynactin Leverage Their Bivalent Character to Form a High-Affinity Interaction. PLoS One *8*.

Simpson, F., Martin, S., Evans, T.M., Kerr, M., James, D.E., Parton, R.G., Teasdale, R.D., and Wicking, C. (2005). A novel hook-related protein family and the characterization of hook-related protein 1. Traffic *6*, 442–458.

Sitaram, P., Anderson, M.A., Jodoin, J.N., Lee, E., and Lee, L.A. (2012). Regulation of dynein localization and centrosome positioning by Lis-1 and asunder during Drosophila spermatogenesis. Development *139*, 2945–2954.

Sladewski, T.E., Billington, N., Ali, M.Y., Bookwalter, C.S., Lu, H., Krementsova, E.B., Schroer, T.A., and Trybus, K.M. (2018). Recruitment of two dyneins to an mRNA-dependent bicaudal D transport complex. Elife *7*.

Smith, D.S., Niethammer, M., Ayala, R., Zhou, Y., Gambello, M.J., Wynshaw-Boris, A., and Tsai, L.H. (2000). Regulation of cytoplasmic dynein behaviour and microtubule organization by mammalian Lis1. Nat. Cell Biol. *2*, 767–775.

Splinter, D., Tanenbaum, M.E., Lindqvist, A., Jaarsma, D., Flotho, A., Yu, K. Lou, Grigoriev, I., Engelsma, D., Haasdijk, E.D., Keijzer, N., et al. (2010). Bicaudal D2, dynein, and kinesin-1 associate with nuclear pore complexes and regulate centrosome and nuclear positioning during mitotic entry. PLoS Biol. *8*.

Splinter, D., Razafsky, D.S., Schlager, M. a., Serra-Marques, a., Grigoriev, I., Demmers, J., Keijzer, N., Jiang, K., Poser, I., Hyman, a. a., et al. (2012). BICD2, dynactin, and LIS1 cooperate in regulating dynein recruitment to cellular structures. Mol. Biol. Cell *23*, 4226–4241.

Suloway, C., Pulokas, J., Fellmann, D., Cheng, A., Guerra, F., Quispe, J., Stagg, S., Potter, C.S., and Carragher, B. (2005). Automated molecular microscopy: The new Leginon system. J. Struct. Biol. *151*, 41–60.

Tabb, D.L., McDonald, W.H., and Yates, J.R. (2002). DTASelect and contrast: Tools for assembling and comparing protein identifications from shotgun proteomics. J. Proteome Res. *1*, 21–26.

Tai, C.-Y., Dujardin, D.L., Faulkner, N.E., and Vallee, R.B. (2002). Role of dynein, dynactin, and CLIP-170 interactions in LIS1 kinetochore function. J. Cell Biol. *156*, 959–968.

Tarricone, C., Perrina, F., Monzani, S., Massimiliano, L., Kim, M., Derewenda, Z.S., Knapp, S., Tsai, L., Musacchio, A., and Ripamonti, V. (2004). Coupling PAF Signaling to Dynein Regulation : Structure of LIS1 in Complex with PAF-Acetylhydrolase. *44*, 809–821.

Terawaki, S.I., Yoshikane, A., Higuchi, Y., and Wakamatsu, K. (2015). Structural basis for cargo binding and autoinhibition of Bicaudal-D1 by a parallel coiled-coil with homotypic registry. Biochem. Biophys. Res. Commun. *460*, 451–456.

Torisawa, T., Nakayama, A., Furuta, K., Yamada, M., Hirotsune, S., and Toyoshima, Y.Y. (2011). Functional dissection of LIS1 and NDEL1 towards understanding the molecular mechanisms of cytoplasmic dynein regulation. J. Biol. Chem. *286*, 1959–1965.

Torisawa, T., Ichikawa, M., Furuta, A., Saito, K., Oiwa, K., Kojima, H., Toyoshima, Y.Y., and Furuta, K. (2014). Autoinhibition and cooperative activation mechanisms of cytoplasmic dynein. Nat. Cell Biol. *16*, 1118–1124.

Toropova, K., Zou, S., Roberts, A.J., Redwine, W.B., Goodman, B.S., Reck-Peterson, S.L., and Leschziner, A.E. (2014). Lis1 regulates dynein by sterically blocking its mechanochemical cycle. Elife *3*, 1–25.

Trokter, M., Mücke, N., and Surrey, T. (2012). Reconstitution of the human cytoplasmic dynein complex. Proc. Natl. Acad. Sci. U. S. A. *109*, 20895–20900.

Tsai, J.W., Bremner, K.H., and Vallee, R.B. (2007). Dual subcellular roles for LIS1 and dynein in radial neuronal migration in live brain tissue. Nat. Neurosci. *10*, 970–979.

Twelvetrees, A.E., Pernigo, S., Sanger, A., Guedes-Dias, P., Schiavo, G., Steiner, R.A., Dodding, M.P., and Holzbaur, E.L.F. (2016). The Dynamic Localization of Cytoplasmic Dynein in Neurons Is Driven by Kinesin-1. Neuron 1–16.

Urnavicius, L., Zhang, K., Diamant, A.G., Motz, C., Schlager, M.A., Yu, M., Patel, N.A., Robinson, C. V., and Carter, A.P. (2015). The structure of the dynactin complex and its interaction with dynein. Science *347*, 1441–1446.

Urnavicius, L., Lau, C.K., Elshenawy, M.M., Morales-Rios, E., Motz, C., Yildiz, A., and Carter, A.P. (2018). Cryo-EM shows how dynactin recruits two dyneins for faster movement. Nature *554*, 202–206.

Vagnoni, A., Hoffmann, P.C., and Bullock, S.L. (2016). Reducing Lissencephaly-1 levels augments mitochondrial transport and has a protective effect in adult *Drosophila* neurons. J. Cell Sci. *129*, 178–190.

Vale, R.D. (2003). The molecular motor toolbox for intracellular transport. Cell *112*, 467–480.

Vaughan, K.T., and Vallee, R.B. (1995). Cytoplasmic dynein binds dynactin through a direct interaction between the intermediate chains and p150Glued. J. Cell Biol. *131*, 1507–1516.

Wang, S., and Zheng, Y. (2011). Identification of a novel dynein binding domain in nudel essential for spindle pole organization in Xenopus egg extract. J. Biol. Chem. *286*, 587–593.

Wang, R.Y.R., Song, Y., Barad, B.A., Cheng, Y., Fraser, J.S., and DiMaio, F. (2016). Automated structure refinement of macromolecular assemblies from cryo-EM maps using Rosetta. Elife *5*.

Wang, S., Ketcham, S. a, Schön, A., Goodman, B., Wang, Y., Yates, J., Freire, E., Schroer, T. a, and Zheng, Y. (2013). Nudel/NudE and Lis1 promote dynein and dynactin interaction in the context of spindle morphogenesis. Mol. Biol. Cell *24*, 3522–3533.

Wang, S., Wu, D., Quintin, S., Green, R.A., Cheerambathur, D.K., Ochoa, S.D., Desai, A., and Oegema, K. (2015). NOCA-1 functions with γ-tubulin and in parallel to Patronin to assemble non-centrosomal microtubule arrays in C. elegans. Elife *4*.

Wang, Y., Huynh, W., Skokan, T.D., and Vale, R.D. (2018). A new calcium-activated dynein adaptor protein, CRACR2a, regulates clathrin-independent endocytic traffic in T cells. BioRxiv.

Washburn, M.P., Wolters, D., and Yates, J.R. (2001). Large-scale analysis of the yeast proteome by multidimensional protein identification technology. Nat. Biotechnol. *19*, 242–247.

Waterman-Storer, C.M., Karki, S., and Holzbaur, E.L. (1995). The p150Glued component of the dynactin complex binds to both microtubules and the actin-related protein centractin (Arp-1). Proc. Natl. Acad. Sci. *92*, 1634–1638.

Whyte, J., Bader, J.R., Tauhata, S.B.F., Raycroft, M., Hornick, J., Pfister, K.K., Lane, W.S., Chan, G.K., Hinchcliffe, E.H., Vaughan, P.S., et al. (2008). Phosphorylation regulates targeting of cytoplasmic dynein to kinetochores during mitosis. J. Cell Biol. *183*, 819–834.

Wilkie, G.S., and Davis, I. (2001). Drosophila wingless and pair-rule transcripts localize apically by dynein-mediated transport of RNA particles. Cell *105*, 209–219.

Wolters, D.A., Washburn, M.P., and Yates, J.R. (2001). An automated multidimensional protein identification technology for shotgun proteomics. Anal. Chem. *73*, 5683–5690.

Xiang, X., Osmani, A.H., Osmani, S.A., Xin, M., and Morris, N.R. (1995). NudF, a nuclear migration gene in Aspergillus nidulans, is similar to the human LIS-1 gene required for neuronal migration. Mol. Biol. Cell *6*, 297–310.

Xu, L., Sowa, M.E., Chen, J., Li, X., Gygi, S.P., and Harper, J.W. (2008). An FTS/Hook/p107 ^{FHIP} Complex Interacts with and Promotes Endosomal Clustering by the Homotypic Vacuolar Protein Sorting Complex. Mol. Biol. Cell *19*, 5059–5071.

Yamada, M., Toba, S., Yoshida, Y., Haratani, K., Mori, D., Yano, Y., Mimori-Kiyosue, Y., Nakamura, T., Itoh, K., Fushiki, S., et al. (2008a). LIS1 and NDEL1 coordinate the plus-end-directed transport of cytoplasmic dynein. EMBO J. *27*, 2471–2483.

Yamada, M., Toba, S., Yoshida, Y., Haratani, K., Mori, D., Yano, Y., Mimori-Kiyosue, Y., Nakamura, T., Itoh, K., Fushiki, S., et al. (2008b). LIS1 and NDEL1 coordinate the plus-end-

directed transport of cytoplasmic dynein. EMBO J. *27*, 2471–2483.

Yeh, T.-Y., Quintyne, N.J., Scipioni, B.R., Eckley, D.M., and Schroer, T.A. (2012). Dynactin's pointed-end complex is a cargo-targeting module. Mol. Biol. Cell *23*, 3827–3837.

Yi, J.Y., Ori-McKenney, K.M., McKenney, R.J., Vershinin, M., Gross, S.P., and Vallee, R.B. (2011). High-resolution imaging reveals indirect coordination of opposite motors and a role for LIS1 in high-load axonal transport. J. Cell Biol. *195*, 193–201.

Ying, W.C., Fava, L.L., Uldschmid, A., Schmitz, M.H.A., Gerlich, D.W., Nigg, E.A., and Santamaria, A. (2009). Mitotic control of kinetochore-associated dynein and spindle orientation by human Spindly. J. Cell Biol. *185*, 859–874.

Zhang, J., Zhuang, L., Lee, Y., Abenza, J.F., Penalva, M.A., and Xiang, X. (2010a). The microtubule plus-end localization of Aspergillus dynein is important for dynein-early-endosome interaction but not for dynein ATPase activation. J. Cell Sci. *123*, 3596–3604.

Zhang, J., Yao, X., Fischer, L., Abenza, J.F., Peñalva, M.A., and Xiang, X. (2011). The p25 subunit of the dynactin complex is required for dynein-early endosome interaction. J. Cell Biol. *193*, 1245–1255.

Zhang, J., Qiu, R., Arst, H.N., Peñalva, M. a., and Xiang, X. (2014). HookA is a novel dynein-early endosome linker critical for cargo movement in vivo. J. Cell Biol. *204*, 1009–1026.

Zhang, K., Foster, H.E., Rondelet, A., Lacey, S.E., Bahi-buisson, N., Bird, A.W., Carter, A.P., Zhang, K., Foster, H.E., Rondelet, A., et al. (2017). Cryo-EM Reveals How Human Cytoplasmic Dynein Is Auto-inhibited and Activated. Cell 1–12.

Zhang, Y., Wen, Z., Washburn, M.P., and Florens, L. (2010b). Refinements to label free proteome quantitation: How to deal with peptides shared by multiple proteins. Anal. Chem. *82*, 2272–2281.

Zhang, Y., Wen, Z., Washburn, M.P., and Florens, L. (2015). Improving label-free quantitative proteomics strategies by distributing shared peptides and stabilizing variance. Anal. Chem. *87*, 4749–4756.

Zheng, S.Q., Palovcak, E., Armache, J.-P., Verba, K.A., Cheng, Y., and Agard, D.A. (2017). MotionCor2: anisotropic correction of beam-induced motion for improved cryo-electron microscopy. Nat. Methods *14*, 331–332.

Zhou, J., Du, Y.-R., Qin, W.-H., Hu, Y.-G., Huang, Y.-N., Bao, L., Han, D., Mansouri, A., and Xu, G.-L. (2009). RIM-BP3 is a manchette-associated protein essential for spermiogenesis. Development *136*, 373–382.

Zybailov, B., Mosley, A.L., Sardiu, M.E., Coleman, M.K., Florens, L., and Washburn, M.P. (2006). Statistical analysis of membrane proteome expression changes in Saccharomyces cerevisiae. J. Proteome Res. *5*, 2339–2347.

Zyłkiewicz, E., Kijańska, M., Choi, W.-C., Derewenda, U., Derewenda, Z.S., and Stukenberg, P.T. (2011). The N-terminal coiled-coil of Ndel1 is a regulated scaffold that recruits LIS1 to dynein. J. Cell Biol. *192*, 433–445.

Appendix A

Supplementary Information for Chapter 2

This appendix has been previously published as:

Morgan E. DeSantis*, Michael A. Cianfrocco*, **Zaw Min Htet***, Phuoc Tien Tran, Samara L. Reck-Peterson#, Andres E. Leschziner#. (2017). Lis1 has two opposing modes of regulating cytoplasmic dynein. ***Cell*** 170(6): 1197-1208.

* denotes equal contributions

# denotes co-senior investigators

A.1 Supplementary figures for Chapter 2

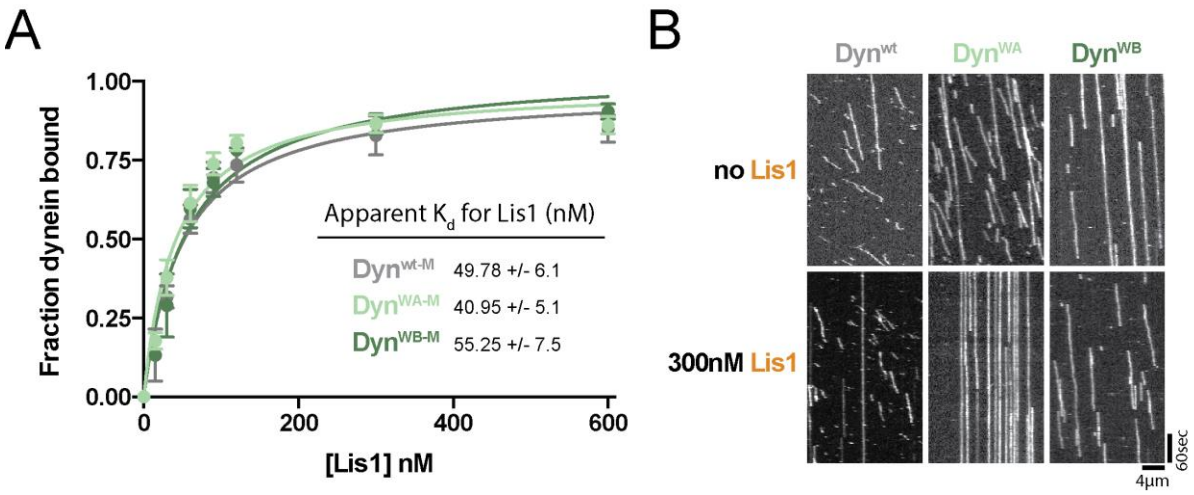

Figure A.1. Affinity measurements for the binding of different dynein constructs to Lis1 and kymographs for those constructs with and without Lis1. (A) Determination of the binding affinity of Lis1 to $Dyn^{wt\text{-}M}$ (grey), $Dyn^{WA\text{-}M}$ (light green), and $Dyn^{WB\text{-}M}$ (dark green) in the presence of 1 mM ATP-Vi. (n=3 technical replicates per each data point). (B) Sample kymographs for Dyn^{wt}, Dyn^{WA} and Dyn^{WB} in the absence, or presence of 300 nM Lis1.

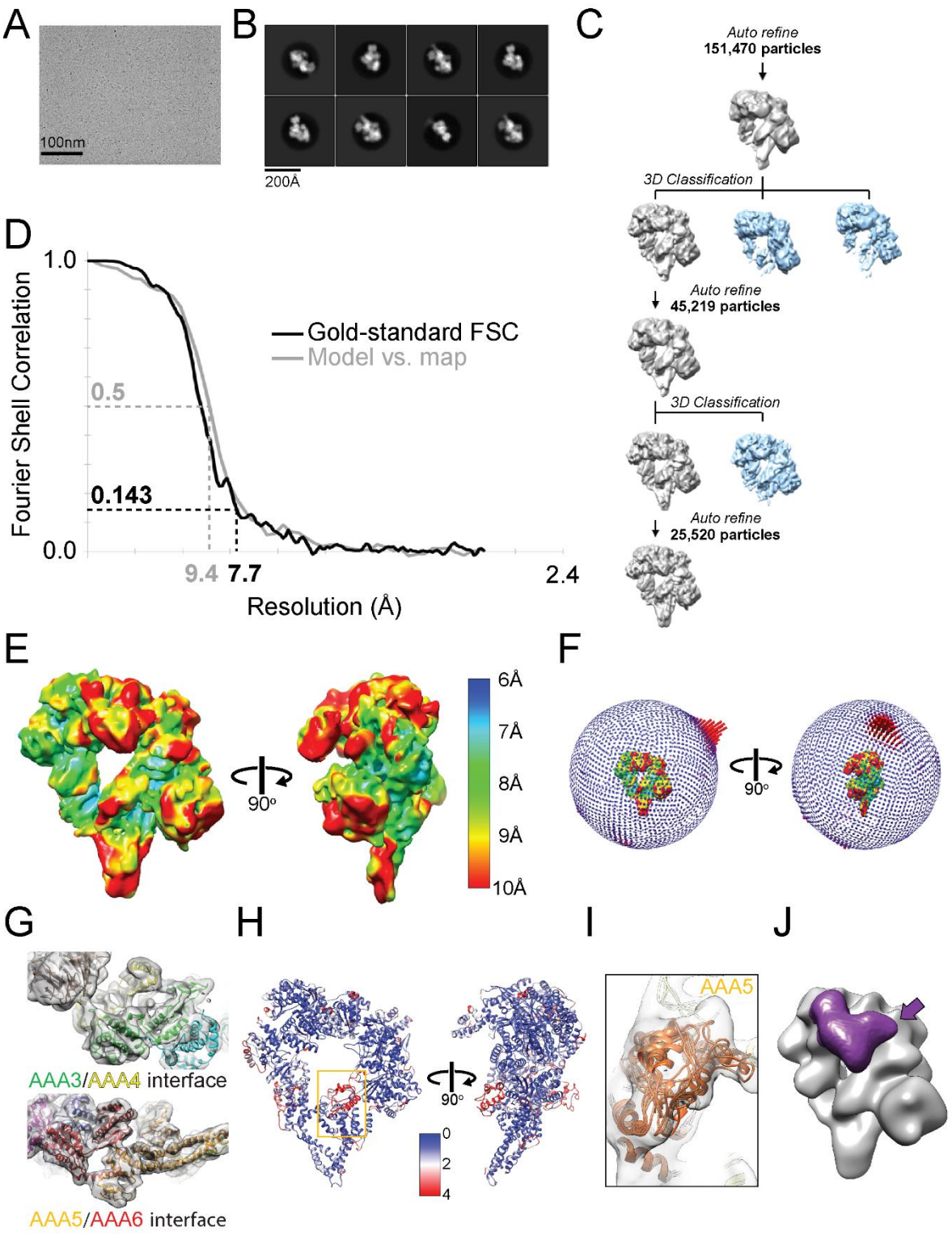

Figure A.2. Cryo-EM structure and model validation of Dyn$^{wt\text{-}M}$:Lis1. (A) Representative drift-corrected cryo-EM micrograph. (B) Representative 2D class averages. (C) 3D alignment and classification strategy (see Methods in Chapter 2 for details). (D) Fourier Shell Correlation (FSC)

(continued) for 3D reconstruction (Gold-Standard FSC) and atomic model against cryo-EM map (Model vs. map). (E) Local resolution analysis of cryo-EM structure calculated by Bsoft. (F) Euler angle distribution. (G) Example cryo-EM densities with the final Rosetta model docked in. (H) RMSD among the top five Rosetta models. Orange box indicates region shown in (I). (I) Zoomed-in view of the cryo-EM density corresponding to the large domain of AAA5, with the top five Rosetta models docked in. This region has the highest RMSD among the Rosetta models. (J) The $Dyn^{wt\text{-}M}$:Lis1 map was filtered to 20Å to reveal more of the N-terminal density of the linker domain, which is indicated by the purple arrow. The linker was segmented and is colored in purple.

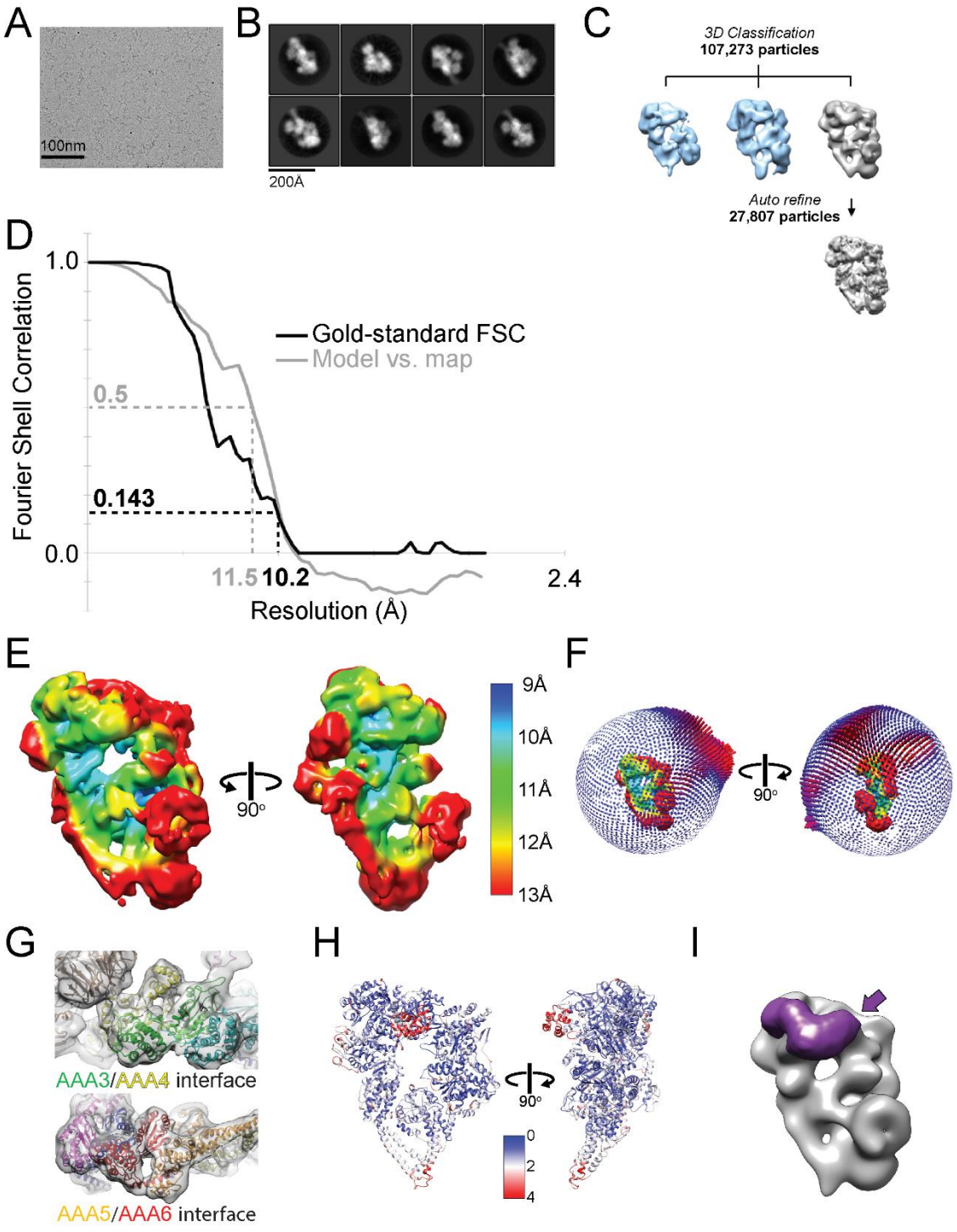

Figure A.3. Cryo-EM structure and model validation of Dyn^{WB-M}:Lis1. (A) Representative drift-corrected cryo-EM micrograph. (B) Representative 2D class averages. (C) 3D alignment and classification strategy (see Methods in Chapter 2 for details). (D) Fourier Shell Correlation (FSC) for 3D reconstruction (Gold-Standard FSC) and atomic model against cryo-EM map (Model vs. map). (E) Local resolution analysis of cryo-EM structure calculated by Bsoft. (F) Euler angle

(continued) distribution. (G) Example cryo-EM densities with the final Rosetta model docked in. (H) RMSD among the top five Rosetta models. (I) The Dyn^{WB-M}:Lis1 map was filtered to 20Å to reveal more of the N-terminal density of the linker domain, which is indicated by the purple arrow. The linker was segmented and is colored in purple.

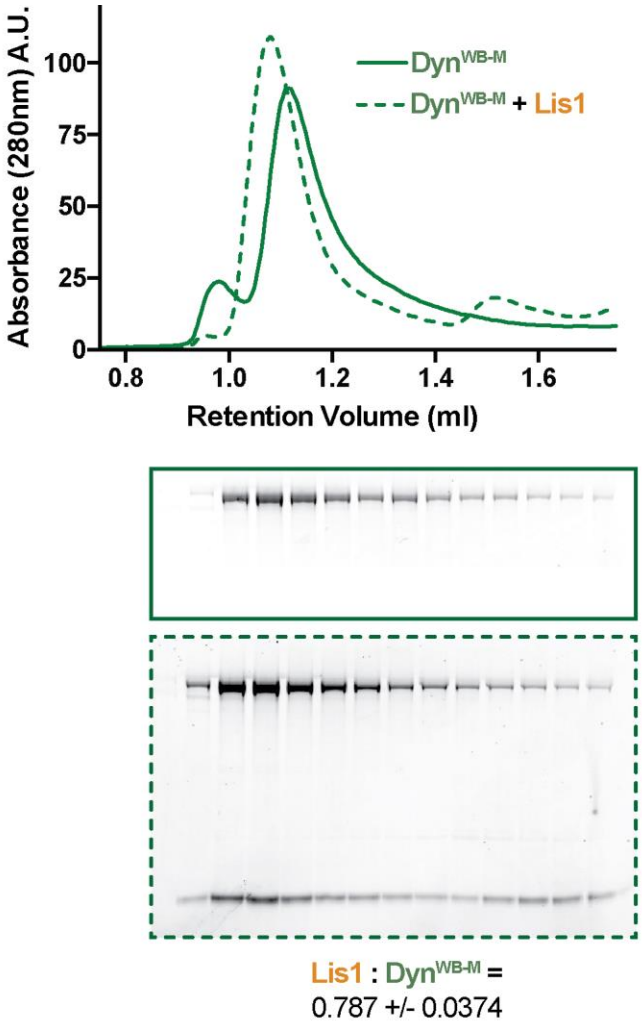

Figure A.4. Stoichiometry analysis of DynWB-M:Lis1 complexes. Stoichiometry analysis of Dyn^{WB-M}:Lis1 complexes purified by size-exclusion chromatography. Band intensities were quantified to determine amount of Dyn^{WB-M} and Lis1 in the peak fraction.

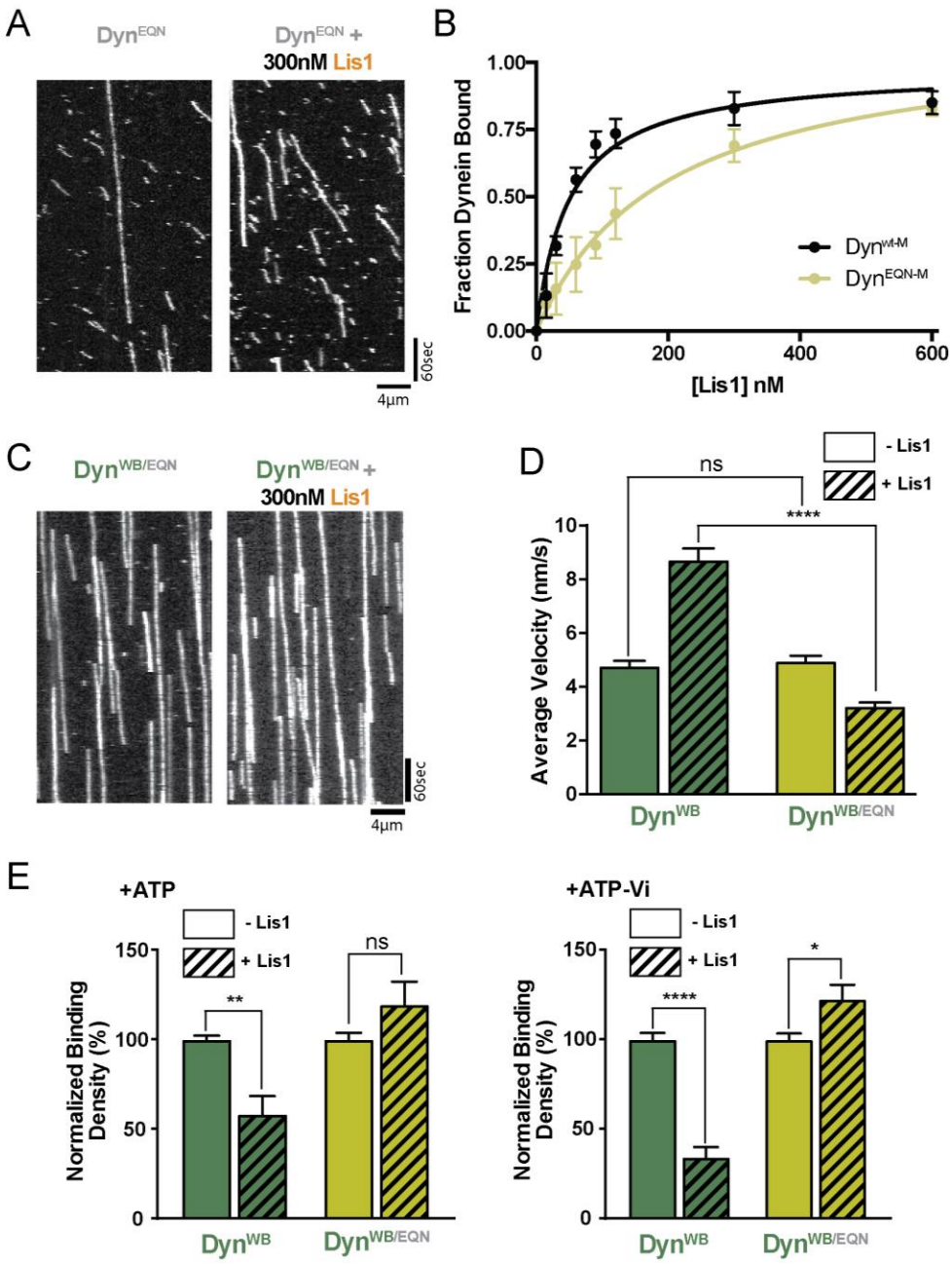

Figure A.5. Binding affinity and velocity comparisons for Dyn^{wt-M} and Dyn^{EQN-M} with and without Lis1. (A) Sample kymographs for Dyn^{EQN} in the absence, or presence of 300 nM Lis1. (B) Determination of the binding affinity of Lis1 to Dyn^{wt-M} (black – data previously shown in Figure S1A) and Dyn^{EQN-M} (yellow) in the presence of 1 mM ATP-Vi (n=3 per each data point). (C) Sample kymographs for Dyn$^{WB/EQN}$ in the absence, or presence of 300 nM Lis1. (D) Average velocities for Dyn^{WB} and Dyn$^{WB/EQN}$ in the absence (solid bars) and presence (hatched bars) of 300 nM Lis1 (n>185 events per data point). (E) Normalized binding densities of Dyn^{WB} and Dyn$^{WB/EQN}$

(continued) in the absence (solid bars) or presence (hatched bars) of 300 nM Lis1, in the presence of ATP (left) or ATP-Vi (right) (n=12 fields of view per data point). Binding densities were normalized by setting those in the absence of Lis1 to 100%.

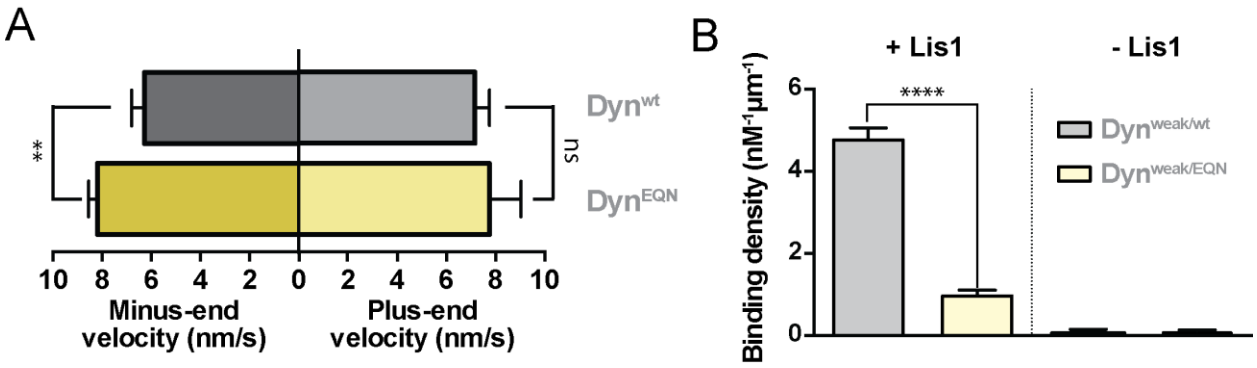

Figure A.6. Velocity measurements for Dyn^{wt} and Dyn^{EQN} and binding density measurements for $Dyn^{weak/wt}$ and $Dyn^{weak/EQN}$ in plus-end recruitment assay. (A) Minus-end and plus-end velocities of Dyn^{wt} (grey) and Dyn^{EQN} (yellow) on dynamic microtubules in the presence of Lis1, Kip2, Bik1 and Bim1 (n>50 events per data point). Statistical significance was calculated using unpaired t-test with Welch's correction. P-values: ns, not significant; **, <0.01. Data are shown as mean and standard error of mean. (B) Microtubule binding densities of $Dyn^{weak/wt}$ (light grey) and $Dyn^{weak/EQN}$ (light yellow) in the presence of Lis1, Kip2, Bik1 and Bim1 (left) or in the presence of Kip2, Bik1 and Bim1 (right) (n=8 fields of view per data point).

A.2 Supplementary tables for Chapter 2

Supplementary table A.1. Summary of cryo-EM data collection and cryo-EM structure determination of $Dyn^{wt\text{-}M}$:Lis1 and $Dyn^{WB\text{-}M}$:Lis1.

Data collection information	**$Dyn^{wt\text{-}M}$: Lis1**	**$Dyn^{wB\text{-}M}$: Lis1**
Microscope	FEI Talos Arctica	FEI Talos Arctica
Voltage (kV)	200	200
Detector	Gatan K2 Summit	Gatan K2 Summit
Pixel size (Å)	0.60	0.60
Defocus range (μm)	1.5-4.0	2.5-5.5
Movies	5614	4826
Frames/movie	53	25
Dose rate (electrons/pixel.s)	10.285	10.00
Total dose (electrons/$Å^2$)	82	50
Number of particles	25,520	27,807
Map-sharpening B-factor ($Å^2$)	-50	-800
Final overall resolution (Å)	7.7	10.2

Supplementary table A.2. Summary of velocity and binding data.

	Average velocity +/- SE (nm/s)
Dyn^{wt}	89.16 +/- 4.54
Dyn^{wt} + 300 nM Lis1	39.55 +/- 2.11
Dyn^{WA}	18.50 +/- 0.52
Dyn^{WA} + 300 nM Lis1	0.22 +/- 0.03
Dyn^{WB}	4.77 +/- 0.19
Dyn^{WB} + 300 nM Lis1	8.73 +/- 0.42
Dyn^{EQN}	81.40 +/- 4.52
Dyn^{EQN} + 300 nM Lis1	42.31 +/- 1.10
$Dyn^{WB/EQN}$	4.96 +/- 0.20
$Dyn^{WB/EQN}$ + 300 nM Lis1	3.28 +/- 0.13
	Apparent K_d +/- SE (nM) for Lis1 in the presence of 1mM ATP-Vi
Dyn^{wt-M}	49.78 +/- 6.1
Dyn^{WA-M}	40.95 +/- 5.1
Dyn^{WB-M}	55.25 +/- 7.5
Dyn^{EQN-M}	196.30 +/- 30.8
	Microtubule binding density +/- SE (pM^{-1} μm^{-1}) in the presence of 1mM ATP
Dyn^{wt}	0.033 +/- 0.002
Dyn^{WA}	0.50 +/- 0.06
Dyn^{WB}	0.50 +/- 0.03
Dyn^{EQN}	0.035 +/- 0.003
$Dyn^{WB/EQN}$	0.48 +/- 0.03
	Microtubule binding density +/- SE (pM^{-1} μm^{-1}) in the presence of 1mM ATP-Vi
Dyn^{wt}	0.037 +/- 0.004
Dyn^{WA}	0.24 +/- 0.03
Dyn^{WB}	0.36 +/- 0.01
Dyn^{EQN}	0.040 +/- 0.002
$Dyn^{WB/EQN}$	0.34 +/- 0.01
	Microtubule binding density +/- SE (pM^{-1} μm^{-1}) in the presence of 1mM ADP
Dyn^{wt}	0.53 +/- 0.03
Dyn^{WA}	1.8 +/- 0.2
Dyn^{WB}	1.6 +/- 0.1
	Microtubule binding density +/- SE (pM^{-1} μm^{-1}) in the absence of nucleotides (Apo)
Dyn^{wt}	1.48 +/- 0.03
Dyn^{WA}	1.8 +/- 0.1
Dyn^{WB}	2.9 +/- 0.1

Supplementary table A.3. *S. cerevisiae* strains used in Chapter 2.

Strain	Genotype
RPY1	W303a (*MATa*, *his3-11,15, ura3-1, leu2-3,112, ade2-1, trp1-1*)
RPY799	W303a *pep4Δ::HIS5, prb1Δ, P_{GAL1}-8HIS-ZZ-SNAP-gs-PAC1, dyn1Δ::cgLEU2*
RPY816	W303a *pep4Δ::HIS5, prb1Δ, P_{GAL1}-8HIS-ZZ-Tev-PAC1, dyn1Δ::cgLEU2, ndl1Δ::Hygro^R*
RPY1099	W303a *pep4Δ::HIS5, prb1Δ, P_{GAL1}-8HIS-ZZ-Tev-KIP2-g- FLAG-ga-SNAP−Kan^R*
RPY1167	W303a *pep4Δ::HIS5, prb1Δ, P_{GAL1}-ZZ-TEV-GFP-3XHA-GST-DYN1(331kDa)-gsDHA-KanR, pac1Δ, ndl1Δ::cgLEU2*
RPY1302	W303a *pep4Δ::HIS5, prb1Δ, PAC11-13xMYC-TRP1, P_{GAL1}-ZZ-Tev-DYN1(331kDa), pac1Δ:: Hygro^R*
RPY1385	*MATa lys2-801 leu2-Δ1 his3-Δ200 trp1-Δ63 DYN1-3XGFP::TRP1, ura3-52::CFP-TUB1::URA3, SPC110-tdTomato::SpHIS5, ura3Δ::KanMX*
RPY1536	W303a *pep4Δ::HIS5, prb1Δ, P_{GAL1}-ZZ-TEV-GFP-3XHA-GST-DYN1(331kDa)$^{K3116A,\ K3117A,\ E3122A,\ R3124A}$-gsDHA-KanR, pac1Δ, ndl1Δ::cgLEU2*
RPY1547	W303a *pep4Δ::HIS5, prb1Δ, P_{GAL1}-8HIS-ZZ-Tev-PAC1^{R275A,R301A,R378A,W419A,K437A}, dyn1Δ::cgLEU2, ndl1Δ::Hygro^R*
RPY1630	W303a *pep4Δ::HIS5, prb1Δ, P_{GAL1}-ZZ-TEV-GFP-3XHA-GST-DYN1(331kDa)^{K2424A}-gsDHA-KanR, pac1Δ, ndl1Δ::cgLEU2*
RPY1635	W303a *pep4Δ::HIS5, prb1Δ, PAC11-13xMYC-TRP1, P_{GAL1}-ZZ-Tev-DYN1(331kDa)^{K2424A}, pac1Δ:: Hygro^R*
RPY1653	W303a *pep4Δ::HIS5, prb1Δ, P_{GAL1}-ZZ-TEV-GFP-3XHA-GST-DYN1(331kDa)^{E2488Q}-gsDHA-KanR, pac1Δ, ndl1Δ::cgLEU2*
RPY1654	W303a *pep4Δ::HIS5, prb1Δ, PAC11-13xMYC-TRP1, P_{GAL1}-ZZ-Tev-DYN1(331kDa)^{E2488Q}, pac1Δ:: Hygro^R*
RPY1705	W303a *pep4Δ::HIS5, prb1Δ, P_{GAL1}-ZZ-TEV-GFP-3XHA-GST-DYN1(331kDa)^{E3012A,Q3014A,N3018A}-gsDHA-KanR, pac1Δ, ndl1Δ::cgLEU2*
RPY1707	W303a *pep4Δ::HIS5, prb1Δ, P_{GAL1}-ZZ-TEV-GFP-3XHA-GST-DYN1(331kDa)$^{E2488Q,\ E3012A,Q3014A,N3018A}$-gsDHA-KanR, pac1Δ, ndl1Δ::cgLEU2*
RPY1708	*MATa lys2-801 leu2-Δ1 his3-Δ200 trp1-Δ63 DYN1^{E3012A,Q3014A,N3018A} -3XGFP::TRP1, ura3-52::CFP-TUB1::URA3, SPC110-tdTomato::SpHIS5, ura3Δ::KanMX*
RPY1713	W303a *pep4Δ::HIS5, prb1Δ, PAC11-13xMYC-TRP1, P_{GAL1}-ZZ-Tev-DYN1(331kDa)^{E3012A,Q3014A,N3018A}, pac1Δ:: Hygro^R*
RPY1717	*MATa lys2-801 leu2-Δ1 his3-Δ200 trp1-Δ63 DYN1-3XGFP::TRP1, ura3-52::CFP-TUB1::URA3, SPC110-tdTomato::SpHIS5, ura3Δ::KanMX, pac1Δ::klURA3*
RPY1725	W303a *pep4Δ::HIS5, prb1Δ, P_{GAL1}-ZZ-TEV-GFP-3XHA-GST-DYN1(331kDa)$^{E3012A,Q3014A,N3018A,\ K3116A,\ K3117A,\ E3122A,\ R3124A}$-gsDHA-KanR, pac1Δ, ndl1Δ::cgLEU2*

A.3 Legends for supplementary files of Chapter 2

Supplementary file A.1. Movie of morph between AAA ring conformations of Dyn^{wt-M}:Lis1 and Dyn^{WB-M}:Lis1. The movie begins with the full atomic model for Dyn^{wt-M}:Lis1. We then remove Lis1 and dynein's linker domain to focus on the AAA ring. The movie morphs three times between the two ring conformations and ends with the full atomic model of Dyn^{WB-M}:Lis1.

Supplementary file A.2. Cα distance coordinate files. Compressed (.zip) directory containing all distance comparisons: Dyn^{wt-M}:Lis1 vs. 4RH7 relative to AAA4L (Figure 2.2H), Dyn^{wt-M}:Lis1 vs. 4AKI relative to AAA4L (Figure 2.2H), Dyn^{WB-M}:Lis1 vs. 4RH7 relative to AAA4L (Figure 2.3F), and Dyn^{wt-M}:Lis1 vs. Dyn^{WB-M}:Lis1 relative to AAA3L (Figure 2.4A). Files must be displayed using UCSF Chimera.

Appendix B

Supplementary Information for Chapter 3

B.1 Supplementary figures for Chapter 3

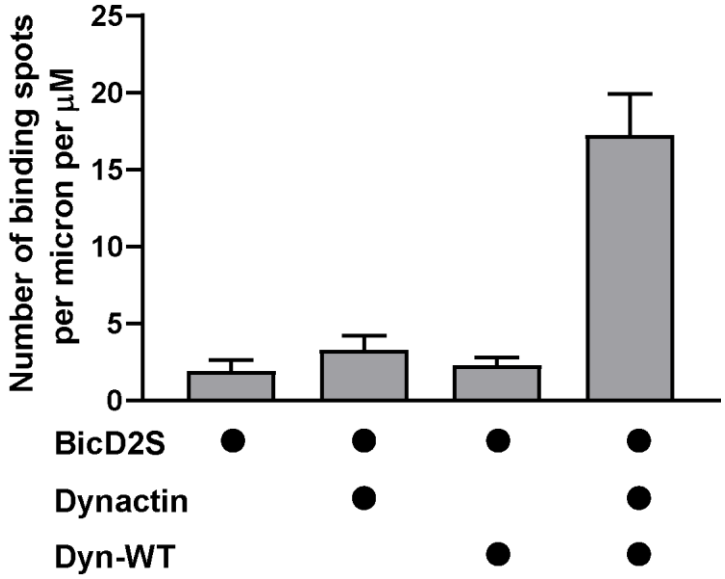

Figure B.1. Truncated BicD2 (BicD2S) only binds to microtubules in the presence of both dynein and dynactin. Average microtubule binding density of fluorescently labeled BicD2S in the presence of dynein, dynactin or both as indicated. Data are shown as mean and standard error of mean.

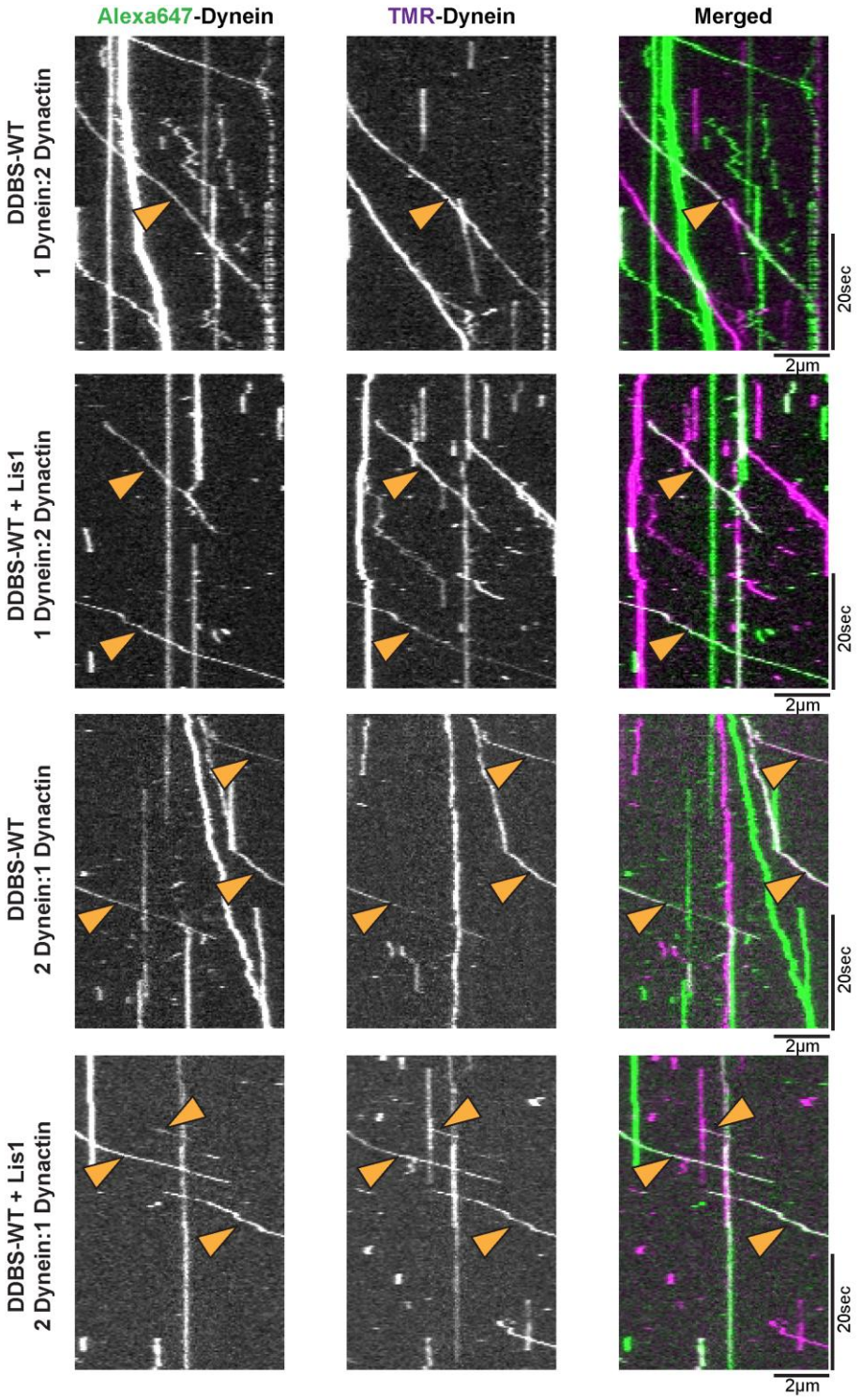

Figure B.2. Representative kymographs of two-color colocalized runs of dynein-dynactin-BicD2S complexes at different dynein to dynactin molar ratio in the presence or absence of Lis1. The Alexa647-dynein and TMR-dynein channels are shown in black and white and the merged image is shown in pseudocolor.

Appendix C

Supplementary Information for Chapter 4

This chapter has been previously published as:

W. B. Redwine*, M. E. DeSantis*, I. Hollyer, **Z. M. Htet**, P. T. Tran, S. K. Swanson, L. Florens, M. P. Washburn, S. L. Reck-Peterson. (2017) The human cytoplasmic dynein interactome reveals novel activators of motility. ***eLife*** 6, e28257.

* denotes equal contributions

C.1 Supplementary figures for Chapter 4

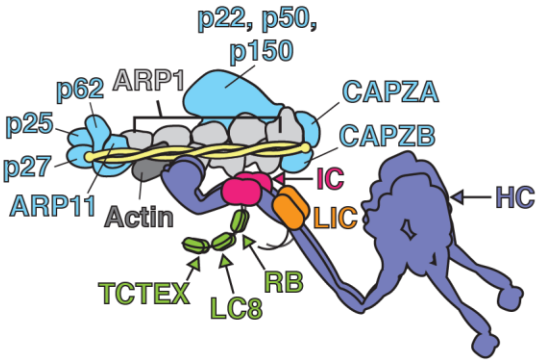

Dynein	Dynactin
DYNC1H1 (heavy chain, HC)	DCTN1 (p150 or p150^{Glued})
DYNC1I1 (intermediate chain 1, IC1)	DCTN2 (p50)
DYNC1I2 (intermediate chain 2, IC2)	DCTN3 (p22)
DYNC1LI1 (light intermediate chain 1, LIC1)	DCTN4 (p62)
DYNC1LI2 (light intermediate chain 2, LIC2)	DCTN5 (p25)
DYNLT1 (light chain TCTEX1)	DCTN6 (p27)
DYNLT3 (light chain TCTEX3)	ACTR1A (Arp1A)
DYNLRB1(light chain Roadblock-1,RB1)	ACTR1B (Arp1B)
DYNLRB2 (light chain Roadblock-2,RB2)	ACTB (β-Actin)
DYNLL1 (light chain LC8-1)	ACTR10 (Arp11)
DYNLL2 (light chain LC8-2)	CAPZA1 (CapZA1)
	CAPZA2 (CapZA2)
	CAPZB (CapZB)

Figure C.1. Schematic of the dynein/dynactin/activator complex. Dynein subunits are uniquely colored except for the light chains (green). Dynactin subunits other than Arp1 (light gray) and actin (dark gray) are colored light blue. The dynactin Arp1 filament (light gray) is indicated with a single label. A coiled coil activator (e.g. BICD2) is depicted and colored yellow. The corresponding gene names, common names, and abbreviations are listed below.

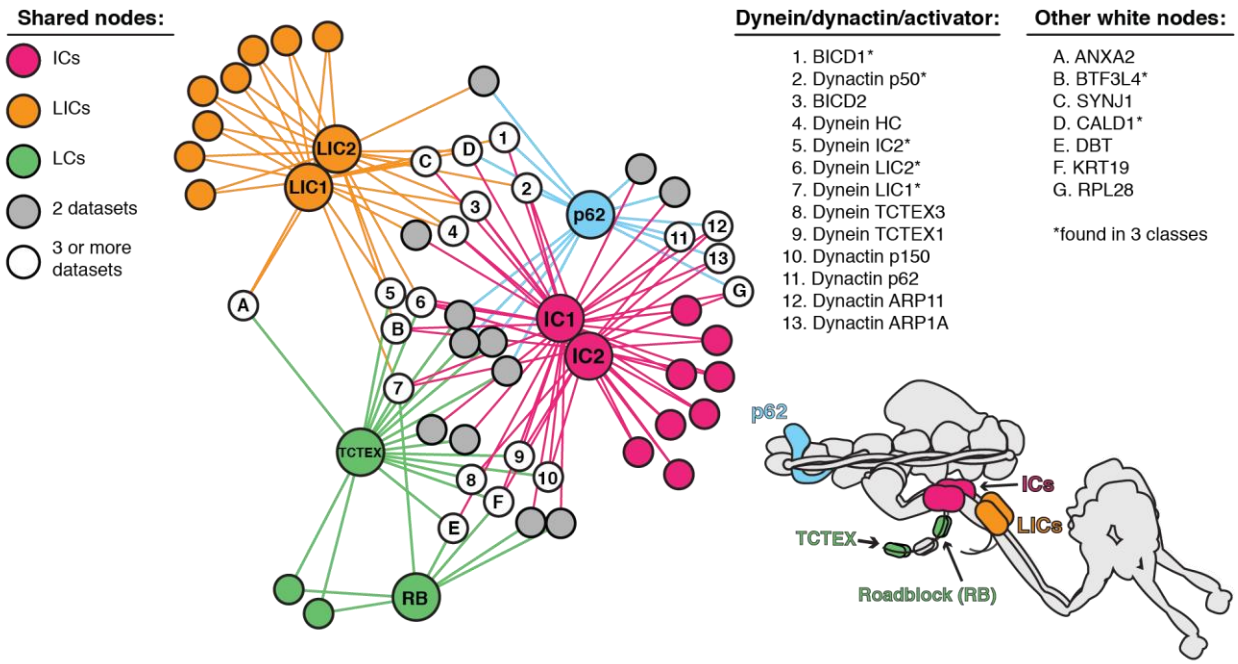

Figure C.2. Enriched and significant hits from dynein and dynactin BioID datasets were used to construct a protein-protein interaction network. Large spheres represent BioID-tagged subunits (color coded according to a schematic of the dynein/dynactin complex, bottom right). Hits (small spheres) specific to a subunit family, color-coded according to their respective subunits: LCs (green), ICs (magenta) and LICs (orange). Gray spheres ("2 datasets") and white spheres ("3 or more datasets") represent hits enriched in two or three separate datasets, respectively. The protein names corresponding to white spheres are listed, right. Dynein and dynactin subunits, and activators are numbered; other hits are indicated with letters. Asterisk denotes hits detected in 3 different subunit classes (e.g. LIC/IC/p62). Lines connecting spheres (edges) are color coded according to their respective datasets. For this figure enrichment is ≥ 3 fold, significance is $p < 0.05$, Student's two-tailed t-test; and average spectral counts are ≥2.

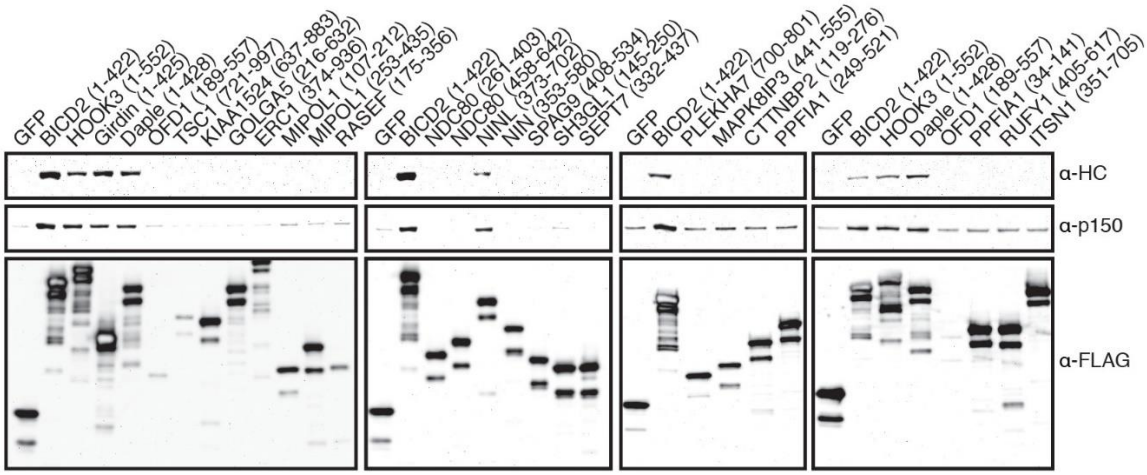

Figure C.3. Candidate and known (BICD2 and HOOK3) activators were tagged with 3×FLAG and immunoprecipitated with α-FLAG antibodies from HEK-293 cells. Western blots with α-HC and α-p150 antibodies were used to determine which proteins co-immunoprecipitated dynein and dynactin.

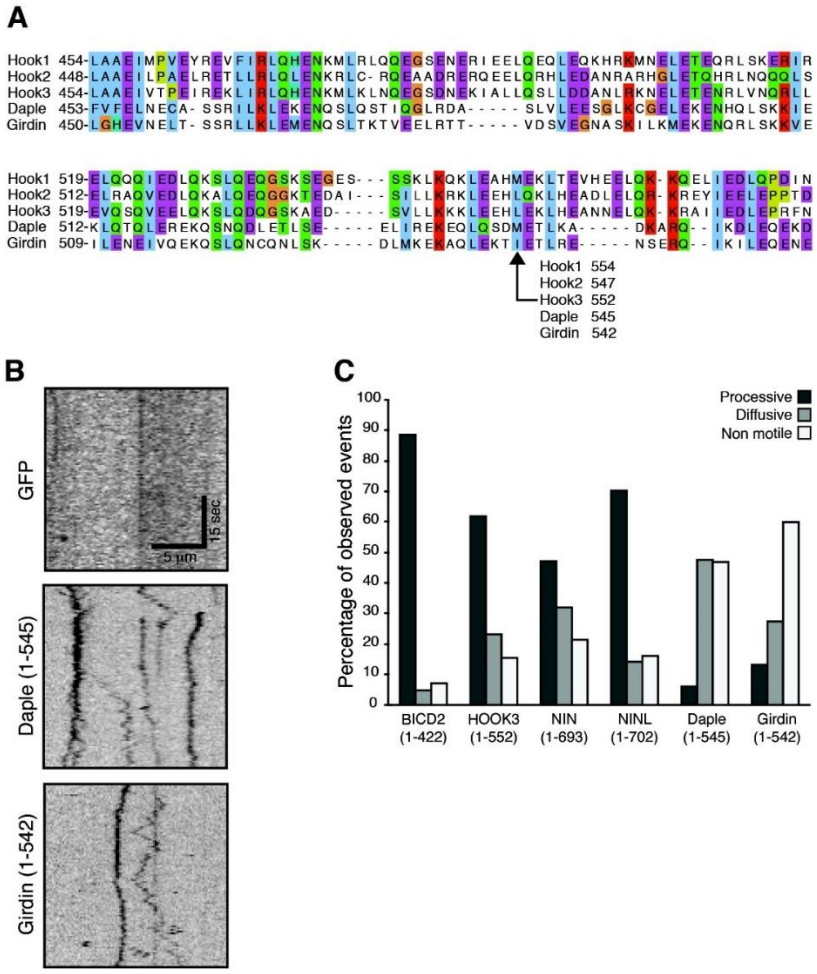

Figure C.4. Screening of potential dynein activators. (A) The amino acid sequences for HOOK1, HOOK2, HOOK3 and two HOOK-related proteins (daple and girdin) were downloaded from Uniprot and aligned using Clustal Omega. A region containing the HOOK3 (1–552) C-terminal truncation point is displayed and the residue in each protein equivalent to HOOK3 (1–552) is indicated. (B) As a control, GFP-3×FLAG was immunoprecipitated with an α-FLAG antibody from HEK-293 cells. No moving GFP signal was detected on microtubules. (C) The percentage of processive, diffusive and non-motile runs (see Materials and methods in Chapter 4) in single-molecule motility assays was analyzed for NIN (1-693), NINL (1-702), girdin (1-542) and daple (1-545) and compared to the known activators BICD2 (1–422) and HOOK3 (1–552).

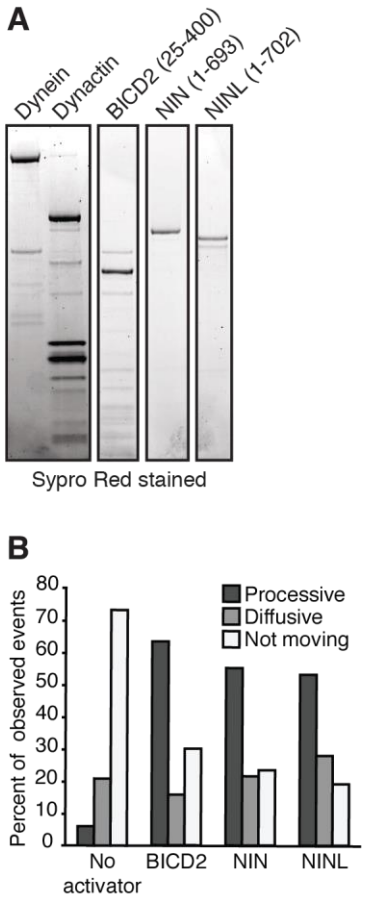

Figure C.5. Purification of dynein, dynactin and activators. (A) Dynein (IC2-SNAP-3×FLAG), dynactin (p62-Halo-3×FLAG) and the activators BICD2 (25-400), NIN (1-693) and NINL (1-702) (GFP-activator-Strep tag) were separately purified and used for the motility assays shown in Figure 5. An SDS-PAGE gel stained with Sypro Red shows the purification of each component. (B) The percentage of processive, diffusive and non-motile events in single-molecule motility assays (as described in E—G) was analyzed.

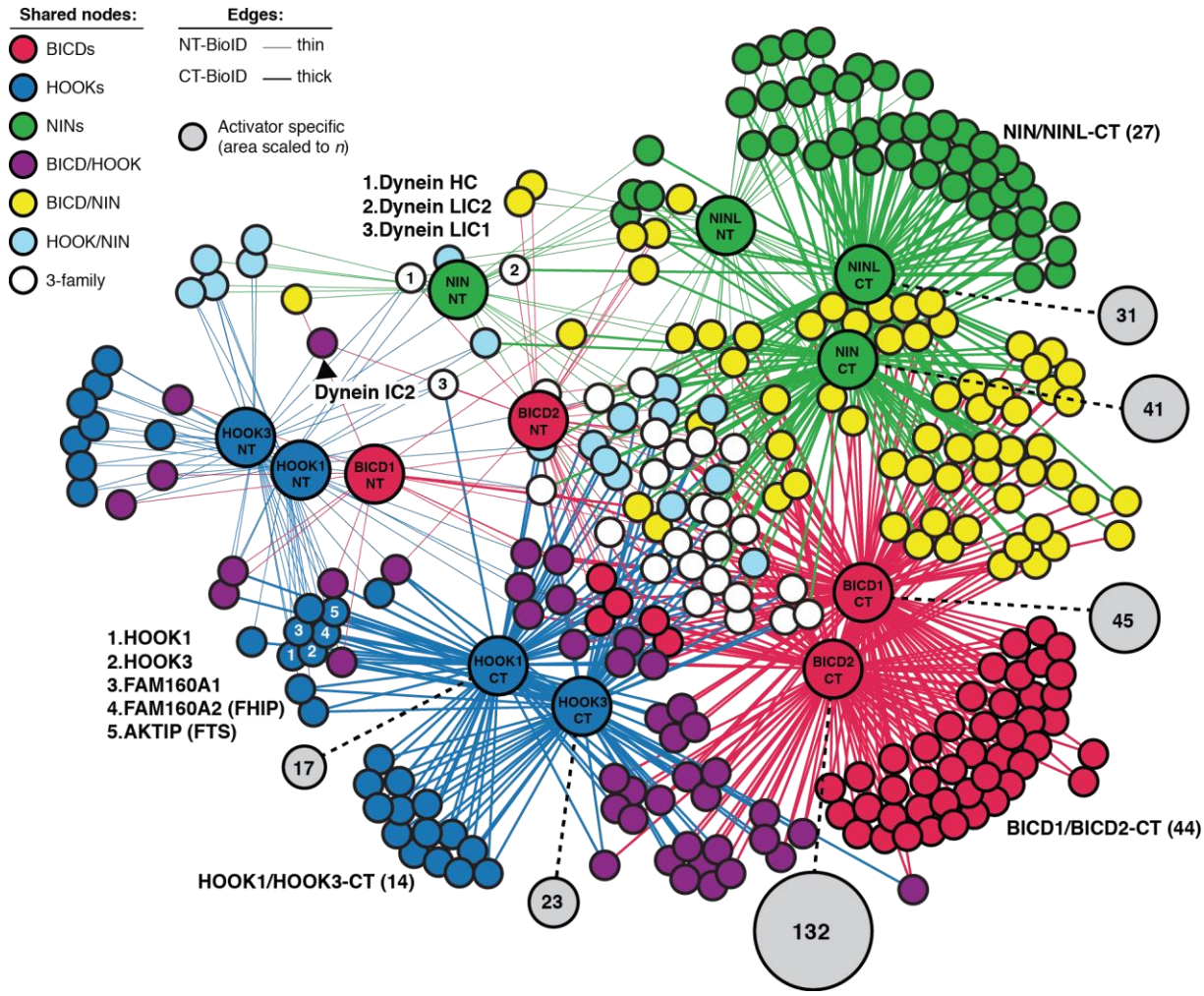

Figure C.6. An interaction map of the N- and C-terminal activator datasets combined. Enriched and significant hits from the combined N- and C-terminal datasets of six activators were used to construct a single protein-protein interaction network. Hits (small spheres) specific to an activator family (color-coded according to their respective activators), and hits shared between activator families (HOOK/BICD, purple; BICD/NIN, yellow; NIN/HOOK, cyan) are shown. White spheres ("3-family") represent hits enriched in at least one activator (NT or CT) from each family. Lines connecting spheres (edges) are color coded according to activator family and termini (NT = thin, CT = thick). The regions encompassing activator family CT-specific overlap are indicated with their respective *n*. The number of unique hits for each dataset is represented as a gray circle that is scaled according to the number of hits and the number of hits is shown. For this figure, enrichment is ≥ 3 fold, significance is $p < 0.05$, Student's two-tailed t-test; and average spectral counts are ≥2. The location of dynein and dynactin subunits and select hits discussed in the text are indicated.

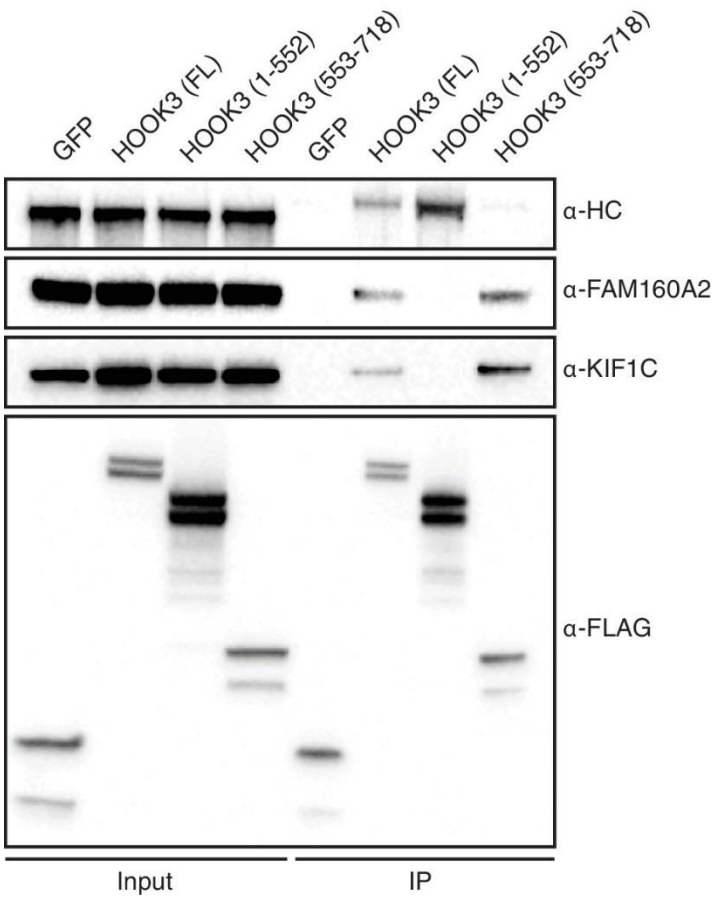

Figure C.7. KIF1C is a novel HOOK3-interacting protein.sfGFP-3×FLAG and full length (FL) HOOK3, HOOK3 (1–552), and HOOK3 (553–718) all tagged with sfGFP and 3×FLAG were immunoprecipitated with α-FLAG antibodies from transiently transfected HEK-293T cells. Western blots with α-HC, α-FAM160A2, α-KIF1C, and α-FLAG antibodies were used to determine which proteins co-immunoprecipitated with each HOOK3 construct.

C.2 Legends for supplementary files for Chapter 4

Supplementary file C.1. Master file of mass spectrometry data related to Figures 4.1, 4.2, 4.3 and 4.6 of Chapter 4 and Figure C.6. This excel file contains all of the mass spectrometry data referenced in the manuscript. The first blue tab corresponds to the Flag immunoprecipitation experiment in Figure 4.1B. The second blue tab contains the dynein core subunits detected in the Flag immunoprecipitation experiment, corresponding to Figure 4.1C. The purple tab contains all mass spectrometry data related to Figure 4.2. The pink tabs contain all of the dynein/dynactin interactome mass spectrometry data. This data was used to generate Figure 4.3C. The green tabs contain all of the activator interactome mass spectrometry data. This data was used to generate Figure 4.6 and Figure C.6. 'NT' and 'CT' indicate that the BioID tag was on the N-terminus or C-terminus of the full-length protein, respectively.

Supplementary file C.2. Mass spectrometry data related to Figure 4.2 of Chapter 4. This excel file contains the mass spectrometry data that was used to generate Figure 4.2C (second tab) and 4.2D (first tab).

Supplementary file C.3. Mass spectrometry data related to Figure 4.3C of Chapter 4 and Figure C.2. The blue tabs contain the BioID interactome data for IC1, IC2, LIC1, LIC2, TcTex, RB, and p62. Only the data for dynein and dynactin subunits and known (BICD2, HOOK1 and HOOK3) and suspected (BICD1) activators are shown. The blue tab titled 'mapping color code' lists the dynein and dynactin subunits enriched in the BioID experiments and graphically displayed in Figure 4.3C. Shading indicates enrichment value: light gray (2–3 fold) or dark gray (≥3 fold), $p<0.05$ (Student's two-tailed t-test). The entire datasets can be found in Supplementary

file C.1 (pink tabs). The pink tabs in this excel file contain all of the significant hits from each BioID tagged dynein and dynactin subunit. Significance was defined as >3 fold enrichment, p-values<0.05 (Students two-tailed t-test), and average spectral counts > 2. This data was used to generate the network shown in Figure C.2. The pink tab titled 'core hits' lists the gene names for all hits, specific hits (unique to each tagged subunit), and hits shared by at least two datasets, for the dynein and dynactin BioID tagged subunits. The pink tab titled 'core Venn' contains the output from the Venn analysis (http://bioinformatics.psb.ugent.be/webtools/Venn/) of the dynein and dynactin core subunit interactomes used to generate the network shown in Figure C.2. Proteins found in only one dataset are listed in the excel file, but not shown in the network.

Supplementary file C.4. Mass spectrometry data related to Figure 4.6 of Chapter 4 and Figure C.6. The green tabs contain all significant hits from the NT and CT BioID tagged activator datasets. Significance was defined as >3 fold enrichment, p-values<0.05 (Students two-tailed t-test), and average spectral counts > 2. The blue tab titled 'NT hits' lists the gene names for all hits, specific hits (unique to each tagged activator), and hits shared by at least two datasets, for the NT-activator BioID tagged subunits. The blue tab titled 'NT Venn' contains the output from the Venn analysis (http://bioinformatics.psb.ugent.be/webtools/Venn/) of the NT activator interactomes used to generate the network shown in Figure 4.6B. Proteins found in only one dataset are listed in the excel file, but not shown in the network. The blue tab titled 'white spheres NT' highlights (in grey) the four hits that were shared by an activator from each activator family (i.e. BICD, HOOK, and NIN). The orange tab titled 'CT hits' lists the gene names for all hits, specific hits (unique to each tagged activator), and hits shared by at least two datasets, for the CT-activator BioID tagged subunits. The orange tab titled 'CT Venn' contains the output from the

Venn analysis (http://bioinformatics.psb.ugent.be/webtools/Venn/) of the CT activator interactomes used to generate the network shown in Figure 4.6B. Proteins found in only one dataset are listed in the excel file, but not shown in the network. The orange tab titled 'white spheres CT' highlights (in grey) the 21 hits that were shared by an activator from each activator family (i.e. BICD, HOOK, and NIN). The pink tabs contain data that contrast all of the activator hits, combining the NT and CT datasets. The pink tab titled 'NT-CT combined hits' contains the gene names that are specific for each termini of each activator or shared between any dataset. The pink tab titled 'NT-CT combined Venn' contains the output from the Venn analysis (http://bioinformatics.psb.ugent.be/webtools/Venn/) of all activator interactomes used to generate the network shown in Figure C.6.

Supplementary file C.5. GO analysis of dynein activator C-terminal BioID datasets. This excel file contains gene ontology analyses using the 'cellular component' option (GO, geneontology.org). The GO terms with p-values<0.05 are shown for hits that were shared in at least three C-terminal BioID datasets; C-terminal hits that were specific to BICD2, HOOK1, HOOK3, NIN, and NINL; and C-terminal hits that were shared by activator family members BICD1 and BICD2, HOOK1 and HOOK3, and NIN and NINL.